

May 6, 1994

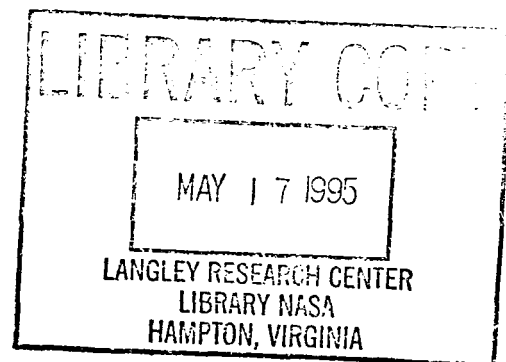
To the Graduate School:

This thesis entitled "Post-Impact Fatigue of Cross-Plied, Through-the-Thickness Reinforced Carbon/Epoxy Composites" and written by Thomas E. Serdinak is presented to the Graduate School of Clemson University. I recommend that it be accepted in partial fulfillment of the requirements for the degree of Master of Science with a major in Engineering Mechanics.

John M. Kennedy
Thesis Advisor

We have reviewed this thesis
and recommend its acceptance:

Sherrill L. Brinson
John A. Bore



Accepted for the Graduate School:

Celine M. Larson

(NASA-TM-110625) POST-IMPACT
FATIGUE OF CROSS-PLIED,
THROUGH-THE-THICKNESS REINFORCED
CARBON/EPOXY COMPOSITES M.S. Thesis
- Clemson Univ. (NASA Langley
Research Center) 176 p

N95-31419

Unclass

G3/39 0052968

DISPLAY 95N31419/2

95N31419*# ISSUE 11 PAGE 2896 CATEGORY 39

RPT#: NASA-TM-110625 NAS 1.15:110625 94/05/00 176 PAGES UNCLASSIFIED
DOCUMENT

UTTL: Post-impact fatigue of cross-ply, through-the-thickness reinforced
carbon/epoxy composites TLSP: M.S. Thesis - Clemson Univ.

AUTH: A/SERDINAK, THOMAS E.

CORP: National Aeronautics and Space Administration. Langley Research Center,
Hampton, VA.

SAP: Avail: CASI HC A09/MF A02

CIO: UNITED STATES

MAJS: /*EPOXY MATRIX COMPOSITES/*FATIGUE (MATERIALS)/*FATIGUE TESTS/*IMPACT
DAMAGE/*REINFORCING FIBERS/*STRESS-STRAIN RELATIONSHIPS/*WOVEN COMPOSITES
MINS: / CARBON FIBERS/ COMPRESSION LOADS/ COMPRESSIVE STRENGTH/ FAILURE MODES/
FATIGUE LIFE/ IMPACT LOADS/ LAY-UP/ REINFORCING MATERIALS/ TEXTILES

ABA: Author

ABS: An experimental investigation of the post-impact fatigue response of
integrally woven carbon/epoxy composites was conducted. Five different
through-the-thickness (TTT) reinforcing fibers were used in an
experimental textile process that produced an integrally woven
(0/90/0/90/0/90/0/90/0) (sub T) ply layup with 21K AS4 carbon tow fiber.
The resin was Hercules 3501-6, and the five TTT reinforcing fibers were
Kevlar, Toray carbon, AS4 carbon, glass, and IM6 carbon. The purpose of

ENTER: MORE

4B. A ^ ==PC LINE 24 COL 9

DISPLAY 95N31419/2

this investigation was to study the post-impact fatigue response of these material systems and to identify the optimum TTT fiber. Samples were impacted with one half inch diameter aluminum balls with an average velocity of 543 ft/sec. Post-impact static compression and constant amplitude tension-compression fatigue tests were conducted. Fatigue tests were conducted with a loading ratio of $R=-5$, and frequency of 4 Hz. Damage growth was monitored using x-radiographic and sectioning techniques and by examining the stress-strain response (across the impact site) throughout the fatigue tests. The static compressive stress versus far-field strain response was nearly linear for all material groups. All the samples had a transverse shear failure mode. The average compressive modulus (from far-field strain) was about 10 Msi. The average post-impact static compressive strength was about 35.5 Ksi. The IM6 carbon sample had a strength of over 40 Ksi, more than 16 percent stronger than average. There was considerable scatter in the S-N data. However, the IM6 carbon samples clearly had the best fatigue response. The response of the other materials, while worse than IM6 carbon, could not be ranked definitively. The initial damage zones caused by the impact loading and damage growth from fatigue loading were similar for all five TTT reinforcing materials. The initial damage zones were circular and consisted of delaminations, matrix cracks and ply cracks. Post-impact fatigue loading caused delamination growth, ply cracking and fiber bundle failures, typically 45

ENTER:

MORE

4B.

A

^

--PC LINE 24 COL 9

DISPLAY 95N31419/2

deg from impact load direction. During the initial 97 percent of fatigue life, delaminations, ply cracks and fiber bundle failures primarily grew at and near the impact site. During the final 3 percent of life, damage grew rapidly transverse to the loading direction as a through-the-thickness transverse shear failure. The stress-strain response was typically linear during the initial 50 percent of life, and stiffness dropped about 20 percent during this period. During the next 47 percent of life, stiffness dropped about 34 percent, and the stress-strain response was no longer linear. The stiffness decreased about 23 percent during the final 3 percent of life. These trends were typical of all the materials tested. Therefore, by monitoring stiffness loss, fatigue failure could be accurately anticipated.

ENTER:

4B•

A

^

--•PC LINE 24 COL 9

POST-IMPACT FATIGUE OF CROSS-PLIED, THROUGH-THE-THICKNESS
REINFORCED CARBON/EPOXY COMPOSITES

A Thesis
Presented to
the Graduate School of
Clemson University

In Partial Fulfillment
of the Requirements for the Degree
Master of Science
Engineering Mechanics

by
Thomas E. Serdinak
May 1994

N95-31419#

ABSTRACT

An experimental investigation of the post-impact fatigue response of integrally woven carbon/epoxy composites was conducted. Five different through-the-thickness (TTT) reinforcing fibers were used in an experimental textile process that produced an integrally woven $[0/90/0/90/0/90/0/90/0]_T$ ply layup with 21K AS4 carbon tow fiber. The resin was Hercules 3501-6, and the five TTT reinforcing fibers were Kevlar, Toray carbon, AS4 carbon, glass, and IM6 carbon. The purpose of this investigation was to study the post-impact fatigue response of these material systems and to identify the optimum TTT fiber.

Samples were impacted with one half inch diameter aluminum balls with an average velocity of 543 ft/sec. Post-impact static compression and constant amplitude tension-compression fatigue tests were conducted. Fatigue tests were conducted with a loading ratio of $R=-5$, and frequency of 4 Hz. Damage growth was monitored using x-radiographic and sectioning techniques and by examining the stress-strain response (across the impact site) throughout the fatigue tests.

The static compressive stress versus far-field strain response was nearly linear for all material groups. All the samples had a transverse shear failure mode. The average compressive modulus (from far-field strain) was about 10 Msi. The average post-impact static compressive strength was about 35.5 Ksi. The IM6 carbon sample had a strength of over 40 Ksi, more than 16% stronger than average. There was considerable scatter in the S-N data. However, the IM6 carbon samples clearly had the best fatigue response. The response of the other materials, while worse than IM6 carbon, could not be ranked definitively.

The initial damage zones caused by the impact loading and damage growth from fatigue loading were similar for all five TTT reinforcing materials. The initial damage

zones were circular and consisted of delaminations, matrix cracks and ply cracks. Post-impact fatigue loading caused delamination growth, ply cracking and fiber bundle failures, typically 45° from impact load direction. During the initial 97% of fatigue life, delaminations, ply cracks and fiber bundle failures primarily grew at and near the impact site. During the final 3% of life, damage grew rapidly transverse to the loading direction as a through-the-thickness transverse shear failure.

The stress-strain response was typically linear during the initial 50% of life, and stiffness dropped about 20% during this period. During the next 47% of life, stiffness dropped about 34%, and the stress-strain response was no longer linear. The stiffness decreased about 23% during the final 3% of life. These trends were typical of all the materials tested. Therefore, by monitoring stiffness loss, fatigue failure could be accurately anticipated.

ACKNOWLEDGMENTS

I would like to express my genuine appreciation to my graduate committee, Dr. Sherrill B. Biggers and Dr. James G. Goree for their recommendations for and endorsement of this manuscript.

I wish to make particular mention of my appreciation for the constant support of my advisor Dr. John M. Kennedy, without whom my successful completion of this graduate program would not have been possible. He has provided a great deal of assistance in every facet of my graduate work.

Additionally, I would like to thank Gary L. Farley and NASA Langley Research Center for providing the material used in this research.

I would also like to thank Linda Cocke, Lynn Henson, Ingrid Jackson, Wanda Reed, and Jackie Swaney for their continual assistance in the preparation of this manuscript and during my time at Clemson.

Finally, I wish to thank my parents, Sue Serdinak and Ed Serdinak, for their unending support and encouragement in all my endeavors. Without their support none of my accomplishments would have been possible.

TABLE OF CONTENTS

	Page
TITLE PAGE	i
ABSTRACT	ii
ACKNOWLEDGMENTS	iv
LIST OF TABLES	vii
LIST OF FIGURES	viii
CHAPTER	
I. INTRODUCTION AND BACKGROUND	1
Impact	2
Damage Evaluation	2
Compression of Damaged Composites	4
Post-Impact Fatigue	6
Fatigue Loading	10
Material Behavior	11
Research Objective	12
II. EXPERIMENTAL PROCEDURE	14
Material Description	14
Impact Device	17
Static Compression Tests	21
Post-Impact Fatigue Tests	25
Evaluation of Damage	33
Radiography	33
Sectioning	34
III. RESULTS	36
Discussion of Post-Impact Loading	36
Impact Damage	38
Static Compression Results	42
Tension-Compression Fatigue Results	49
Fatigue Life	49
Damage Zone Growth	57
Fatigue Cycles	67
Stiffness Loss	82
IV. CONCLUSIONS	93

Table of Contents (Continued)

	Page
APPENDICES	95
A. Impact and Post-Impact Fatigue Loading Damage: Radiographs	96
B. Impact and Post-Impact Fatigue Loading Damage: Photo-Micrographs	107
C. Mechanical Response of Post-Impact Fatigue Loading: Changes in Modulus, Strain and Hysteresis	123
LITERATURE CITED	161

LIST OF TABLES

Table	Page
I. Sample Thicknesses	19
II. Static Compression Results	44
III. S-N Regression Data from Fatigue Data for Each TTT Material	56
IV. Mechanical Properties of TTT Reinforcing Fibers	66
V. Initial Post-Impact Fatigue Stiffnesses	86

LIST OF FIGURES

Figure	Page
1. Typical S-N curves for undamaged and notched laminates	8
2. Stress versus strain for one cycle in a fatigue test	9
3. Integrally woven 3-D architecture	15
4. Integrally woven preform	16
5. Integrally woven carbon/epoxy 16" by 14" composite panel	18
6. Impact device	20
7. Side supports	22
8. Location of strain gages on static compression samples	23
9. Instron load frame and electronic controller	24
10. Geometry of extensometer tabs	26
11. Extensometers	27
12. Extensometer attached to tabs mounted across impact site on sample	28
13. Instron load frame and electronic controller with sample mounted for fatigue test	30
14. Load cycle for fatigue tests	31
15. Location of sectioning cuts	35
16. Radiographs of impact damage in sample from each material group	39
17. Typical post-impact damage in cross-section at center of impact site	41
18. Stress versus far-field strain under static compressive loading	43
19. Compressive elastic modulus calculated from actual and average thicknesses	46
20. Compressive failure strength calculated from actual and average thicknesses	48
21. Maximum compressive stress versus cycles for each material	50

List of Figures (Continued)

Figure	Page
22. Maximum compressive stress versus cycles for all materials	54
23. Radiographs of post-impact fatigue damage from typical test	58
24. Transverse shear failure mode	61
25. Typical cross-section at center of impact site immediately prior to fatigue failure	63
26. Waviness of in-plane fibers	65
27. Stress versus strain across front and back faces at impact site for one cycle early in a typical fatigue test	68
28. Maximum compressive strain from front and back extensometers throughout a typical fatigue test	69
29. Far-field stress versus average strain across impact site during a typical fatigue test	71
30. Far-field stress versus average strain at minimum stress during last full cycle of a typical fatigue test	74
31. Definition of moduli	76
32. Changes in hysteresis throughout a typical fatigue test	77
33. Changes in maximum and minimum strain throughout a typical fatigue test	79
34. Changes in moduli throughout a typical fatigue test	80
35. Stiffness loss throughout each fatigue test	83
36. Average initial post-impact fatigue and undamaged static stiffness for each TTT material	87
37. Normalized stiffness loss throughout each fatigue test	88
38. Stiffness loss regions	91

CHAPTER I

INTRODUCTION AND BACKGROUND

Fiber-reinforced composite materials have advanced from novel materials to the point where they are extensively used in the aerospace industry. Originally, experimental materials were manufactured merely to determine their mechanical properties. Then, composite parts were built and designed to replace metallic components. Recently, numerous components (primarily on fighter planes) have been designed and fabricated to take advantage of the anisotropic nature of fibrous composite materials. The current trend has been to extend the application of fibrous composite materials to large cargo/transport and new military cargo airplanes. Studies have shown that by the year 2000, composites could account for more than half the structural weight of an aircraft [1].

Composites offer significant strength-to-weight improvements over conventional materials, which could reduce the weight of transport aircraft by as much as 25% over aluminum. This would result in a 12% to 15% reduction in fuel consumption or an increase in payload [2]. Additionally, brittle fibrous composites can offer advantageous stiffness-to-weight characteristics. However, brittle composites are extremely sensitive to out-of-plane impacts. This has severely limited the application of these materials to the aerospace industry. Therefore there has been a need for composites that are more tolerant of impact damage. This need is being addressed by the development of tougher resin systems and the use of 3-D fiber architecture. Both approaches offer much better damage tolerance than first generation composites that were made with brittle matrices and no through-the-thickness reinforcement.

Use of composites in aircraft require that impact damage tolerance and damage growth in these composites be evaluated. Over the past two decades there have been numerous studies concerning the mechanical response of composites subjected to impact

loading. Throughout these studies, testing conditions have been varied to model different impact and loading conditions typical of aircraft structural applications.

Impact

There have been several techniques used to create impact damage. The tests ranged from high-velocity ballistic impact to low-velocity impact [3-20]. Depending on the impact conditions, the damage may or may not be visually detectable. In addition to tests evaluating the mechanical response of composites subjected to impact loading, there have also been numerous projects evaluating the mechanical response of composites with notches, surface scratches, and other flaws [21-33].

Composites have been impacted with a variety of impactor masses and geometries. The impact devices have typically been either drop weight impactors or projectile discharging air guns. Drop weight impactors have been used to imitate low-velocity impact, such as manufacturing damage caused by tool impact. Projectile impact damage generally replicates collisions incurred during flight or during take-off or landing.

Regardless of the type of impact being modeled, changes in the mass or velocity of the impactor significantly affect the size and subsequent growth of the damage zone. Studies have been conducted using impact energy as the governing factor in the characterization of damage and damage growth. However impact energy alone has been demonstrated to be an inadequate parameter. The velocity and mass should both be considered in the characterization of impact damage [11] and damage growth [7].

Damage Evaluation

There have been various techniques used to evaluate and monitor damage in composites. Laminates with notches, imbedded delaminations and impact damage have been monitored to study damage growth and failure modes. Nondestructive evaluation techniques offer the most practical and beneficial methods for monitoring flaws. The

obvious advantage of this type of evaluation is that the nondestructive nature of the techniques allows for continued testing of the samples.

Moiré-fringe patterns have been used to show out of plane deformations and plastic zone growth in thin composite laminates [40], and scanning electron microscopy has been used to examine fracture surfaces [9,30,31]. However, the primary nondestructive techniques used for the evaluation of composites have been penetrant-enhanced radiography and ultrasonic C-scanning.

Conventional radiographic procedures have shown poor flaw contrast in low-density inhomogeneous composite materials [39]. This has lead to the development of radio-opaque penetrants and low-kilovolt X-ray radiography procedures. Damage sites have been injected with tetrabromoethane (TBE), diiodobutane, zinc iodide, and other enhancing penetrants. These techniques have lead to the detection of matrix cracking, fiber bundle fractures and delaminations [30-32].

Ultrasonic inspection techniques are more widely used inasmuch as ultrasonic technology has improved and become more available. This procedure involves the emission of high-frequency sounds in periodic bursts from a transducer. The sound waves travel through a coupling medium (typically water) and through the material, and the resulting pulse is monitored by a receiving transducer. Differences in peek amplitudes of the ultrasonic waves transmitted through the material (C-scans) typically are due to delaminations, porosity, or surface defects. However, both conventional C-scans and radiography fail to give information regarding through-the-thickness distribution of damage.

Sectioning has been used to monitor through-the-thickness damage. These sections have been polished and examined using light microscopy [16,40]. This technique has been used to detect delaminations and matrix cracks through-the-thickness of the material.

Compression of Damaged Composites

Much of the kinetic energy imparted during the impact event produces matrix intraply cracking, fiber/matrix debonding, and interply delaminations in a composite laminate. Delaminations reduce the laminate's compressive stability [29] and can greatly diminish the in-plane compressive strength.

Impact damage, which may not be visually detectable, can cause local instability. This can lead to a reduction in static compressive strength, because failure is typically due to local buckling of the in-plane fibers [5]. Predominantly, composite compression tests have been conducted which prevent column-type buckling. However, even when tested in an apparatus designed to prevent macroscopic buckling, the region of weakness in a composite can still delaminate and buckle locally [30].

This buckling failure mode often reduces the static compressive strength of a material by as much as half of its undamaged strength. Avery and Porter [4] demonstrated that both metal and fiber composite panels lose at least 50% of their undamaged strength when impacted with small arms projectiles. Furthermore, Moon and Kennedy [16] found that the compressive strength of a quasi-isotropic composite with low-velocity impact damage was reduced to about one third of its original strength.

Starnes et al. [40] studied successive moiré-fringe patterns of laminates with low-velocity impact damage. At 48% of the specimen residual strength, there was a small circular region of local out-of-plane deformation at the original impact site. The fringe patterns observed between 61% to 98% of the residual strength showed lateral growth of a local buckling region as the load was increased. At 98%, the local buckling region was elliptical, and the length of the major axis (perpendicular to the load direction) was about twice the diameter of the impact site. Examination of the failed specimen confirmed that the damage was confined to a narrow region transverse to the loading direction.

Soutis and Fleck [30] used radiography and microscopy to study the static compressive failure of a composite plate with a single hole. Initial damage in the laminate

consisted of matrix cracking near the hole surrounded by delaminations. Microscopic observations of Liu et al. [9] showed that there is an interaction between matrix cracking and delamination. This damage occurs at the edge of the hole at locations of high in-plane compressive stress. There is also fiber microbuckling that intensifies with increasing load and is confined to areas subjected to high axial compressive stress. At ultimate load the microbuckled zone propagates rapidly transverse to the load direction, and the composite fails.

Microbuckling in the 0° plies is thought to be the critical failure mechanism, and matrix splitting and delamination are thought to be secondary damage modes. Moreover, fiber microbuckling can cause high interlaminar stresses that subsequently lead to additional delamination growth [29]. Several studies have yielded the same conclusions about damage growth and failure modes [3,24,32,33].

The introduction of stress risers, such as notches or impact damage, can lead to damage growth and failure at lower load levels. The reduction of strength has been found to be similar for composites with both notches and impact-induced damage. A drilled hole (notch) was found to be about as detrimental to the strength of a composite as was an impact event causing broken fibers on the surface [21].

Ramkumar [22] studied the effect of imbedded delaminations on compressive failure modes of composite laminates. Imbedded delaminations located just below the 0° surface ply allow large transverse deflections of the delaminated ply. These large deflections cause matrix cracking between fibers. Circular imbedded delaminations induce matrix cracking along 0° lines tangent to the initial circular geometry. Matrix cracks and delaminations then grow in areas subject to high compressive stress, analogous to a laminate with a circular hole. However, in contrast to other studies, Ramkumar's photomicrographs indicate the absence of fiber microbuckling. In all of these studies, failure was found to propagate in an unstable manner.

Stable damage growth is an obvious requirement for damage tolerant aircraft structures. However, composites are non-homogeneous, and even microscopic inconsistencies can lead to changes in damage propagation. Also, local delaminations create local strain concentrations that may cause nominal failure strains below the failure strain of the primary load-bearing plies [34]. Fiber and matrix cracks can also lower the strain levels at which fiber microbuckling initiates.

Since fiber microbuckling is evidently the critical failure mechanism, the strain level at which fiber microbuckling initiates can be an important parameter in predicting compressive strength. At least six factors have been identified which affect the strain levels at which fiber microbuckling initiates: orientation of the supporting plies adjacent to the 0° plies, effects of free surfaces, fiber/matrix interfacial bond strength, degree of initial fiber waviness, thickness of resin-rich regions between the plies, and non-linear resin shear constitutive behavior [33].

Post-Impact Fatigue

If an aircraft structure initially survives impact damage, it may remain in service. The structure, therefore, must be able to withstand post-impact-fatigue loading by maintaining a relatively high residual strength [4]. Consequently, damage tolerance and durability concepts must be developed and evaluated under simulated loading on subcomponents of aircraft structures. Post-impact fatigue loading can be used as a simplistic representation of actual loading on aircraft structural members. Therefore, the post-impact fatigue response of composites can be important for the determination of their applicability to aircraft structures.

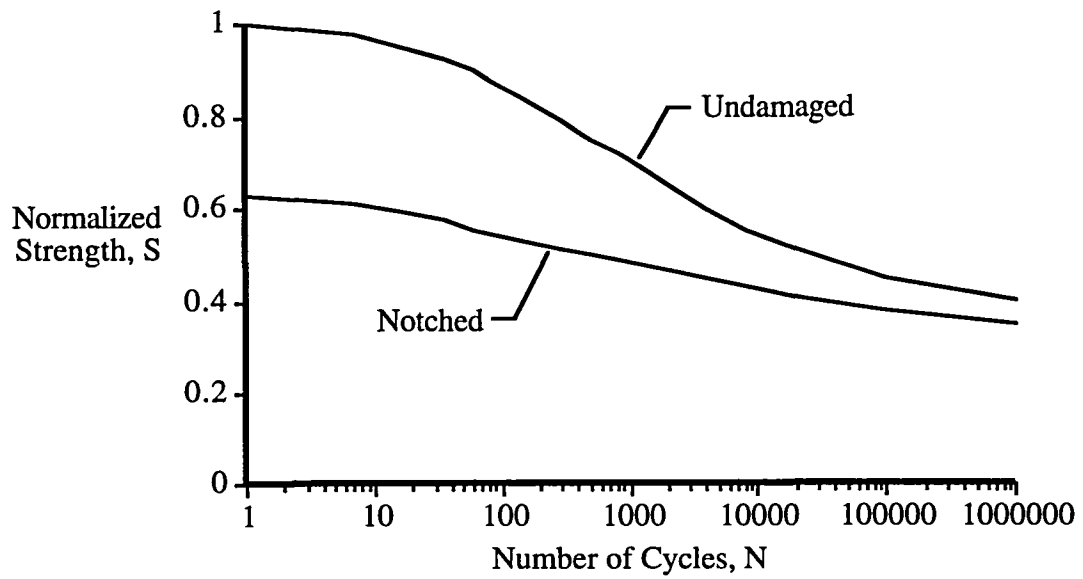
Impact damage greatly reduces the fatigue life in composites. The fatigue response of composites subjected to low-velocity impacts is typically less than the fatigue response of composites with an open hole [8]. However, for many cases the residual static strength after low level cyclic loading is greater than the post-impact static strength [28]. This event is due to the redistribution of stresses in the composite [26]. Obviously, fatigue response

of a composite depends on the severity of the impact event. Damage generally grows more rapidly in composites with half-penetration impact damage than with full-penetration impact damage.

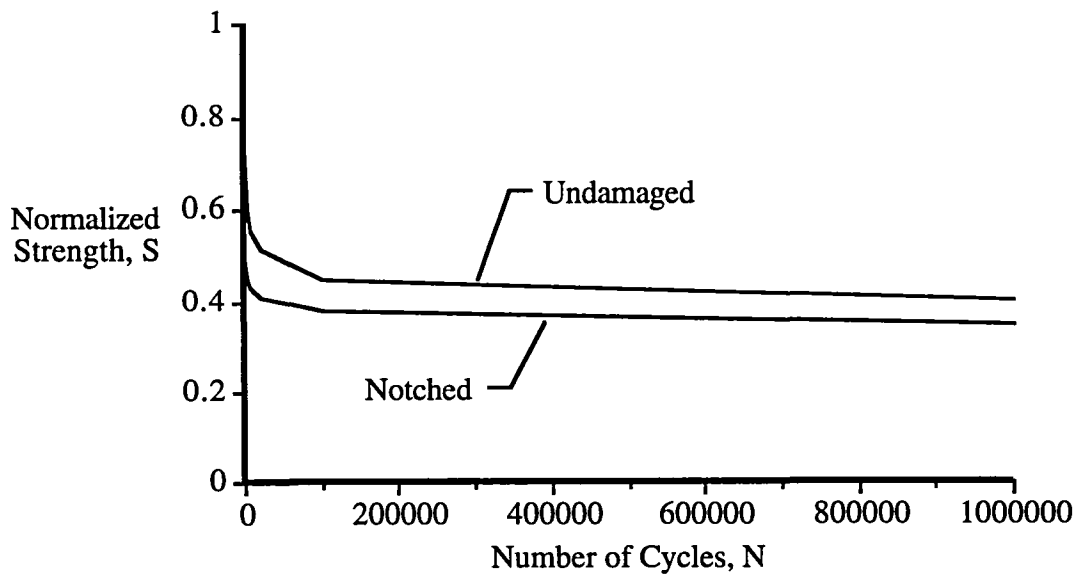
Damage growth mechanisms and failure modes for fatigue loaded composites are essentially the same as those for statically loaded composites. The failure modes due to compressive fatigue loading are well represented by failure modes from static compression tests. Interactions between matrix cracks and delaminations cause fiber microbuckling, which is often considered the main failure mechanism.

The maximum compressive stress plotted versus the number of cycles to failure (S-N curve) can be used to predict life for the given material and loading conditions. Typically, the fatigue strength of an undamaged laminate drops sharply in the short life region, as seen in Figure 1. However in the long life region (greater than 10^5 cycles), the slope of the S-N curve approaches zero [16]. Similarly, the reduction of fatigue strength in damaged laminates is greatest in the short life region. Interestingly, in the long life region, the fatigue strength of laminates with initial damage is similar to the fatigue strength of laminates with no initial damage [25].

In addition to actual damage growth, the fatigue response of a composite can also be described by monitoring strain across the damage site. The stress-strain response for one cycle of a fatigue test is shown in Figure 2. The secant modulus or stiffness for each cycle is the slope of the line between the points of maximum stress and minimum stress. As fatigue damage increases, in the form of matrix cracks and delaminations, stiffness loss increases [35-36]. When the stiffness loss is severe, failure occurs. By monitoring stiffness loss, failure can be predicted for the given material and loading conditions [37]. For an orthotropic fibrous composite lamina there are four in-plane independent elastic constants that characterize material stiffness, assuming a plane stress state. Each constant may change in a different way depending on the damage mode [35]. Therefore, changes in all four independent tensor moduli interact in a complex manner to produce stiffness



a. Log Scale



b. Normal Scale

Figure 1. Typical S-N curves for undamaged and notched laminates.

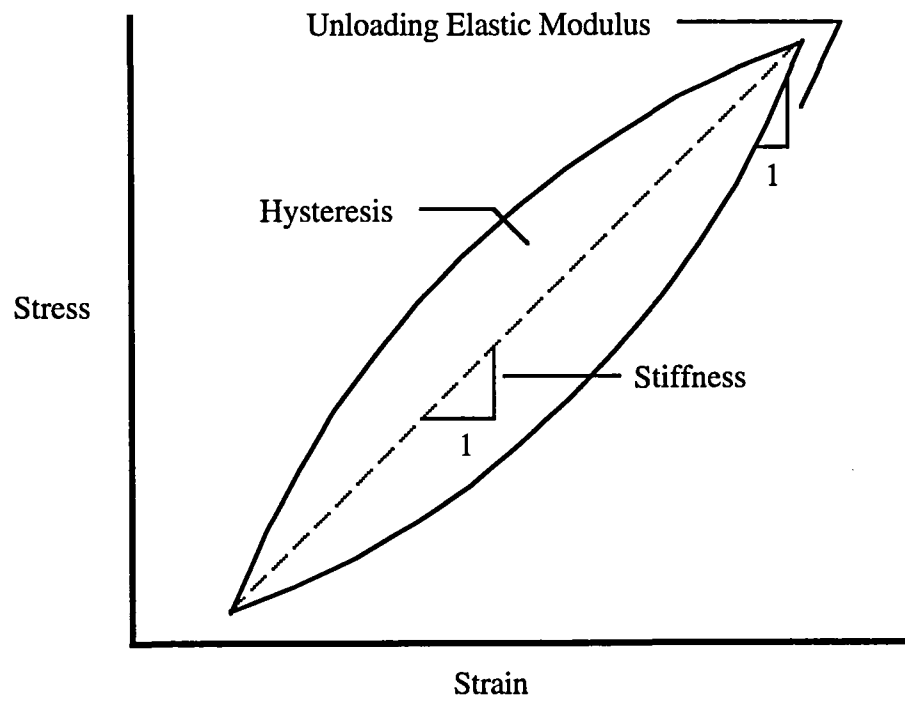


Figure 2. Stress versus strain for one cycle in a fatigue test.

changes in a laminate [35]. Consequently, Johnson [38] introduced the unloading elastic modulus as a more direct indicator of fatigue damage.

Failure can also be predicted for the material and loading conditions by monitoring the hysteresis energy throughout a fatigue test. The hysteresis energy, area enclosed by the stress-strain curve for one cycle, increases as fatigue damage increases. This approach may also be a more direct indicator of fatigue damage, because it does not appear to be influenced by local buckling [16].

Fatigue Loading

Routine inspections are conducted to monitor damage growth in aircraft structural members. The inspection intervals are based on expected damage growth for the given material. If damage zones grow to the pre-determined critical damage length, the aircraft is grounded for repair. Consequently, structural fatigue tests that simulate flight conditions are required as part of the aircraft certification process. Fibrous composites must respond well to fatigue loading to be a viable replacement for conventional materials. However, the material response is dependent on the type of post-impact-fatigue loading.

The fatigue life and damage propagation in a material vary with the loading rate. In general, composites loaded at higher frequencies survive more cycles to failure than composites loaded at lower frequencies [29]. The main cause of this appears to be the relation between frequency and dynamic modulus. Among material groups the initial dynamic modulus varies with the log of the frequency. Also, low-frequency fatigue loading produces more concentrated, local damage with greater damage-induced stiffness reduction. High-frequency loading produces more dispersed damage with less stiffness loss [45]. The author offers no explanation for this mechanical phenomenon.

The material fatigue response is even more dependent on the loading ratio ($R = \text{minimum load}/\text{maximum load}$). Generally, the loading becomes more harmful as the amplitude of the maximum compressive load approaches the amplitude of the maximum tensile load (as R approaches ± 1). Also, cyclic compressive loading is more damaging to

composites than cyclic tensile loading [46]. Therefore $R = -1$ typically corresponds to the harshest constant amplitude fatigue loading on composites.

Material Behavior

The arrangement of lamina in a fibrous composite laminate greatly affects the material's impact response. Differences in ply orientation cause totally different failure modes and failure loads [31]. The direction of the damage propagation depends on the laminate's stacking sequence [23]. Additionally, damage zone size (from impact loading) is typically smaller for thick laminates than thin laminates. However, for low impact velocities, the size of the damage zones is not greatly affected by laminate thickness [12]. Even though the size of damage zone (from impact loading) can be dependent on laminate thickness, it is more dependent on changes in the stacking sequence [11].

Improvements in impact damage tolerance have been made by altering the resin systems in fibrous composites. The impact damage in composites made with tough resin systems is much smaller than the damage found in composites made with brittle resin systems [14]. This improvement has lead to improvements in post-impact compressive strength over brittle resin systems [13]. However, tough resins are up to ten times more expensive than brittle resins.

Through-the-thickness (TTT) reinforcing stitching offers an alternate approach for improving the damage resistance of laminated composites. This type of reinforcement constrains out-of-plane deformation and generally the greater the stitching density, the smaller the area of delamination due to impact [30]. Liu [17] found that TTT stitching can reduce the delamination area in a plate subjected to low-velocity impact by as much as 40 percent.

Although TTT reinforcement reduces the damage zone size from impact loading, compression-after-impact tests have produced varying results. Static compression and fatigue tests on laminates with an open hole demonstrated strength reduction with the addition of TTT stitching [20]. The use of TTT stitching can reduce the undamaged

compression strength of the material by 20 to 25 percent [18,19]. Chung et al. [43] found that stitching through prepreg layers often results in in-plane fiber damage. Additionally, Farley [42] hypothesized that waviness and "kinking" of in-plane fibers caused by the inclusion of TTT reinforcement lead to the strength reduction. It was shown that the surface loop of the TTT reinforcement "kinked" the in-plane fibers in the surface plies in both the stitching and weaving processes. These "kinked" fibers were unable to carry significant compressive loads.

By removing the surface loop and "kinked" fibers, the strength was increased by 7 to 35 percent [42]. Also by improving the material production process, in-plane stitching damage and waviness due to TTT reinforcement could be reduced. Moreover, TTT stitching (like tough resin systems) suppresses delamination propagation [14,43] and usually slows the failure process. Therefore, as production processes improve, TTT reinforcement should improve the damage tolerance and durability of the material systems.

Moon and Kennedy [16] showed that TTT reinforcement could be used instead of tough resin systems to improve damage resistance and tolerance. Undamaged laminates with TTT reinforcement had slightly higher compressive strengths than undamaged, unstitched laminates made with the same uniweave cloth. The fact that these laminates (with TTT stitching) responded better than those from earlier tests [18-20] was attributed to improvements in material production. Stitching also improved the compression-after-impact response for all stitching densities tested. Likewise, laminates with TTT stitching showed better post-impact fatigue response than unstitched laminates. Furthermore, dense stitching offered post-impact fatigue improvements comparable to tough resin systems.

Research Objective

These studies have shown that TTT reinforced composites have substantial potential for use in aircraft structures. However, the post-impact fatigue response of integrally woven TTT reinforced composites has not been adequately studied. Additionally, the mechanical properties of the TTT reinforcing materials that contribute to improvements in

damage growth tolerance have not been investigated. Therefore, this study was initiated to determine the post-impact static compression and tension-compression fatigue response of composites with five different TTT reinforcing materials. Damage growth during fatigue tests was monitored using radiographic and sectioning techniques. Changes in average strain across the impact site of each sample was also monitored to anticipate fatigue failure.

CHAPTER II

EXPERIMENTAL PROCEDURE

Material Description

The materials evaluated in this study were integrally woven composite material with TTT reinforcement, fabricated by Textile Technologies. The preform design was a nine layer noncrimped preform with five layers oriented in the warp direction and four layers oriented in the fill direction. The ply layup was $[0/90/0/90/0/90/0/90/0]_T$. Both warp and fill yarns were 21K filament count AS4 carbon fibers. This 21K yarn consisted of a combination of AS4 sized 12K, 6K and 3K yarns served together with a fine denier PVA monofilament. The serving yarn comprised less than one percent of the total fiber weight. Each of the nine layers had thirteen 21K yarns per inch without interconnection between layers.

The inplane yarns were held together with TTT reinforcement. Five different TTT reinforcements were used: Kevlar 29, 1500 denier; Toray carbon, T-1000; AS4 carbon, 9K; S2 75 1/3 glass (three yarns twisted together); and IM6 carbon, 6K. The TTT yarns originated from the upper and lower surfaces of the preform and looped around a catcher yarn. As shown in Figure 3, the catcher yarn, AS4 carbon fibers, is located in the center of the preform. The preform had TTT reinforcement in both the warp and fill directions with an approximate row spacing of 0.2520 inches and TTT penetration spacing of 0.1260 inches. The TTT yarns in the warp direction were looped around catcher yarn in the fill direction, and TTT yarns in the fill direction were looped around catcher yarn in the warp direction. A preform is shown in Figure 4. Hercules 3501-6 epoxy resin was infiltrated into the preforms using a resin transfer molding (RTM) technique, and the materials were cured in an autoclave [19]. The resin infiltration and material curing were performed at The NASA Langley Research Center.

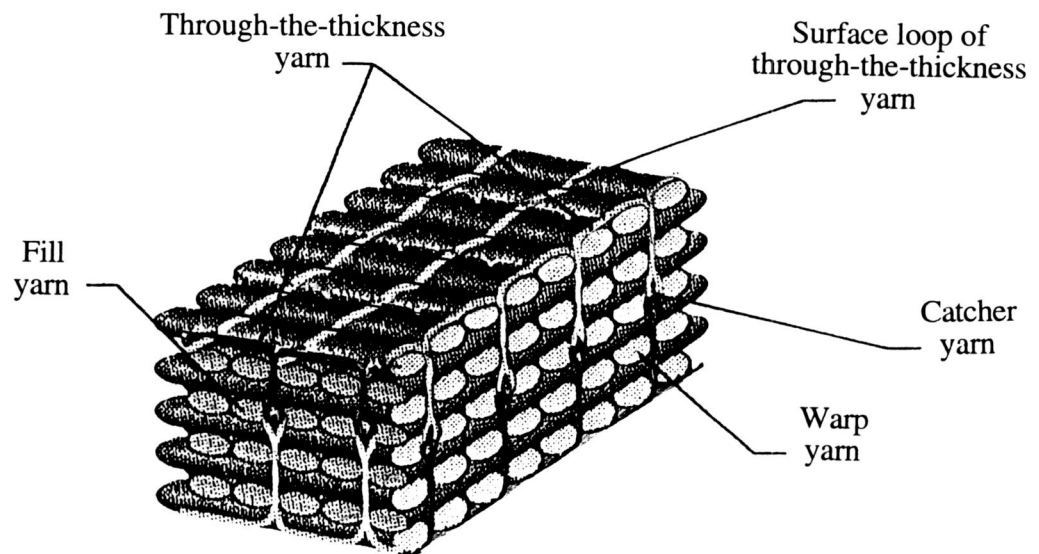


Figure 3. Integrally woven 3-D architecture.

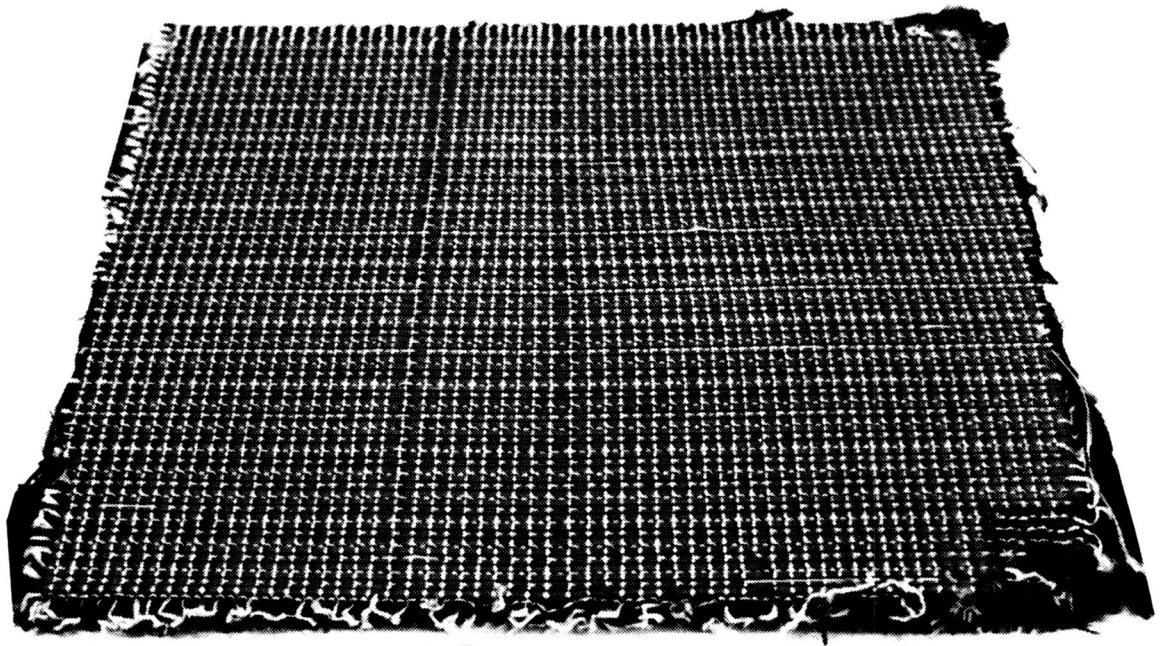


Figure 4. Integrally woven preform (Kevlar TTT reinforcement).

The composite panels were produced in sixteen by fourteen inch panels, as shown in Figure 5. The panels were cut into four inch wide by sixteen inch long samples with a diamond tipped circular saw blade. The edges were cut parallel to the TTT reinforcement surface loops on the top zero degree ply.

The thickness varied by as much as four percent across the width of a sample. The average thickness of each sample was determined from the thickness at each edge of the sample in the middle of test section. The average thickness among the five materials varied significantly. However, there was little variation among each material group, as shown in Table I.

Each sample was C-scanned with SONIX ultrasonic testing equipment to check for material flaws. A 5 MHz transducer scanned each sample with 0.01000 inch scanning increments. There were no significant flaws found in any of the tested samples.

Impact Device

The impact device consisted of a 0.50 caliber machine gun barrel pressurized with nitrogen, as shown in Figure 6. Half inch diameter aluminum balls were loaded into the barrel, and a tank of nitrogen was used to pressurize a plenum to 85 psi. A solenoid was triggered to release the pressurized nitrogen through a half inch orifice into the barrel. A counter at the end of the barrel was used to determine the velocity of each ball.

The counter consisted of two HAD-1000A photodiodes. The photodiodes were separated by six inches. The time in which each ball traveled through this distance was determined with a 500 KHz crystal oscillator (divided from 1 MHz). The velocity (ft/sec) was given by dividing 250,000 by the number of oscillations. The uncertainty in this experimental set-up was about 0.27%, or 1.5 ft/sec.

Each sample was impacted at the geometric center. The average velocity was 543.4 ft/sec with a standard deviation of 7.3 ft/sec. During impact, the ends of each sample were held in place with the hydraulic grips of the testing machine. Approximately ten inches of each sample was unconstrained, and the front face of each sample was approximately one

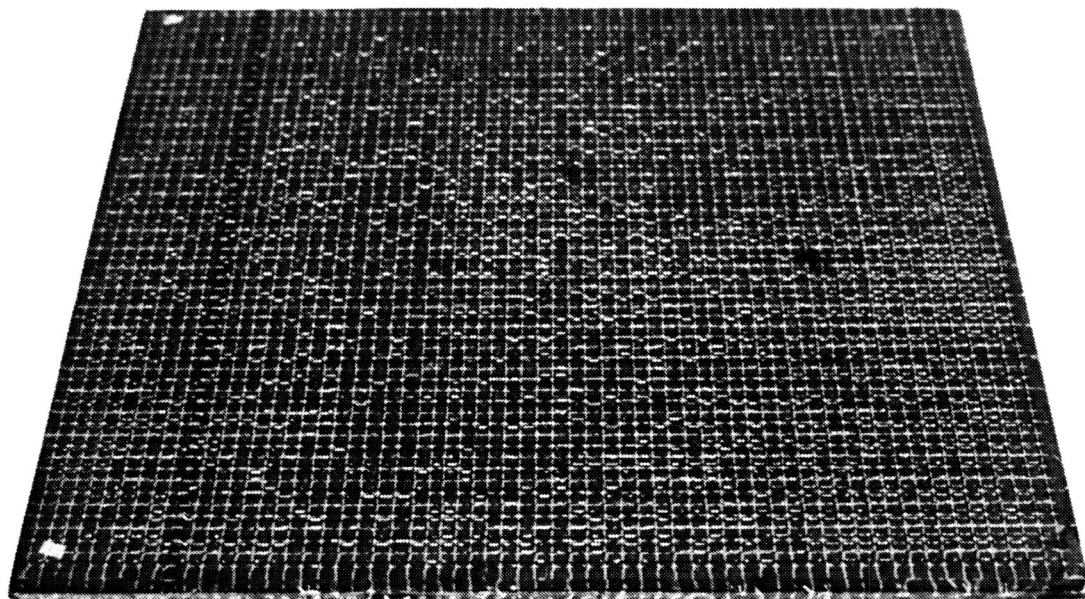


Figure 5. Integrally woven carbon/epoxy 16" by 14" composite panel (Kevlar TTT reinforcement).

Table I. Sample Thicknesses

TTT Reinforcement	Average Thickness (in)	Standard Deviation
Kevlar 29	0.249	0.006
Toray Carbon	0.247	0.003
AS4 Carbon	0.292	0.005
S2 75 1/3 Glass	0.246	0.006
IM6 Carbon	0.274	0.007
Totals	0.262	0.019

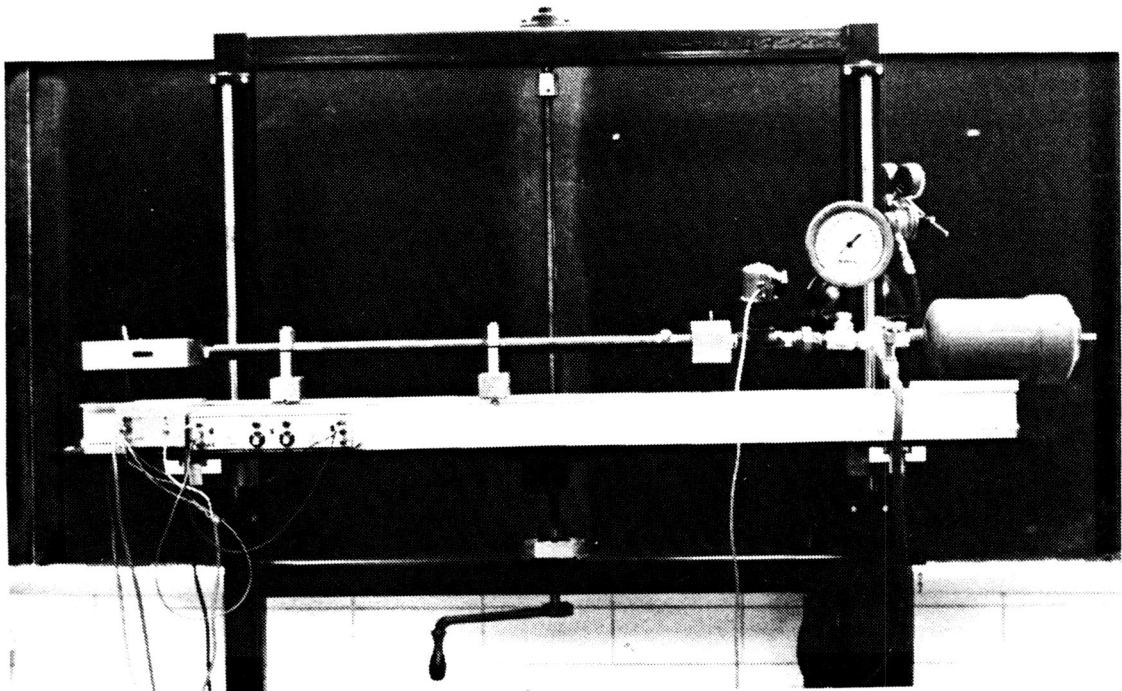


Figure 6. Impact device.

foot from the end of the gun barrel. In order to slow the ball after rebounding off the sample, foam rubber was attached around the end of the barrel.

Static Compression Tests

Static compression tests were conducted on one sample from each of the five TTT reinforcement groups. Ten inch knife edge side supports were used to simply support the sides of each specimen, as shown in Figure 7. The supports prevented global buckling. Teflon strips, 0.060 inches thick and 0.400 inches wide, were used to prevent fretting of the samples at the knife edges.

Each sample had one strain gage on the front and one on the back, 2.5 inches below the impact site, as shown in Figure 8. To prepare each surface for the strain gage, a nominal 0.050 inch by 0.025 inch area was sanded with a coarse 80 grit paper at the location of each gage. Each surface was then wet sanded with 320 grit paper and a water-based acidic surface cleaner. Next, a water-based alkaline surface cleaner was used to clean the surfaces. Each gage was then coated with a catalyst, glued to the surface with a cyanoacrylate adhesive, and coated with polyurethane.

The front and back strain gages were aligned in the loading direction to determine uniaxial strain. The gages were Micro-Measurements precision strain gages, type CEA-06-250UW-350 (0.250 inch gage length, 350 ohms resistance). The gages were connected in a full Wheatstone bridge circuit. A Vishay Instruments Bridge Amplifier and Meter were used for bridge completion and amplification. The analog output was connected to a Metrabyte STA-20 analog and digital interface board to supply the average strain data.

Compression tests were conducted on the 56 kip servo-hydraulic Instron 1332 load frame with an Instron 8500 series electronic controller shown in Figure 9. Hydraulic grips were used to exert pressure on four inch by three inch aluminum tabs which were mounted to the ends of each sample. The grip pressure was set at 3000 psi. The samples were tested to failure under load control at a rate of 5.0 kips/min., which produced a corresponding strain rate of approximately 0.0005 per minute.

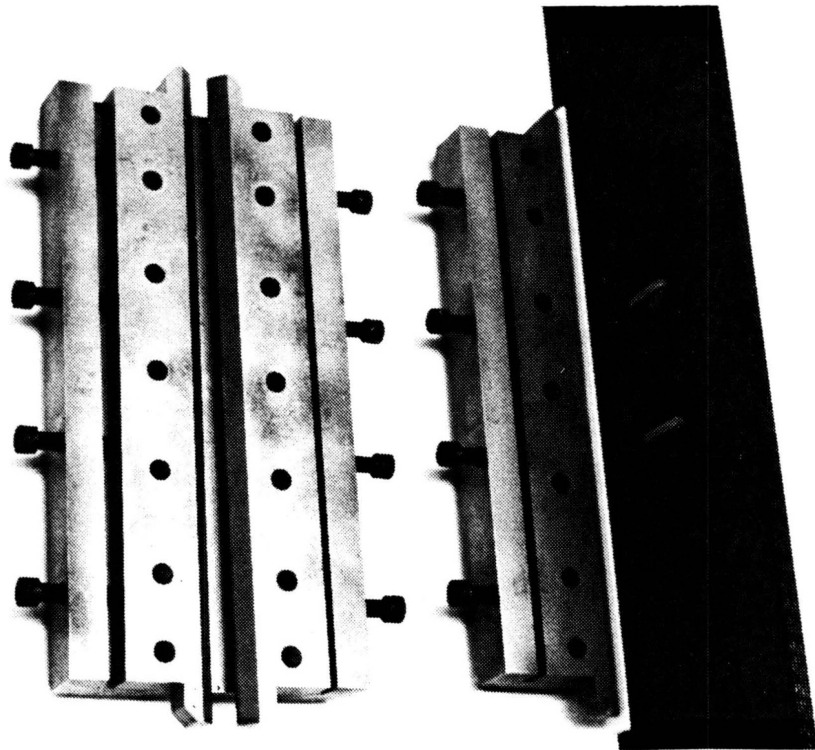


Figure 7. Side supports.

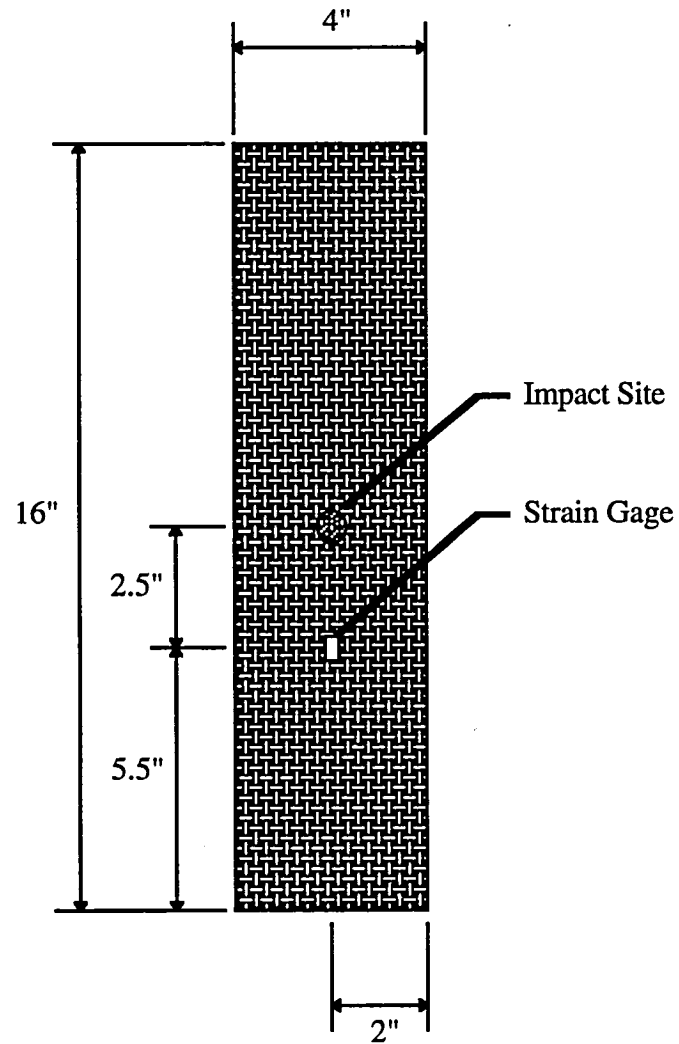


Figure 8. Location of strain gages on static compression samples.

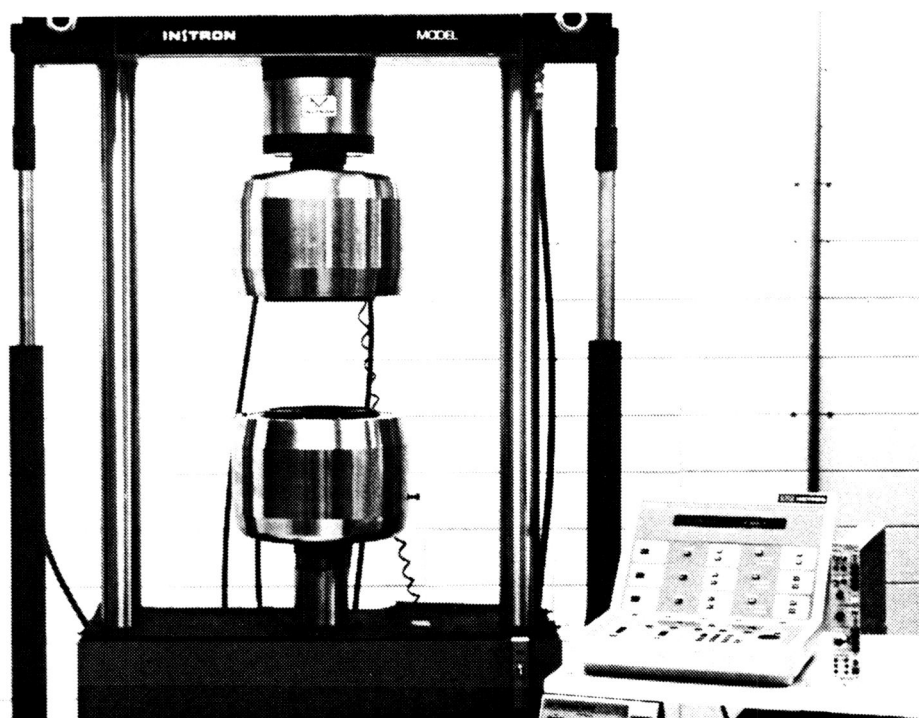


Figure 9. Instron load frame and electronic controller.

Labtech Notebook data acquisition and process control software package, version 4.26, were used to collect the raw data with an IBM PC. The instrument outputs were acquired with the Metrabyte board. The Instron electronic controller provided the output for the load data. The data were sampled at a rate of one cycle per second, thus producing load and strain readings every 83 pounds.

Post-Impact Fatigue Tests

To prepare the samples for fatigue testing, extensometer tabs were mounted above and below the damage sites on both sides of the samples. The extensometer tabs were machined from 0.125 inch thick aluminum. Each tab was 0.200 inches high and 0.450 inches wide at the base, as shown in Figure 10. The top of each tab was 0.800 inches wide and had a 0.025 inch deep groove to hold the extensometer knife edges. The surfaces of the composites were prepared for bonding tabs using a procedure similar to that used for the application of strain gages. A nominal 0.50 inch by 0.75 inch area was sanded with a coarse 80 grit paper at the location of each tab. Each surface was then wet sanded with 320 grit paper and thoroughly cleaned with a water-based alkaline surface cleaner. Each tab was degreased using 1-1-1 Trichloroethane.

The tabs were mounted one inch above and one inch below the center of the impact site on each side of the samples. The tabs were bonded to the samples with Hysol EA 9309 NA two part epoxy adhesive. The adhesive was allowed to cure for at least 24 hours before testing. The adhesive effectively held the tabs in place; the adhesive never failed prior to the sample failing.

Instron extensometers, shown in Figure 11, were attached to the front and back of each sample. The knife edges of the extensometers were attached to the tabs, as shown in Figure 12, with GB Electrical nylon cable ties. Extension over both sample faces was monitored throughout the tests to provide information about out-of-plane deformation.

The front extensometer, Instron catalog number 2620-828, had a range of ± 0.05

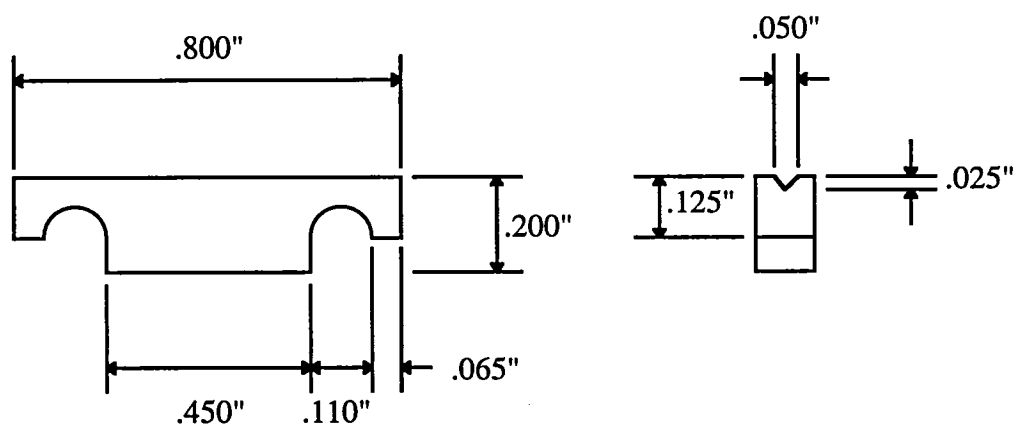


Figure 10. Geometry of extensometer tabs.



Figure 11. Extensometers.

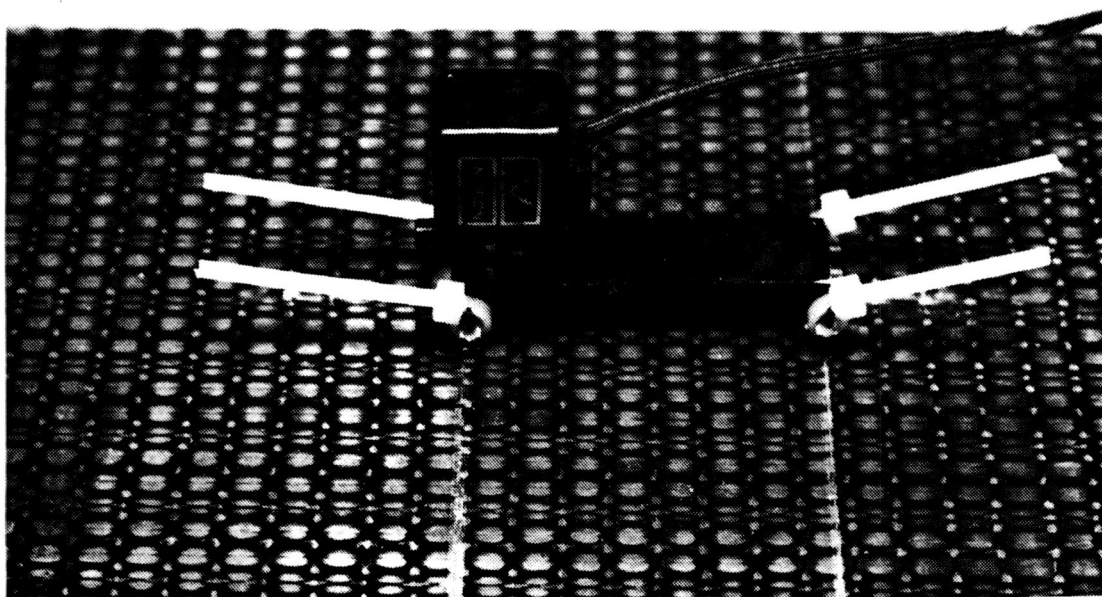


Figure 12. Extensometer attached to tabs mounted across impact site on sample.

inches. The back extensometer, Instron catalog # 2620-830, had a range of ± 1 millimeter. Every sample failed before either extensometer exceeded its range.

The front extensometer was connected to the Instron electronic controller. The analog output from the controller was connected to the Metrabyte board. The back extensometer was connected to a Vishay Instruments Group 2310 Signal Conditioning Amplifier, serial number 093787. The excitation voltage was input to the 25 pin extensometer connector at pins 1 and 2, plus and minus respectively. The output signal to the amplifier came from pins 14 and 15, minus and plus respectively. The excitation voltage was set at one volt DC with a gain of 3700. The output from the amplifier was also connected to the Metrabyte board. There was some interference in this signal. The "noise" caused variations in the output voltage of about ± 0.005 volts. This caused strain variations of about ± 10 microstrain, or about $\pm 0.1\%$ of the maximum compressive strain at fatigue failure.

The extensometers were calibrated with a Romford Essex T18-18 super micrometer. Each extensometer was attached to the super micrometer with rubber bands. The extensometer voltages were monitored with the Labtech Notebook data acquisition software. Each extensometer was calibrated according to guidelines presented in ASTM Standard Practice Verification and Classification of Extensometers (E83) [44]. Each extensometer had a B-1 classification. [44]

Fatigue tests were conducted using the same 56 kip servo-hydraulic Instron load frame and test set-up used for compression testing (except extensometers were used and strain gages were not), as shown in Figure 13. The data acquisition system was capable of reading voltage accurate to ± 0.0005 volts. Therefore, load readings could be measured in 27 pound increments, and strain could be measured in increments of 1 micro strain.

The loading wave form was sinusoidal, as shown in Figure 14, with a loading ratio $R = -5$. Each sample was tested at a frequency of 4 Hz. The maximum compressive load for each sample was chosen as a percentage of the static compressive strength for each

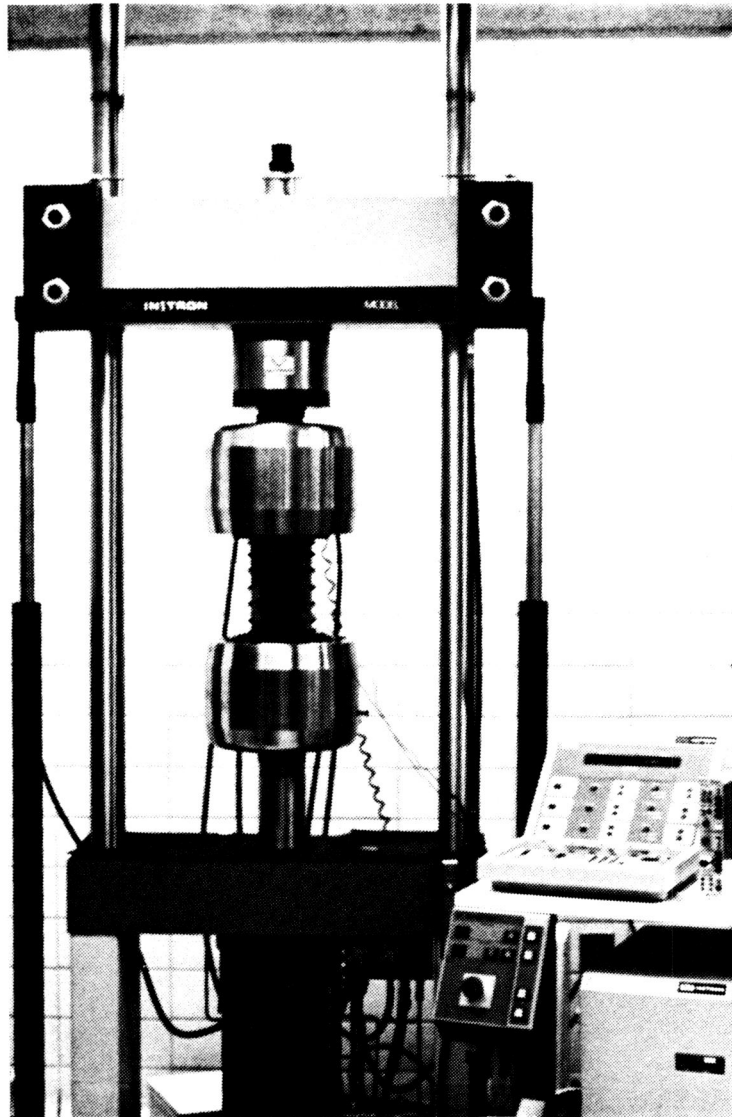


Figure 13. Instron load frame and electronic controller with sample mounted for fatigue test.

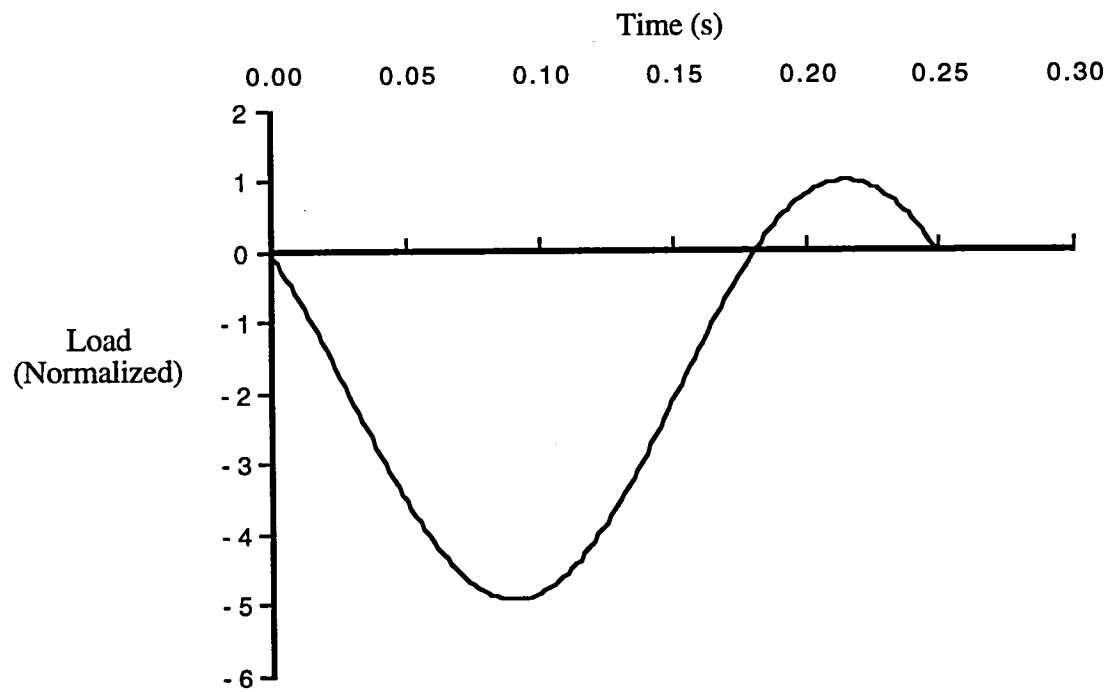


Figure 14. Load cycle for fatigue tests ($R = -5.0$, frequency = 4 Hz).

material. Percentages ranged from approximately 55% to 80% of the static strength. Samples that survived one million cycles in a fatigue test were considered to have achieved infinite life.

Limits were set on the electronic controller to stop the loading immediately after failure. Limits were set on the extension of the front extensometer, position of the cross-head, load on the sample, and number of fatigue cycles. To protect the extensometers, the tests were stopped when the maximum negative extension of the front extensometer reached -0.040 inches.

Data was collected with the Labtech Notebook data acquisition system at a sampling rate of 600 Hz for one half second. Three BASIC programs, written by the author, were used to trigger the data acquisition system at points of interest during each fatigue test. "GetTimes" was used to enter the times when data points needed to be recorded, and these times were written to a file on the computer's hard drive. Then, "Timer2" was used to record data at the given points. At each point, two cycles of fatigue data were written to a hard drive. These data were then merged with the previously acquired data on a floppy disk. Up to 75 data points were stored on each 1.6 MB floppy.

Typically, several data points (sampling every 100 to 400 cycles) were recorded early in a fatigue test, and several were recorded toward the end. Fewer points (sampling every 2000 to 25,000 cycles) were recorded in the middle of a fatigue test. The maximum negative extension of the front extensometer was monitored to determine when each sample was near failure. When this extension began to rapidly increase, many of the tests were paused. At that point, "EndTimer" was used to record the data for every cycle until failure. One hundred and sixty cycles were recorded on each floppy.

After each fatigue test, the raw data were analyzed with four PASCAL programs. Each data point consisted of one half second or two cycles of data. However, data were not necessarily recorded starting at the beginning of a cycle. Therefore, each program read the data at each point from the floppy disks and truncated the data set to one full cycle.

This cycle was then analyzed to determine the maximum and minimum strains, secant modulus (stiffness), hysteresis, loading modulus, unloading modulus, and out-of-plane deformation.

"Crunch" was used to analyze each cycle of data from "Timer2." "EndCrunch" was used to analyze each cycle of data at the end of the fatigue tests from "EndTimer." "Evaluate" was used to analyze one particular data point, and it gives all the stress and strain values for the given cycle from "Timer2." Likewise, "EndEvaluate" was used to analyze one data point at the end of a fatigue test from "EndTimer." The programs mentioned in previous paragraphs are included in the "User's Guide for Collecting Data from Fatigue Tests", Department of Mechanical Engineering report number TR-94-137-ME-AM.

Evaluation of Damage

Radiography

In addition to quantitatively monitoring damage growth with stiffness loss, X-radiographic techniques were used to document damage. Ten fatigue samples were evaluated, two from each TTT reinforcement group. The strain across the impact site on the front face of each sample was monitored in order to regulate damage growth. The fatigue tests were interrupted and samples were evaluated at predetermined levels of compressive strain across the damage zone on the front face. Each sample was evaluated after impact, at a maximum compressive strain of 0.005, at a maximum compressive strain of 0.007, and immediately prior to failure (typically at a maximum compressive strain of about 0.010).

Damage was monitored using an X-ray opaque dye. The dye consisted of 60 g zinc iodide, 10 mL water, 10 mL isopropyl alcohol, and 1 mL photo-flow. The dye was injected into surface cracks while the specimen was under a static tensile load of approximately four kips. The dye was allowed to soak for approximately five minutes before the sample was removed from the testing machine. Additional dye was then allowed

to soak through-the-thickness of the specimen for approximately ten minutes before the excess dye was wiped off the specimen face.

Type 55 Polaroid film was mounted approximately one quarter inch from the back face of the specimen, over the damage zone. A Philips (type number 9421 070 01202) K 140 Be tubehead was placed about six inches from the front face of the specimen. The tubehead was controlled with a Philips 220 Kv 50/60 Hz standard control box, type number 9421 070 17112. The film was exposed to a 37 Kv x-ray flux for three minutes.

Sectioning

Ten samples were sectioned to evaluate impact and fatigue damage. The five samples (one from each material group) fatigued nearly to failure, which were radiographed, were cross-sectioned. Five impacted samples (one from each material group), with no static or fatigue loading, were also evaluated. Each sample was cut parallel to its sides, as shown in Figure 15, and wet-sanded with 240, 320, 400, and 600 grit paper. The samples were then photographed and examined under a microscope.

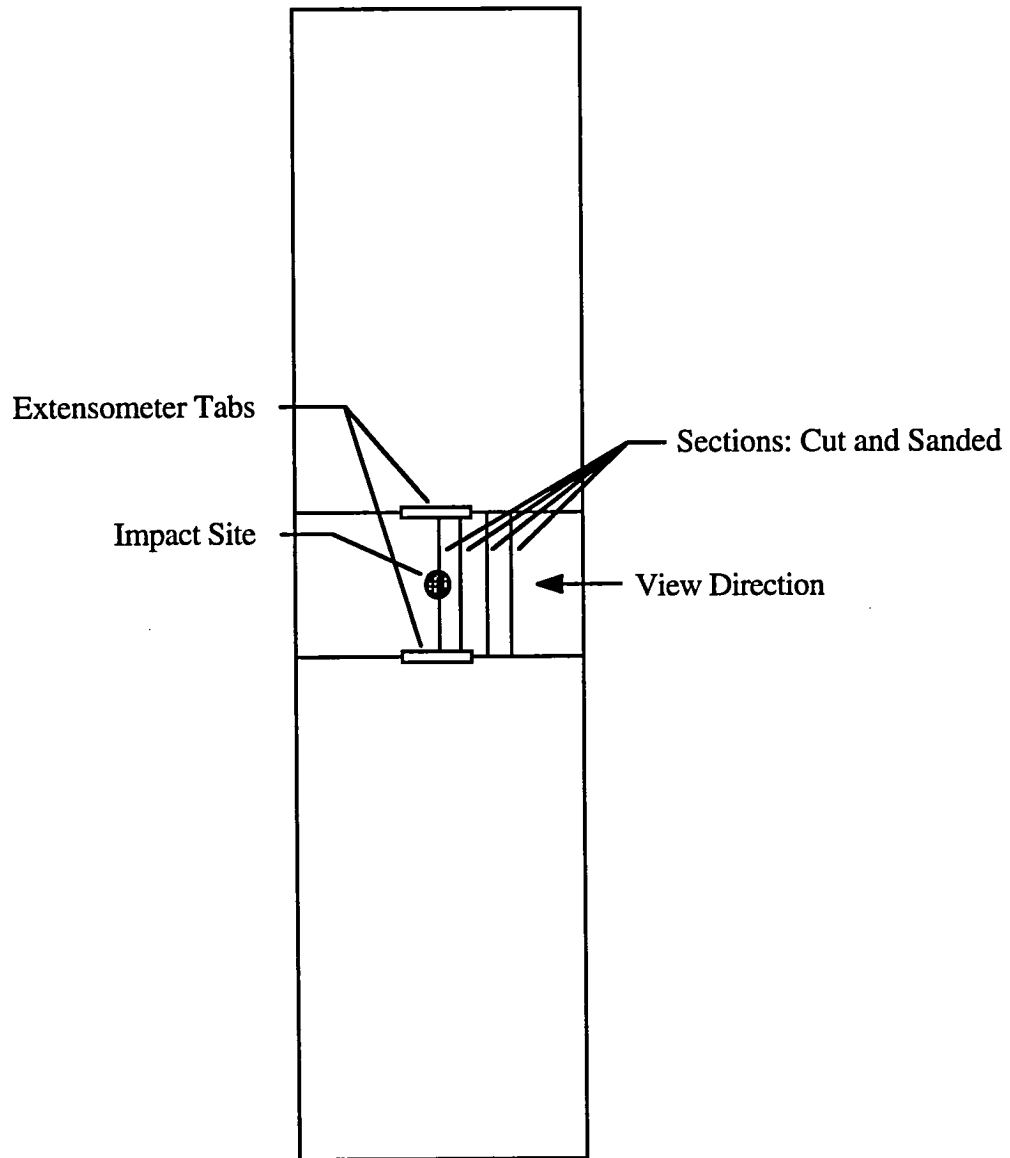


Figure 15. Location of sectioning cuts.

CHAPTER III

RESULTS

Discussion of Post-Impact Loading

The FAA and Department of Defense require that aircraft structures survive one lifetime without detectable damage from normal in-service use. Therefore, aircraft structural members that sustain damage (that may not be visually detectable) from impact loading must be able to maintain structural integrity under subsequent loading. Post-impact loading experienced by aircraft structural members must be simulated to study material response so that the structure can be confidently designed and certified. However, different components are subjected to different post-impact loading conditions. Likewise, different regions of the same component are subjected to different loading conditions. For example, the top surface of a wing, outboard of the landing gear, experiences maximum tensile loading when the fully-fueled aircraft is taxing. During flight this surface undergoes compressive loading, primarily.

This research was conducted to study the response of carbon/epoxy composites with different integrally woven TTT reinforcements to post-impact fatigue loading. The TTT reinforcing fibers were Kevlar 29, 1500 denier; Toray carbon, T-1000; AS4 carbon, 9K; S2 75 1/3 glass; and IM6 carbon, 6K. The TTT reinforcement was integrally woven with 21K AS4 carbon tow fiber. The experimental textile process produced composites with a $[0/90/0/90/0/90/0/90/0]_T$ ply layup. Specifically, these tests were conducted to study the behavior of integrally woven composites under simulated aircraft loading conditions and to determine which of the tested TTT reinforcing fibers is the best. This laminate configuration would probably never be used in an aircraft structural member, because it contains only 0° and 90° plies. However, the experimental textile process

provides low cost model materials that can be used to evaluate different TTT reinforcements.

The composites were impacted to produce intermediate-velocity, low-mass impact damage. The composites were then loaded in both static compression and tension-compression fatigue to failure. The static tests were conducted to determine mechanical properties and to observe the compressive failure modes. These tests also established a baseline for determining the load ranges of the fatigue tests.

The fatigue loading conditions were chosen as a simplified representation of loading experienced by the top surface of a wing (outboard of the landing gear). The magnitude of the compressive load during normal flight is about twice the magnitude of the tensile load when the aircraft is on the ground. The wing experiences variable amplitude loading during flight and may reach limit loads in tension or compression. Limit tensile load is about the same as the load experienced when the fully fueled aircraft is taxiing. Limit compressive load is about five times the magnitude of limit tensile load [47]. Therefore, the loading ratio of $R = -5.0$ (maximum compressive load five times maximum tensile load) was chosen because it represents one tension-compression limit load cycle. It also represents the harshest compressive loading a wing could experience during one ground-air-ground cycle. Additionally, there is little difference in fatigue response for loading ratios between $R = -2$ (representative of normal flight) and $R = -5$ [47].

Since a wing seldom experiences limit loading, and a ground-air-ground cycle represents an entire flight, one million cycles was considered infinite life. The loading frequency of four hertz was chosen to produce low-frequency effects in a reasonable time frame.

The fatigue tests were conducted to determine the relationship between maximum compressive fatigue stress and specimen life. X-radiography and sectioning were used to monitor damage zone growth. The stress-strain response of the materials at individual

cycles during fatigue tests was monitored as an indicator of damage and to anticipate specimen life.

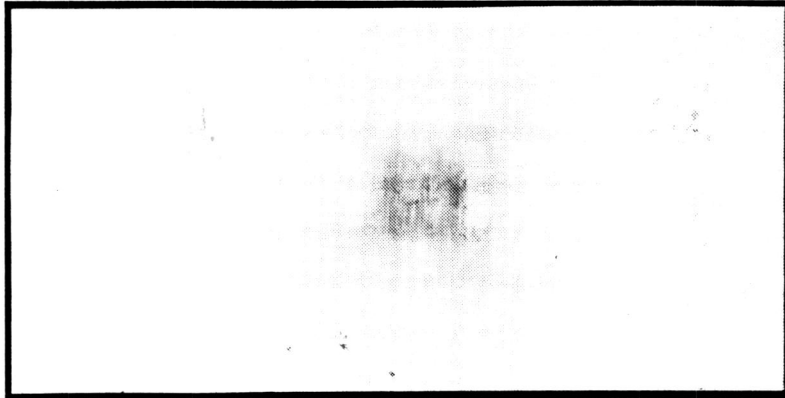
Impact Damage

The size and shape of the damage zones caused by impact were observed using x-radiographic and sectioning techniques. Post-impact radiographs of one sample of each material are shown in Figure 16. The black and gray regions represent damage. The light gray regions do not represent damage; this was apparently caused by the dye being absorbed by the TTT reinforcing fibers. The samples were typically soaked with dye only near the damage zone. Therefore, these light gray regions surround the damage zones.

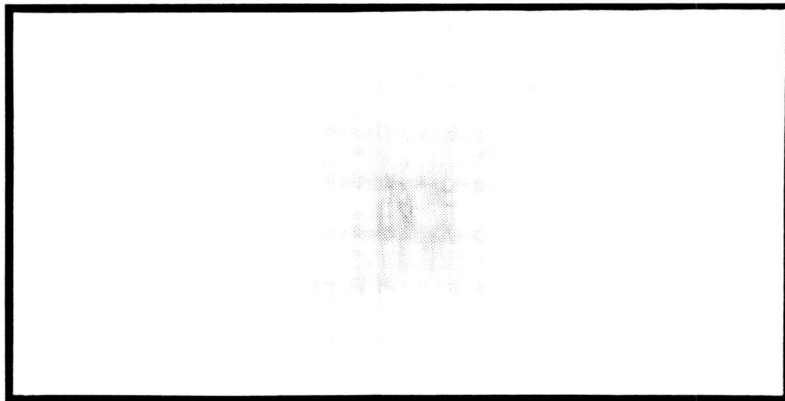
The radiographs showed larger, less-pronounced damage zones in the IM6 carbon and AS4 carbon samples than the other materials. This may have been caused by variations in sample thickness; the AS4 carbon and IM6 carbon samples were the thickest. The x-ray exposure time and intensity were the same for each sample. Therefore, the thicker samples produced a general view of the damage zone, while the thinner samples produced more detail of cracks and delaminations. Also, it was often difficult to inject dye into surface cracks; some samples absorbed more dye than others. The glass sample, for example, appeared to have very little impact damage. Yet, with the use of sectioning (to be discussed later), the amount of damage was found to be similar for each sample. Therefore, these differences in the initial damage zones were probably merely artifacts of the radiographic process and do not represent differences in the actual damage states.

Variations in thickness and problems with dye absorption made it difficult to establish differences in size and shape of the damage zones. However, each sample had a nearly circular damage zone. Also, the radiographs showed more damage slightly away (about 1/8 inch) from the center of the impact site.

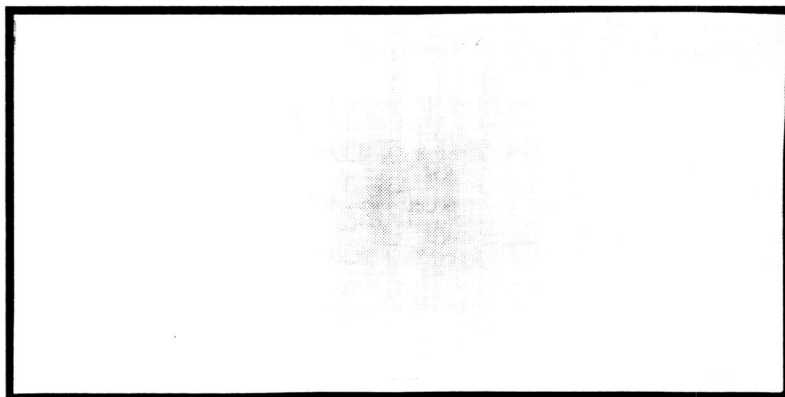
Each sample was cross-sectioned (cut and polished) at four locations and viewed under a microscope, as shown in Appendix B. At the impact site there were many matrix cracks, ply cracks and delaminations, as shown in Figure 17. The matrix cracks were



a. Kevlar

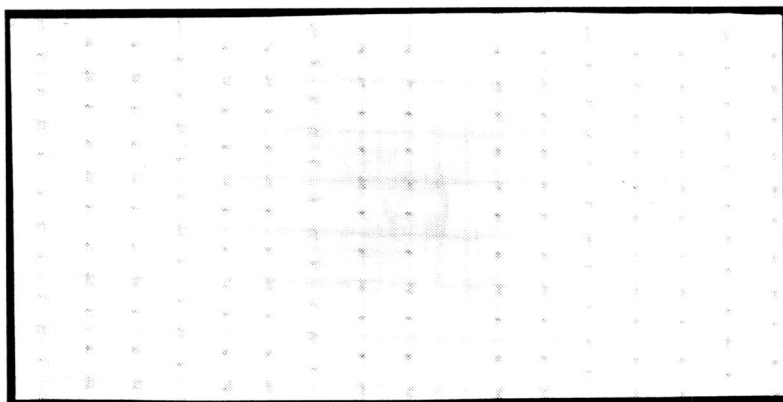


b. Toray carbon

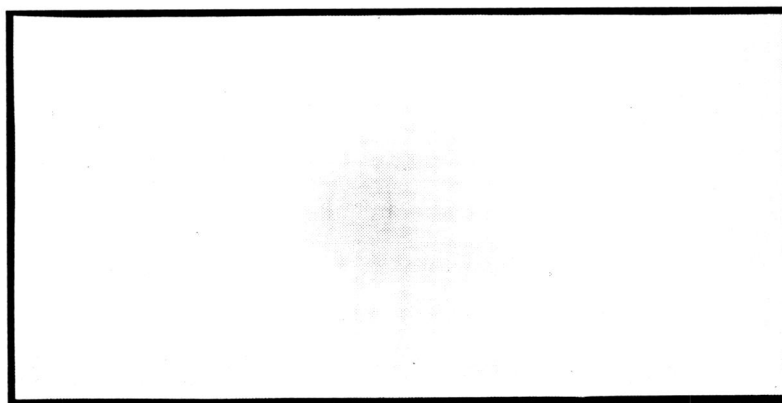


c. AS4 carbon

Figure 16. Radiographs of impact damage in sample from each material group.



d. Glass



f. IM6 carbon

Figure 16. (Continued)

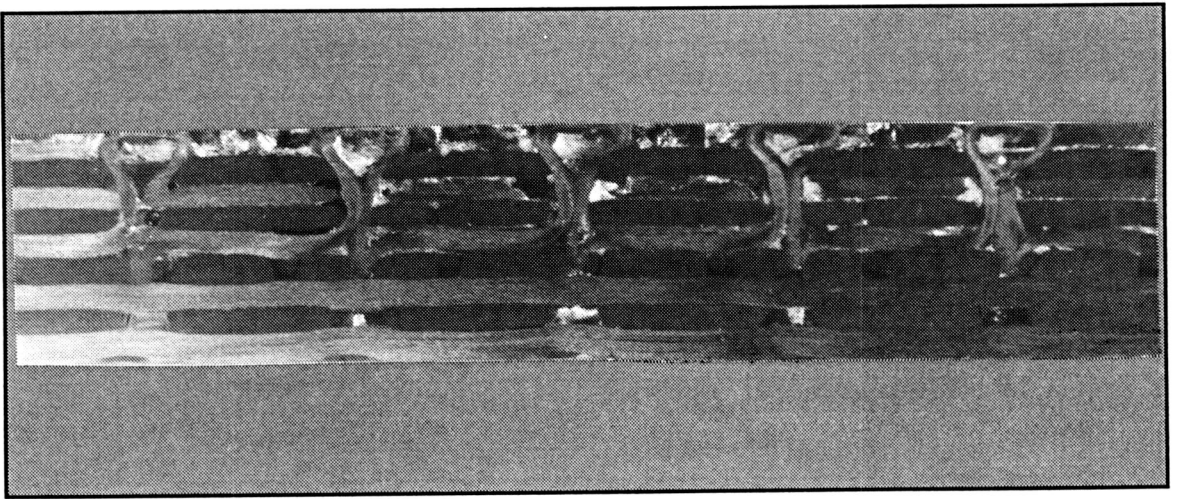


Figure 17. Typical post-impact damage in cross-section at center of impact site (IM6 carbon reinforcement; impacted on top face).

scattered but usually went through the 90° plies and were parallel to the impact load direction. Also, the cracks appeared to be more prevalent through resin pockets. The size and location of the delaminations and ply cracks also varied considerably.

At less than 0.2 inches from the center of impact, there was slightly less damage in each sample. This is clearly shown in Figure 16-b. Cracks and delaminations were still prevalent. At about 0.3 inches from the center of impact, there was typically more damage. The damage still consisted of scattered cracks and delaminations. Delaminations were often constrained between sections, as shown on the radiographs. At about 0.5 inches from the center of impact, there was considerably less damage. However, there were still some cracks and a few delaminations. This damage did not show up on the radiographs.

Static Compression Results

The static stress versus far-field strain response was essentially linear for all specimens tested. However, immediately before failure, the far-field strain decreased slightly as the load increased. It is speculated that this decreasing far-field strain corresponded to a rapid increase in the strain over the damaged area. A typical stress versus far-field strain curve is shown in Figure 18. Each sample had a transverse shear failure mode, presumably caused by local fiber instability.

The static compressive properties for all five TTT reinforcements determined from the stress versus far-field strain curves are shown in Table II. Compressive elastic modulus and static strength values were calculated using both actual sample thickness and average thickness of all samples tested.

The average compressive elastic modulus using measured thicknesses was slightly greater than 10 Msi. The Toray carbon sample had an elastic modulus greater than 12 Msi, nearly 19% higher than average. The modulus of the glass sample, about 11 Msi, was also much higher than average. In contrast, the AS4 carbon sample had an elastic modulus of about 8.5 Msi, more than 16% lower than average.

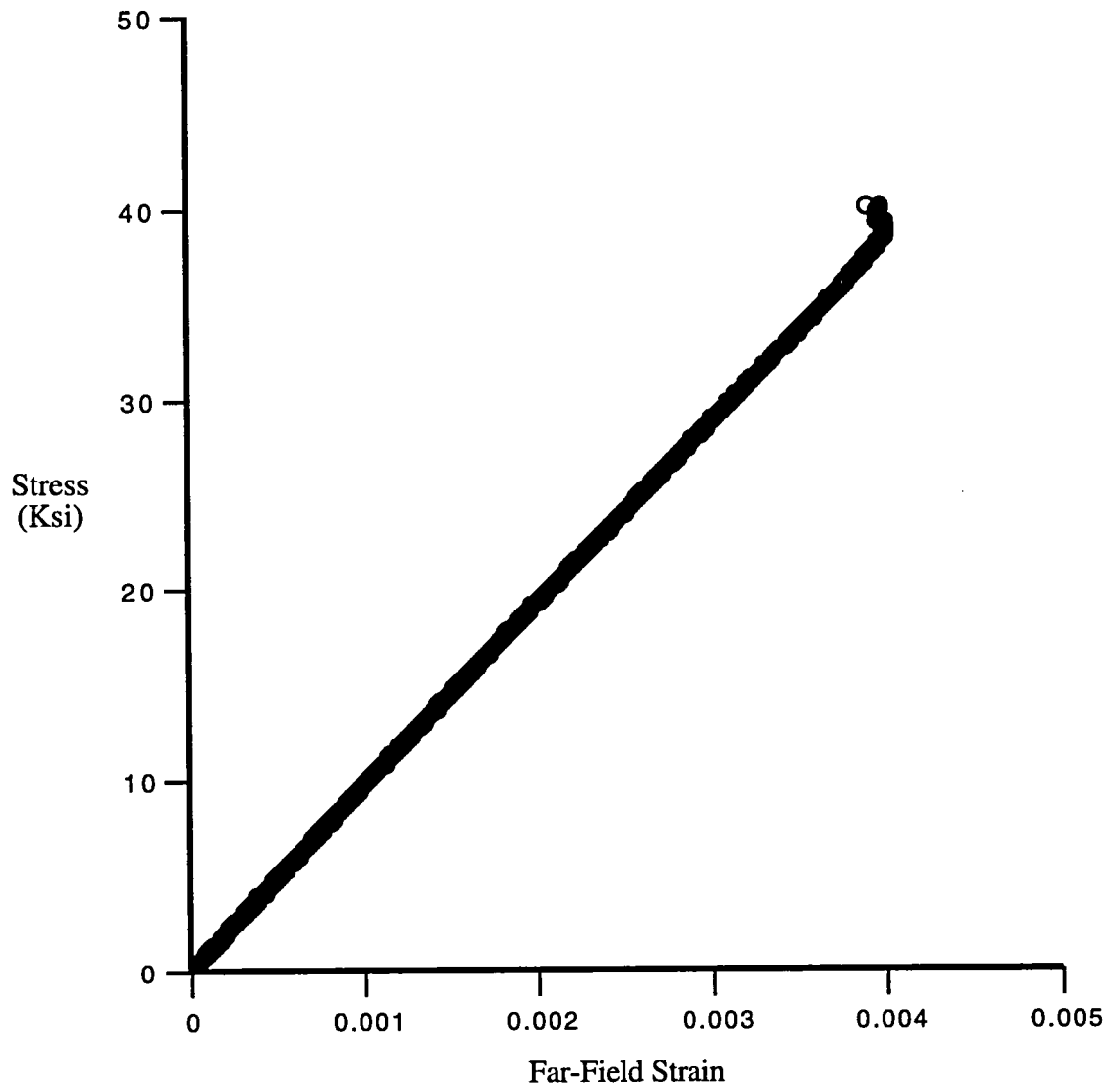


Figure 18. Stress versus far-field strain under static compressive loading (IM6 carbon TTT reinforcement).

Table II. Static Compression Results

TTT Reinforcement	Elastic Modulus (Msi)		Compressive Strength (Ksi)		Far-Field Min. Strain
	Act. Thick.	Avg. Thick.	Act. Thick.	Avg. Thick.	
Kevlar 29	9.537	9.141	34.366	32.939	0.003491
Toray Carbon	12.021	11.431	33.086	31.463	0.002441
AS4 Carbon	8.459	9.512	35.894	40.364	0.004248
S2 75 1/3 Glass	11.006	10.217	34.825	32.328	0.002804
IM6 Carbon	9.565	9.926	40.118	41.632	0.004006
Average	10.118	10.046	35.658	35.745	0.003398
Standard Dev.	1.249	0.783	2.405	4.333	0.000688

The large variations in elastic modulus were caused by differences in material thickness; the thickest samples had the lowest modulus. Differences in thickness can be attributed to differences in the size of the TTT reinforcement and to variations in the fiber volume fraction in each sample. However, even though fiber volume fractions may differ, all samples contained the same number of 21K AS4 carbon tows in both the warp and fill yarns. And, fiber is the dominant contributor to the strength and stiffness of a laminate. Therefore, the elastic modulus would not vary from material to material if the thickness did not vary.

To account for variations in fiber volume fraction, the modulus was calculated using the average thickness of all the samples tested. The average compressive elastic modulus using the average thickness was slightly larger than 10 Msi. As shown in Table II, the Toray carbon specimen had the highest modulus, almost 11.5 Msi (nearly 14% higher than average). The modulus of both the glass and IM6 carbon samples were close to average. The AS4 carbon sample and the Kevlar sample each had a modulus lower than average. The elastic modulus calculated using both the actual and average thicknesses is shown in Figure 19.

The average post-impact static compressive strength using measured thicknesses was about 35.5 Ksi. The sample with IM6 carbon TTT reinforcement was considerably stronger than the others tested; the compressive strength was greater than 40 Ksi. The IM6 carbon sample was more than 16% stronger than the average of the other materials tested. The Toray carbon sample had the lowest strength, about 33 Ksi. The other three samples had similar strengths.

In contrast to elastic modulus, compressive strength should vary with differences in thickness. Increasing the specimen's thickness increases global stability and, thus may increase the compressive strength. However, additional resin pockets or increased waviness (possibly caused by large TTT fiber bundles) in the tows would be detrimental to compressive strength. Resin pockets could cause micromechanical instability in the load-

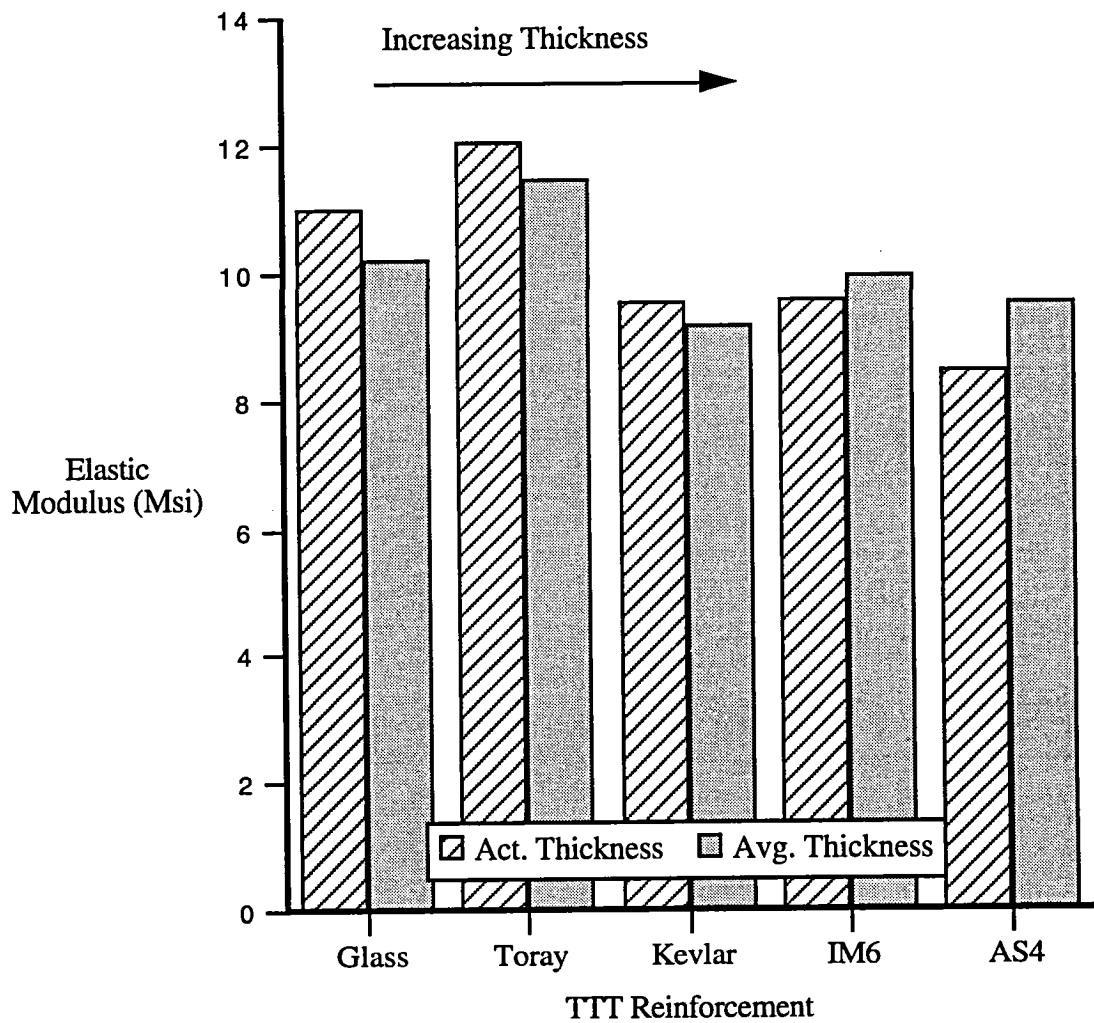


Figure 19. Compressive elastic modulus calculated from actual and average thicknesses.

carrying fibers. This, as well as fiber waviness, could initiate fiber microbuckling at lower loads. Obviously, causes of thickness variation can lead to differences in compressive strength. However, there are so many factors associated with different thicknesses that it is unclear how thickness differences affect strength.

The strongest sample (IM6 carbon) was also thicker than average. Additionally, the thickest sample (AS4 carbon) was stronger than the three thinnest samples (Kevlar, Toray carbon, and glass). When compressive strengths were calculated using average thickness, the IM6 carbon and AS4 carbon samples were stronger than average. The Kevlar, Toray carbon, and glass samples were significantly weaker than average. Compressive strength (calculated with the average thickness) of the two strongest samples was greater than the strength from actual thicknesses, as shown in Figure 20. Likewise, strength (calculated with average thickness) of the three weakest samples was less than the strength from actual thicknesses.

There appears to be some credence in using the average thickness in determining modulus but not in calculating strengths. Therefore, all subsequent data was calculated using the actual thickness of each sample.

The average maximum compressive far-field strain was about 3400 micro strain, as shown in Table II. The AS4 carbon and IM6 carbon samples had the greatest compressive far-field strain. The maximum compressive far-field strain for the Kevlar sample was near the average of all samples. The Toray carbon and glass samples had the lowest compressive strain.

In summary, the IM6 carbon sample had the greatest compressive strength and far-field strain. The AS4 carbon sample had the lowest modulus. The Toray carbon and glass samples had the largest compressive modulus and lowest far-field strain. The Kevlar sample had a nearly average strength, maximum compressive strain, and modulus.

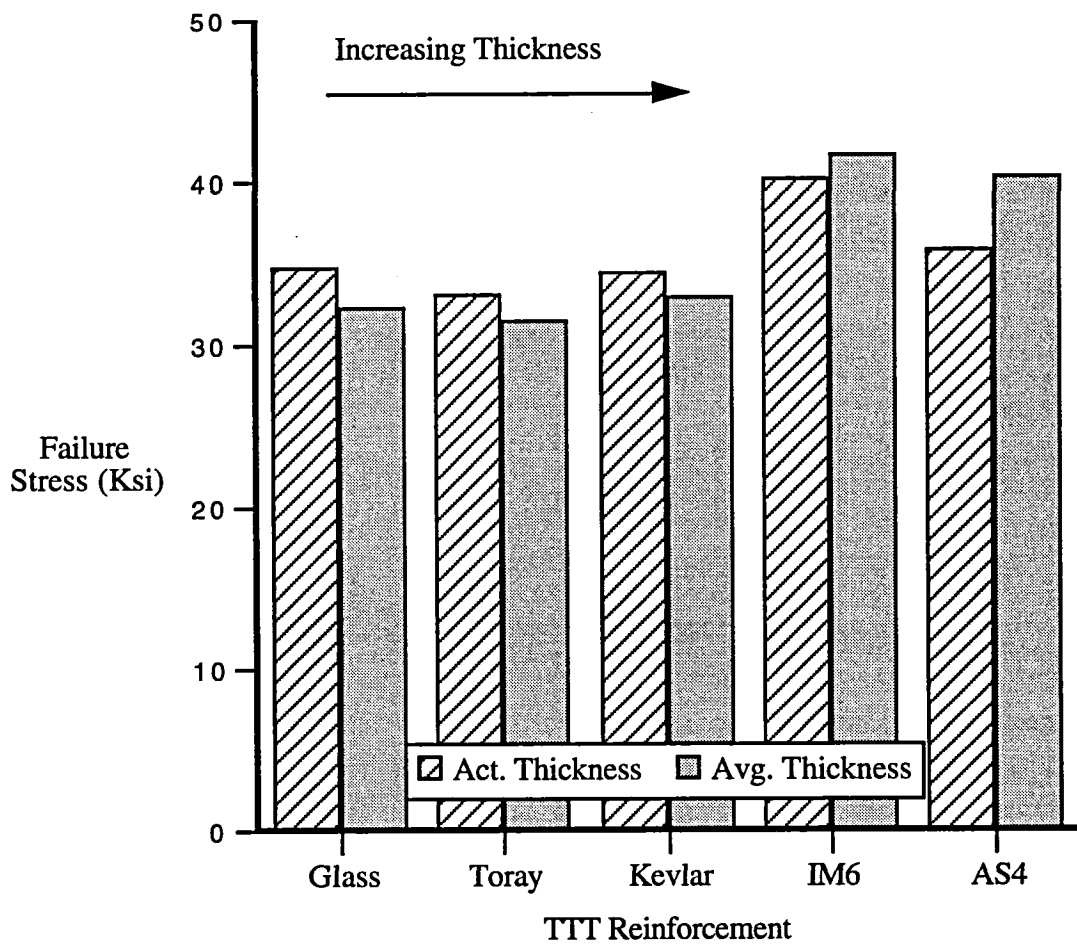


Figure 20. Compressive failure strength calculated from actual and average thicknesses.

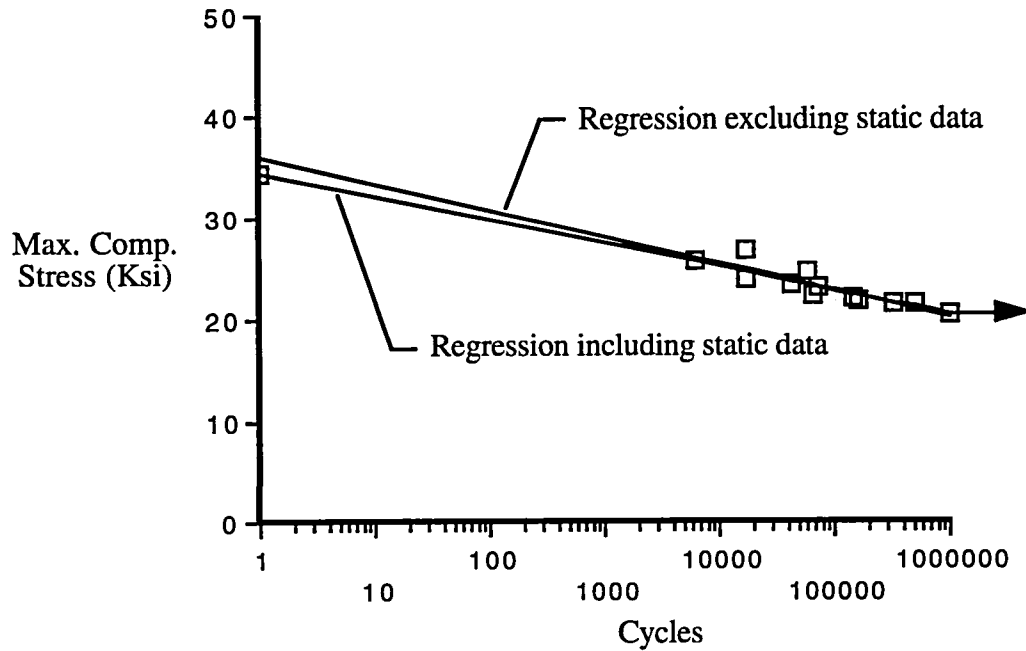
Tension-Compression Fatigue Results

After the post-impact static compression response was established for all five TTT reinforcement material groups, tension-compression fatigue tests were conducted. Damage zone growth was monitored in each material. The mechanical response, displacement across the impact site, of each material was also monitored throughout each test to quantitatively monitor damage growth.

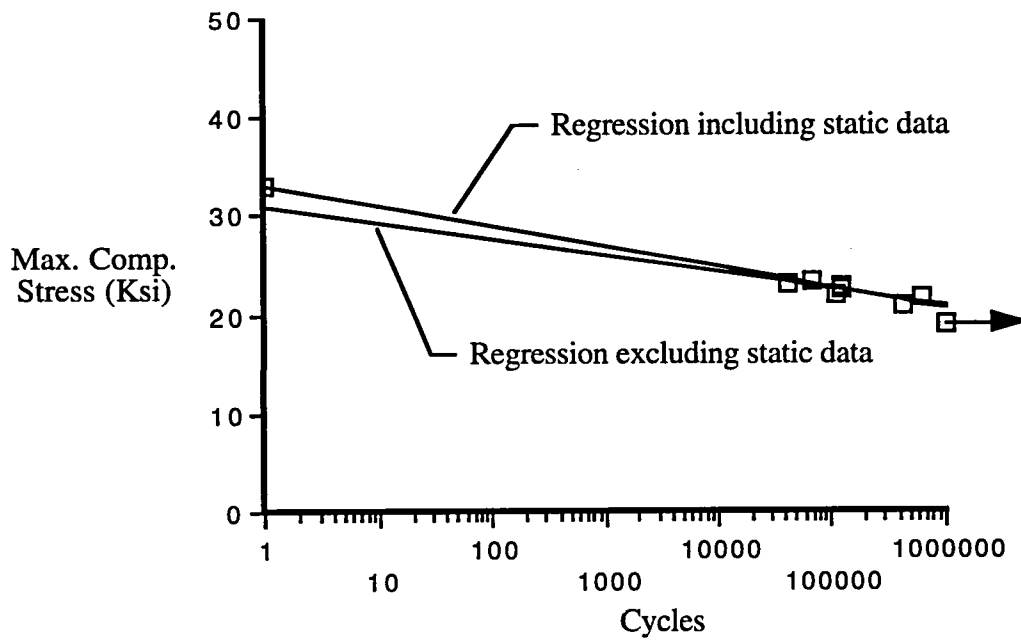
Fatigue Life

Tension-compression fatigue investigations were conducted with the maximum compressive stress varying from 57% to 79% of the static compressive strength. The maximum compressive fatigue stress was plotted versus the number of fatigue cycles for each sample tested. S-N curves are displayed for each of the five TTT reinforcements in Figure 21. The static compressive strengths were plotted as single cycles fatigue tests. One infinite life test was conducted for each TTT reinforcement and is indicated by the arrow extending to the right on the figure. In all cases these samples showed little indication of damage growth at the end of one million cycles. Each S-N curve includes two best fit linear relations on the normal-log plot. Linear regressions were determined from both fatigue data only and from fatigue data with static data. In both cases, data from the infinite life tests were not used to determine the linear regressions.

For each TTT reinforcement the data points did not significantly deviate from the linear regression. However, the static compression strengths did not correspond to the fatigue data. The linear regressions of the fatigue data of the average of all five specimens tested approximate the static strengths to be about 10% lower than the actual strengths. The AS4 carbon material had the largest difference between the actual and approximated strength. A linear regression determined without including the static test approximates the static strength to be about 27% lower than the actual static strength. The difference between actual static strength and strength approximated with long-life fatigue data is

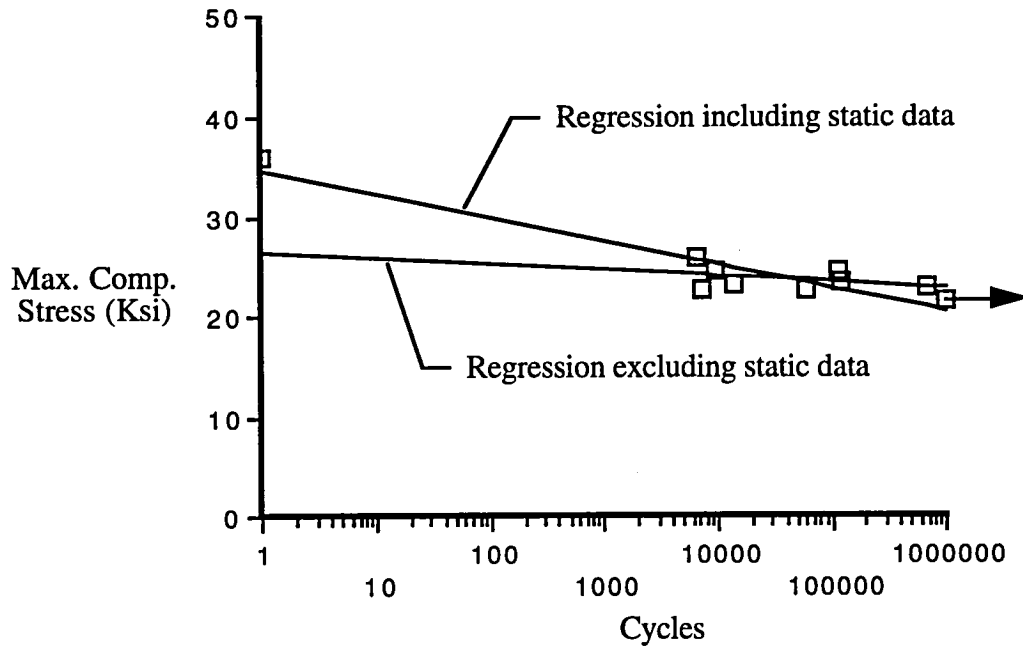


a. Kevlar

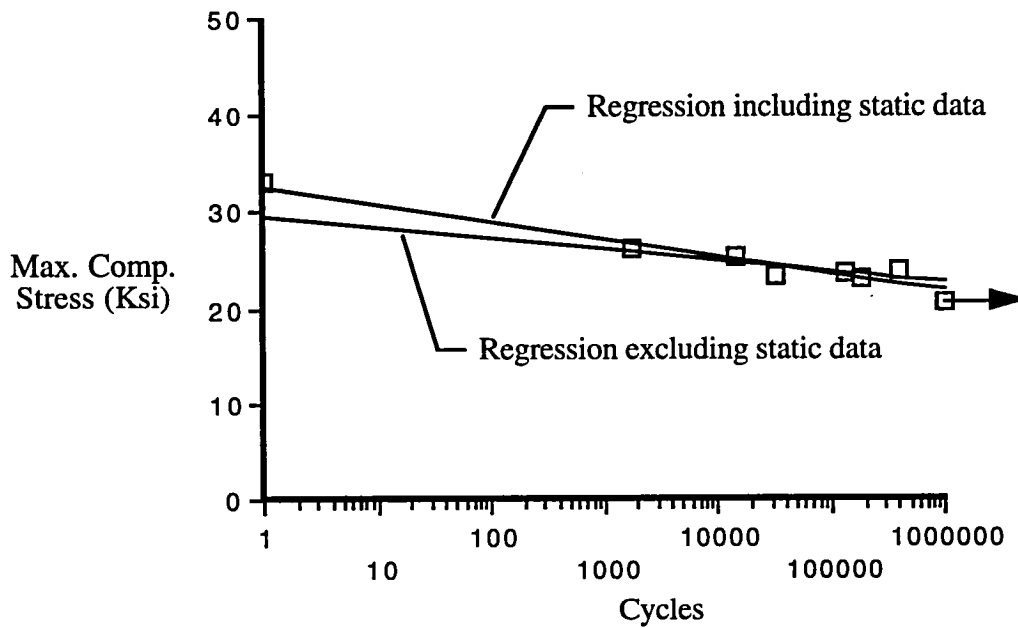


b. Toray Carbon

Figure 21. Maximum compressive stress versus cycles for each material.



c. AS4 Carbon



d. Glass

Figure 21. (Continued)

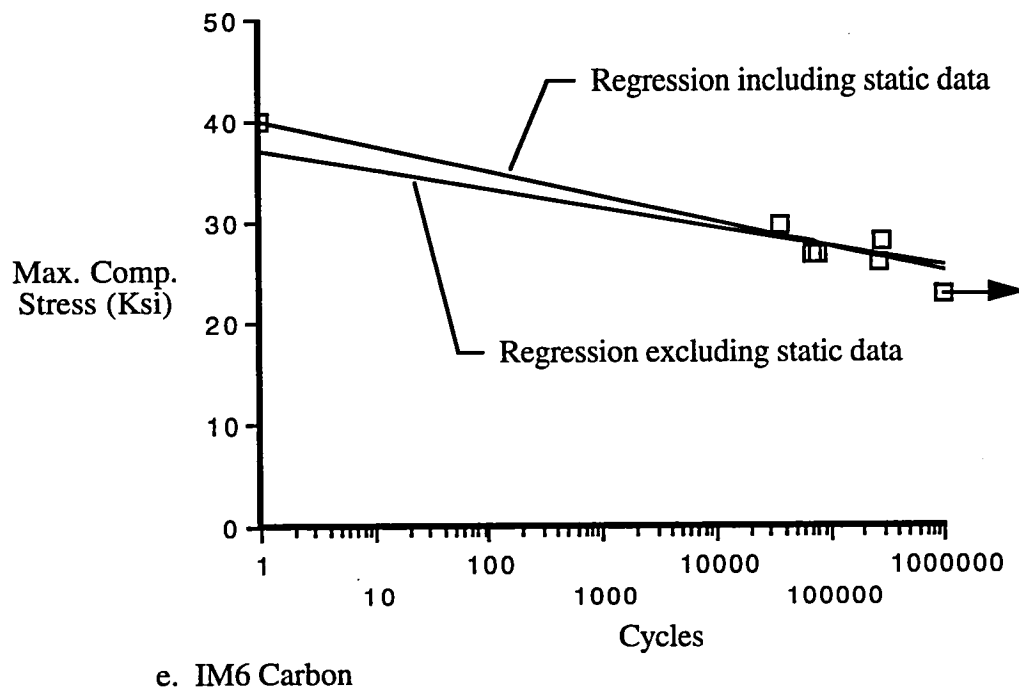


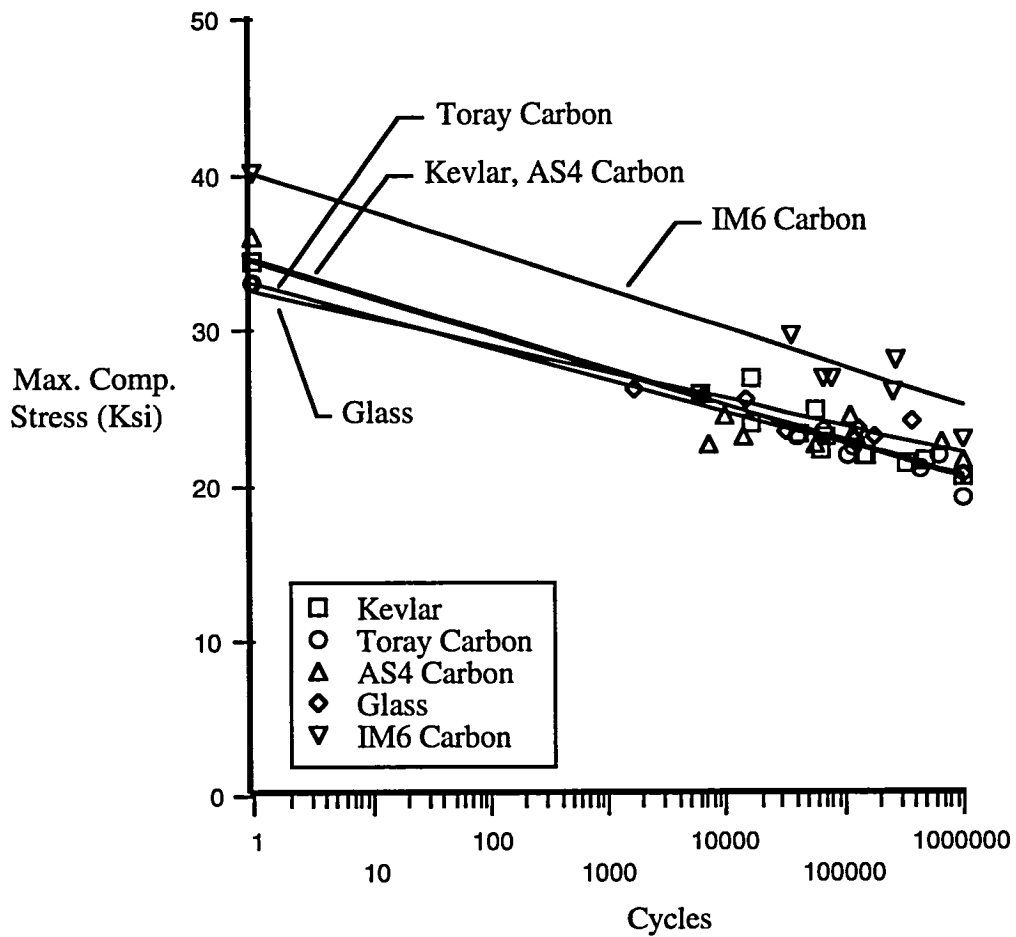
Figure 21. (Continued)

reasonable, because a typical S-N curve for a notched sample is not actually linear. As shown in Figure 1, the curve drops in the short life region and is nearly linear for longer life. However, data from the Kevlar tests contradicts this. The linear regression of the fatigue data approximates the static strength to be almost 5% higher than the actual static strength. This may indicate that the sample used to determine the static strength was not representative of the other Kevlar samples.

Figure 22-a shows the S-N response and linear regression including static data for all TTT reinforcements. The slopes of the regression lines are all similar. This would indicate that damage grew in a similar manner for all materials tested. Also, the IM6 carbon samples had a better response than the other materials. However, the significance of this information is unclear, because the static data probably should not be included in the regressions for determining fatigue response.

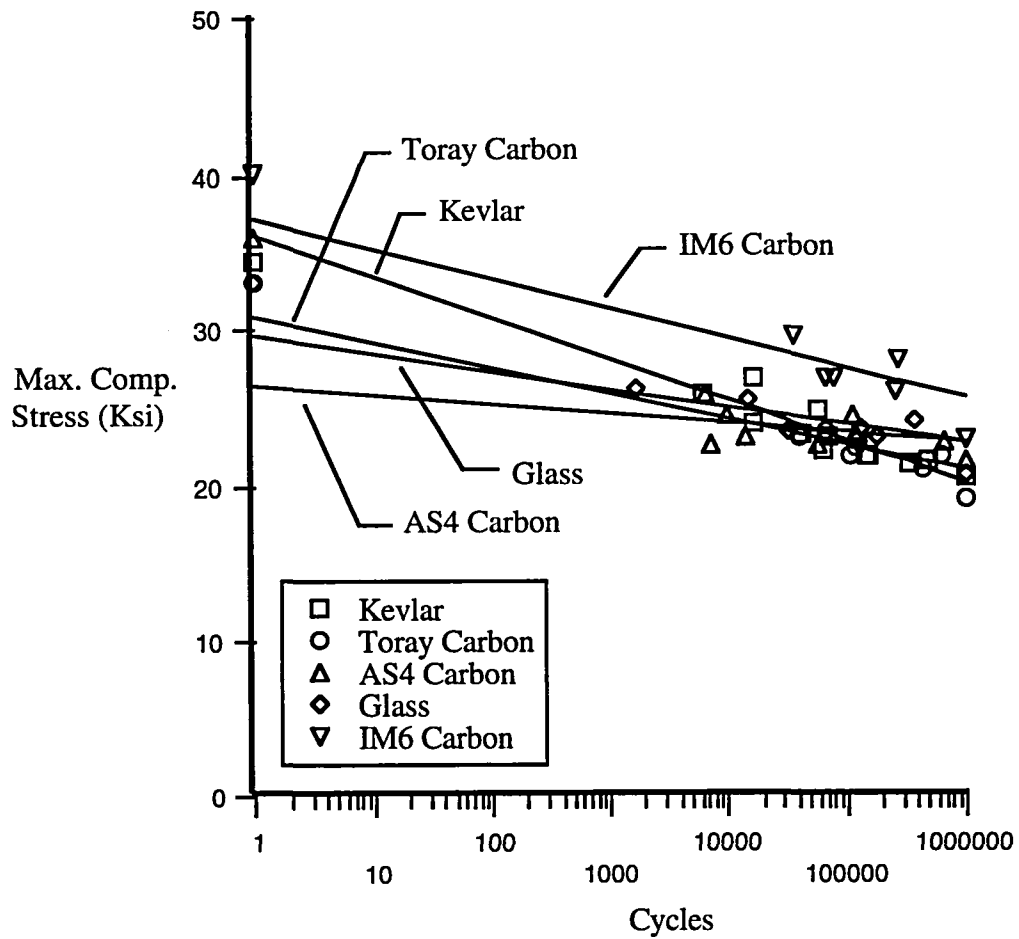
Since the S-N curve for notched samples is nearly linear beyond the short life region, the regression line determined excluding the static data should more accurately represent the fatigue response. As shown in Figure 22-b, the slopes of the regression lines determined from just fatigue data varied considerably between material groups. The regression of the Kevlar samples had the greatest negative slope, indicating greater sensitivity to increases in fatigue load levels. In contrast, the AS4 carbon regression had the smallest negative slope, indicating less sensitivity to increases in fatigue load levels.

The S-N regressions can be more easily compared by contrasting the fatigue stress levels at zero cycles and at one million cycles. Comparisons of the approximated stress levels at zero cycles provides information that can be used merely to compare fatigue response for each material at high stress levels (this is not intended to be a way of predicting life in high stress level fatigue tests). The IM6 carbon and Kevlar regressions had the highest stresses at zero cycles, as shown in Table III. This indicates good fatigue response at high stress levels. The AS4 carbon regression had the lowest zero cycle stress, nearly 18 % below average. This is indicative of poor fatigue response in the short life



a. Regressions including static data

Figure 22. Maximum compressive stress versus cycles for all materials.



b. Regressions excluding static data

Figure 22. (Continued)

Table III. S-N Regression Data from Fatigue Data for Each TTT Material

TTT Reinforcement	Slope (Ksi/# cycles)	Stress at 0 cycles (Ksi)	Stress at infinite life (Ksi)
Kevlar 29	-2.659	36.177	20.223
Toray Carbon	-1.636	30.846	21.030
AS4 Carbon	-0.586	26.337	22.821
S2 75 1/3 Glass	-1.129	29.587	22.813
IM6 Carbon	-1.926	37.227	25.671
Average	-1.587	32.035	22.512
Standard Deviation	-0.710	4.098	1.876

region. The stress levels at infinite life (one million cycles) of the regressions were similar for most of the materials tested. The IM6 carbon regression had the highest infinite life stress, about 14% above average. This indicates that the IM6 samples responded well in the long life region in addition to the short life region. The Kevlar regression had the lowest infinite life stress. So, although Kevlar responded well at high stress levels, it responded poorly at lower stress levels.

The IM6 carbon samples clearly had the best fatigue response. The other materials responded differently under different load levels. For applications that require high load levels, Kevlar could be a good alternative to IM6 carbon, while AS4 carbon would not. For applications that require longer life, Kevlar should apparently be avoided.

Since there was little variation of impact damage between materials, the amount of variation in the S-N data seems to be quite large. The causes of the differences are not clear. However, there was significant scatter in the S-N data within material groups. The primary cause of this scatter was probably variability in the material from sample to sample. There were differences in fiber waviness and resin content (voids and resin-rich regions). The size and position of the TTT reinforcing yarns may have contributed to these problems. The shape of the TTT loops (around the catcher yarn) varied considerably. These variations demonstrate the need for improvements in the production process. Also, more fatigue testing should be conducted with these materials. The only clear conclusion that can be drawn is that the IM6 carbon samples performed better than the other materials.

Damage Zone Growth

X-radiographic techniques were used to monitor changes in size and shape of the damage zone. Ten samples were monitored (two from each material group), and the radiographs are shown in Appendix A. Radiographs throughout a typical fatigue test are shown in Figure 23. The black areas at the top and bottom of the radiographs represent the extensometer tabs, and the circular gray areas represent the epoxy used to attach the tabs.

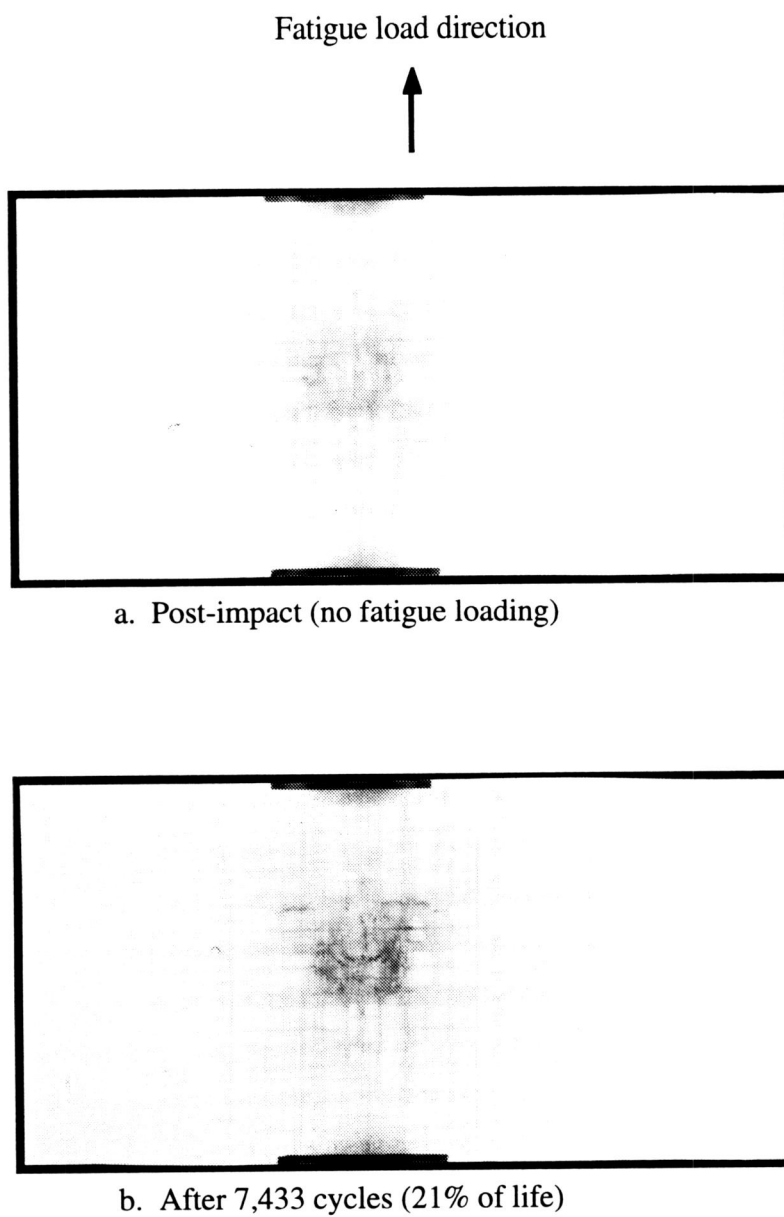


Figure 23. Radiographs of post-impact fatigue damage from typical test (IM6 carbon TTT material).

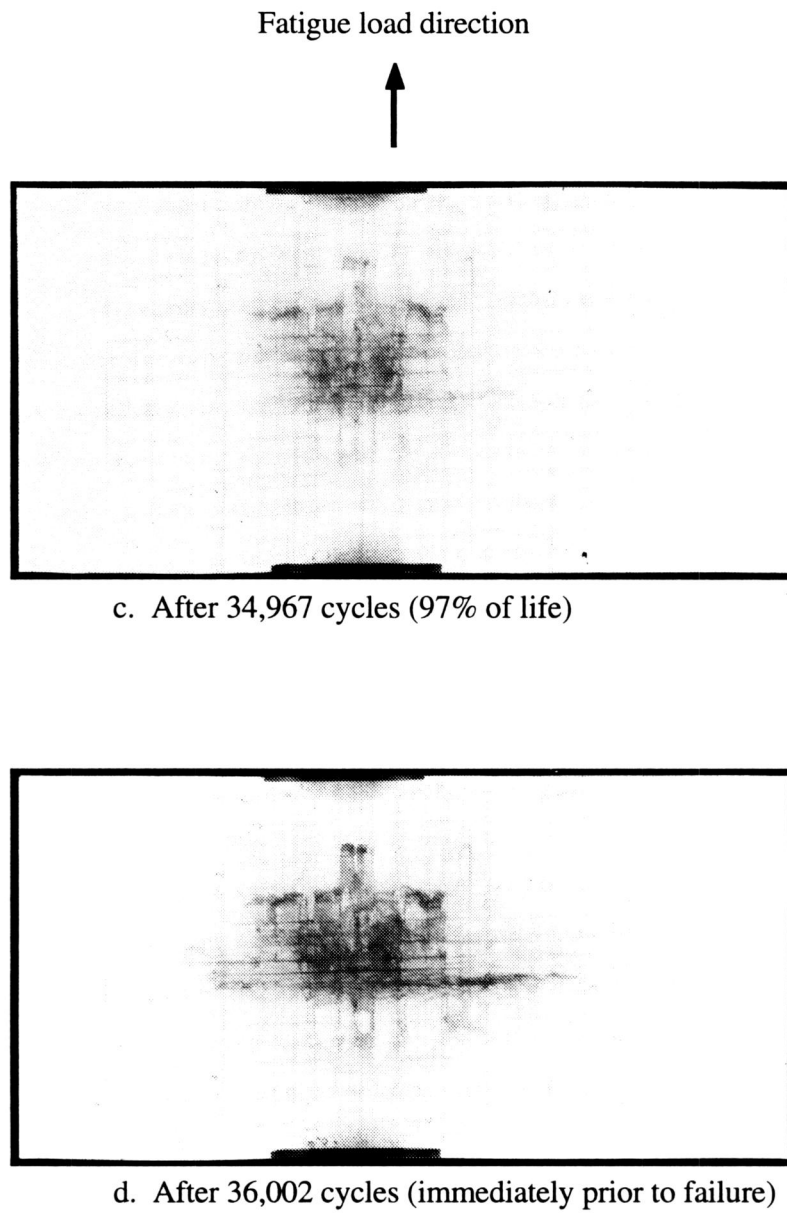


Figure 23. (Continued)

Early in life, there was little growth in the size of the initial circular damage zones. As shown in Figure 23-b, at about 21% of life the damage zone was darker and slightly larger. There were new cracks through the center of the impact site and more delaminations in the circular region around the center. These darker damage zones indicate that most of the damage growth occurred through-the-thickness of the sample at the impact site. However, there were also some new cracks and delaminations extending out of the initial damage zone.

Late in life, the size of the damage zone grew more rapidly. At about 97% of life, as shown in Figure 23-c, the damage zone was significantly darker. Additionally, there was much more damage growth transverse to the loading direction. There was also some damage growth, in the form of delaminations, in the loading direction. During the initial 96% to 97% of life, damage growth was chiefly restricted to the initial impact-induced damage zone. Once this initial damage zone was essentially saturated with cracks and delaminations, the damage grew rapidly away from the impact site and caused failure.

During the final 3% of fatigue life, delaminations and transverse shear failures grew (from the impact site) in a narrow zone transverse to the loading direction. Figure 23-d shows the damage zone immediately prior to failure, presumably within the last 0.3% of life. Each sample that was loaded to failure, had a transverse shear failure mode through-the-thickness of the laminate, as shown in Figure 24. All the material groups appeared to grow damage in the same manner. However, the glass material appeared to have damage zones that were wider in the loading direction than the other materials. Also, the transverse shear failure did not grow directly from the center of the impact site; the failure extended from damage that had grown in the fatigue loading direction.

Five samples, one from each material group, were sectioned to determine their failure modes, as shown in Appendix B. These samples were previously loaded in fatigue to about 99.9% of life and were sectioned parallel to the loading direction. At the impact site there were many scattered fiber bundle failures, ply cracks and delaminations. There

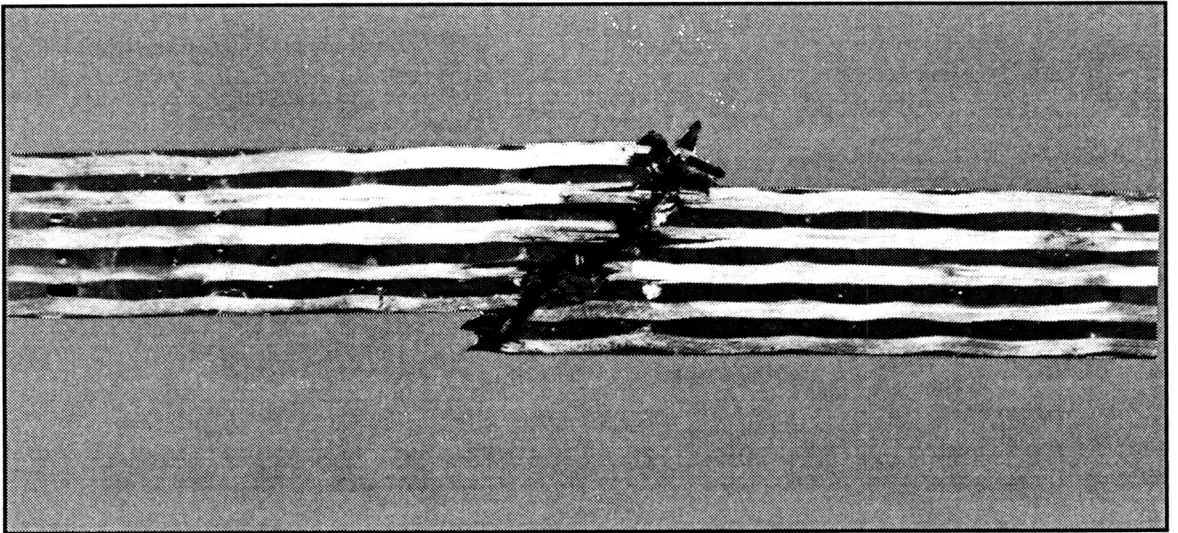


Figure 24. Transverse shear failure mode (Impacted on top face).

were fiber bundle failures (through their thickness) parallel to the impact load direction, as shown in Figure 25. Also, a series of fiber bundle failures were scattered in a plane parallel to the 90° fibers and rotated $\pm 45^\circ$ from the 0° fiber direction. As shown in Figure 25, these failures typically extended through the entire cross-section of each sample. They were probably the result of local instability and showed the transverse shear failure mode prevalent in these materials. Away from the impact site, fiber bundle failures, ply cracks and delaminations were still present. The 45° transverse shear failures often extended far from the center of the damage zone. They are represented on the radiographs by the long narrow black regions transverse to the load direction. The 45° failures are assumed to have been caused by the fatigue loading, while the failures parallel to the impact load direction are believed to be a result of the impact event.

The failure mechanism appeared to be the same for each material. It was visually observed that the delaminations typically grew one cell at a time. In other words delamination growth was constrained by the TTT reinforcing fibers. Under a compressive load the delaminations opened and exerted tensile loads on the surrounding TTT fibers. After repeated loading the delaminations grew to neighboring cells; this is believed to have been caused by transverse shear failures at or near catcher yarns or stretching of TTT reinforcing yarns.

In summary, early in life delaminations grew through-the-thickness of the samples near the impact site. Once the local delaminations were prevalent enough to reduce the local stability, the in-plane fibers failed in transverse shear. This process continued until the impact site was saturated with damage. The failures then rapidly grew transverse to the loading direction.

The transverse shear failure modes are assumed to have been caused by the reduction of local stability. There were various differences in the samples that could lead to differences in the number of cycles before reaching critical instability. Local resin-rich zones or voids near the in-plane tows or waviness caused by large TTT fiber bundles could

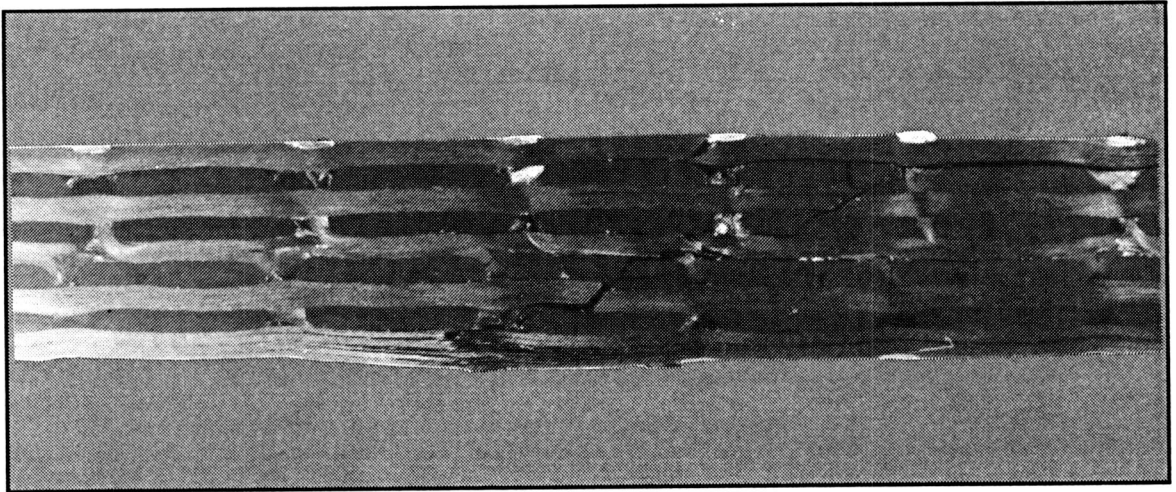


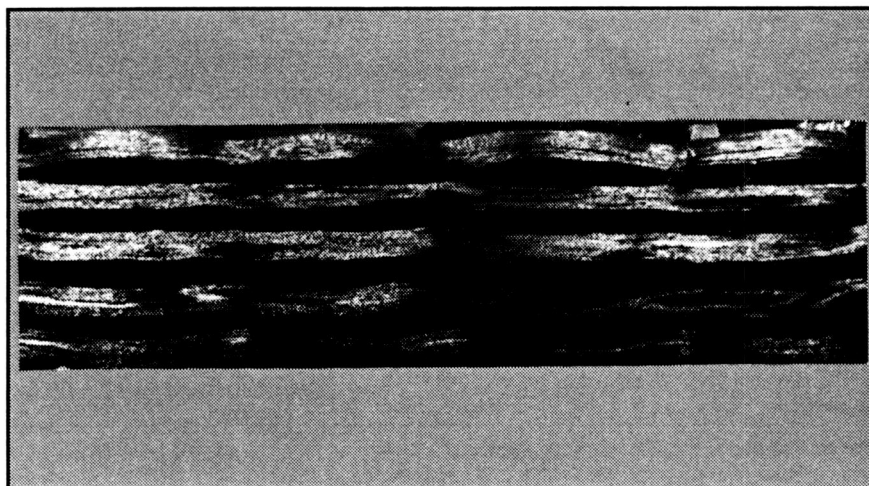
Figure 25. Typical cross-section at center of impact site immediately prior to fatigue failure (Kevlar reinforcement; impacted on top face).

reduce the local stability. Additionally, TTT fibers with a low elastic modulus would stretch more easily when the delaminations open under compressive loading. This would increase local instability by allowing delaminations to grow more rapidly between cells (that were originally constrained by TTT reinforcing fibers). All of these events could contribute to increases in local instability, which would cause transverse shear failure.

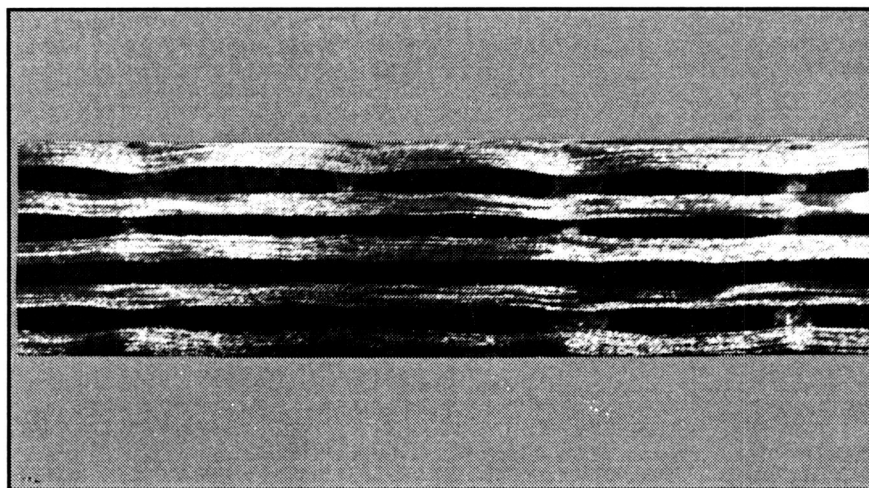
Sectioning revealed that there were many fairly large pockets of resin, as well as many voids in the samples tested. Also, there were variations in the waviness of the in-plane fibers, as shown in Figure 26. The waviness varied throughout each sample, between samples, and between material groups. The AS4 carbon samples generally exhibited the largest degree of waviness. This was evidently caused by the large AS4 carbon TTT reinforcing fiber yarns. The estimated yarn diameter of each TTT material is shown in Table IV. The AS4 carbon yarns had the largest diameter, nearly twice that of the IM6 carbon yarns. Toray carbon also had a diameter larger than average, over 40% greater than IM6 carbon. This probably degraded the materials' fatigue response, especially the AS4 carbon materials. The samples with IM6 carbon TTT reinforcing fibers had the best fatigue response, and IM6 carbon had a yarn diameter smaller than average.

The fatigue response also appeared to be influenced by elastic modulus. As shown in Table IV, the Kevlar and glass yarns had the lowest modulus. Since both Kevlar and glass had smaller yarn diameters than IM6 carbon, the low modulus may have prevented these materials from achieving a fatigue response similar to IM6 carbon. The IM6 carbon yarns had the highest modulus. Toray carbon also had a high modulus. This apparently indicates that optimum fatigue response would be achieved using TTT yarns that were small in diameter and had high modulus.

The tensile strength did not appear to influence fatigue response. Toray carbon had the highest strength and second highest modulus. Yet, the fatigue response was more affected, presumably, by the large yarn diameter. Also, the material with the smallest yarn diameter, glass, had an above average tensile strength but a low modulus. Therefore, large



a. AS4 carbon



b. Glass

Figure 26. Waviness of in-plane fibers.

Table IV. Mechanical Properties of TTT Reinforcing Fibers

TTT Reinforcement	Estimated ^a Yarn Diameter (inches)	Nominal Filament Modulus (Msi)	Nominal Tensile Strength (Ksi)
Kevlar 29	0.0170	10.2	336
Toray Carbon	0.0241	42.7	1024
AS4 Carbon 9K	0.0334	33.0	580
S2 75 1/3 Glass	0.0139	12.8	683
IM6 Carbon 6K ^b	0.0171	43.5	745
Average	0.0211	28.4	674
Standard Deviation	0.0070	14.3	224

a. Kevlar diameter was quoted from manufacturer and had fiber volume fraction of 80%. Others were estimated assuming 80% fiber volume fraction.

b. Nominal tensile strength given for IM6 carbon 12K.

All other values quoted from manufacturer [48-51].

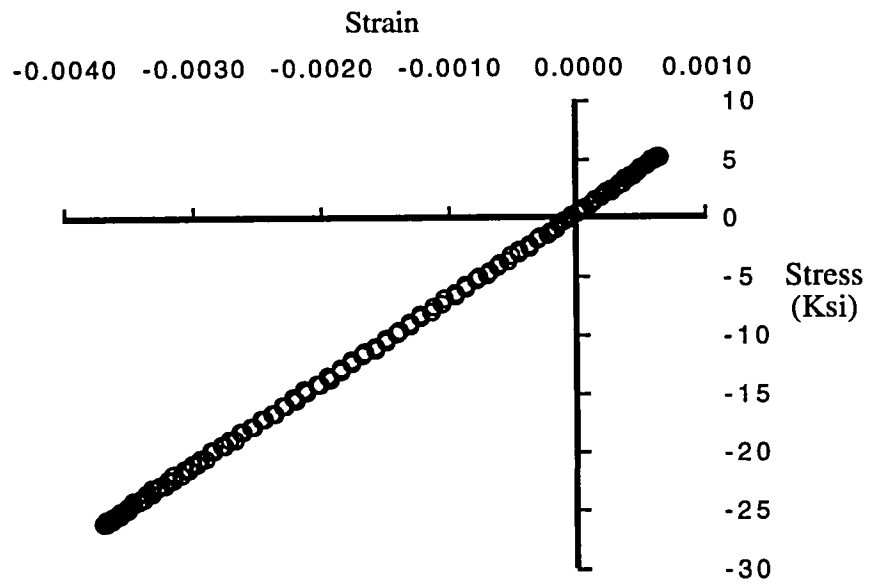
yarn diameter and low modulus appear to be the main causes of degraded fatigue response. There may have been other contributing factors, such as fiber volume fraction variations and the presence of matrix voids. However, since the weaving and epoxy infiltration processes were the same for all the materials, yarn diameter and modulus could be the controlling influences of fiber microbuckling initiation.

Fatigue Cycles

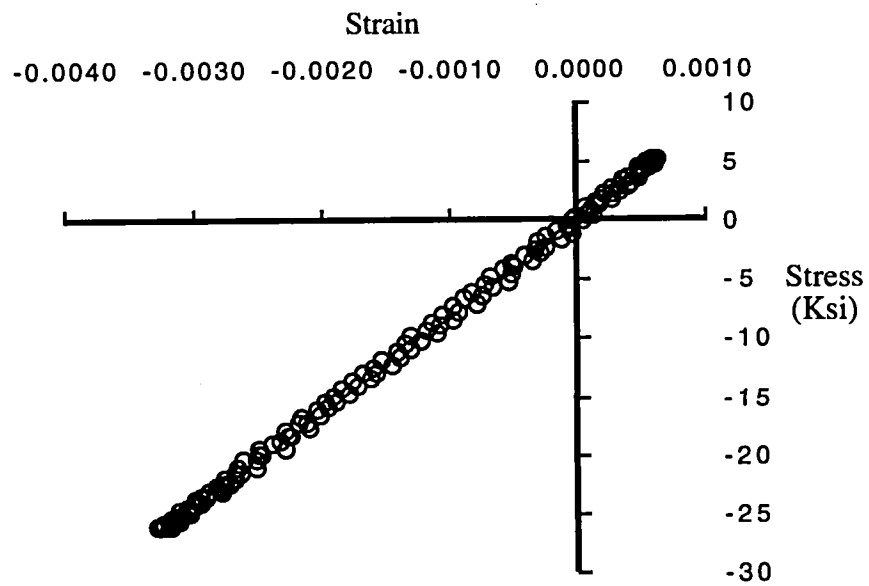
In addition to determining the S-N response, the stress-strain response of the materials was monitored periodically throughout each fatigue test. Stress was plotted versus strain for both the front and back extensometers for selected cycles during each fatigue test (the front extensometer was mounted over the damage zone on the impacted face of each sample). Typically, the shape of the stress-strain curves was similar for both the front and back extensometers. Figure 27 shows the stress-strain response for both extensometers early in a typical fatigue test.

It was visually observed that there was considerably less damage across the back face of the sample than across the front face (impacted face). Therefore, as the compressive load on the sample increased, the front strain (compressive) increased more than the back strain, which created local bending at the damage site. The sample incurred the most bending at the maximum compressive strain for each cycle. Figure 28 shows the maximum compressive strain (over the front and back faces) plotted versus fatigue cycles; the lines represent discrete data points. The maximum compressive front strain increased at a faster rate than the maximum compressive back strain until approximately 80% of life. After that point, bending decreased dramatically until failure. Although bending varied greatly from sample to sample throughout each fatigue test, this was a typical response.

The relevance of amount of bending incurred is not clear. Local bending (determined from extensometer data) is not a direct indicator of damage growth. Global bending, caused by warped samples or loading misalignment, also influences local bending. Additionally, measured bending strain was artificially elevated due to the method



a. Front face



b. Back face

Figure 27. Stress versus strain across front and back faces at impact site for one cycle early in a typical fatigue test (IM6 carbon TTT reinforcement).

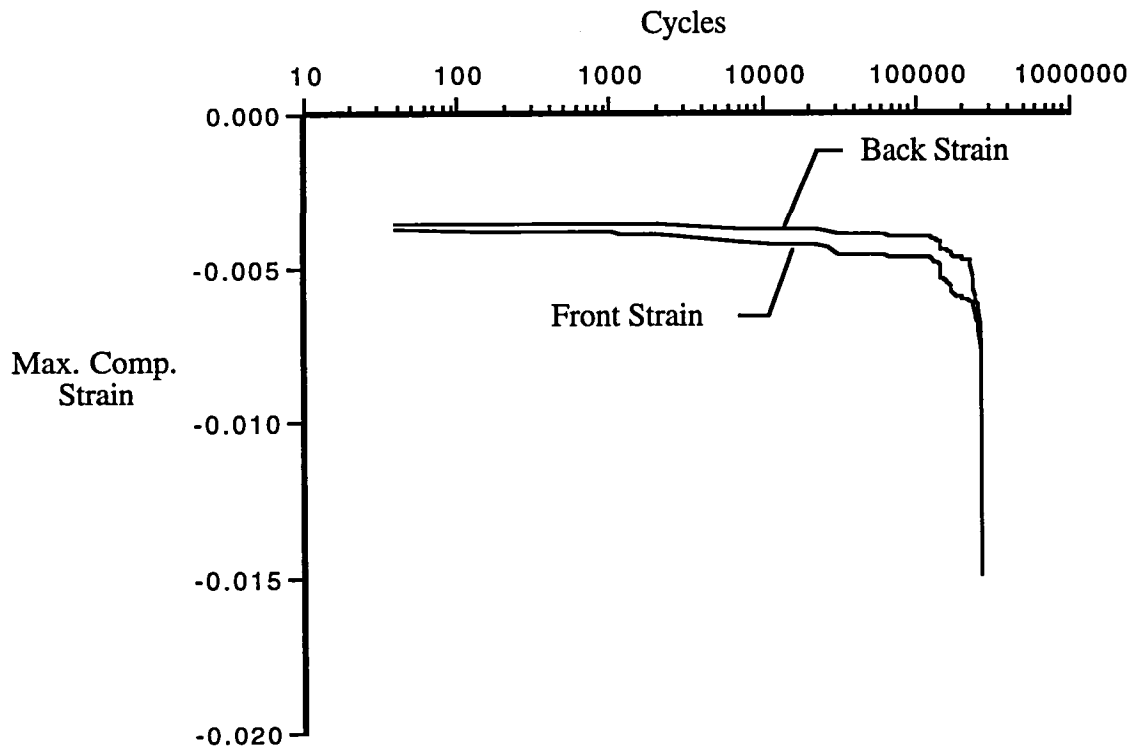


Figure 28. Maximum compressive strain from front and back extensometers throughout a typical fatigue test (IM6 carbon TTT reinforcement).

used to attach the extensometers. If it was possible to attach the extensometers directly to the samples at the neutral surface, no strain due to bending would be measured. However, due to specimen thickness and tabbing, considerable bending strain was measured.

Yet, this bending data may have provided some meaningful information about damage and damage growth. Since the maximum compressive strain across the front of the sample was greater than the strain across the back during the beginning of each test, the back faces of the samples did not appear to be significantly affected by impact. Also, the initial damage seemed to grow through-the-thickness of the samples (from the impacted face to the back face). This was also shown on the radiographs, as damage intensified in the impact region.

Stiffness and hysteresis data determined from each extensometer varied significantly. Therefore, the average strain across the impact site was used to calculate all subsequent data. Figure 29 shows the stress versus average strain response of a sample at various cycles throughout a typical fatigue test. The stress-strain response was essentially linear until approximately 57% of life (cycle # 152,000). The non-linearity then became more pronounced until failure. The loading and unloading portions of the stress-strain curves followed essentially the same path until approximately 97% of life (cycle # 262,000). Then, the loading and unloading curves moved apart until failure.

The last few cycles showed the greatest changes in size and shape of the stress-strain curve. In particular, after experiencing the maximum compressive stress, the compressive strain continued to increase. This indicates that damage was growing rapidly and corresponds to the transverse shear failure growth. This is clearly shown in Figure 30 for the last complete cycle before failure.

Changes in size and shape of the stress-strain curve were monitored throughout each fatigue test by observing changes in hysteresis, maximum and minimum strain, and moduli. The hysteresis energy (actually strain energy density) is the area enclosed by the stress versus strain curve. This area was approximated by numerical integration using the

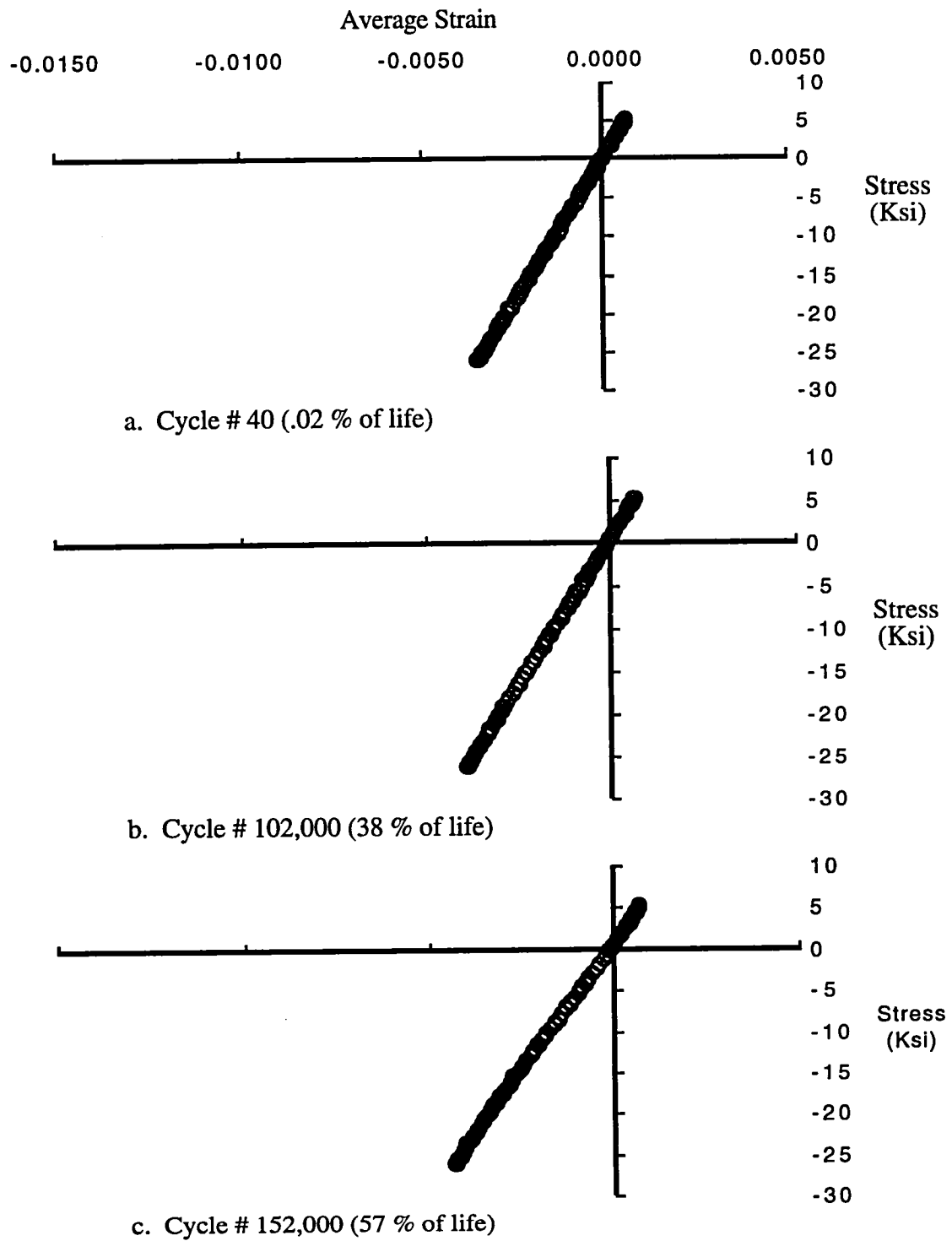
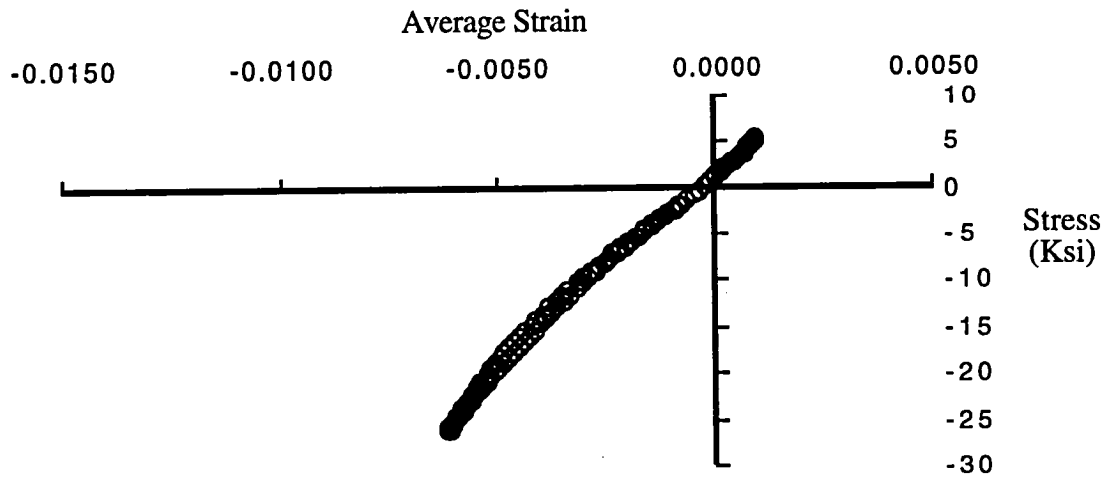
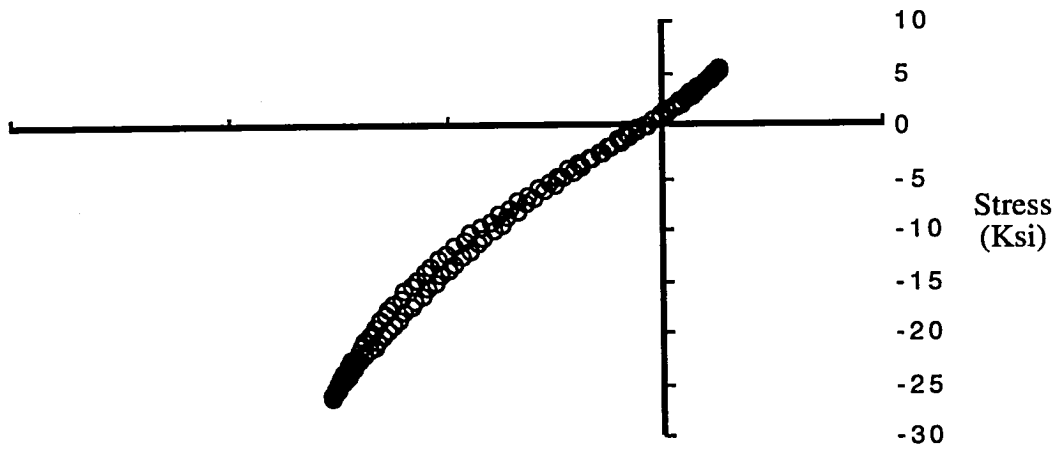


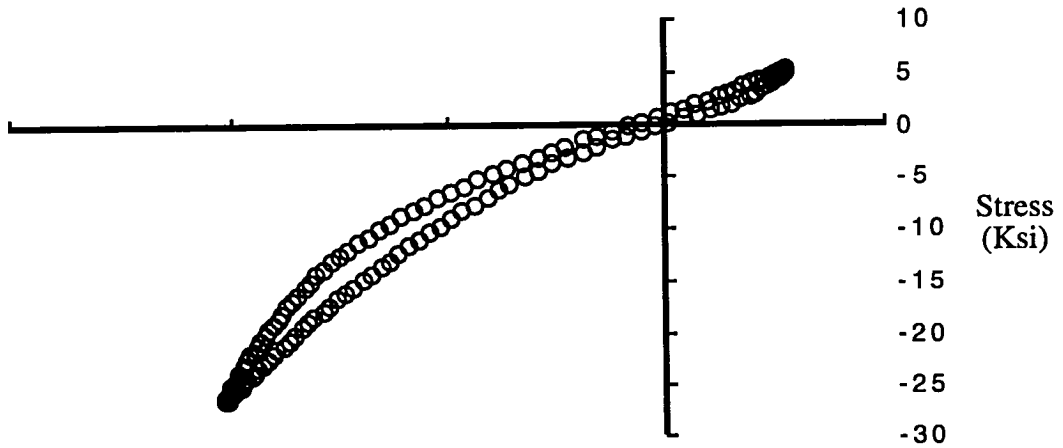
Figure 29. Far-field stress versus average strain across impact site during a typical fatigue test (IM6 TTT reinforcement).



d. Cycle # 262,000 (97 % of life)



e. Cycle # 267,000 (99 % of life)



f. Cycle # 269,003 (>99 % of life)

Figure 29. (Continued)

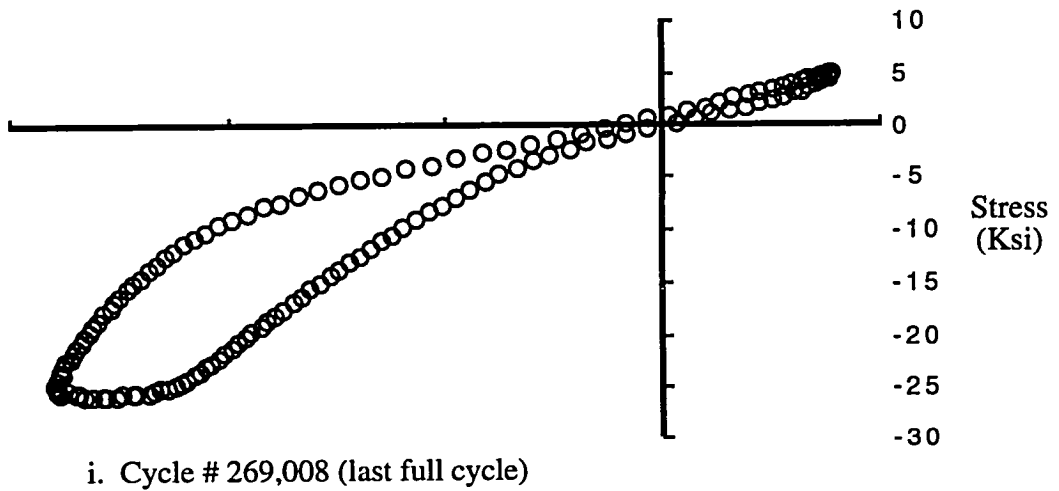
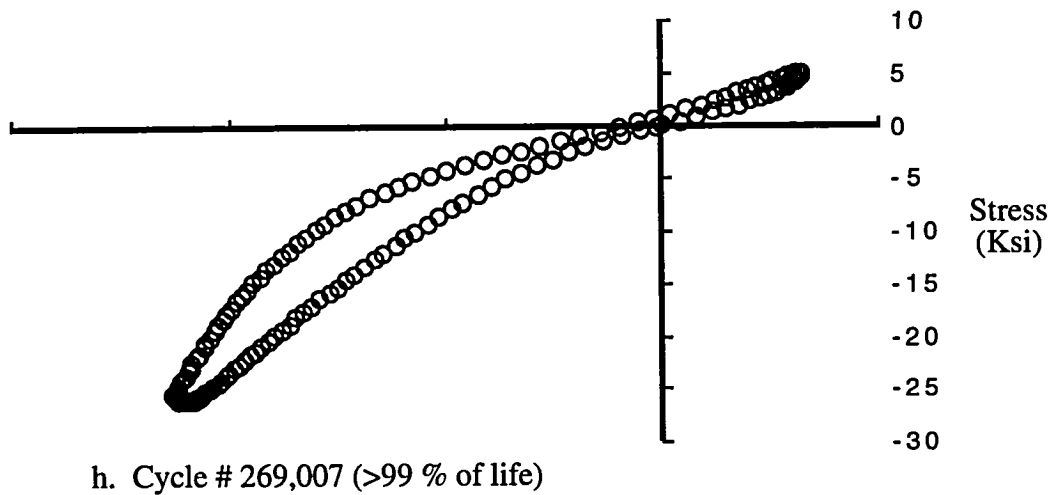
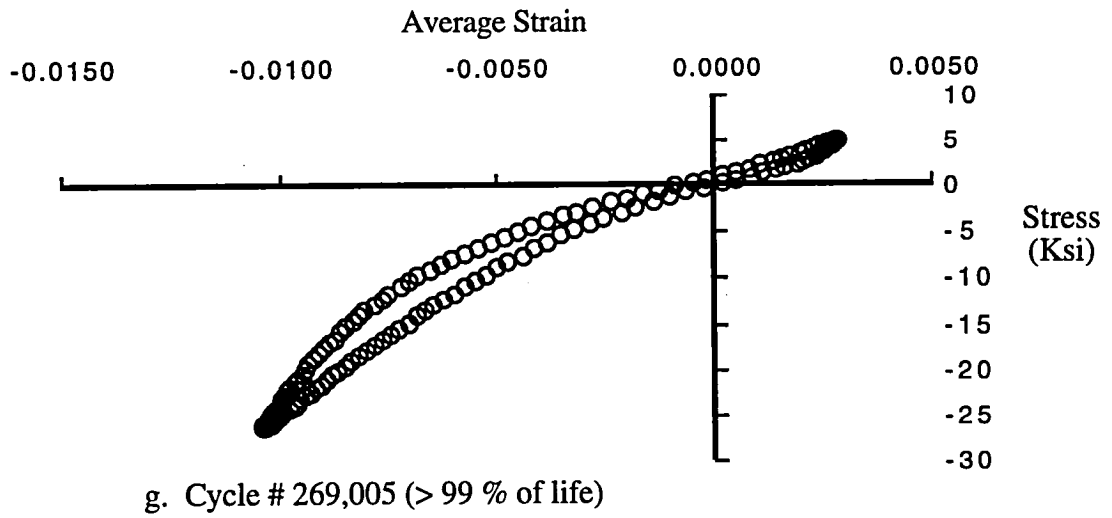


Figure 29. (Continued)

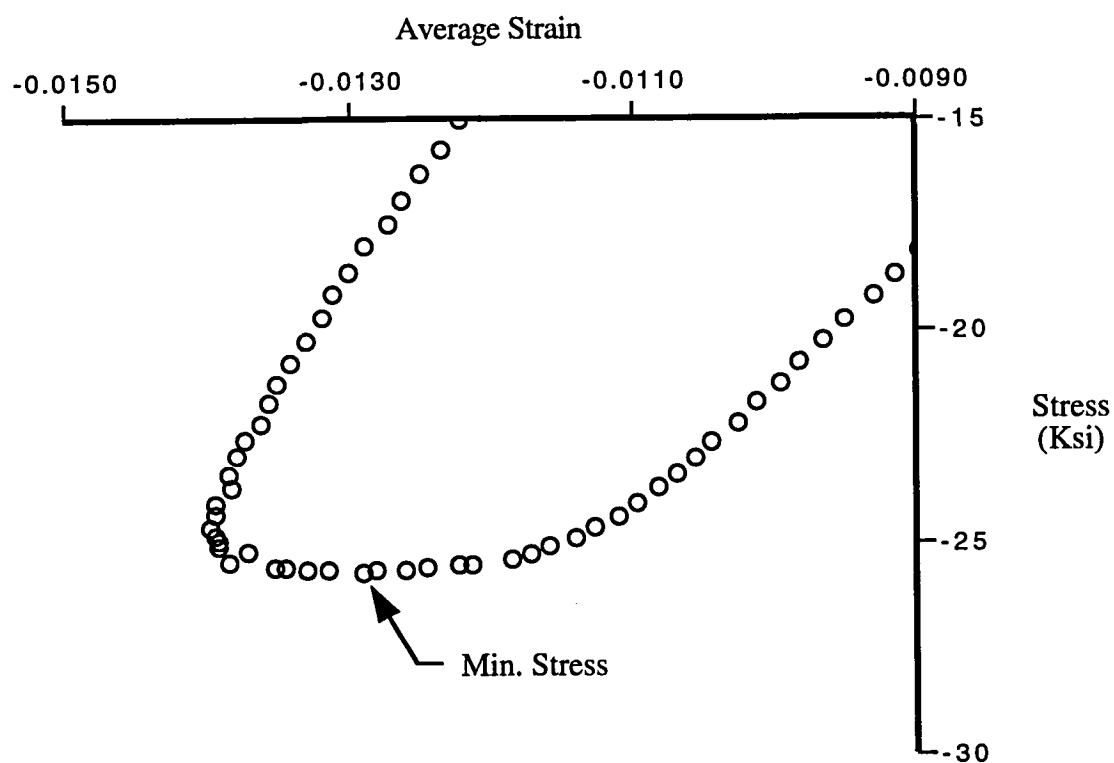


Figure 30. Far-field stress versus average strain at minimum stress during last full cycle of a typical fatigue test (IM6 TTT reinforcement).

trapezoidal rule for successive points. Three moduli were calculated for each cycle, as shown in Figure 31. The secant modulus is the slope of the line between the maximum stress and corresponding strain and the minimum stress and corresponding strain. The unloading modulus is a linear regression of the curve when the sample begins to unload from the maximum tensile stress. Likewise, the loading modulus is a linear regression of the curve when the sample begins to load from the maximum compressive stress. The regressions were calculated for the unloading and loading modulus with twelve and eleven points respectively. This typically corresponded to a strain range of 300 to 1400 micro strain.

Figure 32 shows the hysteresis (strain energy density) throughout a typical fatigue test. The hysteresis was generally small throughout the initial 97% of the test. However, there was some scatter in these data. This may have been partially caused by the method used to approximate these values. Additionally, hysteresis is essentially a measure of the dissipated energy during a fatigue cycle. This may be due to plastic material response and damage development and growth. It is conceivable that hysteresis energy could increase and then decrease during a fatigue test. Transverse shear failures and ply cracks would contribute to increases in hysteresis. The development and growth of this damage is typically not consistent. This sort of damage propagation could cause slight variations in the shape of stress-strain curve, even early in fatigue life. Therefore, these slight variations in hysteresis energy may indicate a change in the damage zone, although not significant.

However, hysteresis increased dramatically within the last 3% of fatigue life. According to the radiographic data, the majority of the damage growth during the initial 97% of life occurred through-the-thickness of the sample at the impact site, and damage rapidly grew transverse to the load direction from the impact site during the final 3% of life. This indicates that increases in hysteresis correspond to large increases in damage zone size (growth away from the impact site) and establish that failure is imminent.

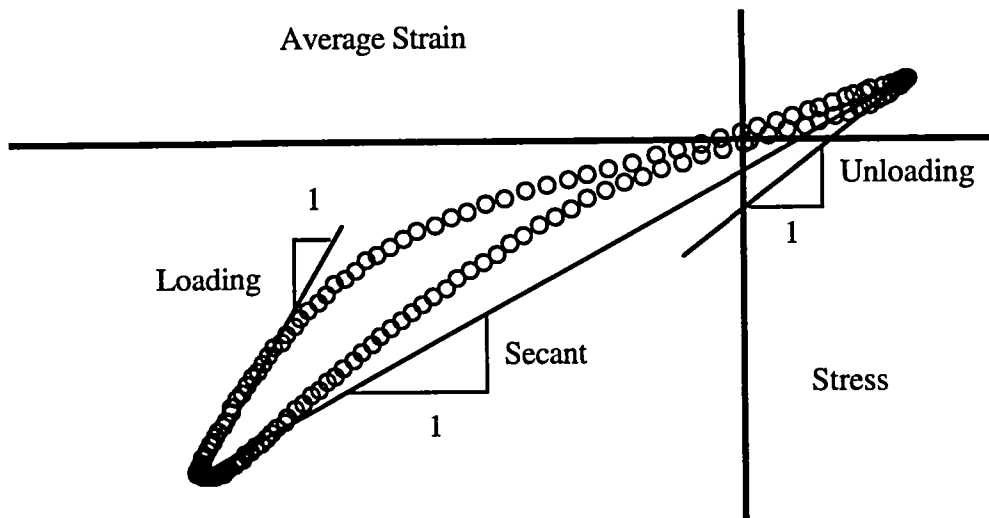


Figure 31. Definition of moduli.

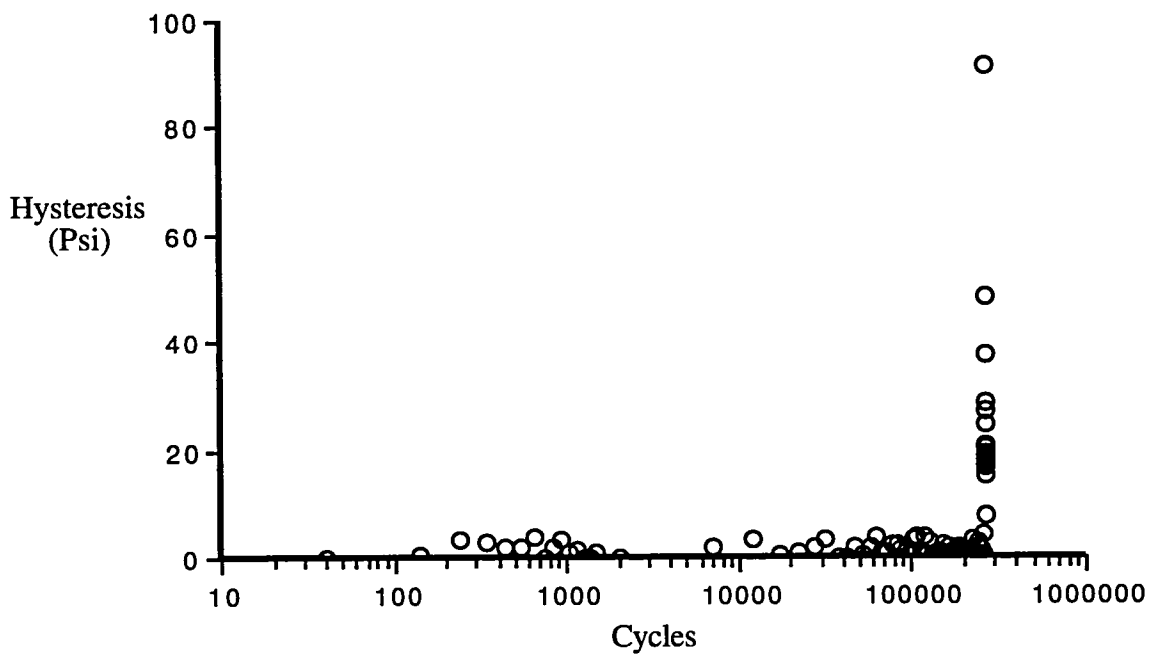


Figure 32. Changes in hysteresis throughout a typical fatigue test (IM6 carbon reinforcement).

Figure 33 shows the maximum and minimum average strain throughout a typical fatigue test. The average maximum strain varied little through the first half of the test. However, at approximately 54% of the sample's fatigue life, the maximum strain started to increase slightly. Similarly, the average minimum strain started to decrease more quickly at about 54% of the sample's life. There is no obvious correlation between this strain response and damage zone growth. However, this evidently coincides with the stress-strain response becoming non-linear. During the final 3% of life, the maximum strain increased rapidly, and the minimum strain decreased rapidly. Similar to large changes in hysteresis, large changes in maximum and minimum strain correspond to large growth of the damage zone.

Figure 34 shows the moduli throughout a typical fatigue test. The secant modulus gradually decreased for about the first half of the test. At approximately 54% of the sample's fatigue life, the secant modulus started to decrease more rapidly; again, this corresponded to a non-linear stress-strain response across the impact site. At approximately 97% of life, the secant modulus dropped off dramatically. This rapid decrease continued until failure, depicting rapid damage growth. For this test, the secant modulus for the last cycle was approximately 24% of the secant modulus at the beginning of the fatigue test.

The unloading modulus was essentially the same as the secant modulus for each cycle. However, the unloading modulus had considerably more scatter. This was due to the small strain range used in the linear regression of the data. There were also inaccuracies in stress and strain data introduced by the load and displacement recording procedure.

As with the unloading modulus, the linear regression caused scatter in the loading modulus approximations. However, the loading modulus showed little, if any, change throughout the fatigue test. There appeared to be no modulus degradation as was the case with the secant and unloading modulus.

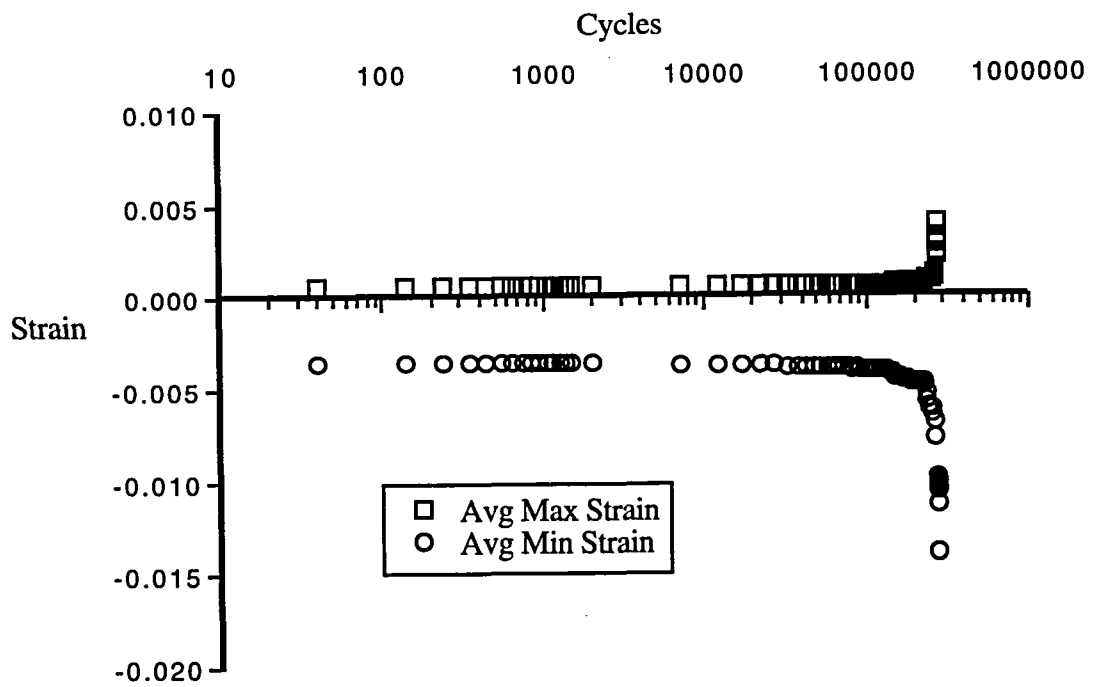


Figure 33. Changes in maximum and minimum strain throughout a typical fatigue test (IM6 carbon reinforcement).

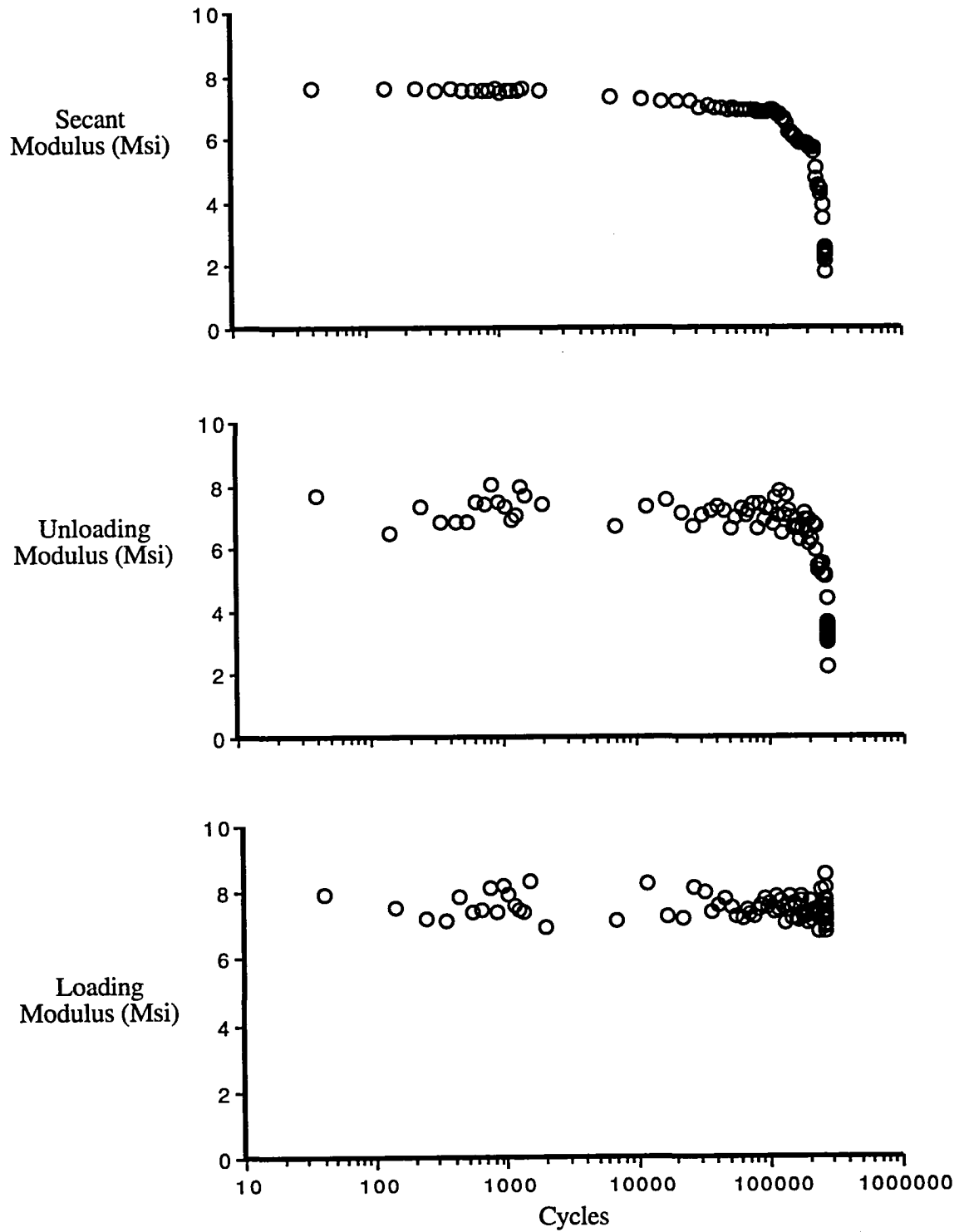


Figure 34. Changes in moduli throughout a typical fatigue test (IM6 carbon reinforcement).

Damage growth, which corresponds to changes in shape of stress-strain curves, is represented by changes in moduli. As damage increased, in the form of ply cracks and transverse shear failures, the stress-strain response under tensile loading was affected (delaminations would not change the tensile response). Decreases in unloading modulus represent increases in displacement across the impact site caused by damage growth. However, damage growth (including delamination growth) occurred chiefly when the sample was being compressed. At the maximum compressive load delaminations and ply cracks were opened, and transverse shear failures were pushed together. The loading modulus measured the stiffness under compressive loading as delaminations and ply cracks began to close and transverse shear cracks began to open. Changes in secant modulus represented an average stiffness response to damage growth. Secant modulus was influenced by all forms of damage growth. Interestingly, the unloading modulus clearly had the same fatigue response as the secant modulus.

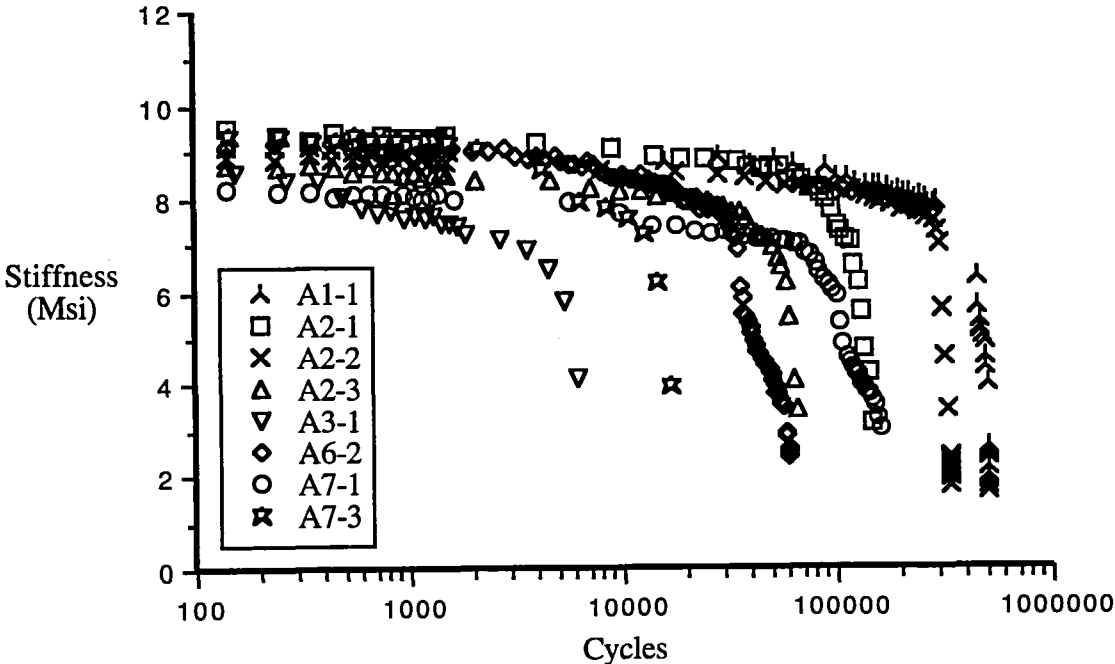
These trends were typical of the fatigue response for each TTT reinforcement, as shown in Appendix C. By monitoring hysteresis, maximum and minimum strain, and secant and unloading modulus, throughout a fatigue test, the number of cycles to failure can be accurately anticipated. Within the final 3% of life, minimum strain and secant and unloading modulus significantly decrease, while hysteresis and maximum strain increase significantly. Additionally, the maximum and minimum strain and secant and unloading modulus also show some variation by about 50% of fatigue life, unlike hysteresis data. Consequently, life can possibly be estimated earlier by monitoring maximum strain, minimum strain, secant modulus, or unloading modulus. Changes in both maximum and minimum strain are inherently incorporated in changes in secant modulus. Therefore, monitoring the secant modulus offers a simpler approach than monitoring both strains or the unloading modulus. Consequently, the secant modulus provided the most useful information in attempting to anticipate failure.

Stiffness Loss

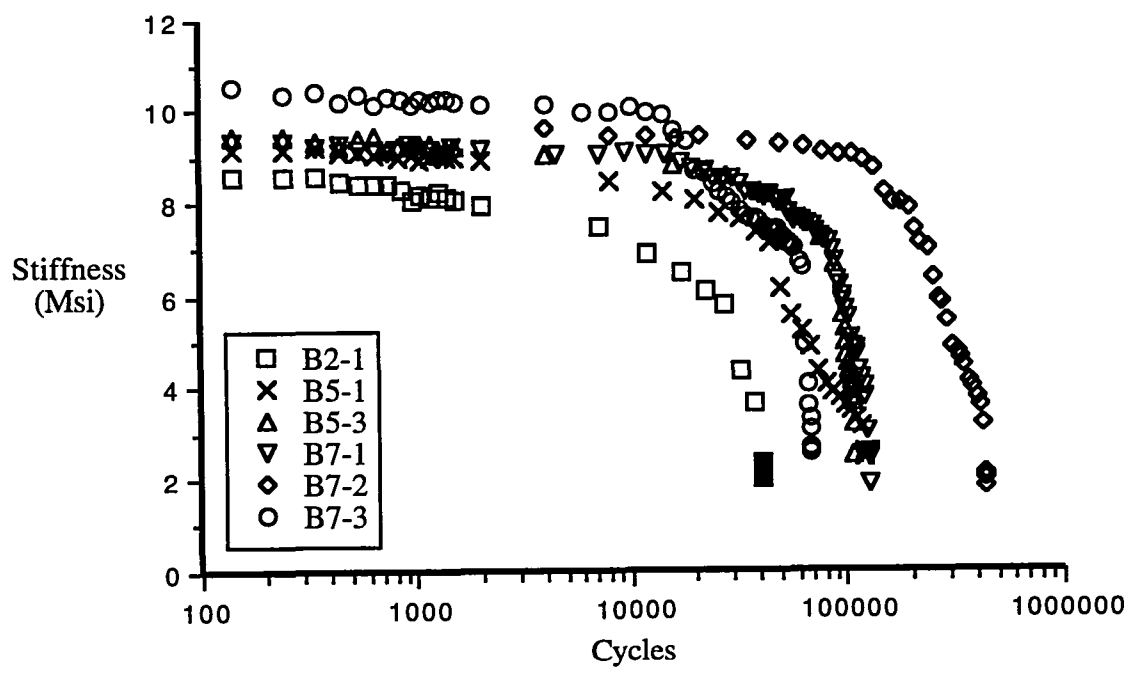
Figure 35 shows stiffness (secant modulus) loss throughout the fatigue life of each sample tested. These curves varied with the number of cycles to failure for each sample. Yet, the samples all had the same stiffness loss trends, with limited variations. The stiffness at the beginning of the fatigue tests did vary somewhat. The average initial post-impact fatigue stiffness for all the samples tested was about 8.8 Msi, as shown in Table V. The Toray carbon samples had the highest initial post-impact fatigue stiffness, approximately 9.7 Msi. The AS4 carbon samples had the lowest stiffness, about 8 Msi.

The materials with the largest undamaged static stiffness (from static stress versus far-field strain data) had the largest initial post-impact fatigue stiffness, as shown in Figure 36. The Toray carbon and glass samples had the greatest reductions (caused by impact damage) in stiffness, 19% and 17% respectively. The IM6 carbon samples had a stiffness reduction of about 14%. Also, the Kevlar and AS4 carbon samples had the smallest stiffness reduction, both about 5%. However, only one static test was conducted for each material. If the assumption is again made that the TTT reinforcement does not affect stiffness (and impact damage did not vary between material groups), the average stiffness for all materials could be used to calculate stiffness reduction. Therefore, the most accurate representation of the data shows that damage caused from the impact event reduced the stiffness by about 12% for all the materials tested.

The stiffness loss curves were normalized to compare stiffness loss for samples with different fatigue lives, as shown in Figure 37. The number of cycles was normalized with the number of cycles to failure, and stiffness was normalized with the initial post-impact fatigue stiffness. Interestingly, the stiffness loss curves were similar for all samples and all TTT reinforcements tested. There were essentially three different stiffness loss regions, as shown in Figure 38. Typically, there was little stiffness loss in the first 50% of the test. There was significantly more stiffness loss over the next 47% of the test. And, the stiffness dropped dramatically over the final 3% of the test. Although there was some

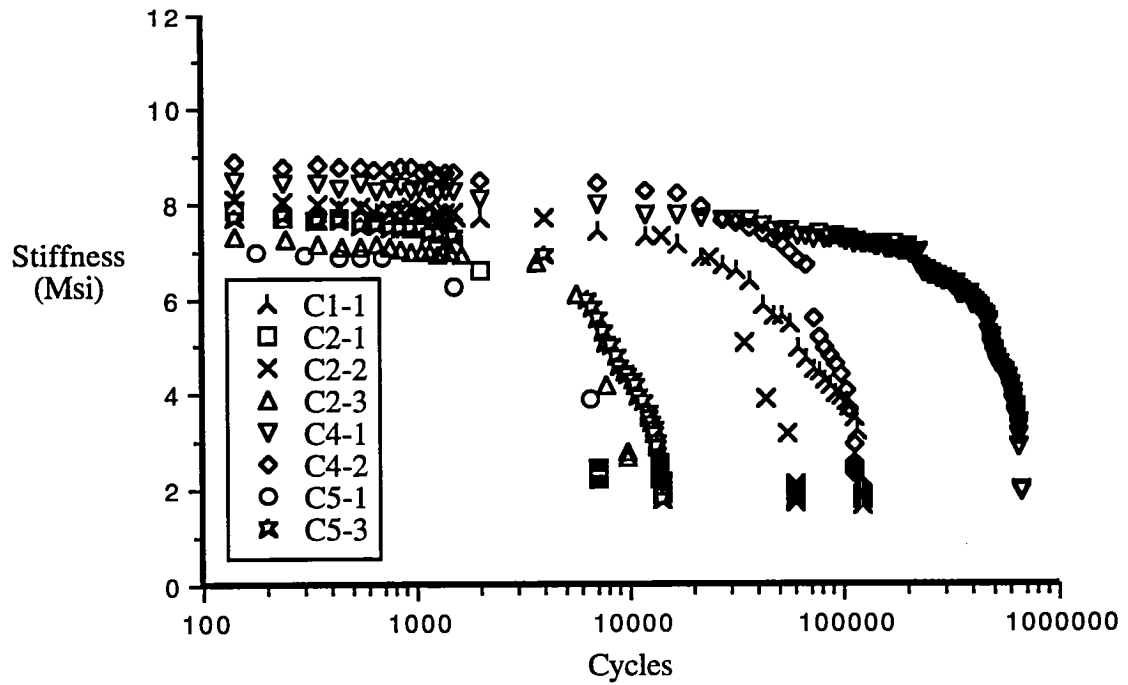


a. Kevlar

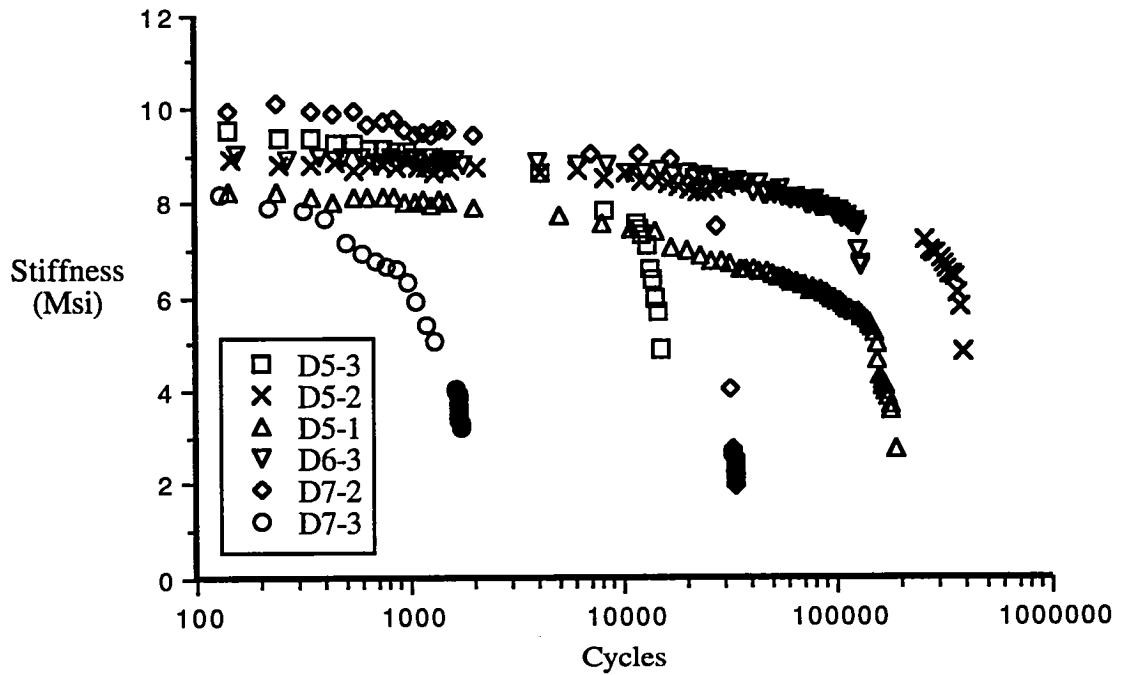


b. Toray carbon

Figure 35. Stiffness loss throughout each fatigue test.

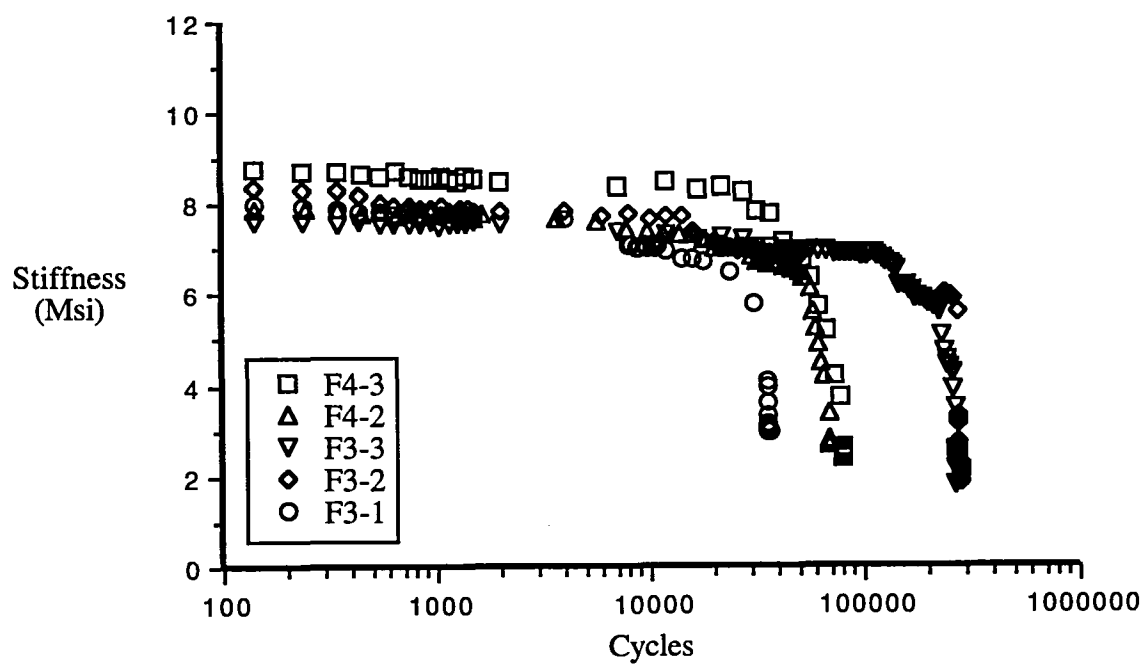


c. AS4 carbon



d. Glass

Figure 35. (Continued)



e. IM6 carbon

Figure 35. (Continued)

Table V. Initial Post-Impact Fatigue Stiffnesses

TTT Reinforcement	Average Stiffness (Msi)	Standard Deviation (Msi)
Kevlar 29	9.090	0.438
Toray Carbon	9.690	0.535
AS4 Carbon	8.019	0.548
S2 75 1/3 Glass	9.136	0.627
IM6 Carbon	8.243	0.372
Average	8.813	0.804

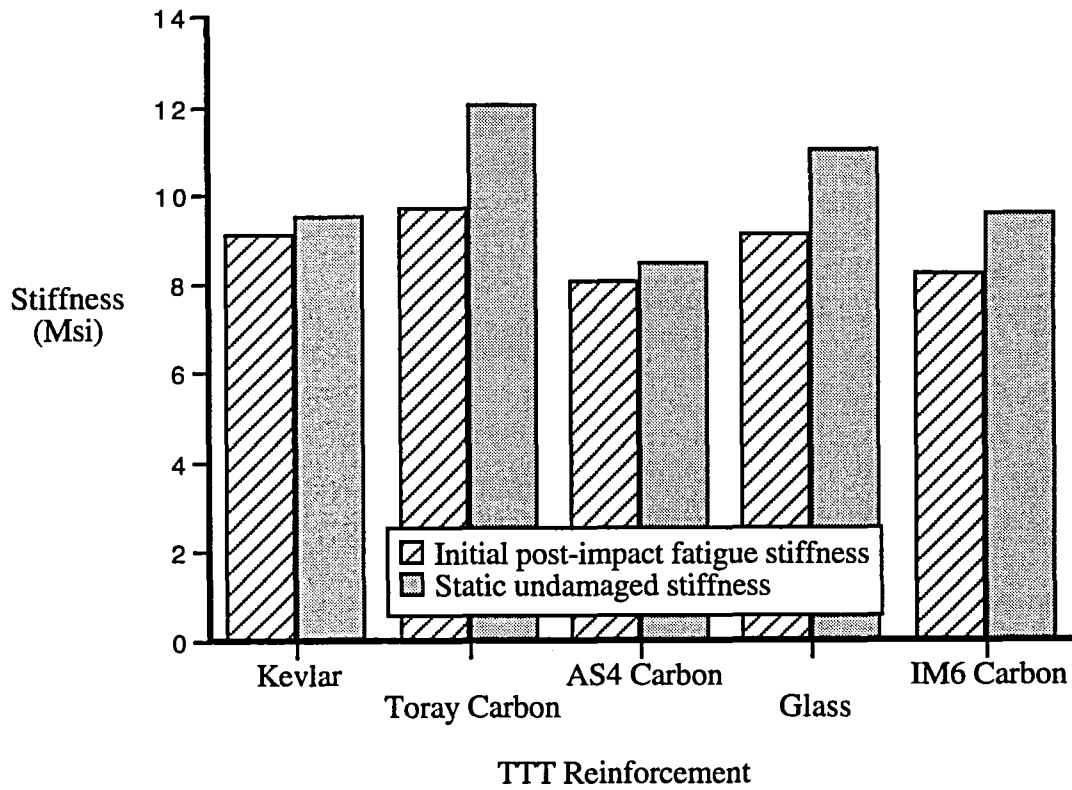
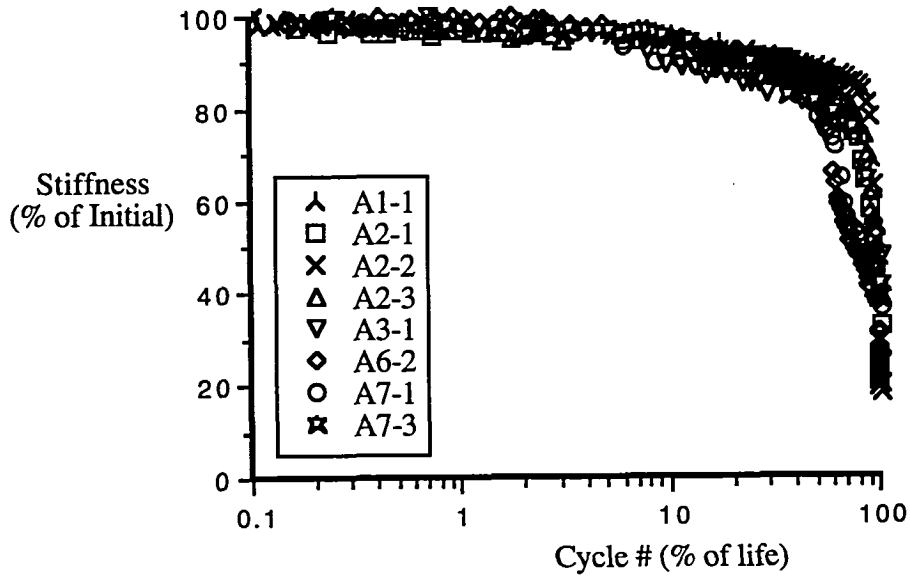
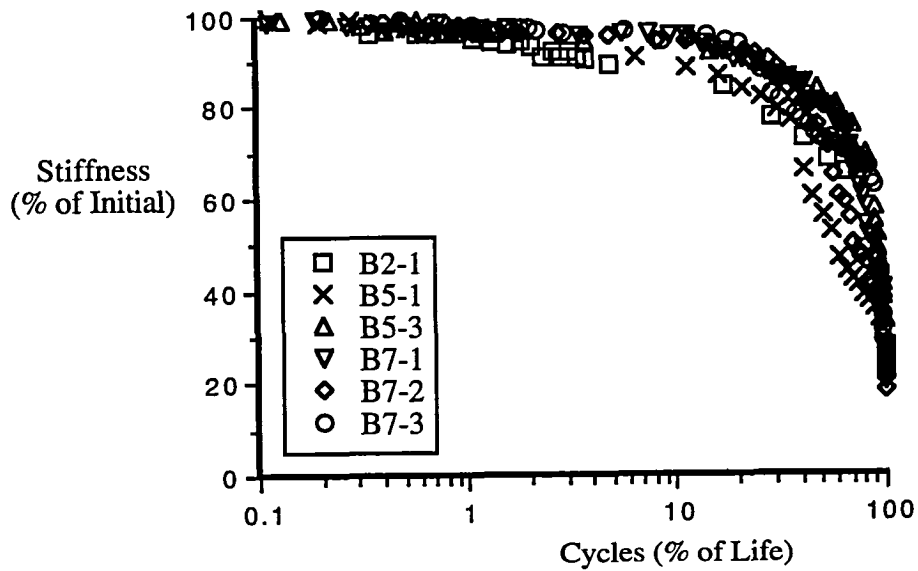


Figure 36. Average initial post-impact fatigue and undamaged static stiffness for each TTT material.

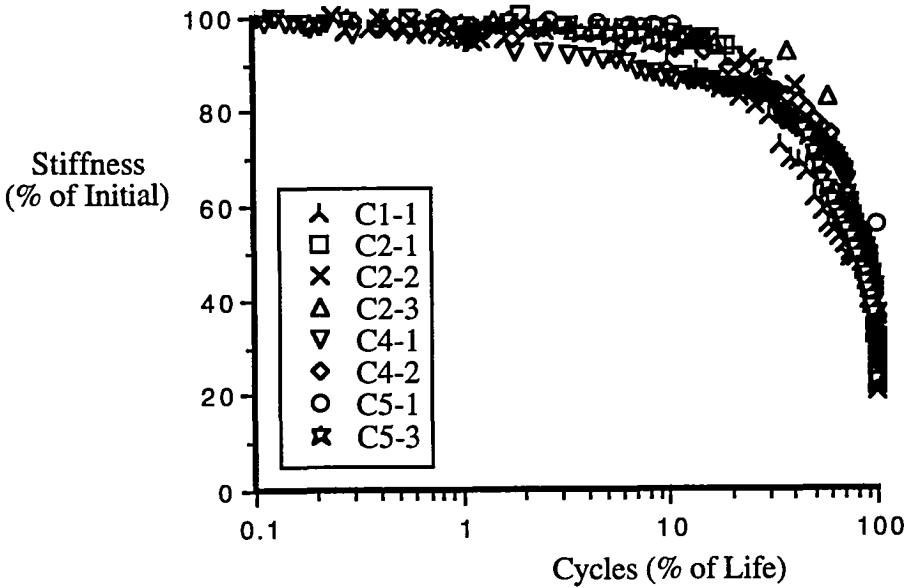


a. Kevlar

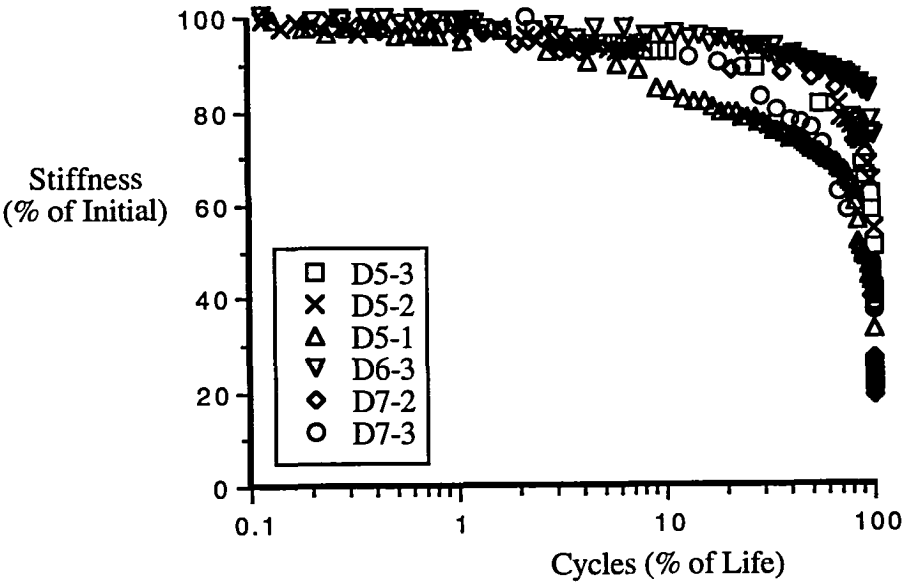


b. Toray carbon

Figure 37. Normalized stiffness loss throughout each fatigue test.

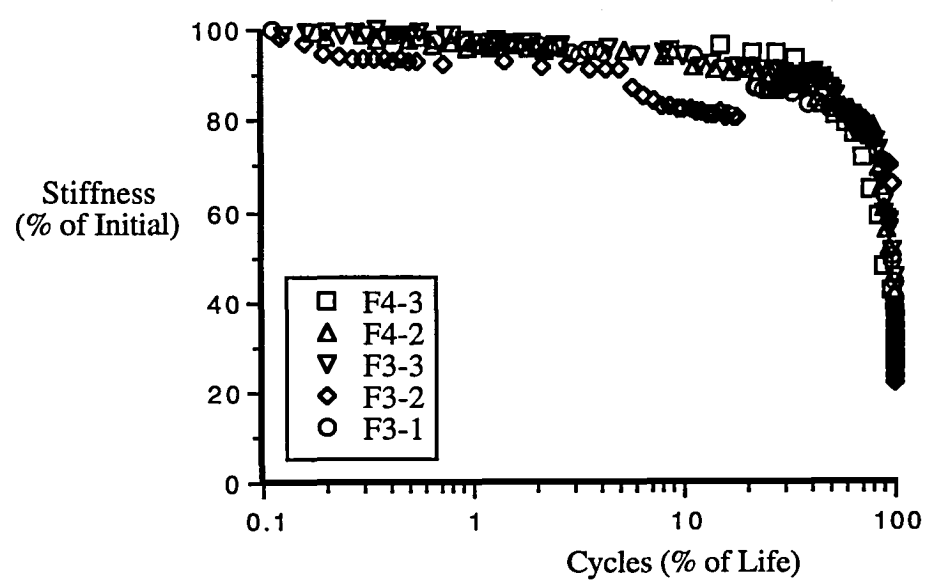


c. AS4 carbon



d. Glass

Figure 37. (Continued)



e. IM6 carbon

Figure 37. (Continued)

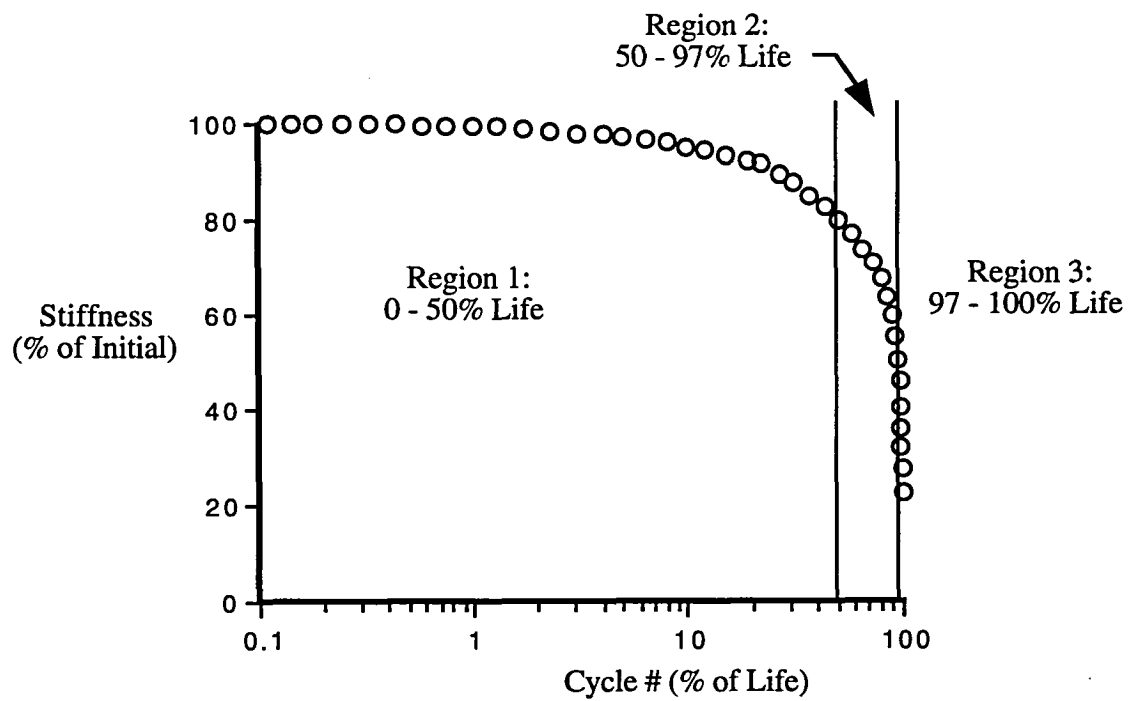


Figure 38. Stiffness loss regions.

variation between materials, the same trends applied to all material groups. At 50% of life, the average stiffness was 80% of the initial post-impact fatigue stiffness. At 97% of life, the average stiffness was 46% of initial. And, immediately prior to failure, the average stiffness was 23% of initial. The fact that these trends were fairly consistent among and between material groups verifies that fatigue failure could be accurately anticipated.

Stiffness loss regions appeared to coincide with three modes of damage growth. During the initial 50% of life (region 1), damage grew in the form of fiber bundle failures, ply cracks and delaminations at and near the impact site. The stress versus strain (across impact site) response was linear in this stiffness loss region. During the next 47% of life (region 2), damage also grew in the form of fiber bundle failures, ply cracks and delaminations in the vicinity of the impact site. However, the stress-strain response was no longer linear, and the stiffness degraded enough to allow significant transverse shear failures. In the final 3% of life (region 3), the transverse shear cracks rapidly propagated transverse to the loading direction and caused failure.

CHAPTER IV

CONCLUSIONS

Past research showed that TTT reinforcing stitching constrains impact damage and post-impact fatigue damage growth nearly as well as more expensive tough resin systems. This study was conducted to compare the response of integrally woven carbon/epoxy composites with five different TTT reinforcing materials: Kevlar, Toray carbon, AS4 carbon, glass, and IM6 carbon.

The damage caused by intermediate-velocity, low-mass impact was similar for all five materials. The circular damage zones consisted of delaminations, matrix cracks and ply cracks. Post-impact fatigue loading also produced similar damage growth for all the material groups. The stress-strain response (measured across the impact site) was typically linear during the initial 50% of fatigue life, as delaminations, ply cracks and transverse shear failures grew at and near the impact site. During the next 47% of life, the stress-strain response was no longer linear, and damage continued to grow through-the-thickness of the samples at and near the impact site. Damage grew rapidly transverse to the loading direction during the final 3% of life and caused transverse shear failure modes.

Damage growth was well characterized by monitoring stiffness loss across the impact site. The impact event caused an average stiffness reduction by about 12% for all the materials tested. The post-impact stiffness typically dropped 20% during the initial 50% of life, 34% during the next 47% of life, and 23% during the final 3% of life. By monitoring stiffness loss, fatigue failure could accurately be anticipated. Also, rapid increases in hysteresis (strain energy density) occurred during the final 3% of life.

The samples with IM6 carbon TTT reinforcement clearly had the best post-impact fatigue response. IM6 carbon also had the highest static compressive strength. The

average static compressive strength and elastic modulus for all materials were about 35.5 Ksi, and 10 Msi, respectively.

The materials evaluated had many inconsistencies. With improvements in production processes, the variations among material groups may be reduced. The performance of materials with different TTT reinforcing fibers subjected to post-impact fatigue loading could then provide additional insight into the damage-constraining characteristics of TTT fibers. The contributions of the material properties (elastic modulus, yarn diameter, etc.) of the TTT reinforcing fibers could then be evaluated. Low-cost fibers with optimum TTT reinforcing capabilities might then be developed. Additional tests should also be conducted which provide a comprehensive fatigue evaluation of one material system; these should include variations in impact loading and R ratio, as well as variable amplitude loading.

However, the results presented herein provide a good evaluation of integrally woven materials for one fatigue environment with one impact loading condition. This study provided substantial insight into the post-impact fatigue response of integrally woven composites with different TTT reinforcing fibers.

APPENDICES

Appendix A

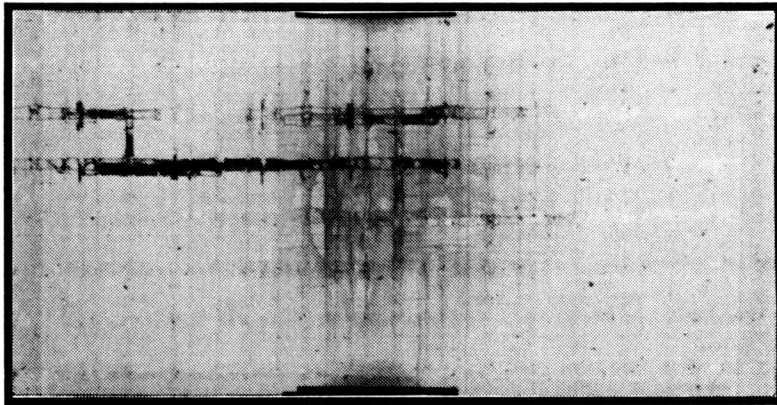
Impact and Post-Impact Fatigue Loading Damage: Radiographs

Radiographs were conducted by exposing film to a 37 Kv x-ray flux for 3 min. The maximum compressive strain across the damage zone increased as the amount of damage increased. Radiographs were recorded: (a) prior to fatigue loading, (b) at a maximum compressive strain of 0.005, (c) at a maximum compressive strain of 0.007, and (d) immediately prior to failure. The cycle number after which each radiograph was conducted and the percentage of the number of cycles to failure are given for each radiograph. The maximum compressive stress (S_c) and the number of cycles to failure (N_f) are given for each sample. Samples are labeled as indicated below.

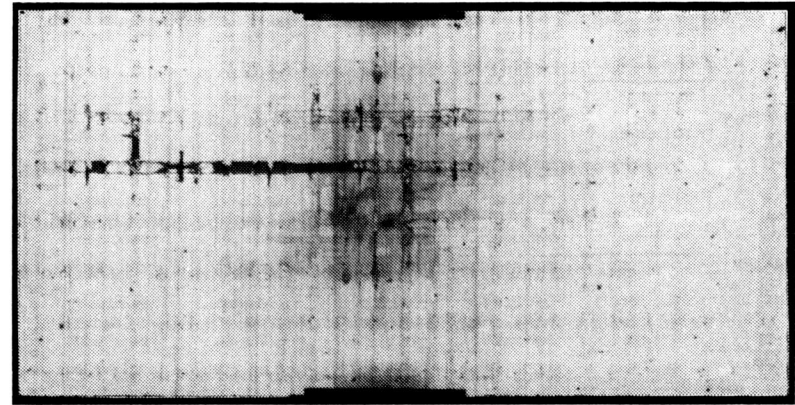
A3-1

			SAMPLE NUMBER
			PANEL NUMBER
			TTT REINFORCEMENT

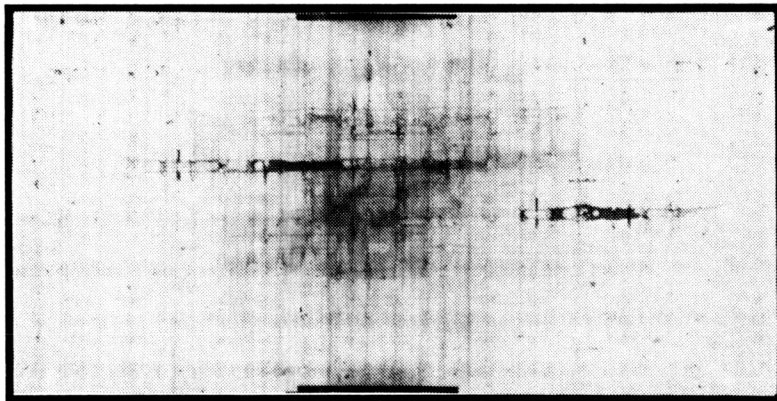
A - Kevlar 29, 1500 denier
 B - Toray Carbon, T-1000
 C - AS4 Carbon, 9k
 D - S2 75 1/3 Glass
 F - IM6 Carbon, 6k



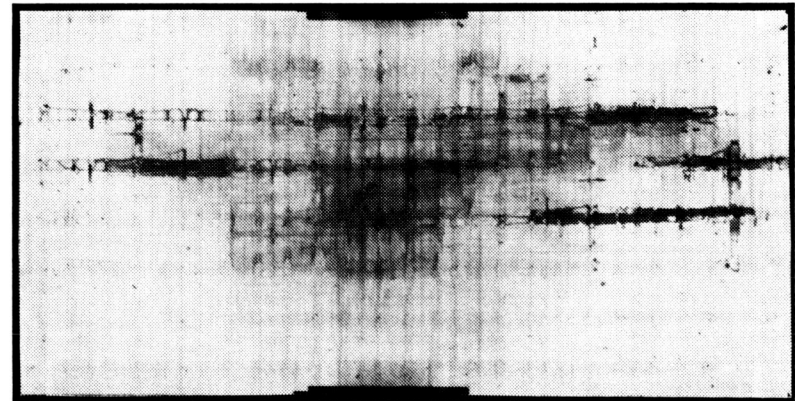
a. 0 cycles (post-impact)



b. 446,288 cycles (89.0 % of life)

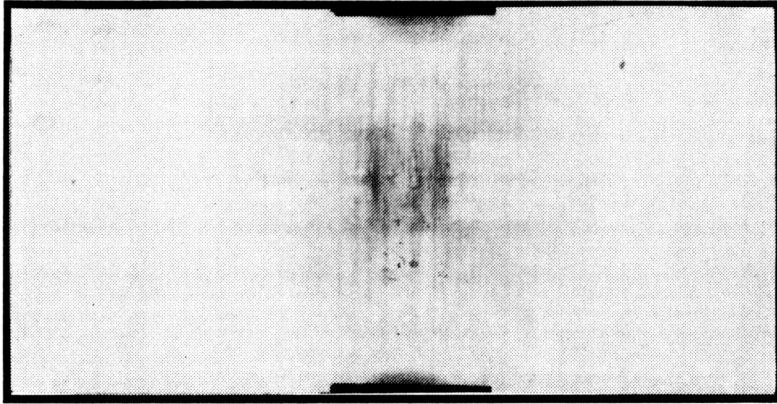


c. 497,173 cycles (99.2% of life)

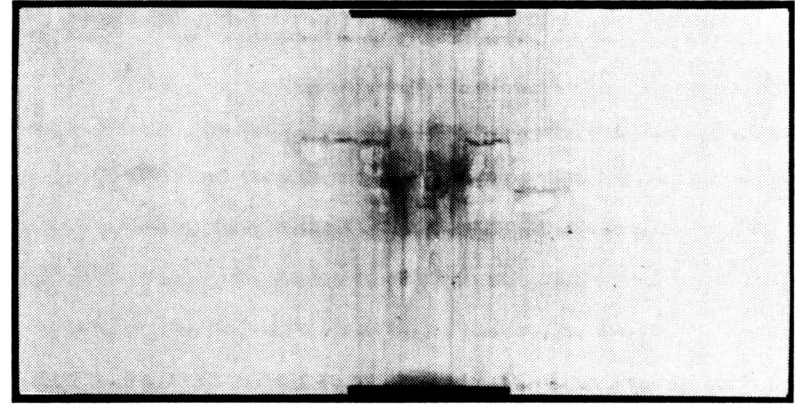


d. 501,212 cycles (near failure)

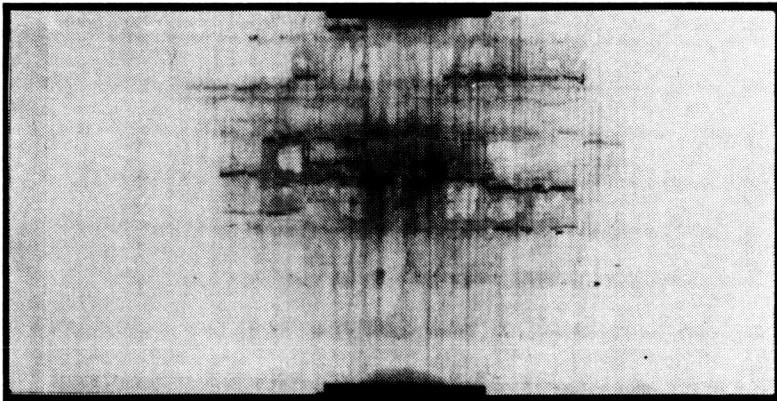
Sample A1-1
 $S_c = 21,650$ psi (63.0 % of static), $N_f = 501,227$ cycles



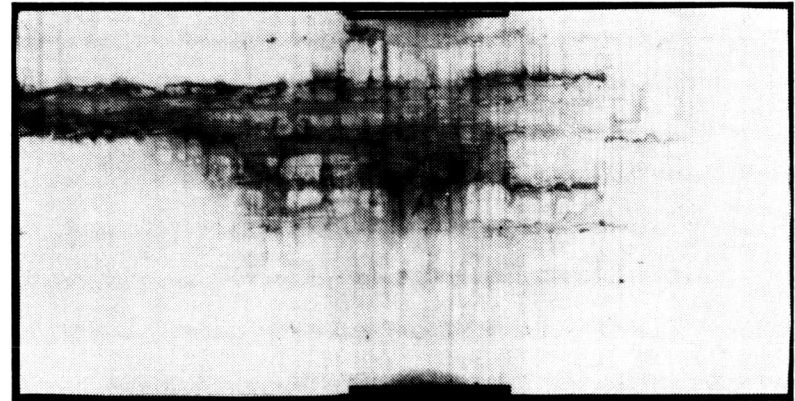
a. 0 cycles (post-impact)



b. 11,463 cycles (68.4 % of life)

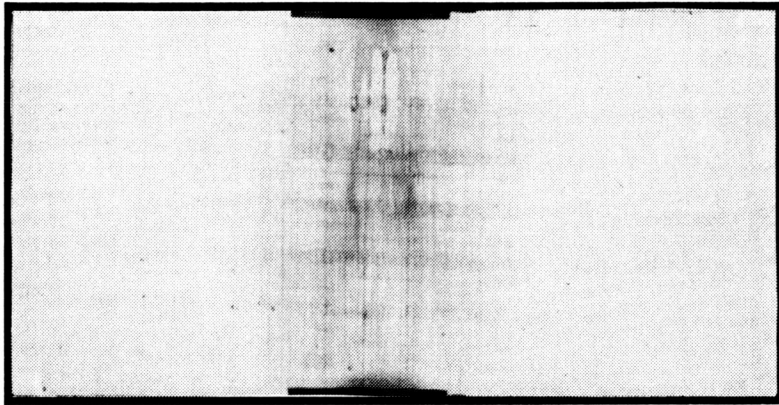


c. 16,243 cycles (96.9% of life)

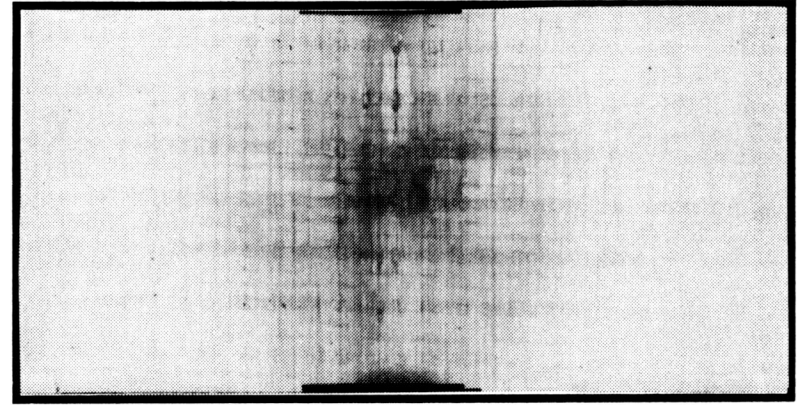


d. 16,768 cycles (last cycle prior to failure)

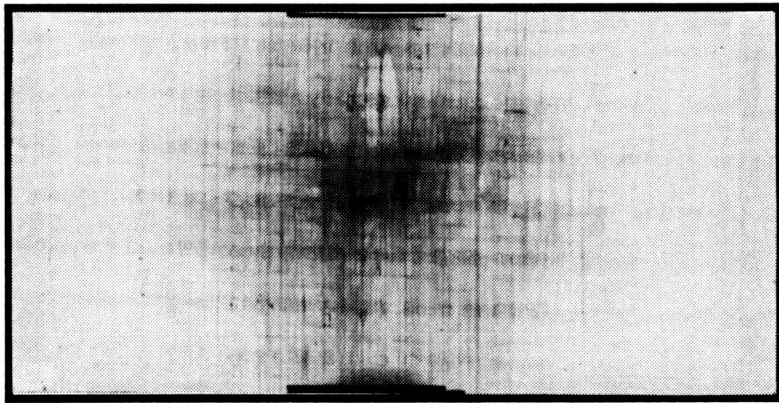
Sample A7-3
 $S_c = 24,056$ psi (70.0 % of static), $N_f = 16,768$ cycles



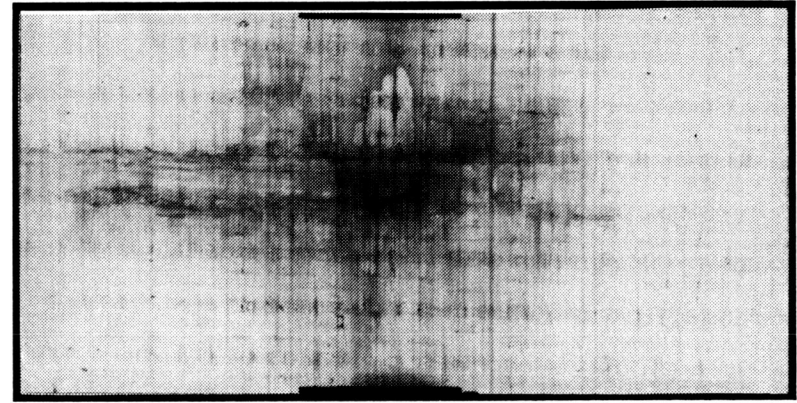
a. 0 cycles (post-impact)



b. 95,840 cycles (88.8 % of life)

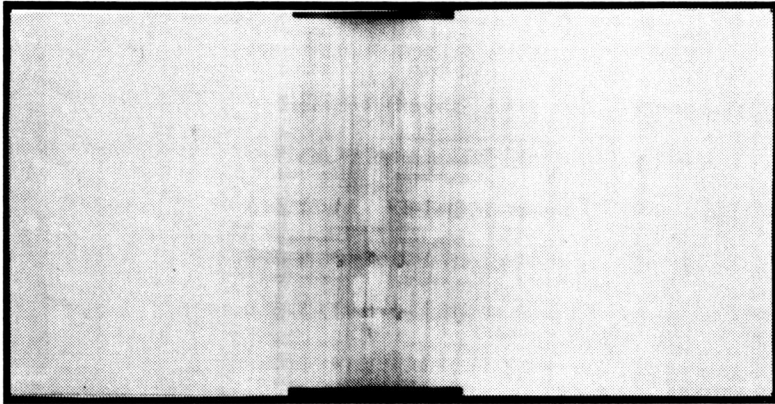


c. 106,741 cycles (98.9% of life)

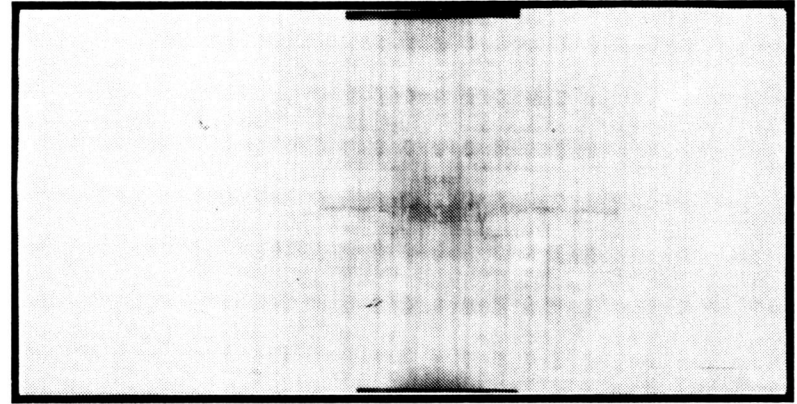


d. 107,903 cycles (near failure)

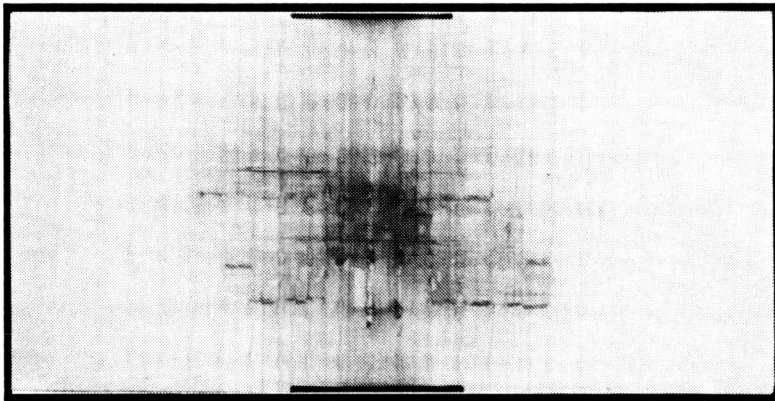
Sample B5-3
 $S_C = 22,002$ psi (66.5 % of static), $N_f = 107,905$ cycles



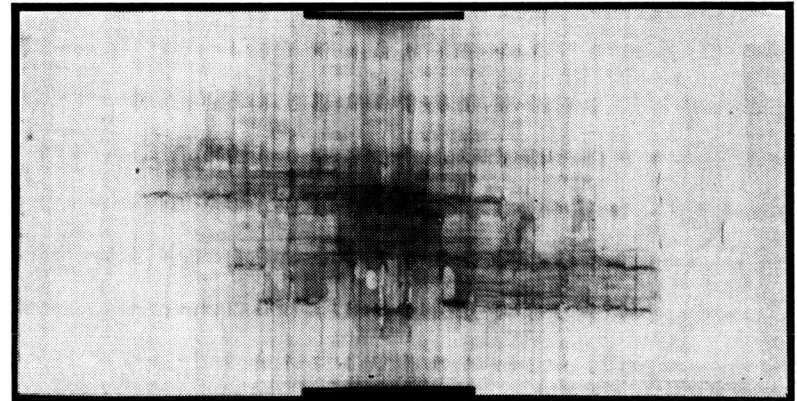
a. 0 cycles (post-impact)



b. 43,532 cycles (63.5% of life)

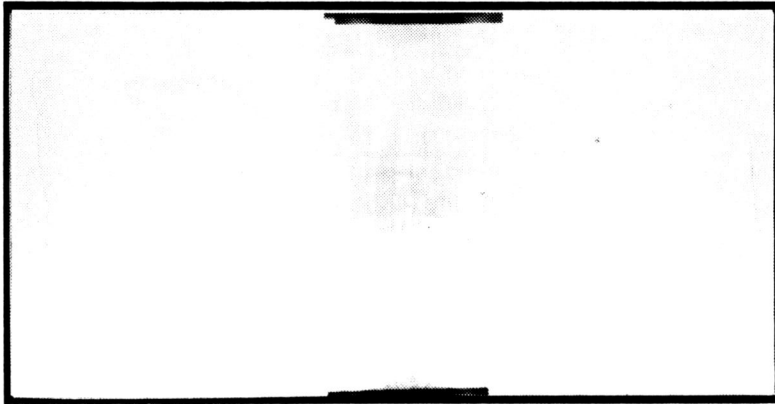


c. 66,927 cycles (97.6% of life)

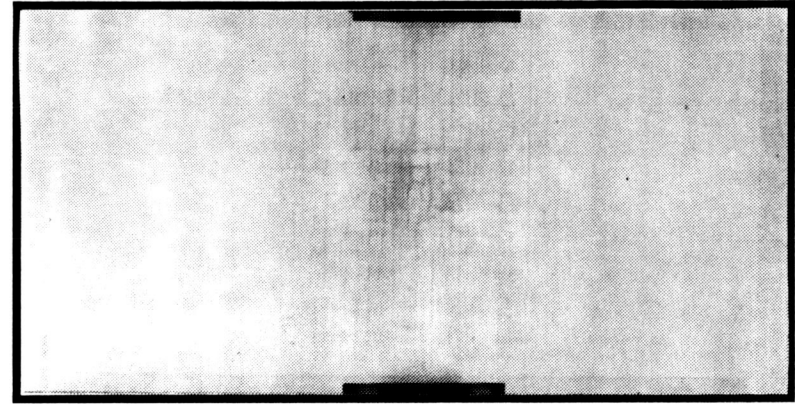


d. 68,597 cycles (near failure)

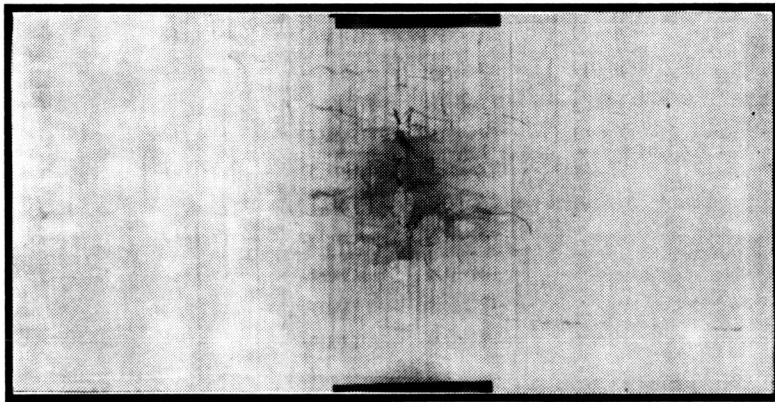
Sample B7-3
 $S_c = 23,491$ psi (71.0 % of static), $N_f = 68,597$ cycles



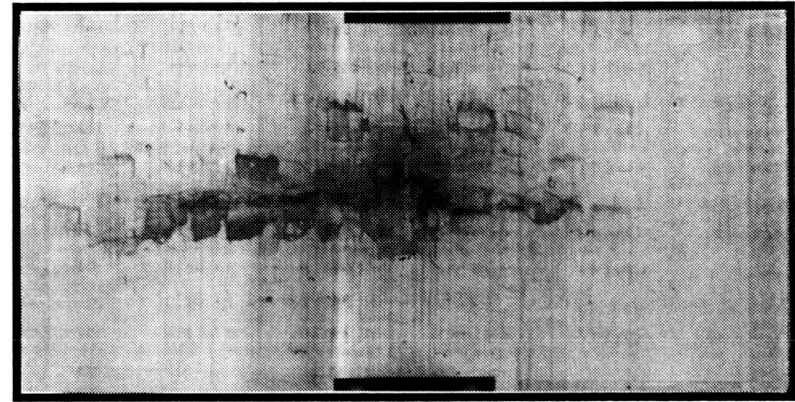
a. 0 cycles (post-impact)



b. 3,210 cycles (44.7 % of life)

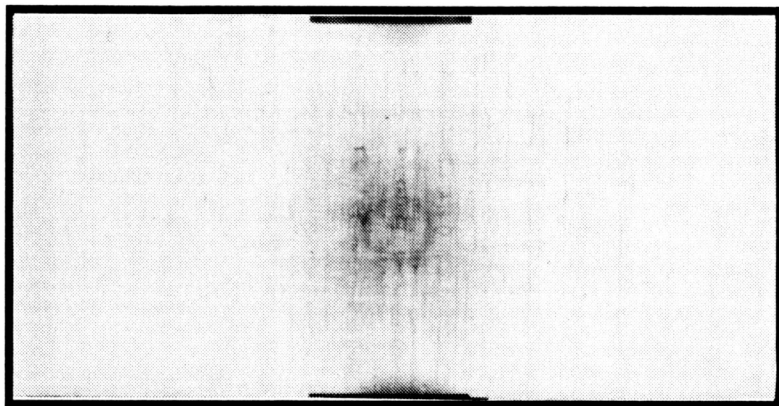


c. 7,020 cycles (97.8% of life)

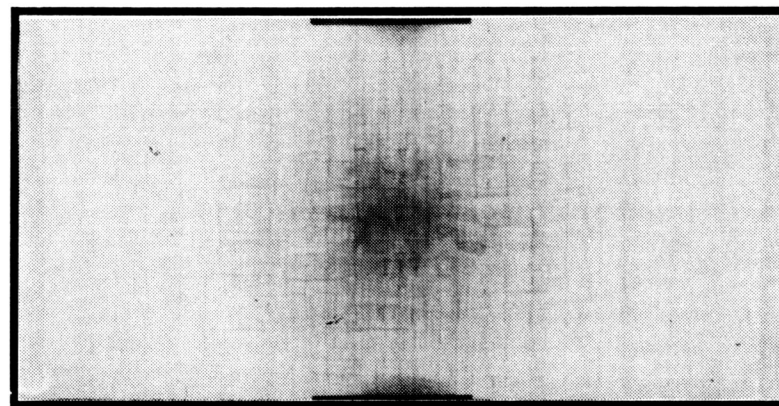


d. 7,181 cycles (near failure)

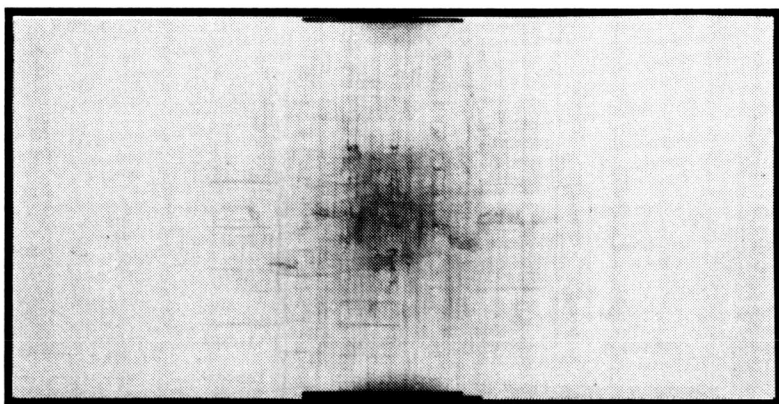
Sample C2-1
 $S_C = 22,573$ psi (62.9 % of static), $N_f = 7,181$ cycles



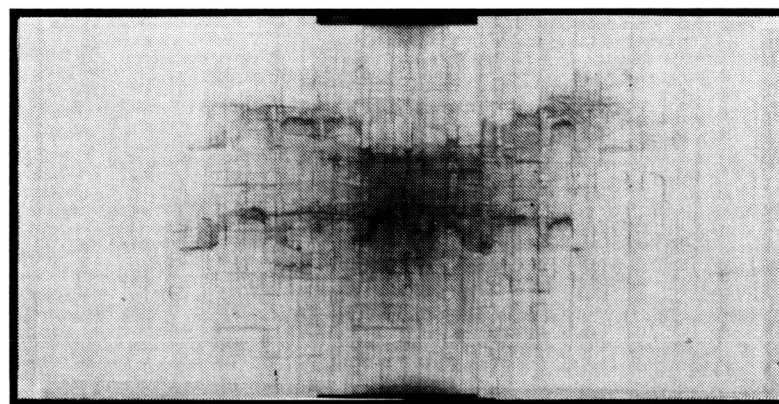
a. 0 cycles (post-impact)



b. 6,196 cycles (44.1 % of life)

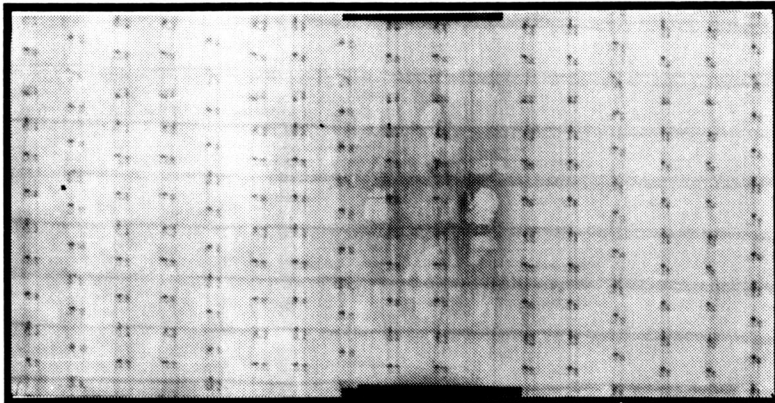


c. 11,879 cycles (84.5% of life)

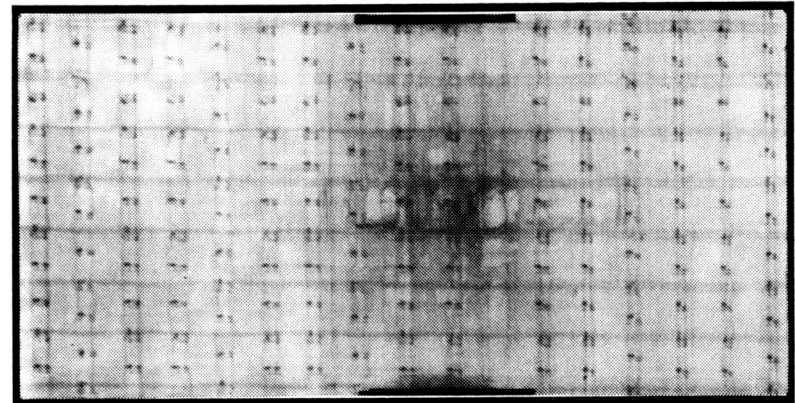


d. 13,713 cycles (near failure)

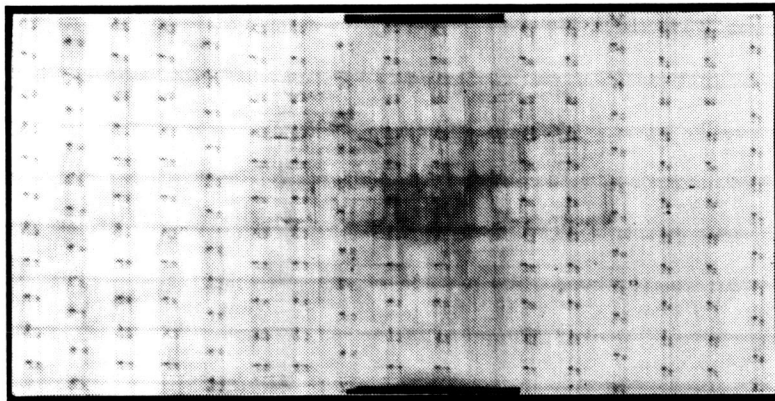
Sample C5-3
 $S_C = 23,152$ psi (64.5 % of static), $N_f = 14,053$ cycles



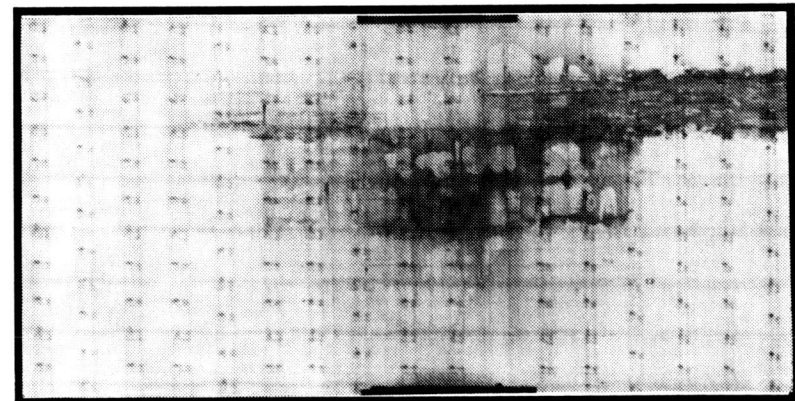
a. 0 cycles (post-impact)



b. 255,167 cycles (66.2% of life)

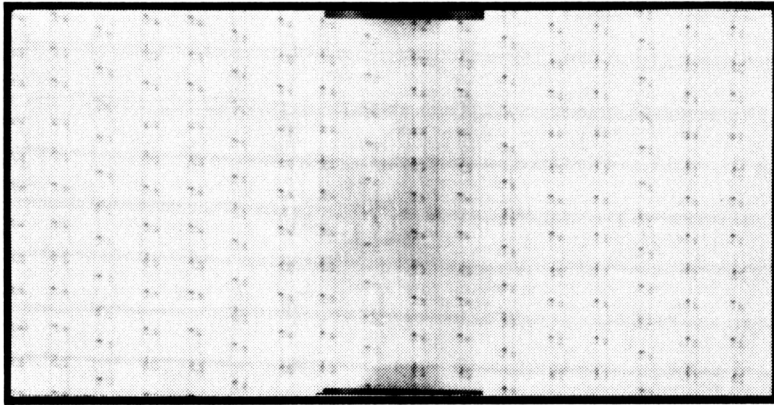


c. 383,159 cycles (99.5% of life)

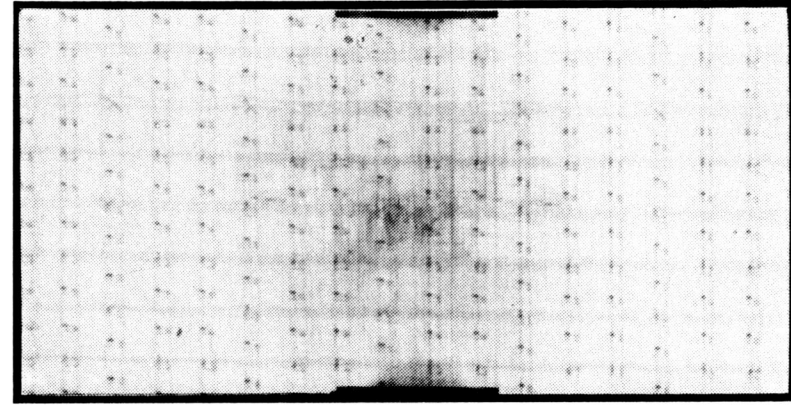


d. 385,190 cycles (last cycle prior to failure)

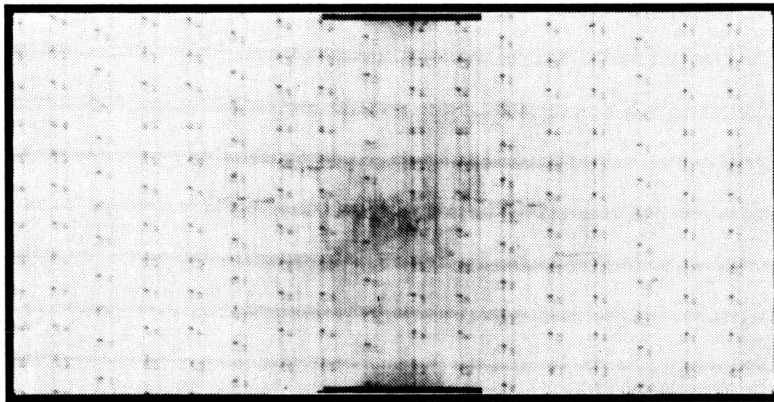
Sample D5-2
 $S_C = 24,108$ psi (72.9 % of static), $N_f = 385,190$ cycles



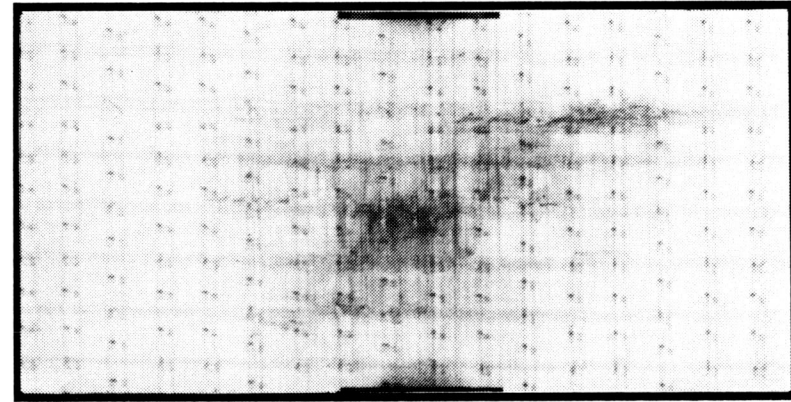
a. 0 cycles (post-impact)



b. 11,398 cycles (77.3 % of life)

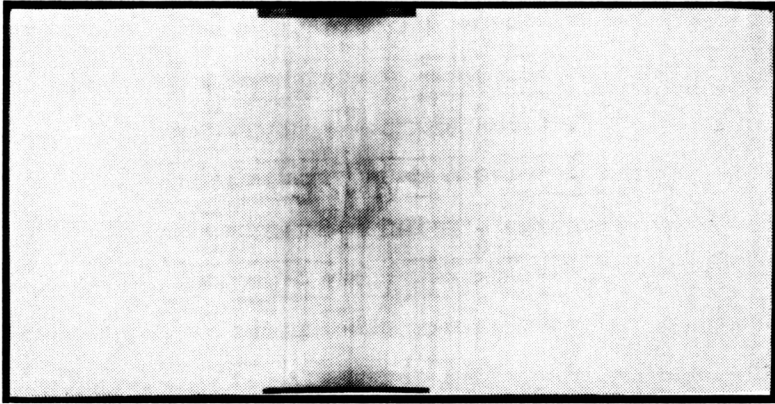


c. 13,803 cycles (93.6% of life)

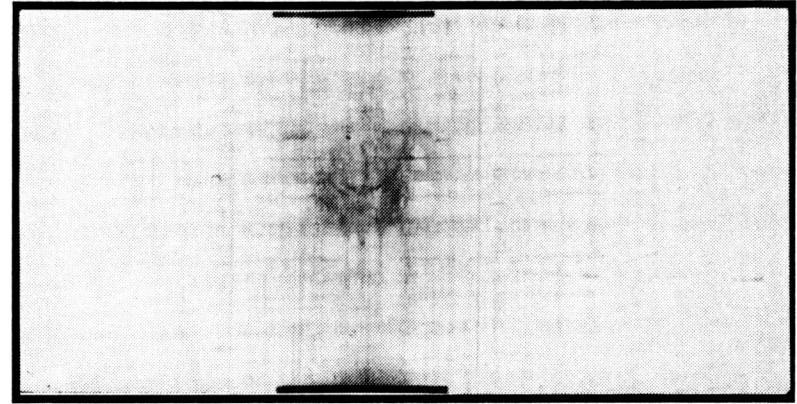


d. 14,751 cycles (near failure)

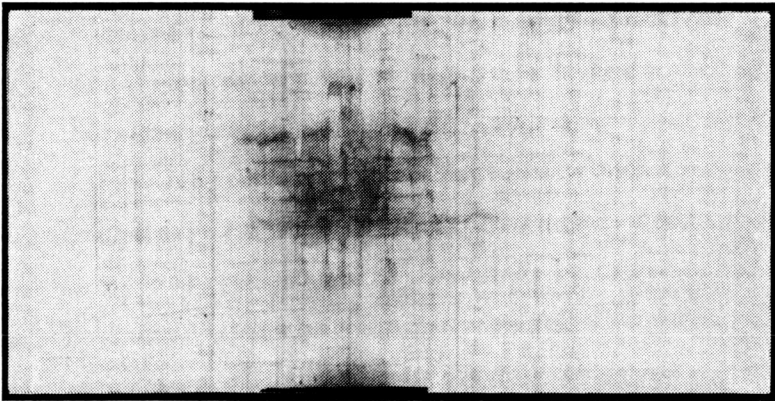
Sample D5-3
 $S_c = 25,458$ psi (77.0 % of static), $N_f = 14,751$ cycles



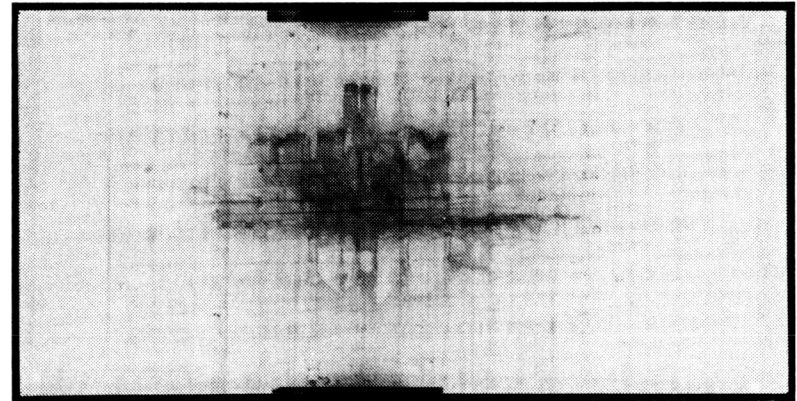
a. 0 cycles (post-impact)



b. 7,433 cycles (20.6 % of life)

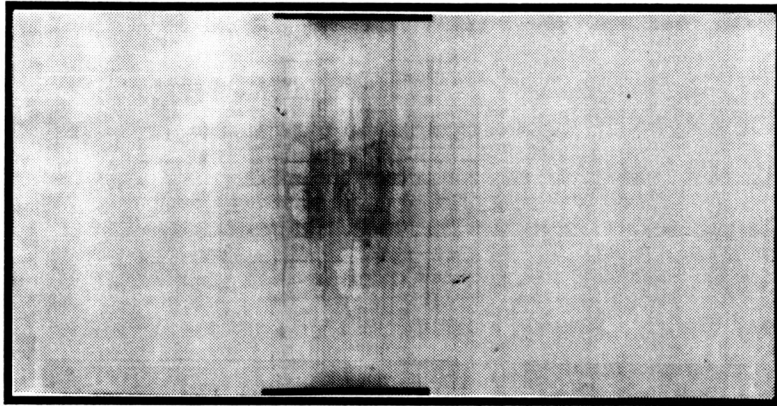


c. 34,967 cycles (97.1% of life)

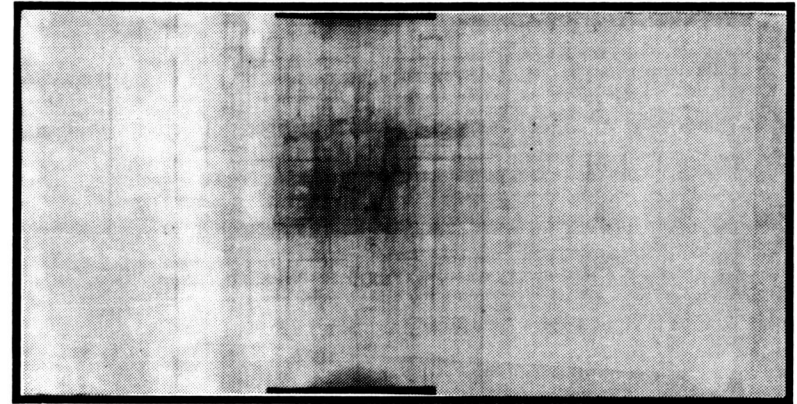


d. 36,002 cycles (near failure)

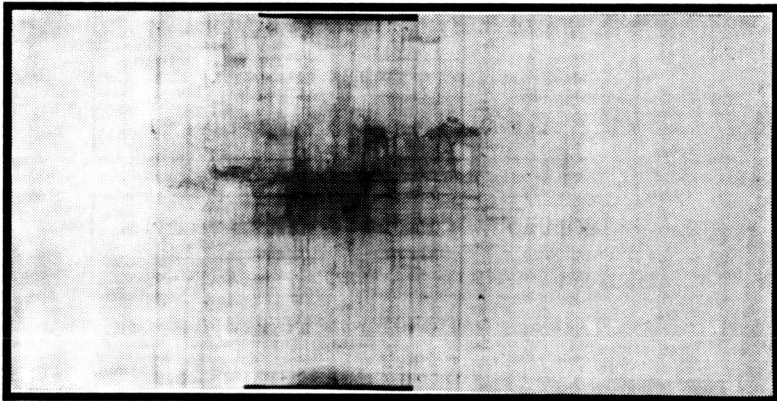
Sample F3-1
 $S_C = 29,688$ psi (74.0 % of static), $N_f = 36,002$ cycles



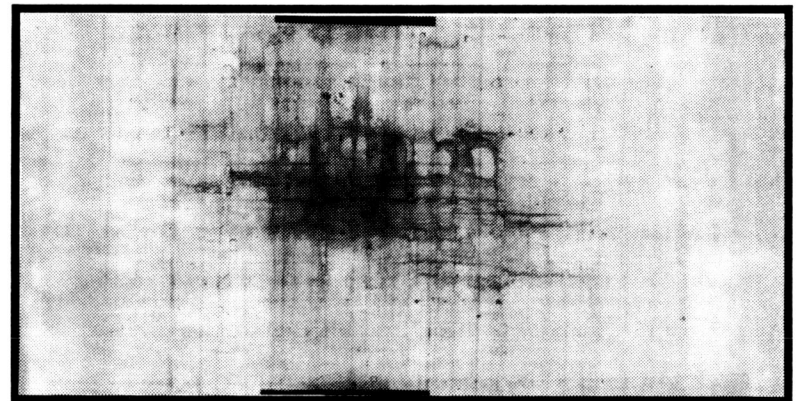
a. 0 cycles (post-impact)



b. 237,198 cycles (85.4 % of life)



c. 275,145 cycles (99.0% of life)



d. 277,146 cycles (near failure)

Sample F3-2
 $S_c = 28,083$ psi (70.0 % of static), $N_f = 277,875$ cycles

Appendix B

Impact and Post-Impact Fatigue Loading Damage: Photo-Micrographs

Samples with impact and post-impact fatigue damage were sectioned and photographed with a magnification of about 4.5. Sectioning locations are shown on radiographs. The section number and distance to the estimated center of impact (d_c) is given for each photo-micrograph. The maximum compressive stress (S_c) and the number of cycles to failure (N_f) are given for each fatigue sample. All fatigue tests were conducted at a stress ratio of $R = -5$ and a frequency of four hertz. Samples are labeled as indicated below.

A3-1



SAMPLE NUMBER

PANEL NUMBER

TTT REINFORCEMENT

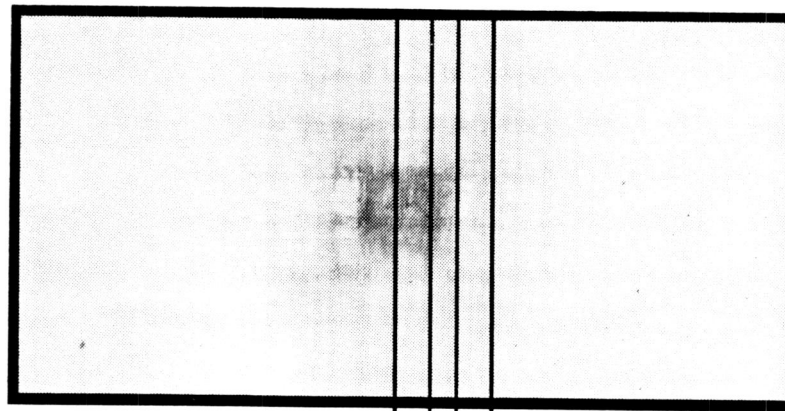
A - Kevlar 29, 1500 denier

B - Toray Carbon, T-1000

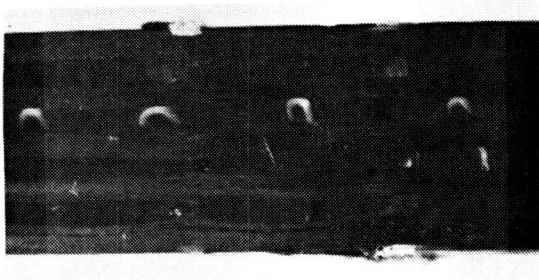
C - AS4 Carbon, 9k

D - S2 75 1/3 Glass

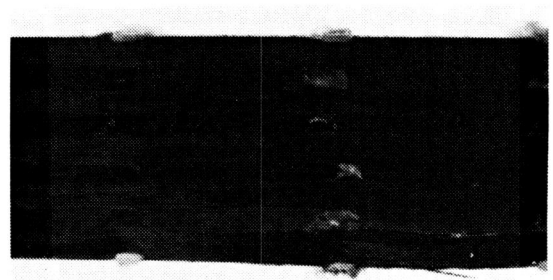
F - IM6 Carbon, 6k



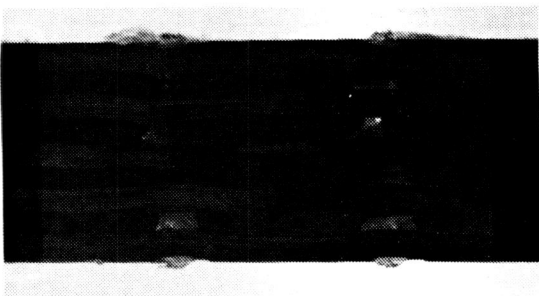
Section #: 4 3 2 1



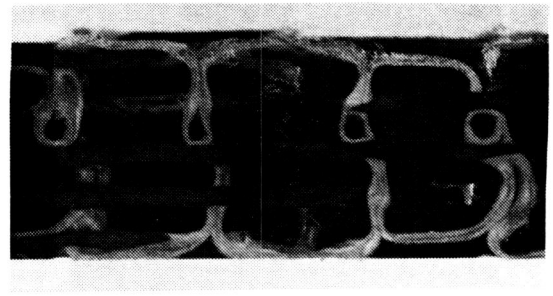
4. $d_c = 0.001''$



3. $d_c = 0.188''$

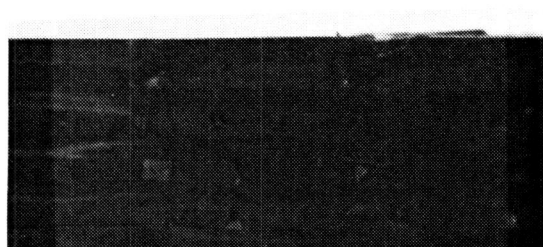
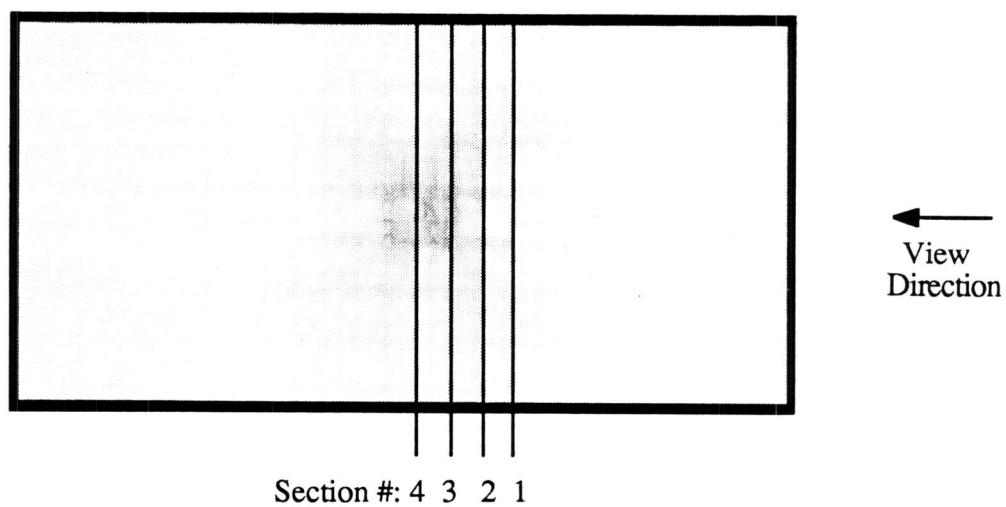


2. $d_c = 0.328''$

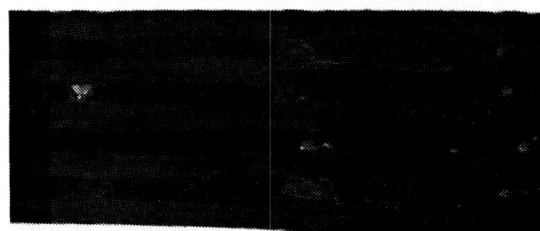


1. $d_c = 0.500''$

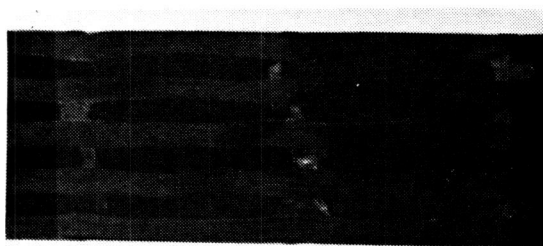
Sample A4-1
Post-Impact



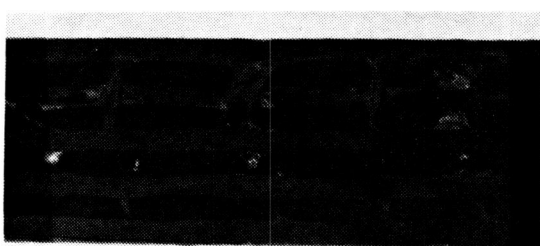
4. $d_c = 0.057''$



3. $d_c = 0.229''$

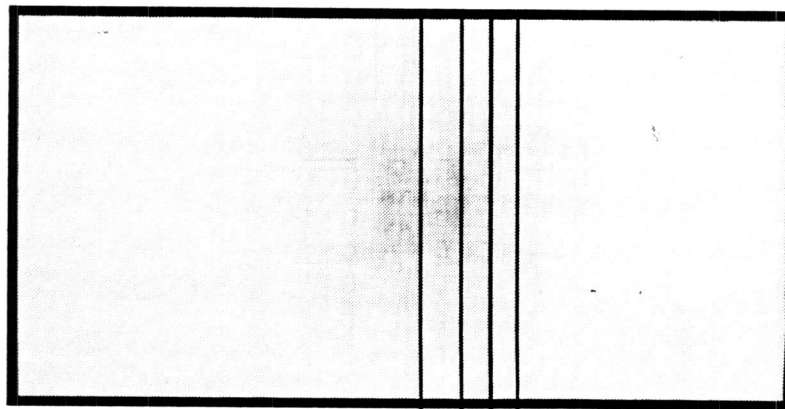


2. $d_c = 0.385''$

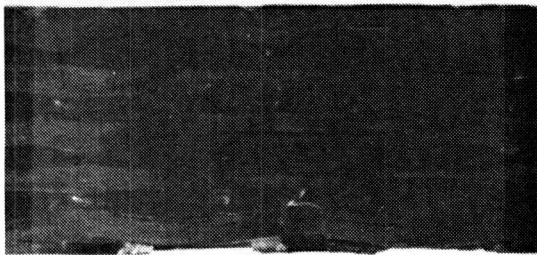


1. $d_c = 0.545''$

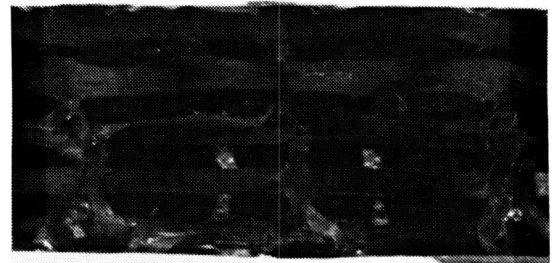
Sample B1-3
Post-Impact



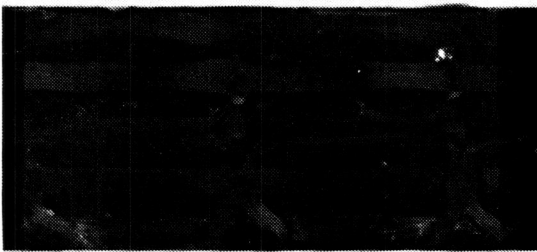
Section #: 4 3 2 1



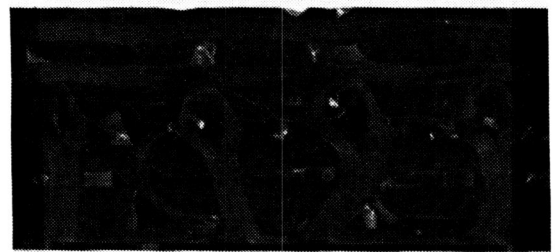
4. $d_c = 0.042''$



3. $d_c = 0.230''$

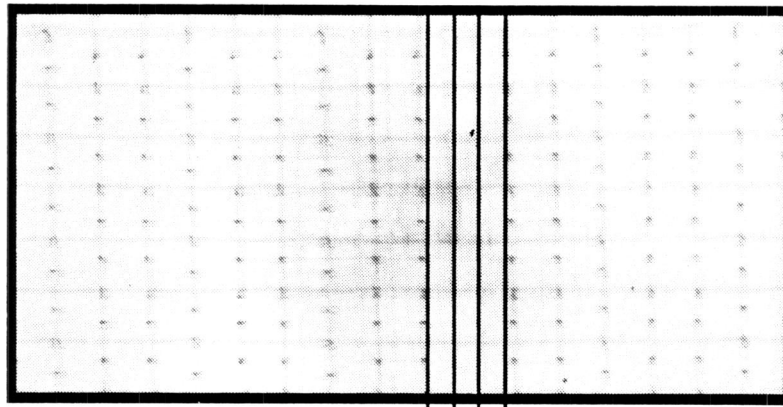


2. $d_c = 0.407''$



1. $d_c = 0.533''$

Sample C5-2
Post-Impact

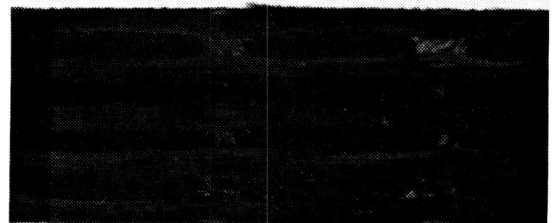


←
View
Direction

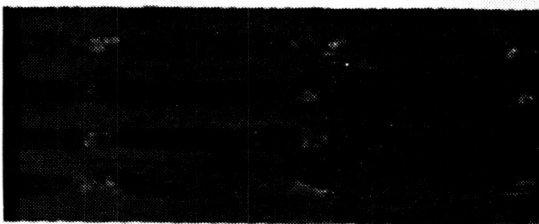
Section #: 4 3 2 1



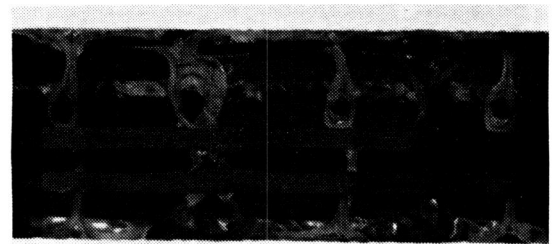
4. $d_c = 0.047''$



3. $d_c = 0.203''$

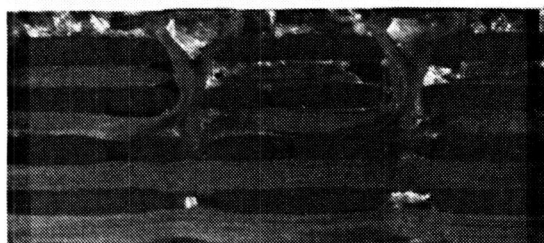
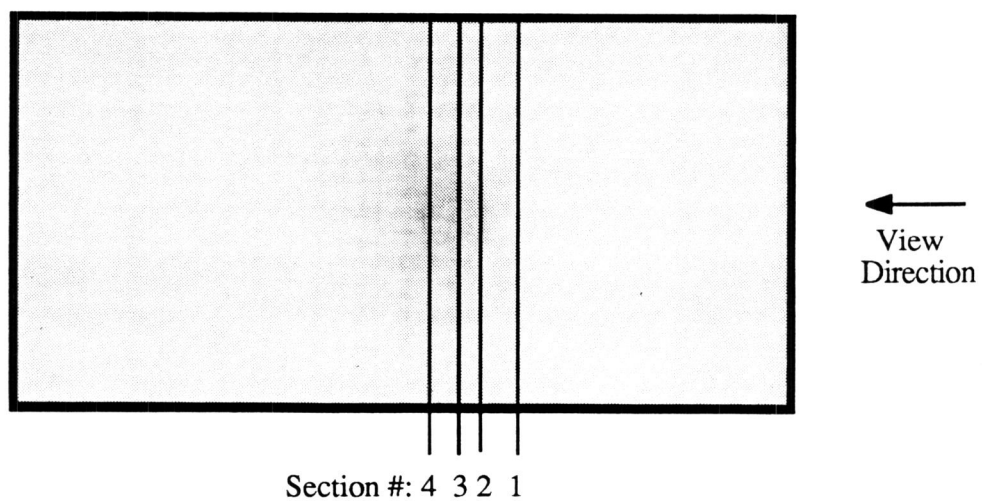


2. $d_c = 0.329''$

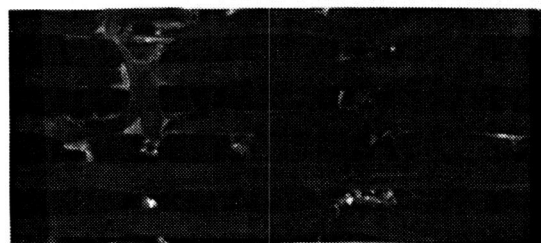


1. $d_c = 0.460''$

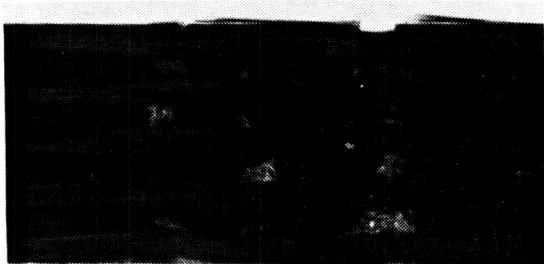
Sample D7-2
Post-Impact



4. $d_c = 0.001''$



3. $d_c = 0.154''$

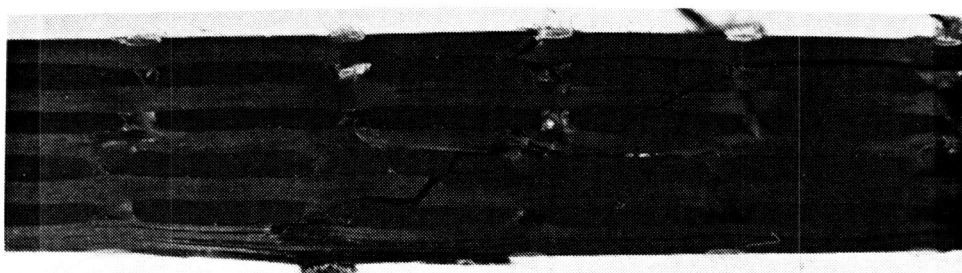
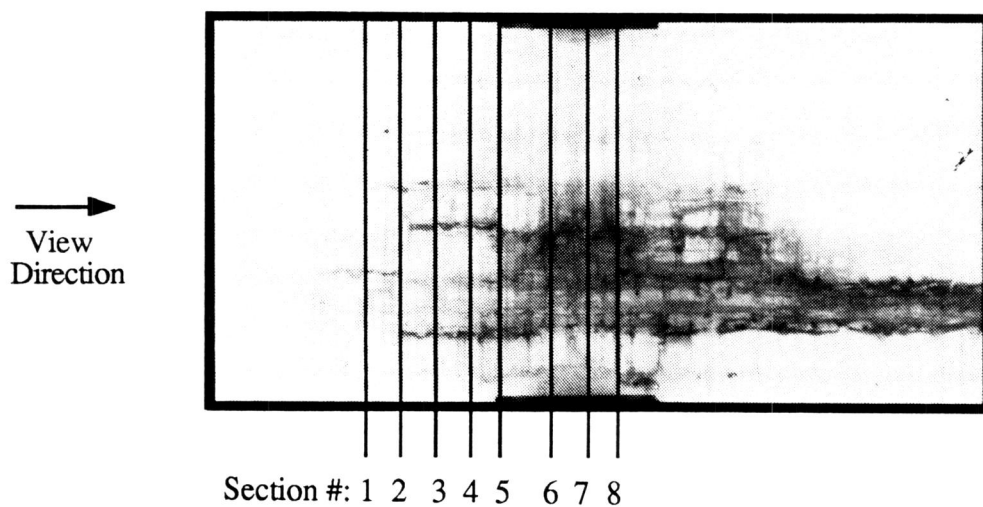


2. $d_c = 0.268''$



1. $d_c = 0.456''$

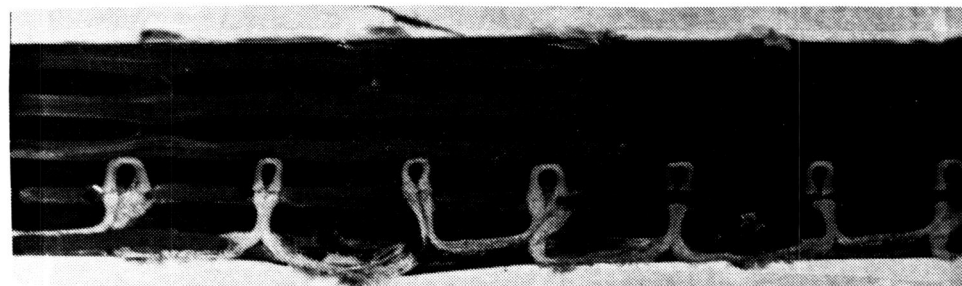
Sample F4-2
Post-Impact



8. $d_c = 0.116"$

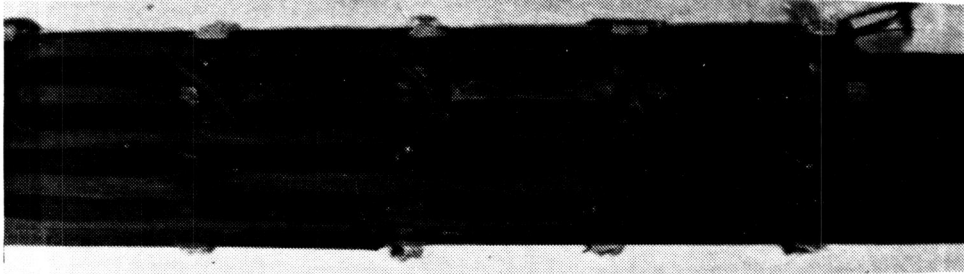
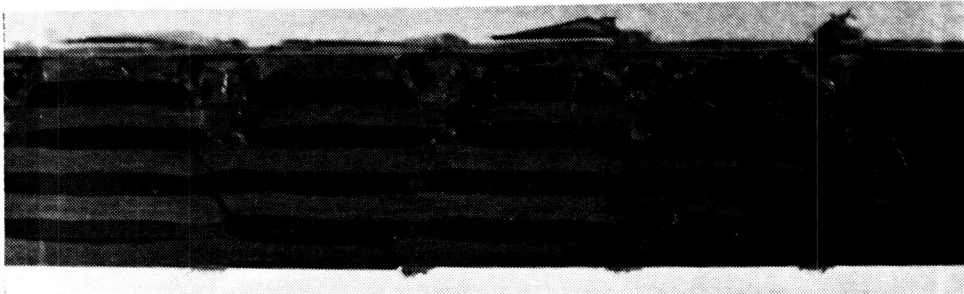
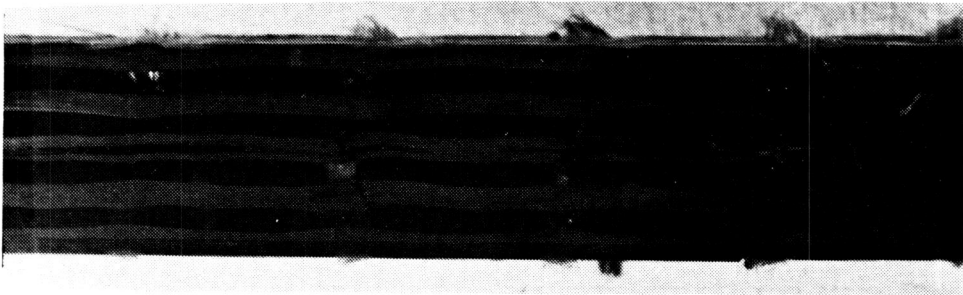
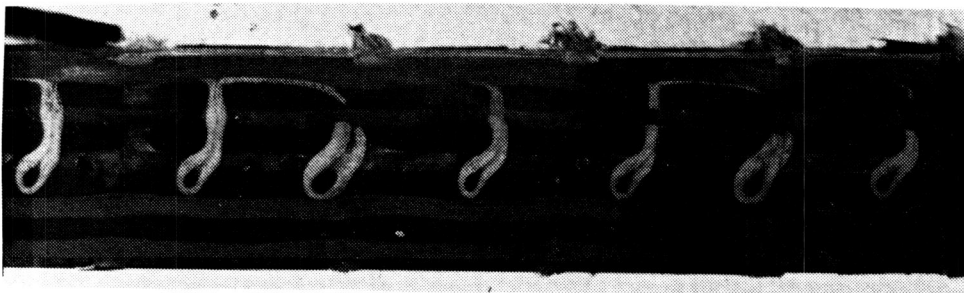


7. $d_c = 0.036"$

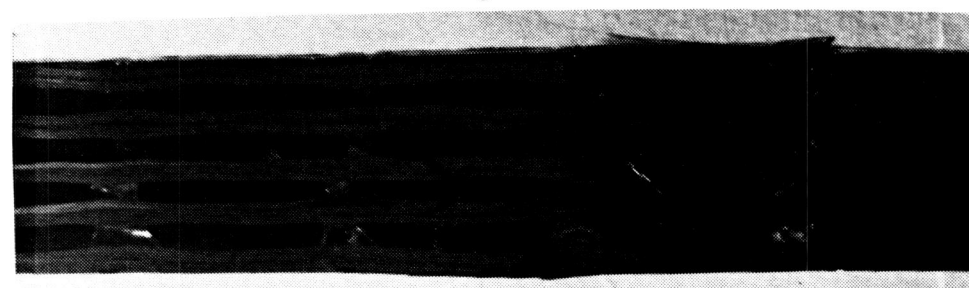
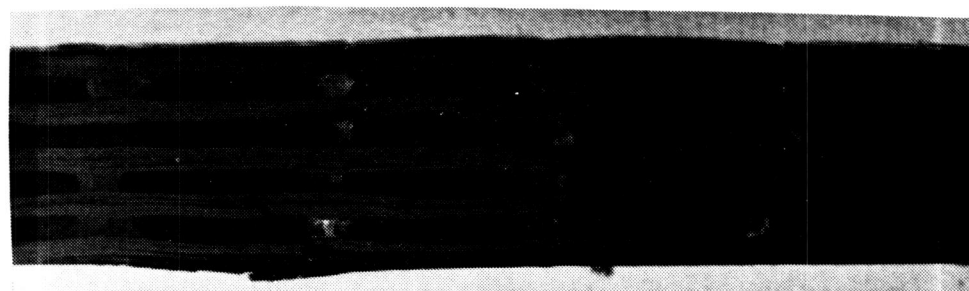
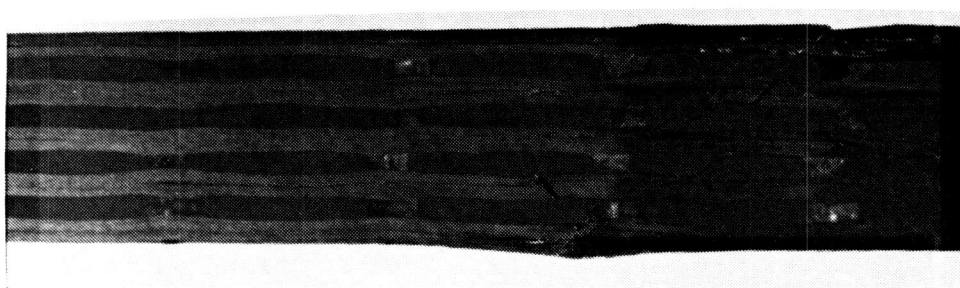
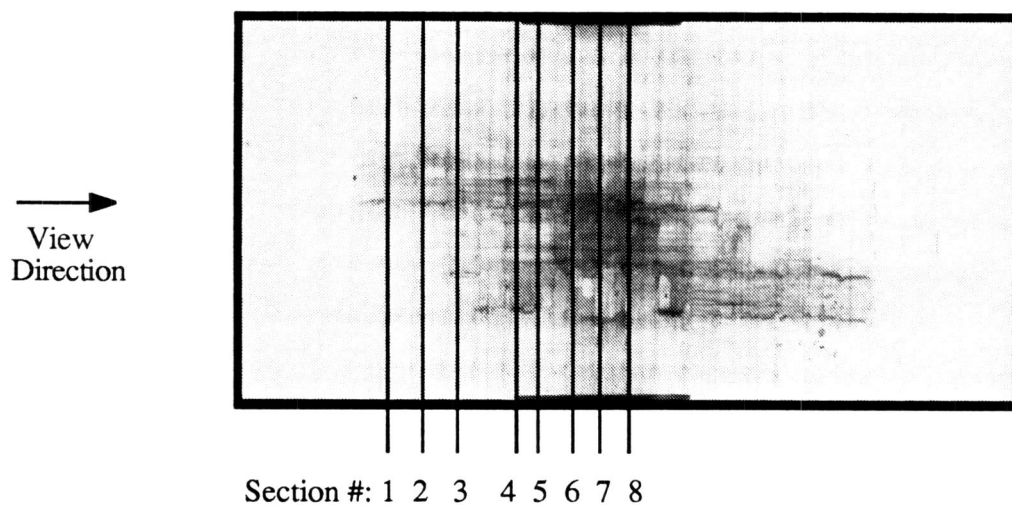


6. $d_c = 0.236"$

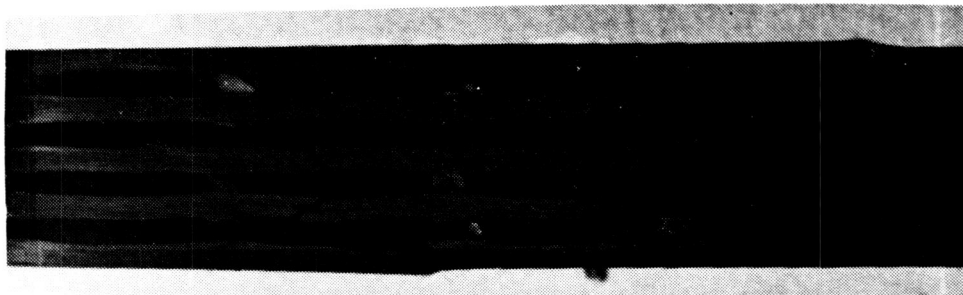
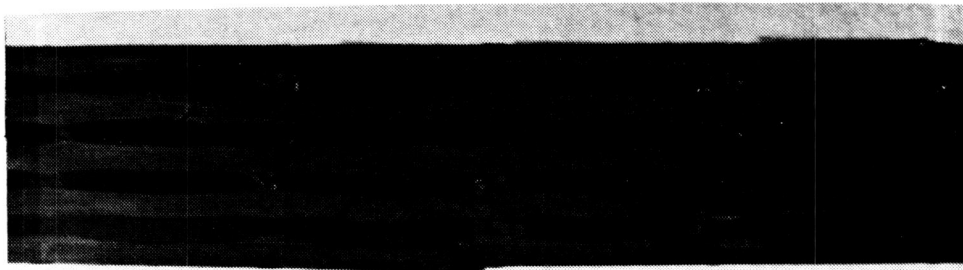
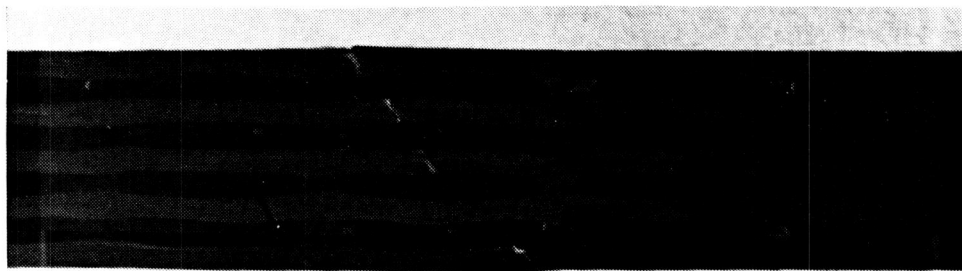
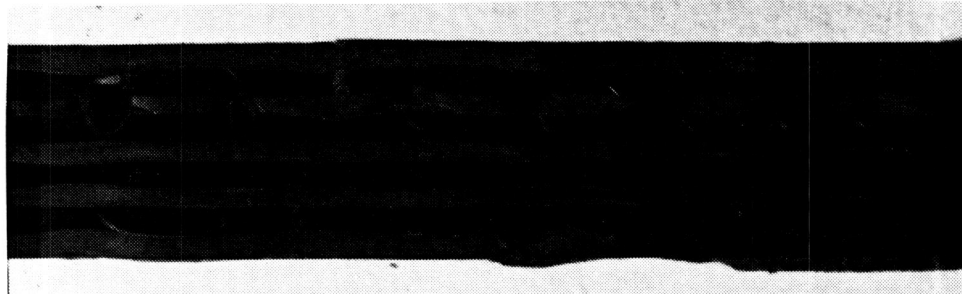
Sample A7-3
 $S_c = 24,056$ psi (70.0 % of static), $N_f = 16,768$ cycles

5. $d_c = 0.482''$ 4. $d_c = 0.638''$ 3. $d_c = 0.814''$ 2. $d_c = 0.998''$ 1. $d_c = 1.180''$

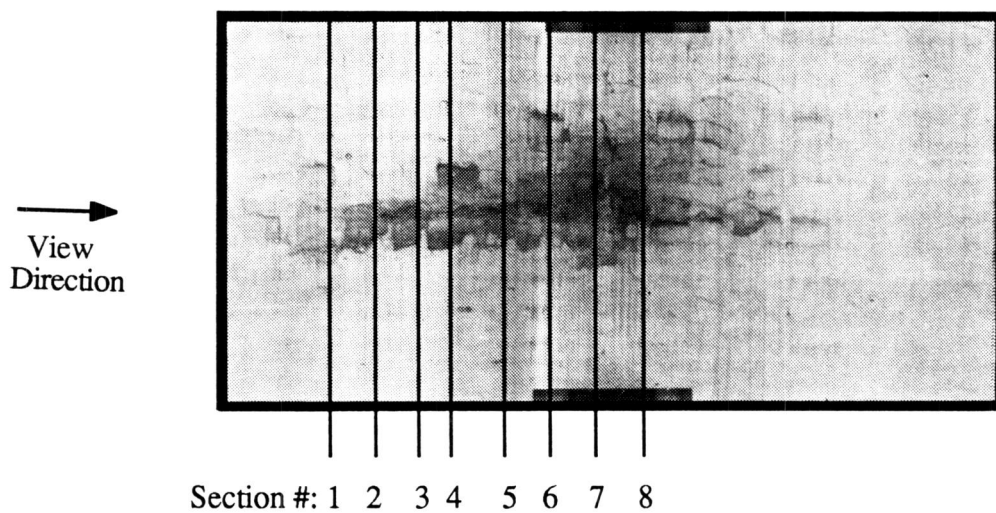
Sample A7-3 (Continued)



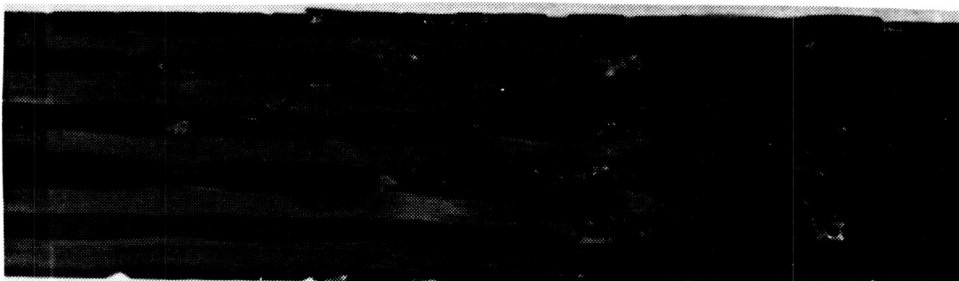
Sample B7-3
 $S_C = 23,491$ psi (71.0 % of static), $N_f = 68,597$ cycles

5. $d_c = 0.405''$ 4. $d_c = 0.500''$ 3. $d_c = 0.822''$ 2. $d_c = 0.990''$ 1. $d_c = 1.164''$

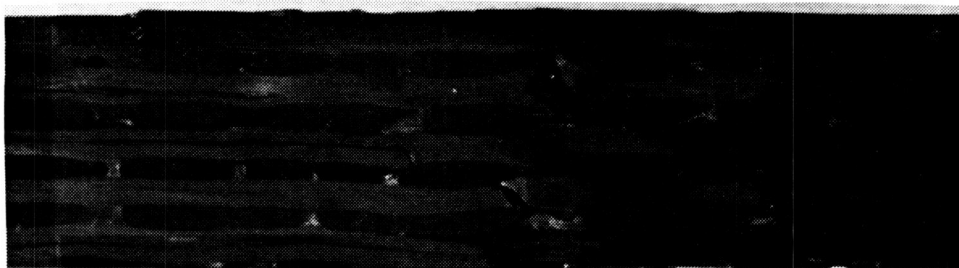
Sample B7-3 (Continued)



8. $d_c = 0.168''$



7. $d_c = 0.092''$



6. $d_c = 0.334''$

Sample C2-1
 $S_c = 22,573$ psi (62.9 % of static), $N_f = 7,181$ cycles



5. $d_c = 0.554''$



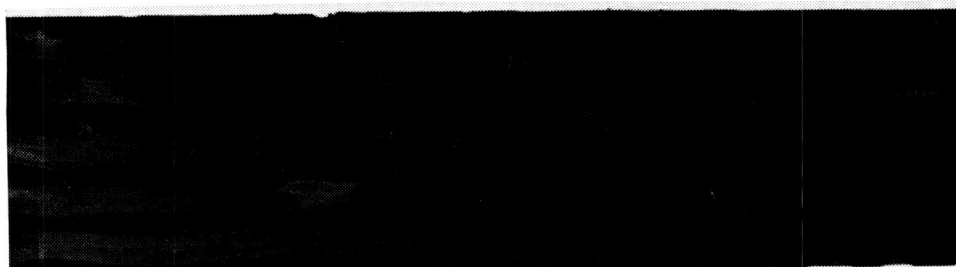
4. $d_c = 0.811''$



3. $d_c = 0.999''$

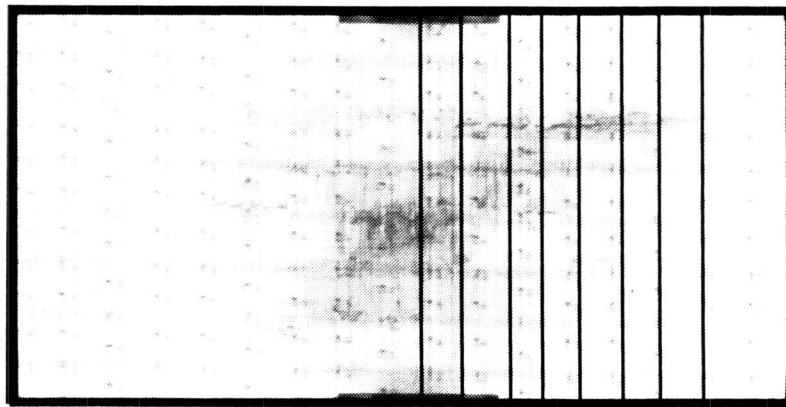


2. $d_c = 1.215''$



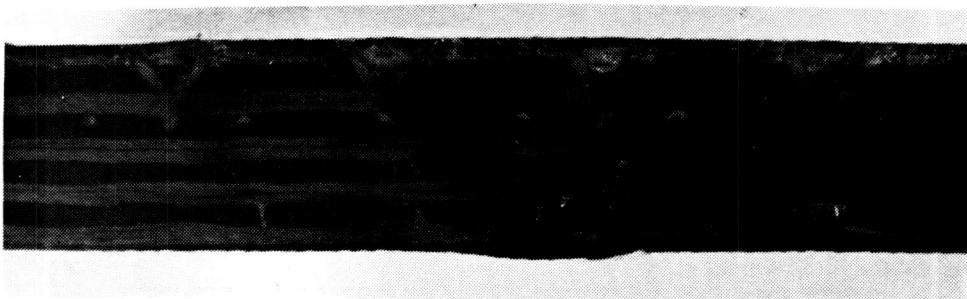
1. $d_c = 1.450''$

Sample C2-1 (Continued)

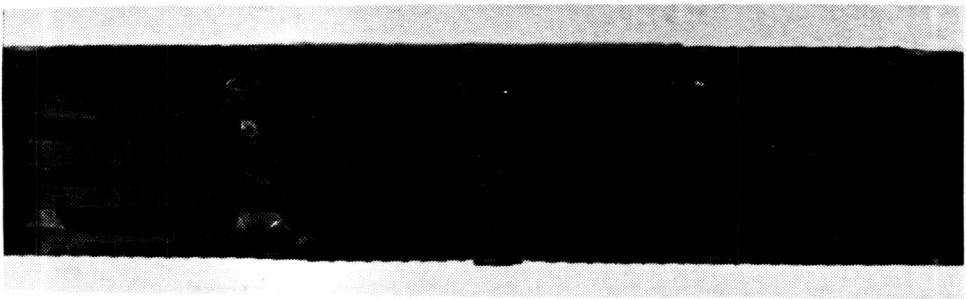


←
View
Direction

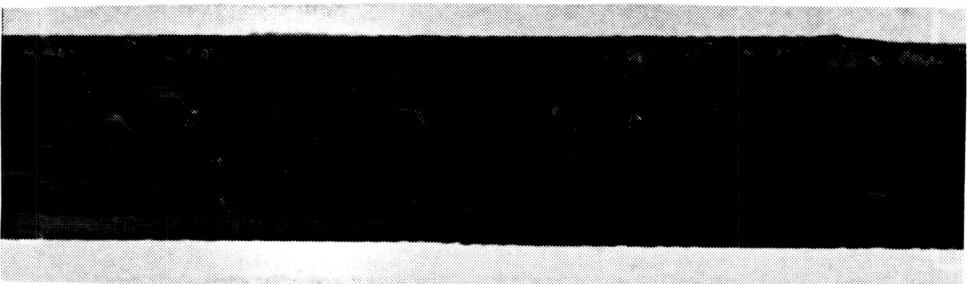
Section #: 8 7 6 5 4 3 2 1



8. $d_c = 0.013''$

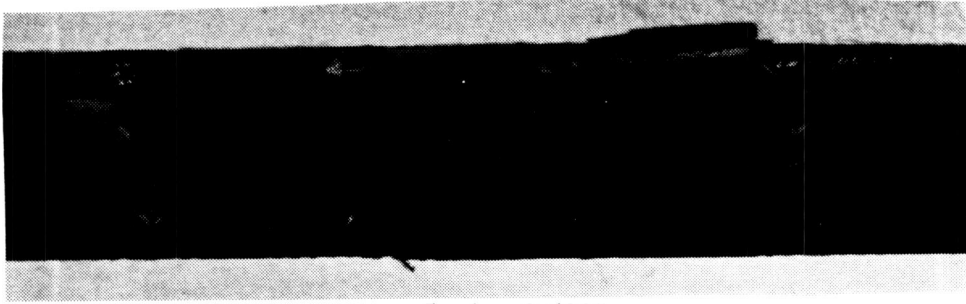
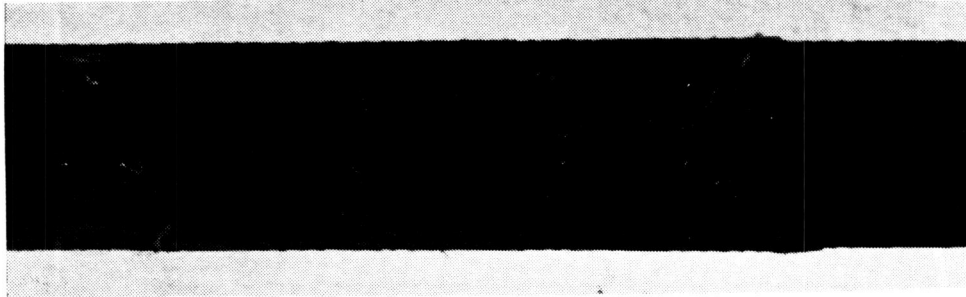
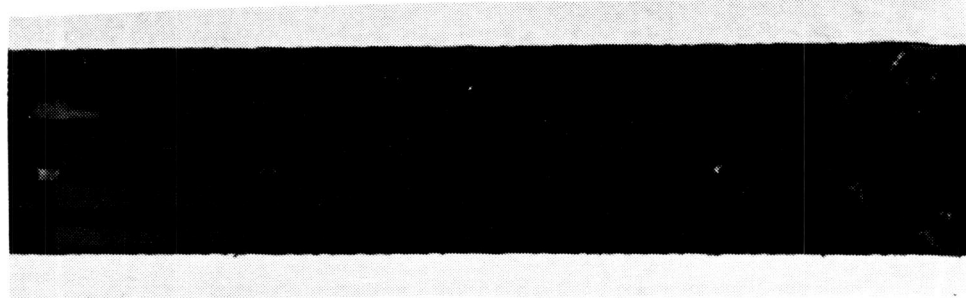
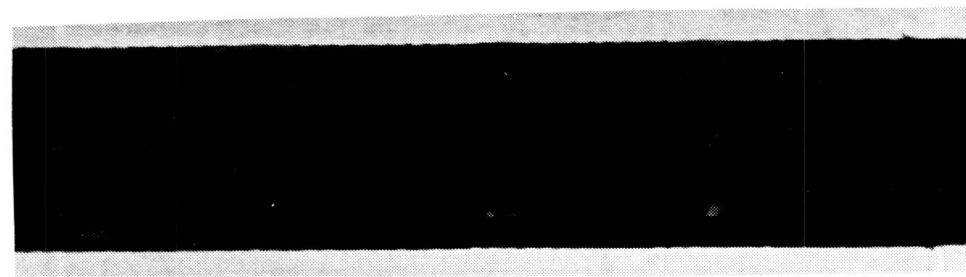
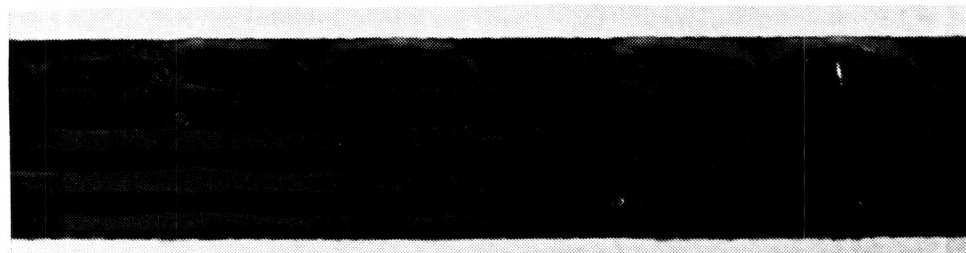


7. $d_c = 0.212''$

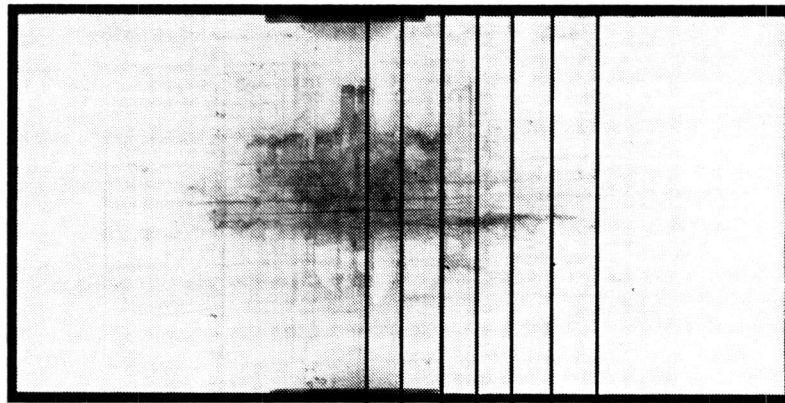


6. $d_c = 0.446''$

Sample D5-3
 $S_C = 25,458$ psi (77.0 % of static), $N_f = 14,751$ cycles

5. $d_c = 0.602''$ 4. $d_c = 0.799''$ 3. $d_c = 1.038''$ 2. $d_c = 1.232''$ 1. $d_c = 1.455''$

Sample D5-3 (Continued)



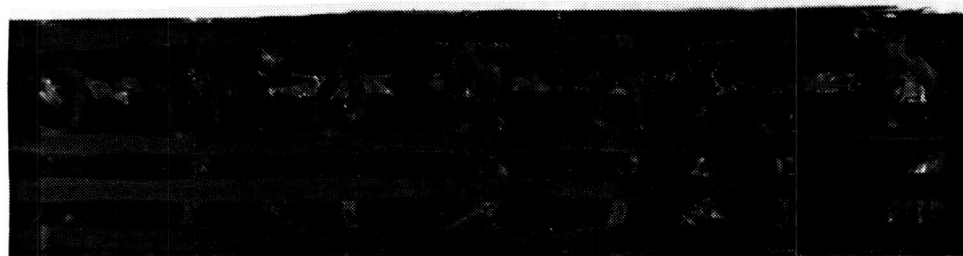
Section #: 7 6 5 4 3 2 1



7. $d_c = 0.062"$



6. $d_c = 0.235"$

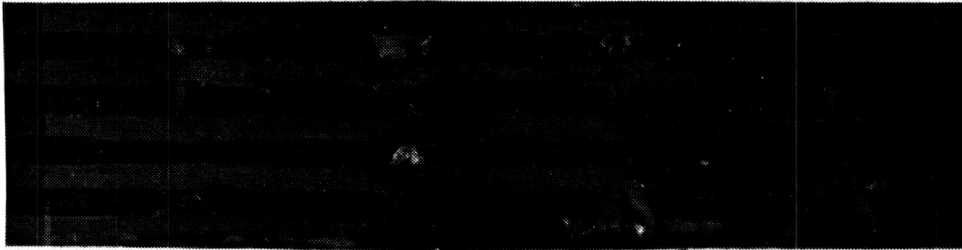


5. $d_c = 0.440"$

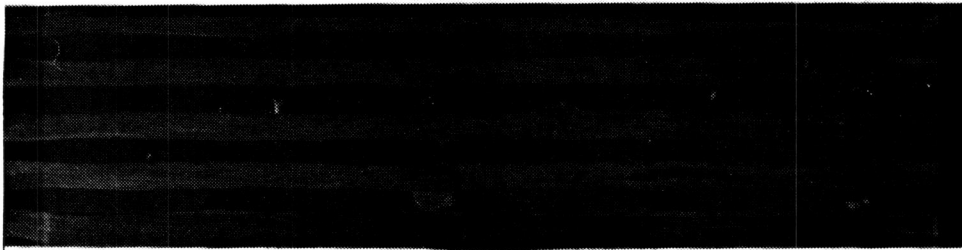
Sample F3-1
 $S_c = 29,688$ psi (74.0 % of static), $N_f = 36,002$ cycles



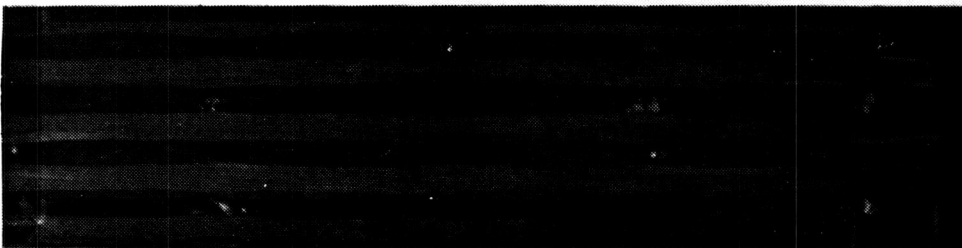
4. $d_c = 0.622''$



3. $d_c = 0.811''$



2. $d_c = 1.016''$



1. $d_c = 1.248''$

Sample F3-1 (Continued)

Appendix C

Mechanical Response of Post-Impact Fatigue Loading: Changes in Modulus, Strain, and Hysteresis

Unloading and secant moduli, average maximum and minimum strain, and hysteresis are plotted versus cycles for each sample. The secant modulus data is presented as a line so that unloading and secant moduli are more easily distinguished; the line represents discrete data points. All fatigue tests were conducted at a stress ratio of $R = -5$ and a frequency of four hertz. Samples which survived one million cycles were considered to have reached infinite life, and these tests were stopped. The maximum compressive stress (S_c) and the number of cycles to failure (N_f) are given for each sample. Samples are labeled as indicated below.

A3-1



SAMPLE NUMBER

PANEL NUMBER

TTT REINFORCEMENT

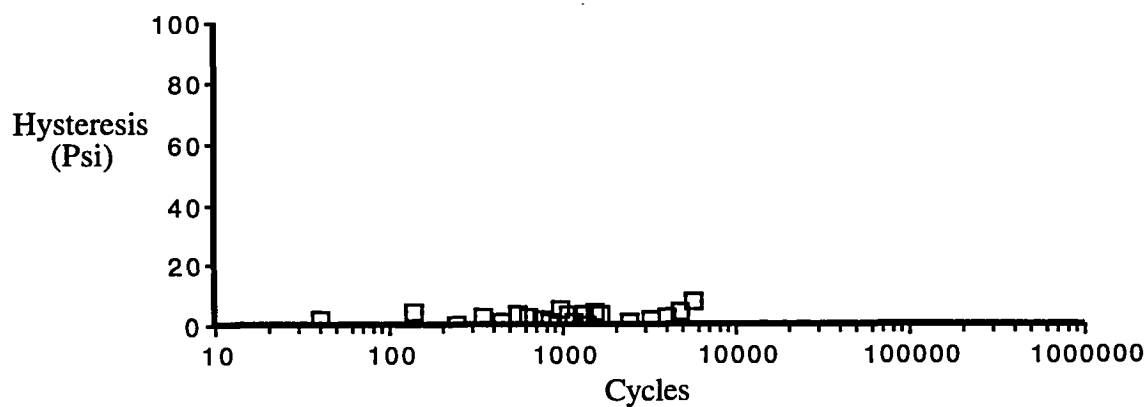
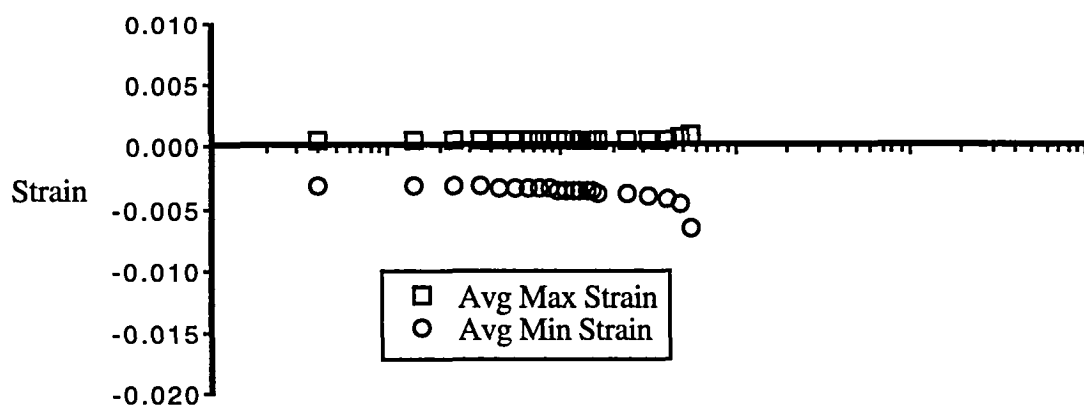
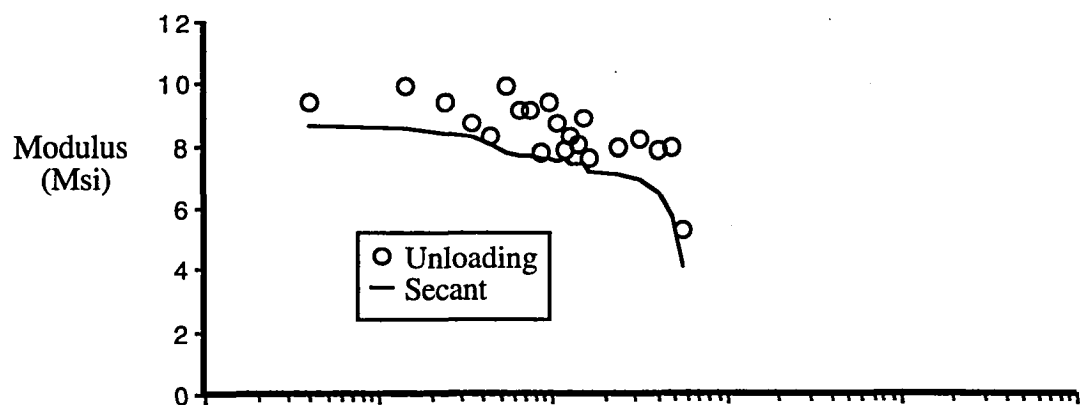
A - Kevlar 29, 1500 denier

B - Toray Carbon, T-1000

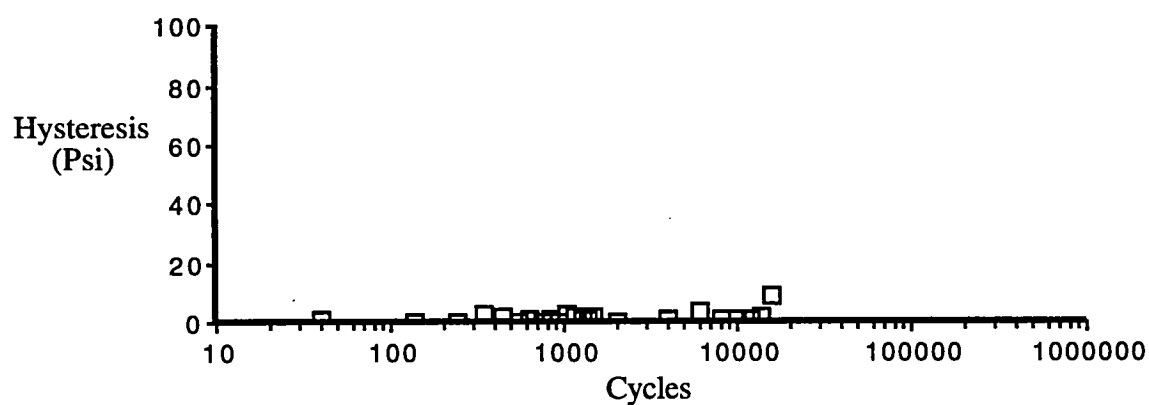
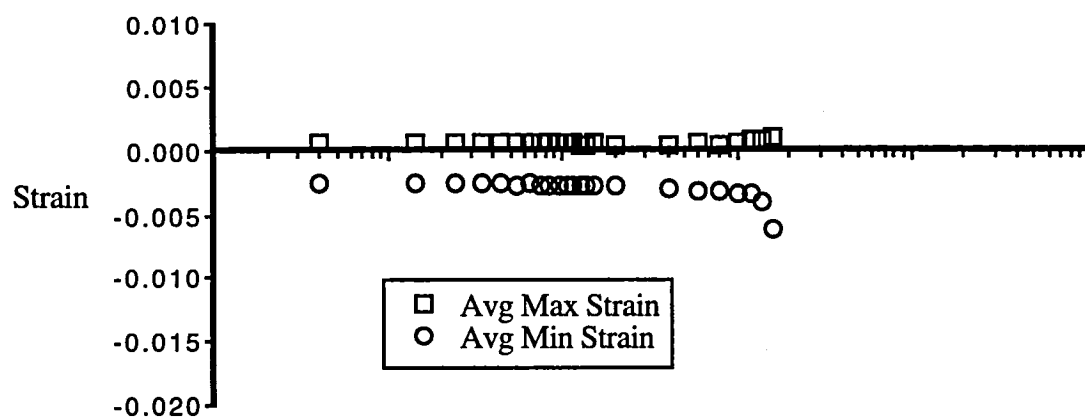
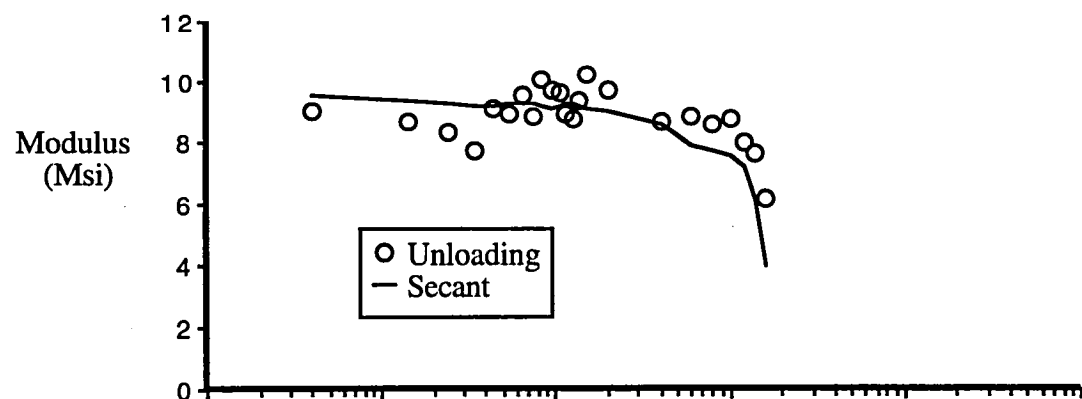
C - AS4 Carbon, 9k

D - S2 75 1/3 Glass

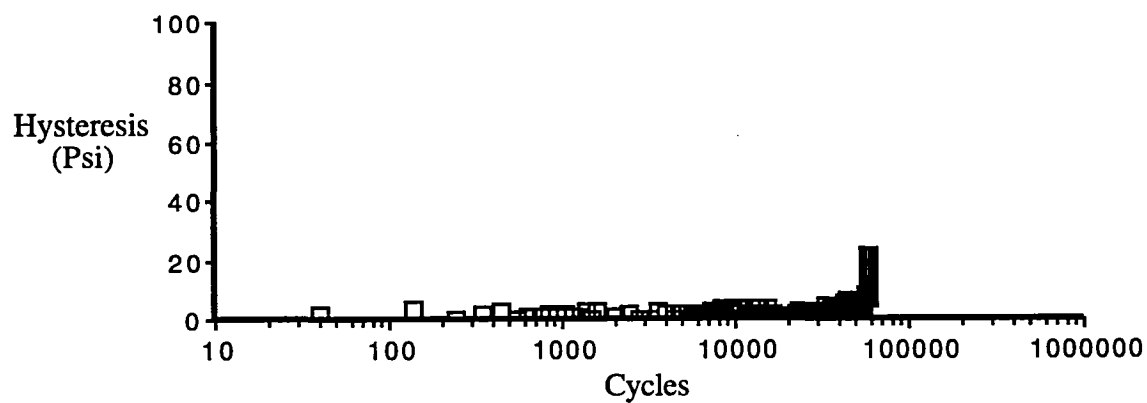
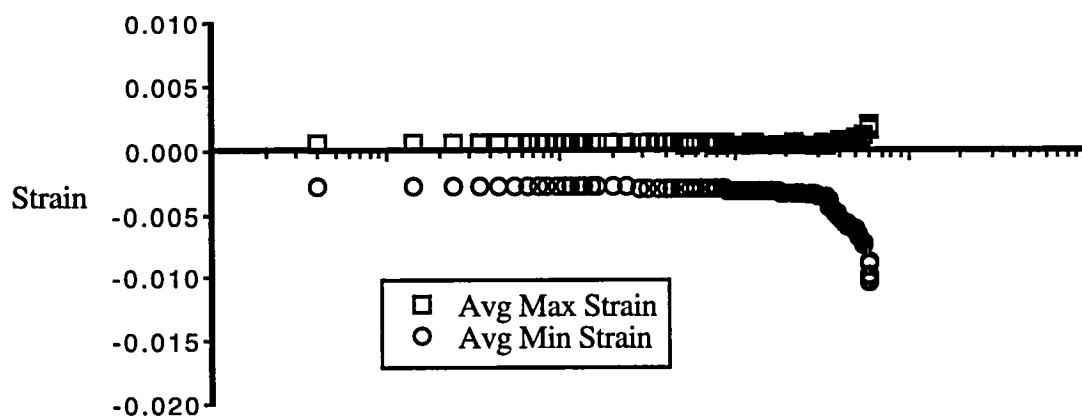
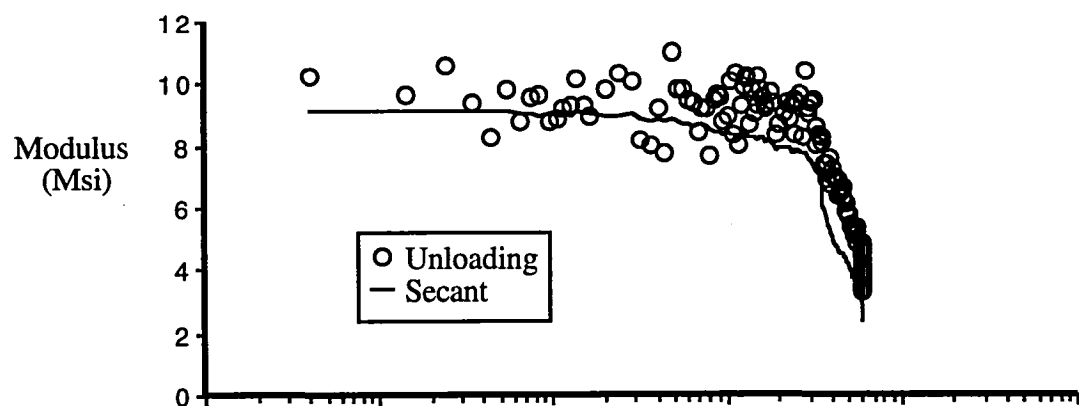
F - IM6 Carbon, 6k



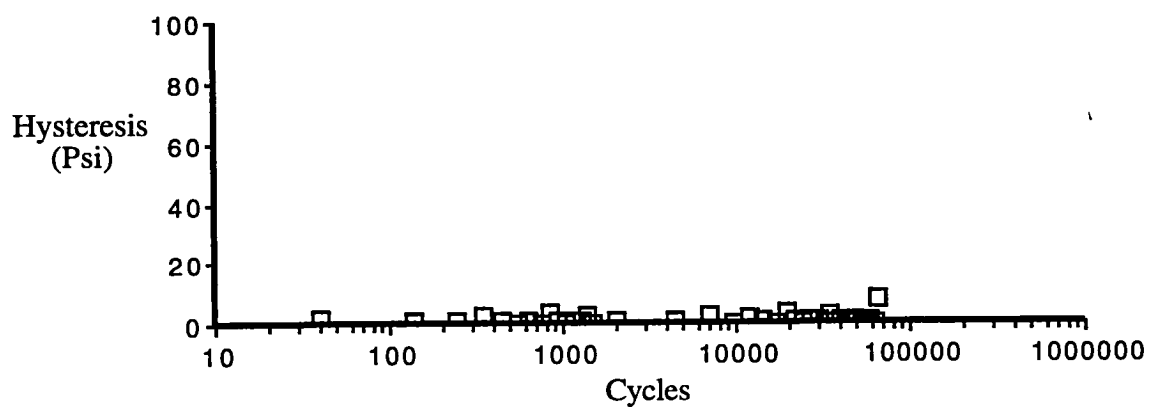
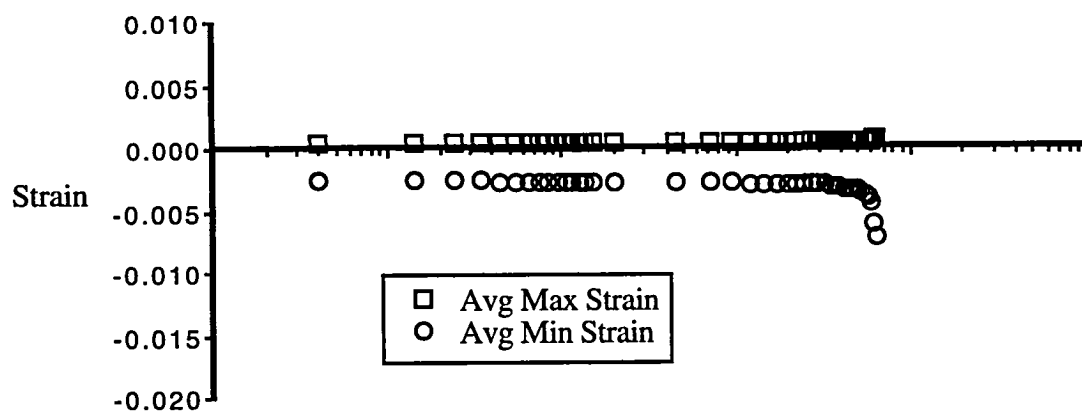
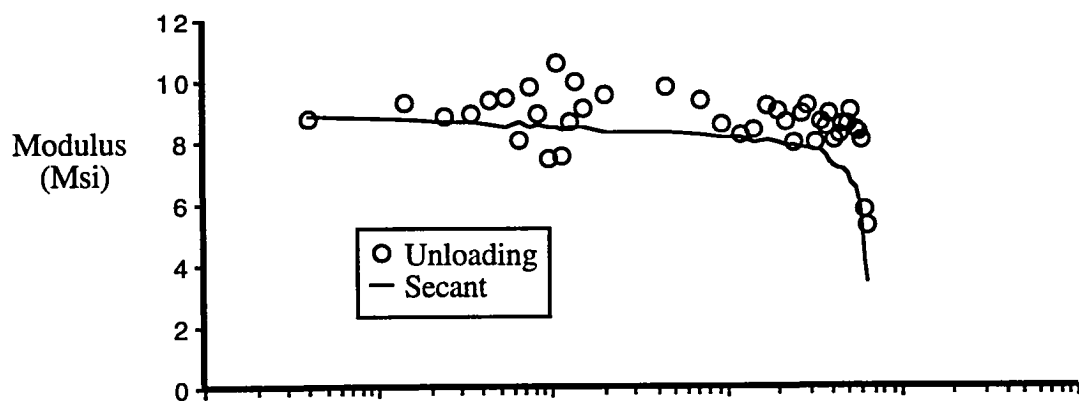
Sample A3-1
 $S_c = 25,775$ psi (75.0 % of static), $N_f = 6,202$ cycles



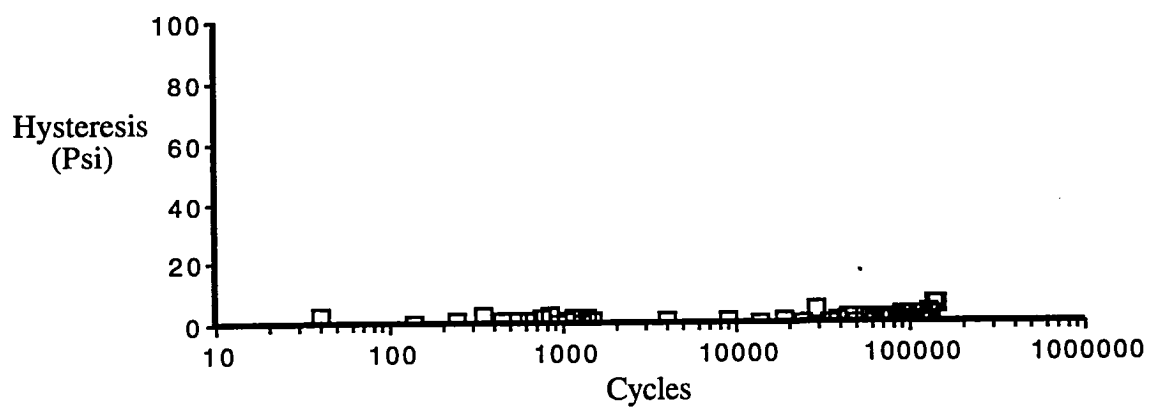
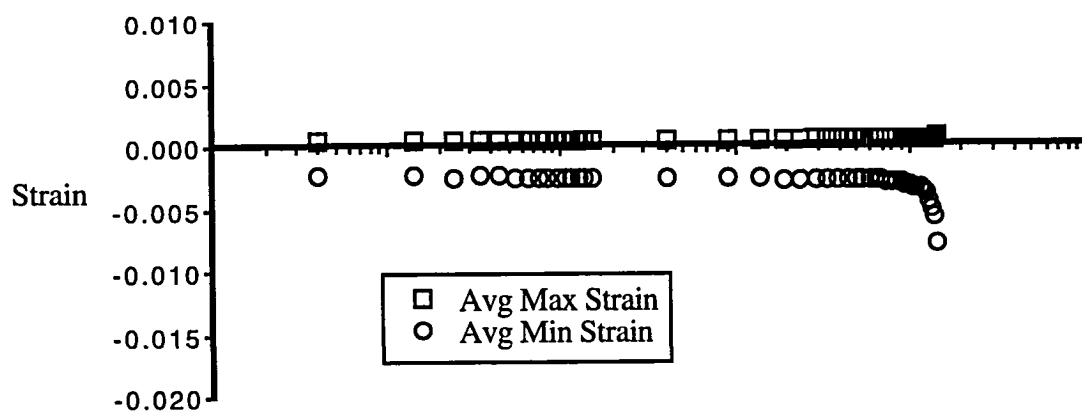
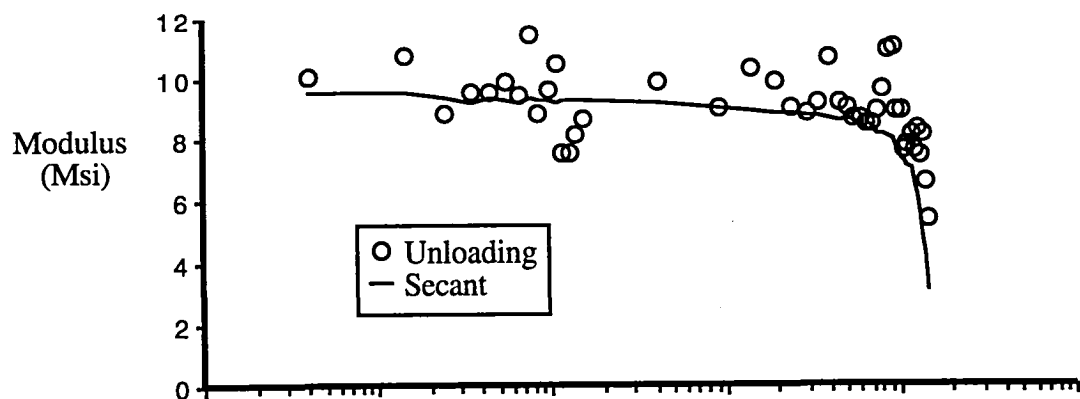
Sample A7-3
 $S_c = 24,056$ psi (70.0 % of static), $N_f = 16,768$ cycles



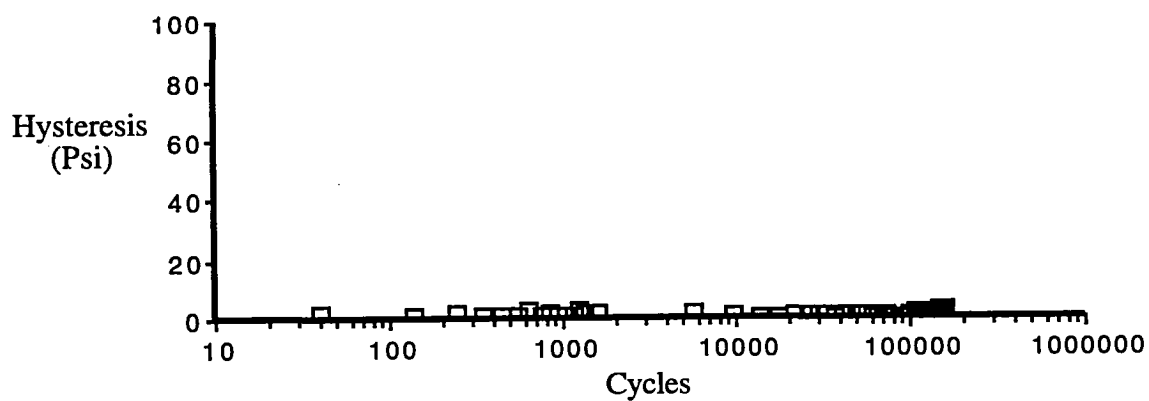
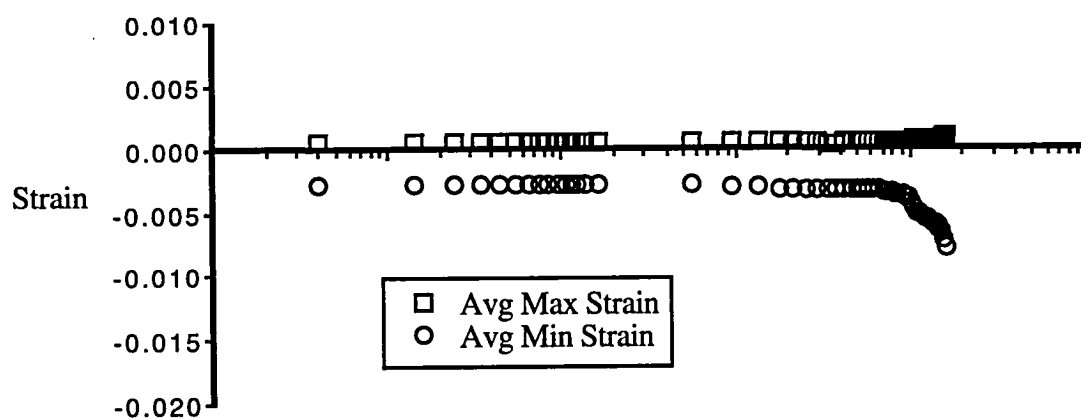
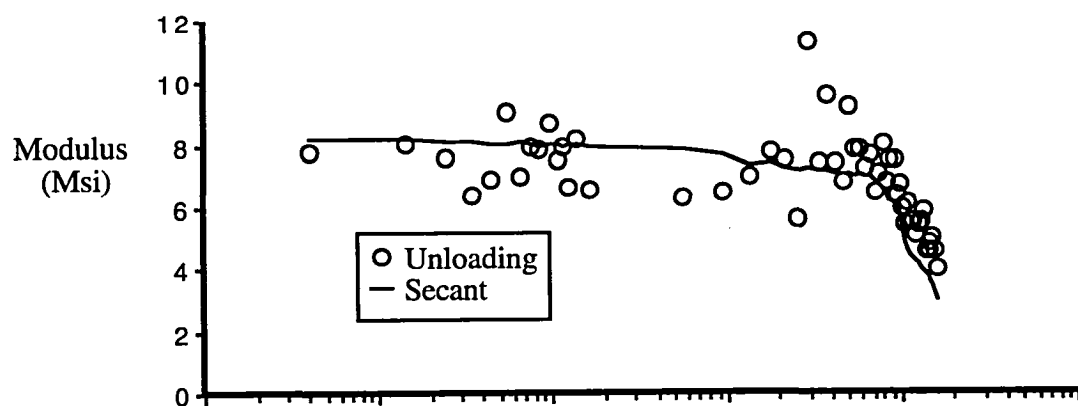
Sample A6-2
 $S_c = 24,744$ psi (72.0 % of static), $N_f = 58,954$ cycles



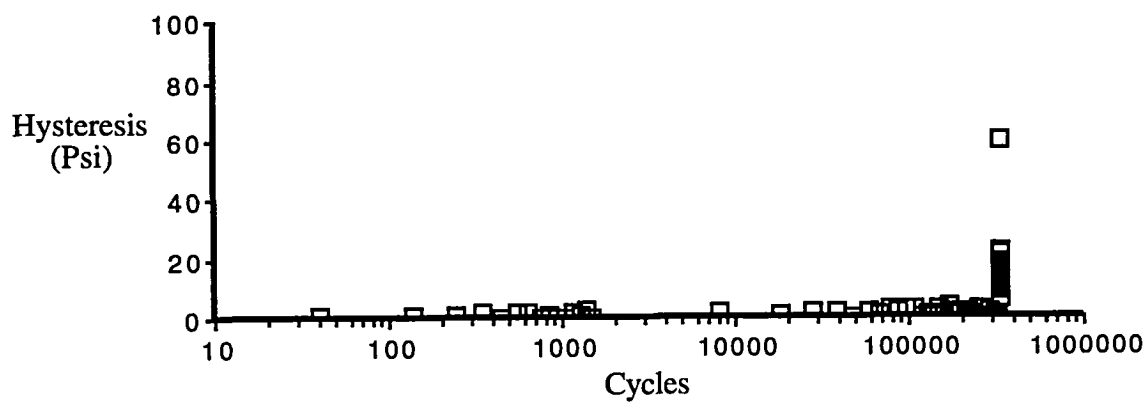
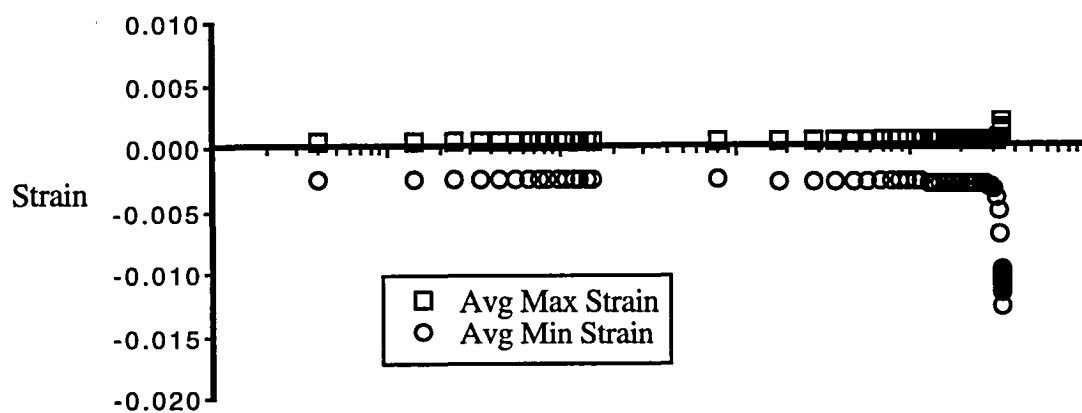
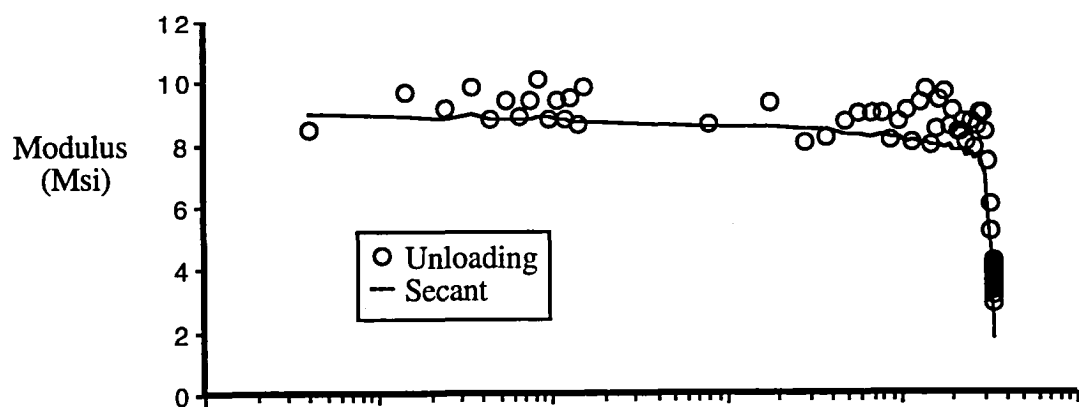
Sample A2-3
 $S_C = 22,338$ psi (65.0 % of static), $N_f = 65,462$ cycles



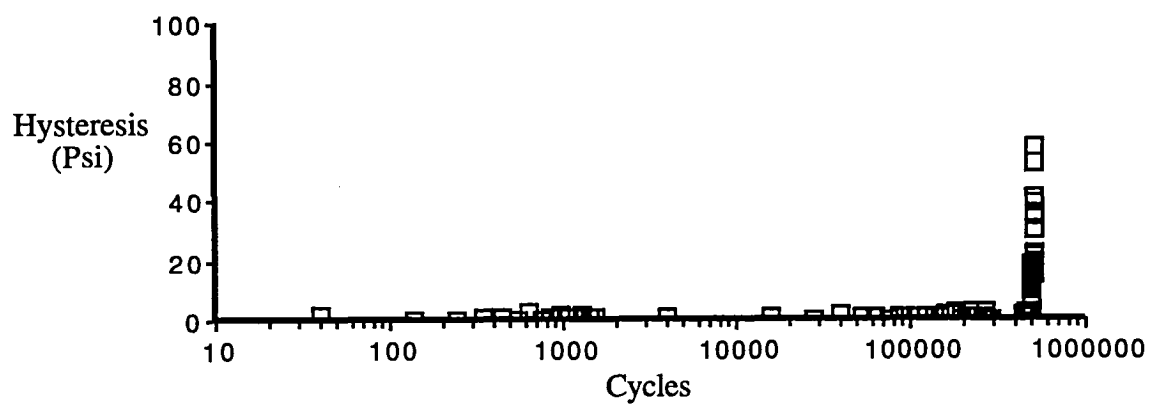
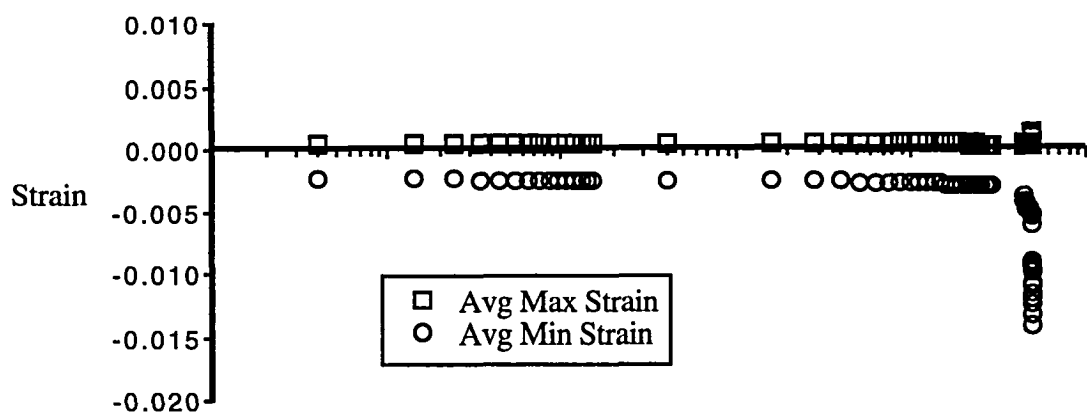
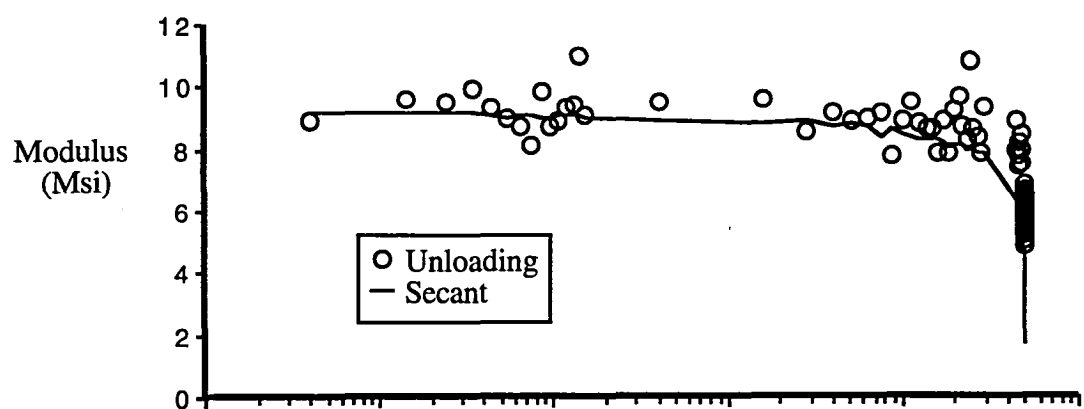
Sample A2-1
 $S_c = 21,994$ psi (64.0 % of static), $N_f = 144,546$ cycles



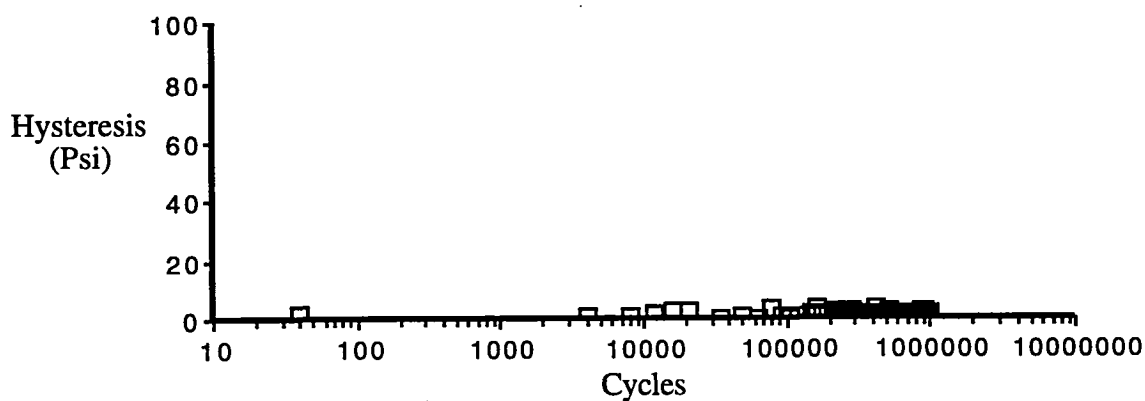
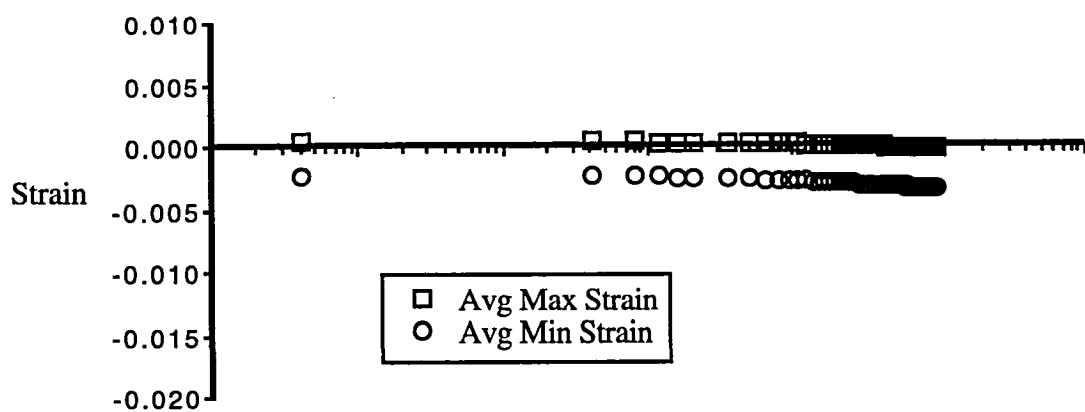
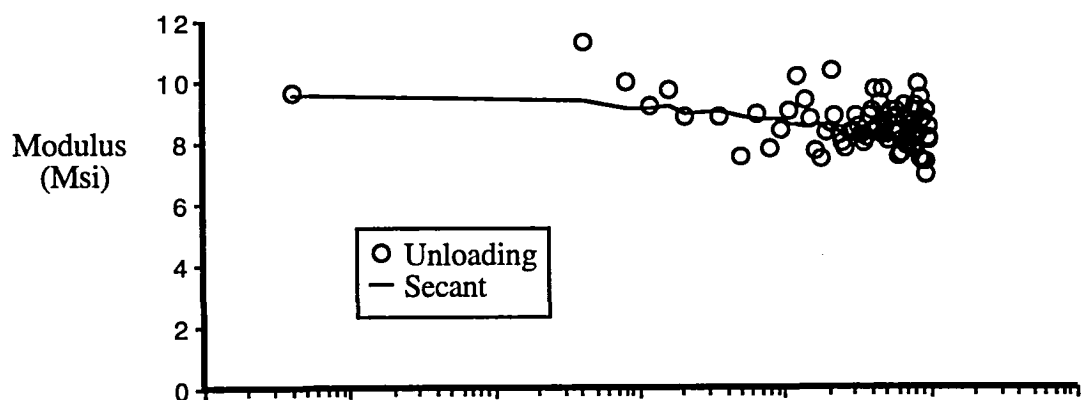
Sample A7-1
 $S_C = 21,973$ psi (63.9 % of static), $N_f = 159,415$ cycles



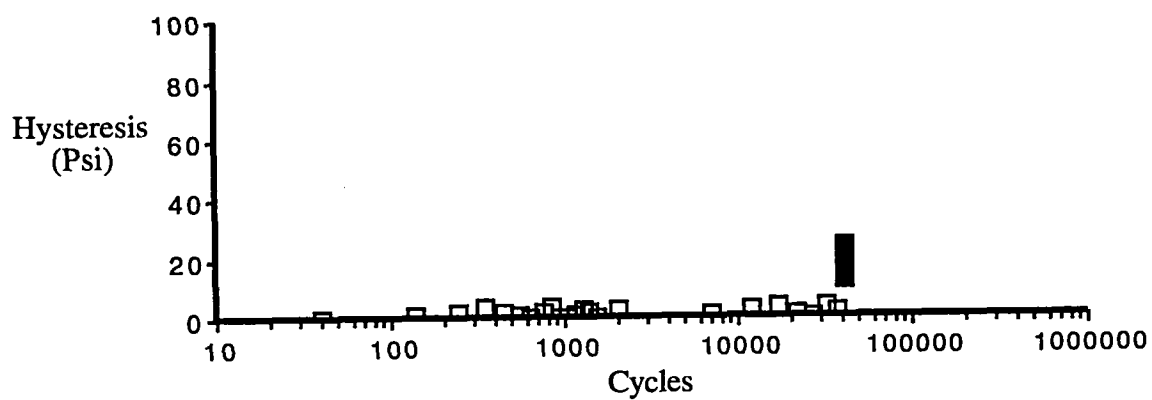
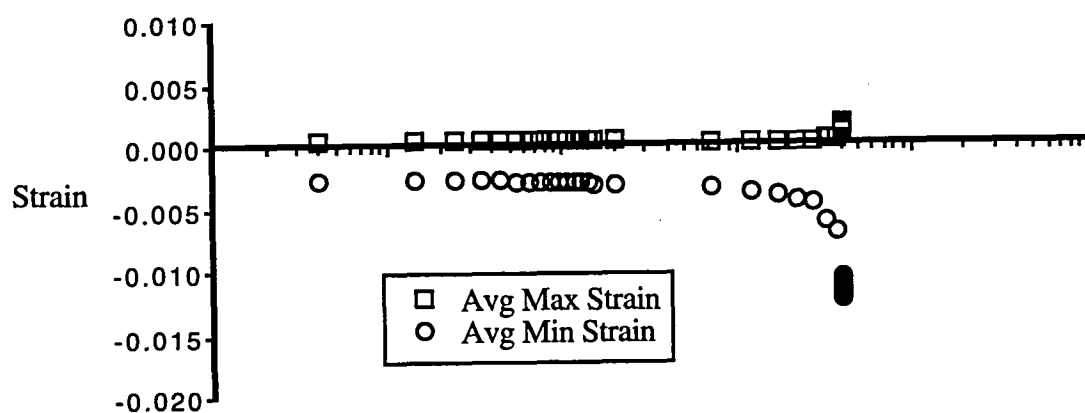
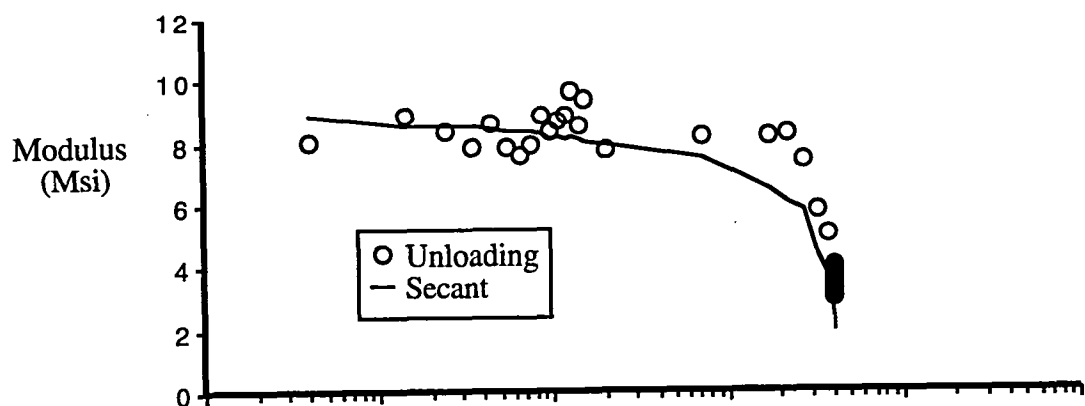
Sample A2-2
 $S_c = 21,479$ psi (62.5 % of static), $N_f = 332,077$ cycles



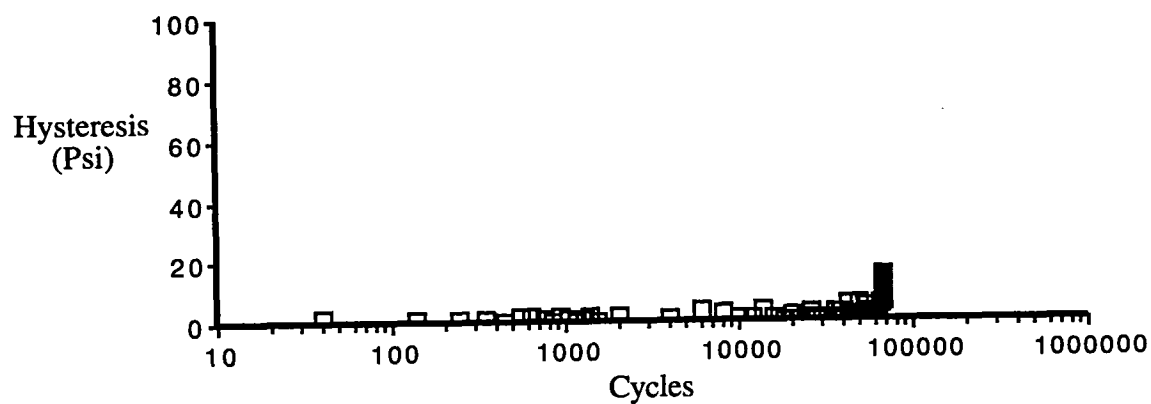
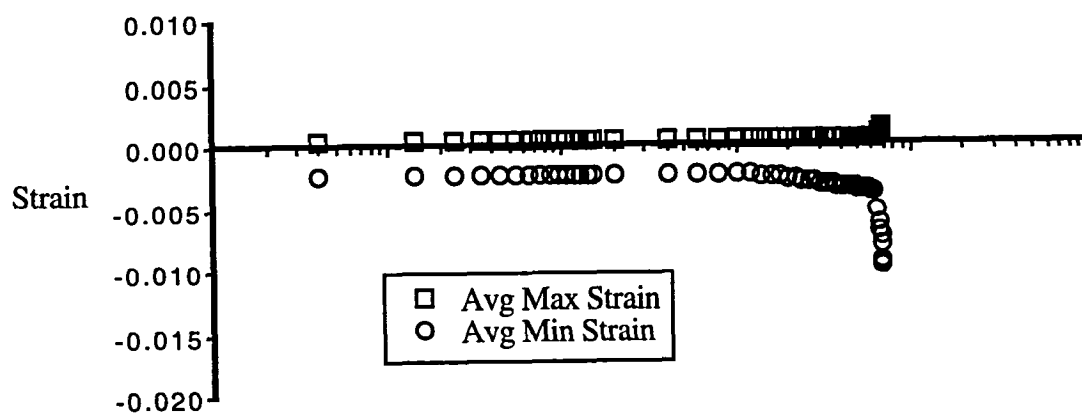
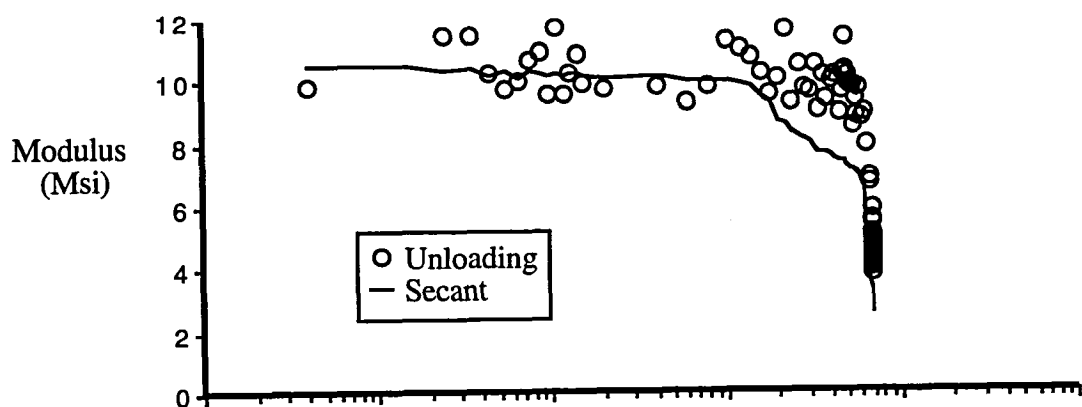
Sample A1-1
 $S_c = 21,650$ psi (63.0 % of static), $N_f = 501,227$ cycles



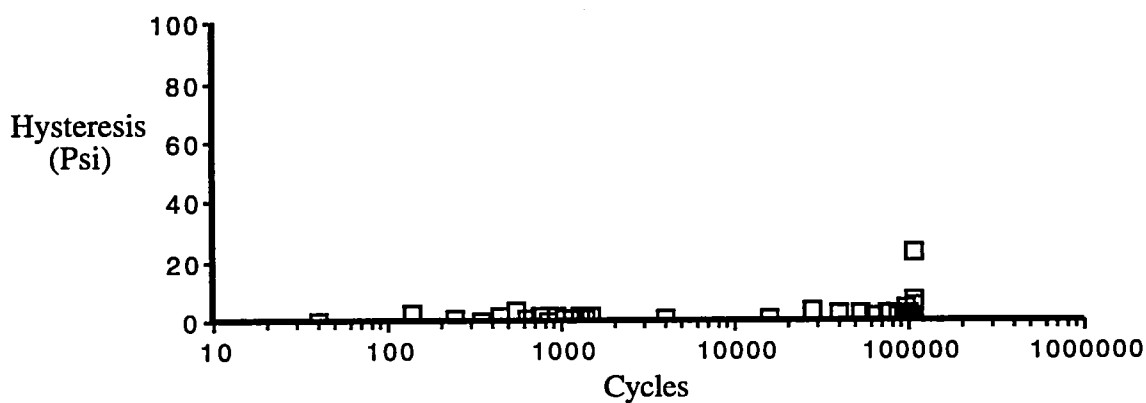
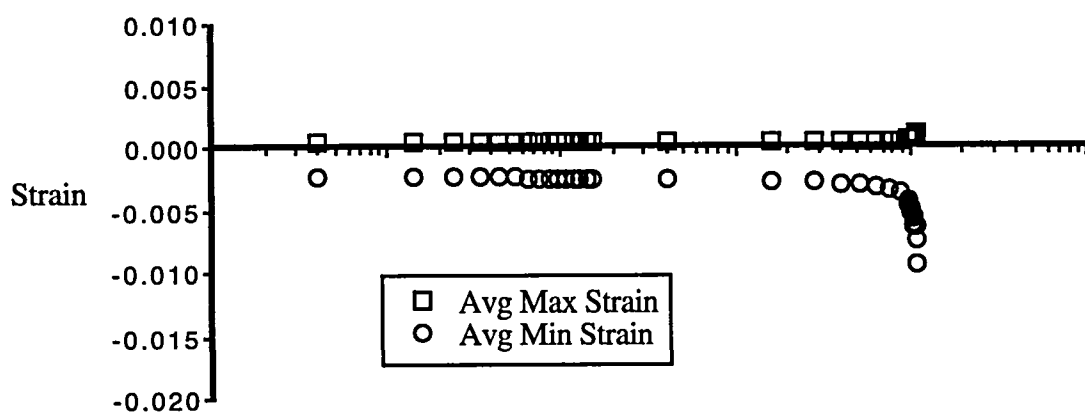
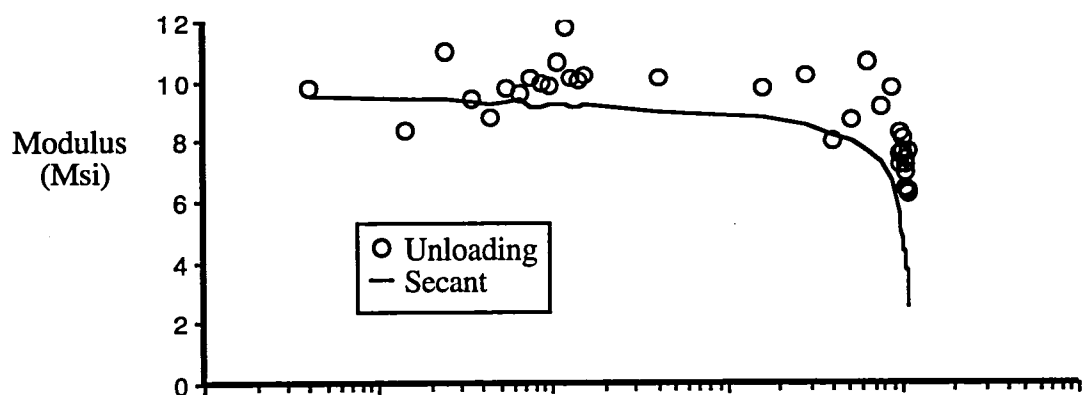
Sample A7-2
 $S_c = 20,620$ psi (60.0 % of static), $N_f = 1,000,000$ cycles (infinite)



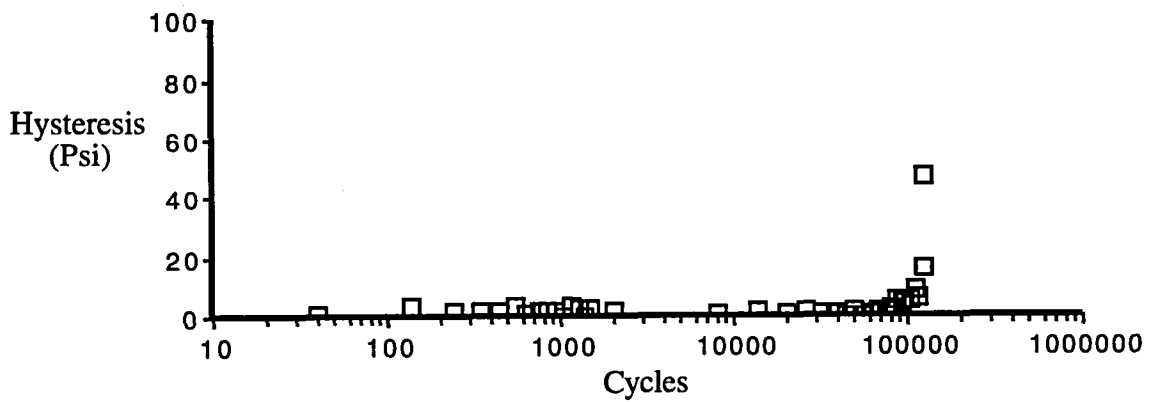
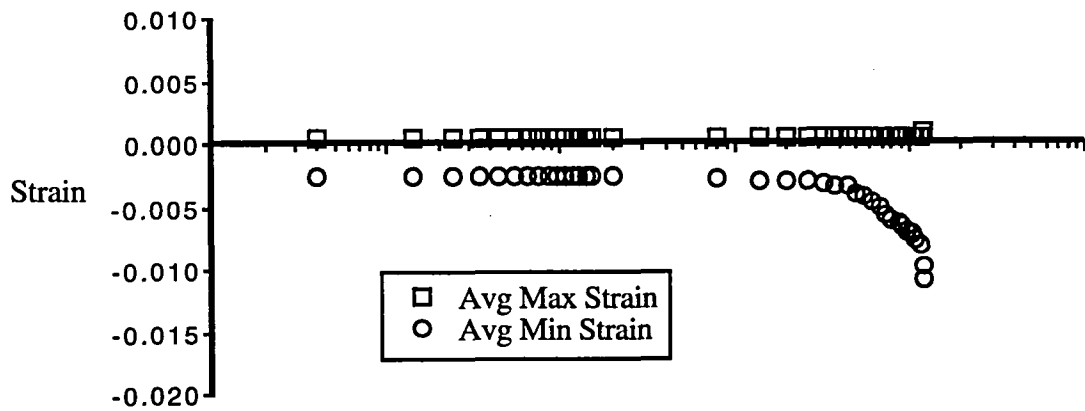
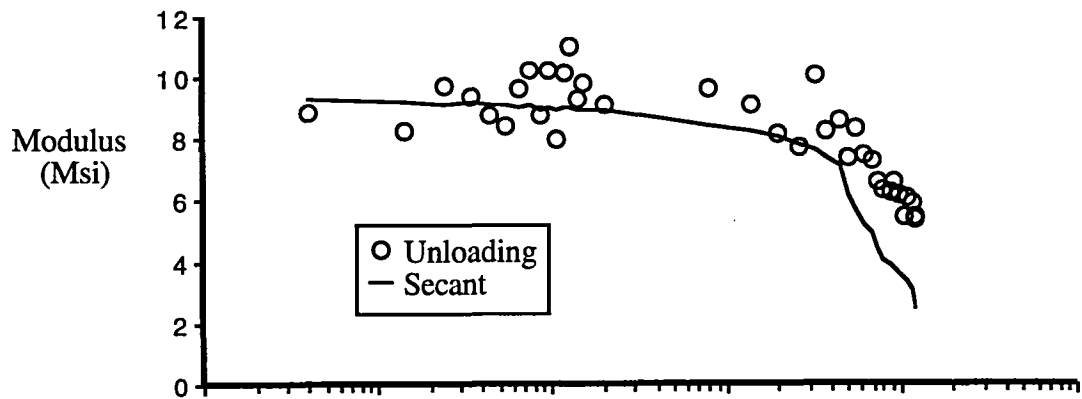
Sample B2-1
 $S_c = 23,161$ psi (70.0 % of static), $N_f = 40,748$ cycles



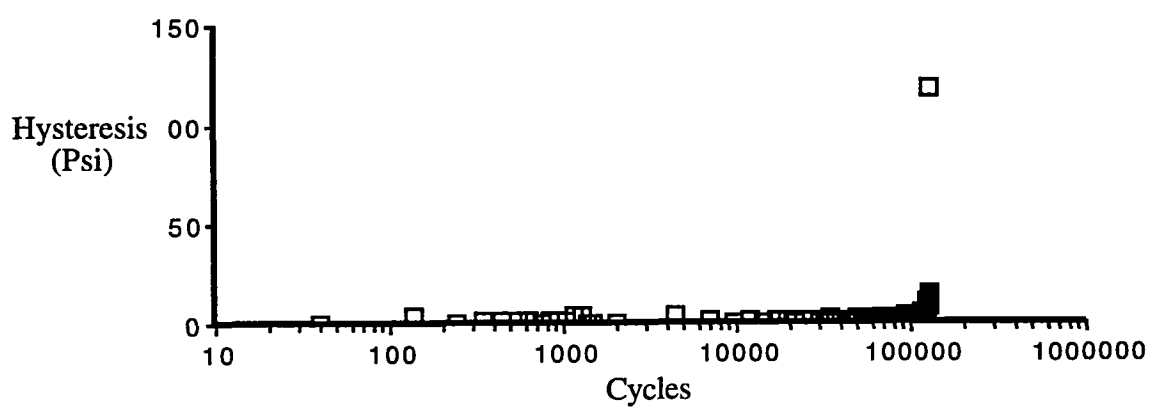
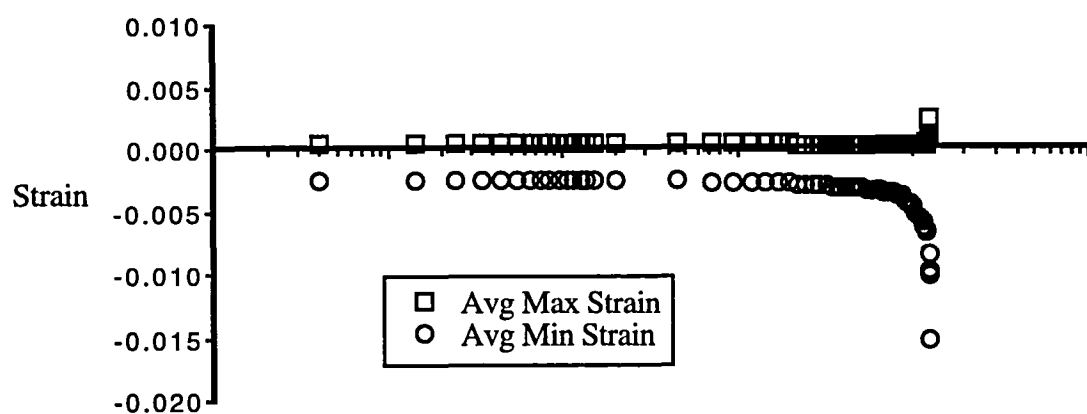
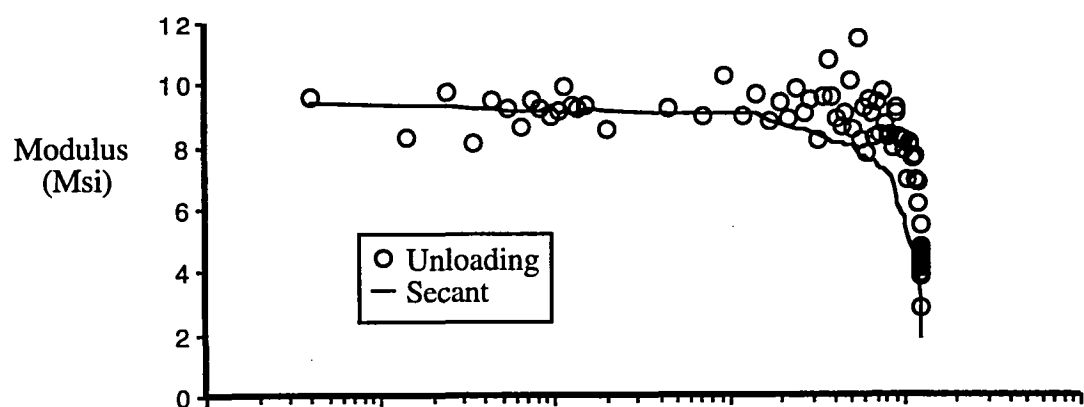
Sample B7-3
 $S_C = 23,491$ psi (71.0 % of static), $N_f = 68,597$ cycles



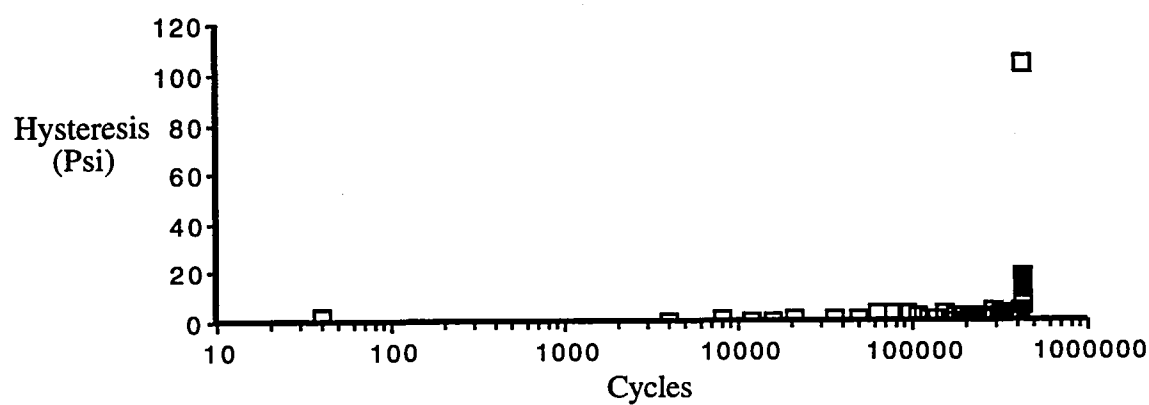
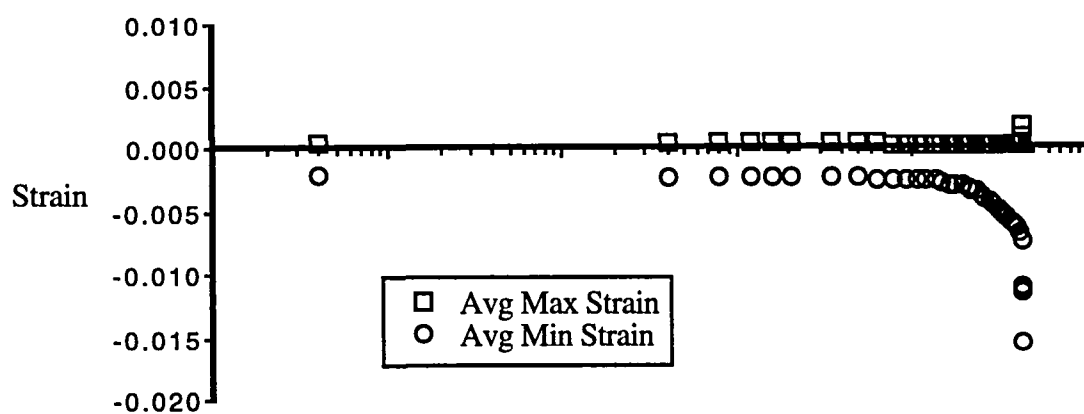
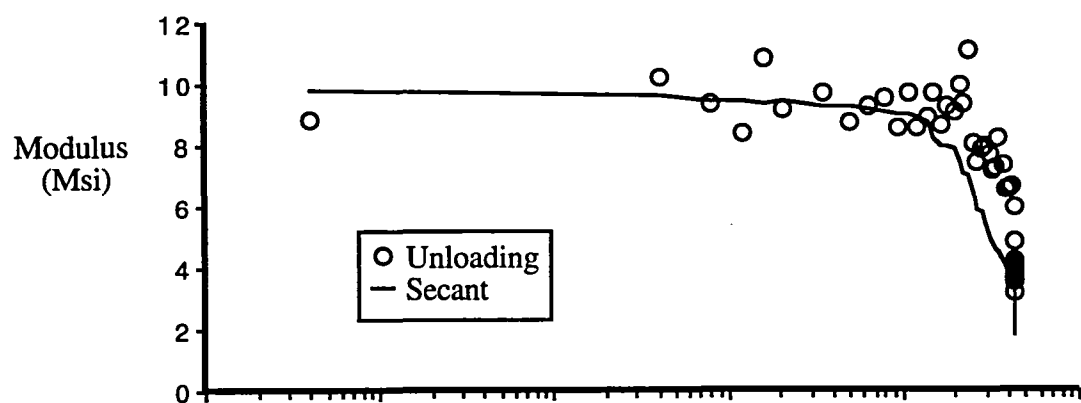
Sample B5-3
 $S_C = 22,002$ psi (66.5 % of static), $N_f = 107,905$ cycles



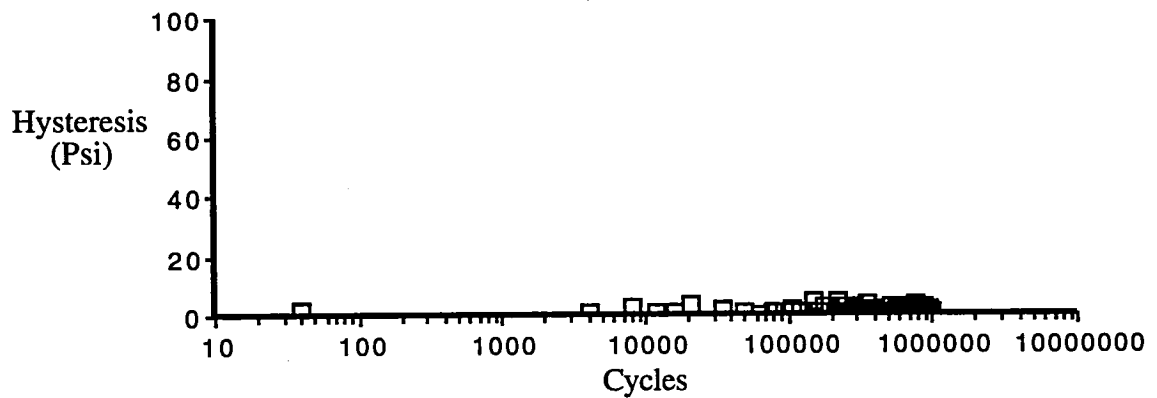
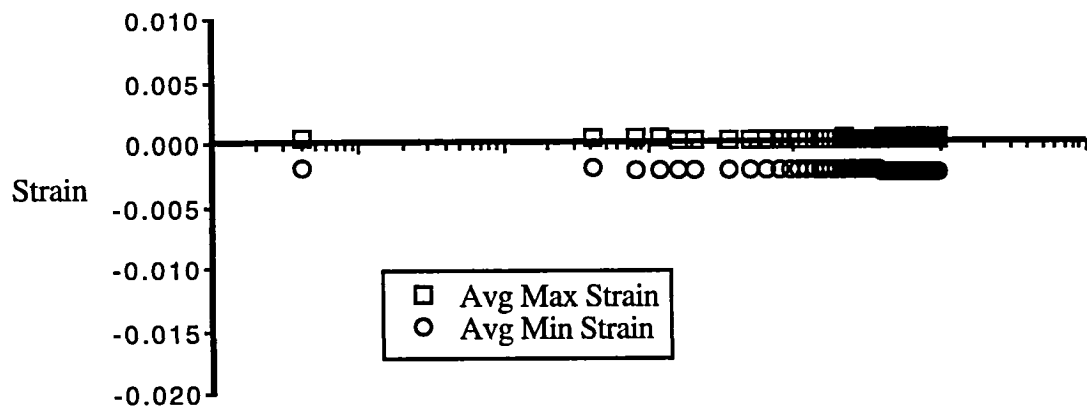
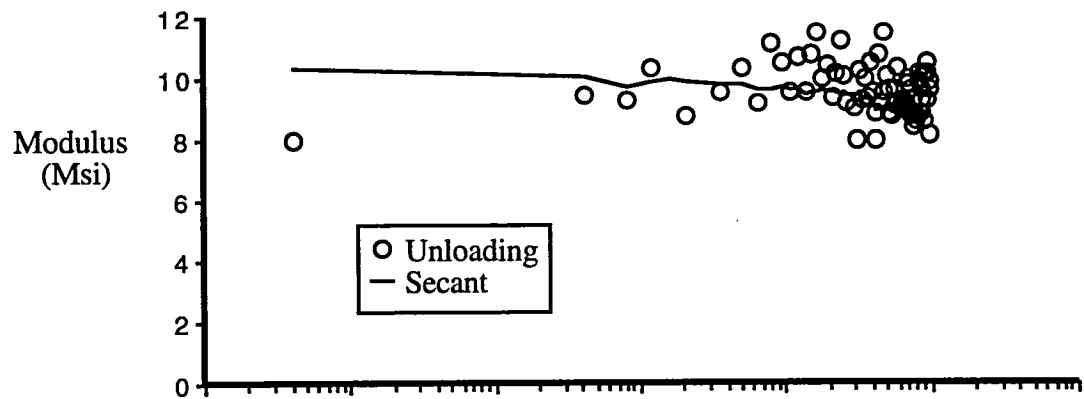
Sample B5-1
 $S_C = 22,499$ psi (68.0 % of static), $N_f = 121,544$ cycles



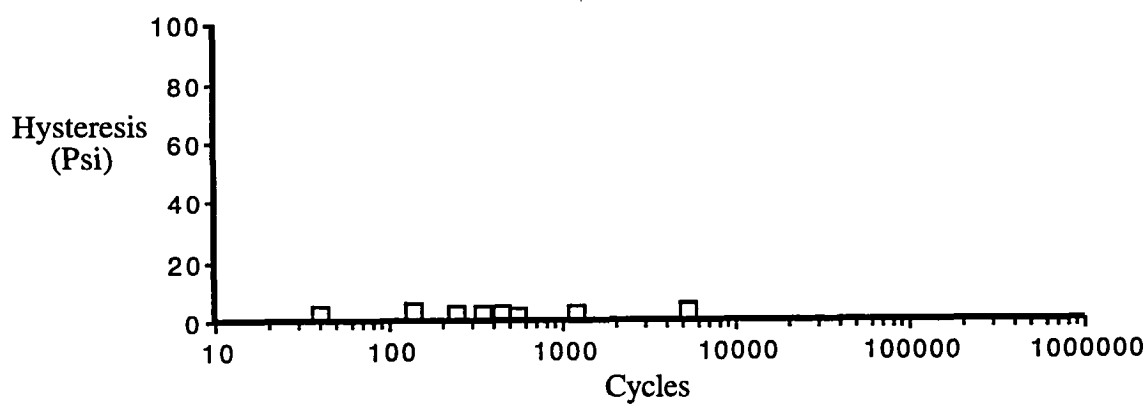
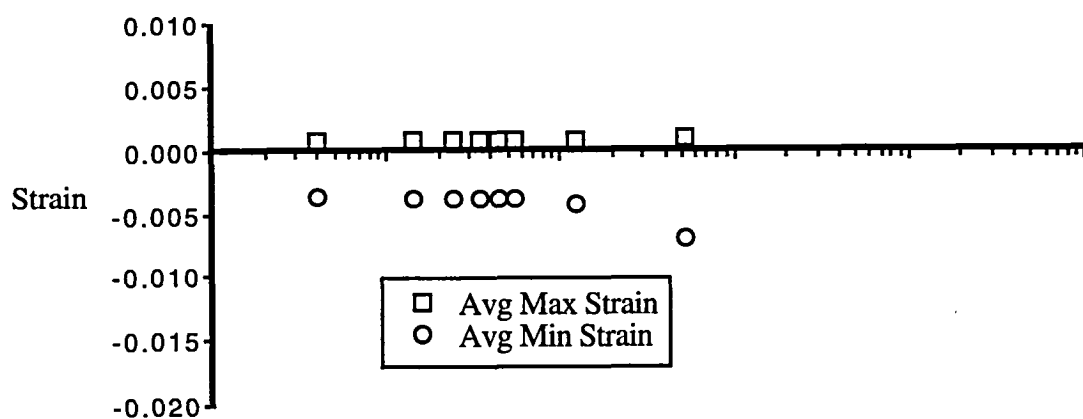
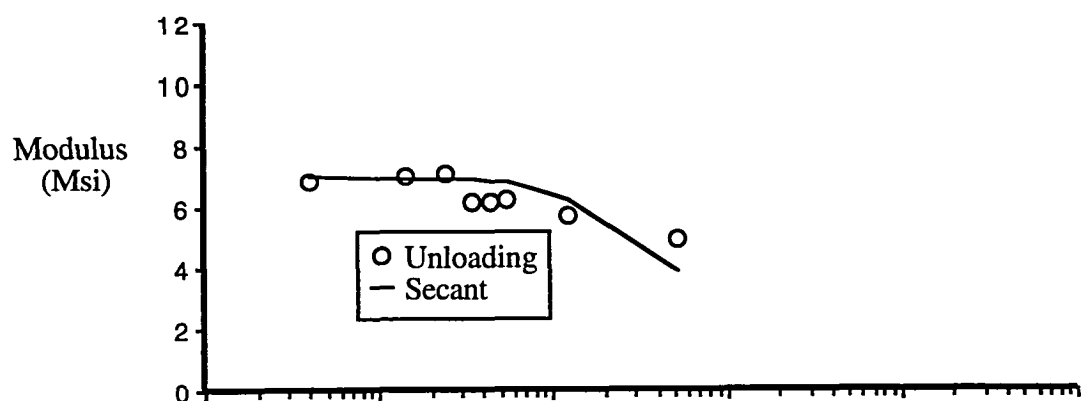
Sample B7-1
 $S_c = 22,830$ psi (69.0 % of static), $N_f = 126,071$ cycles



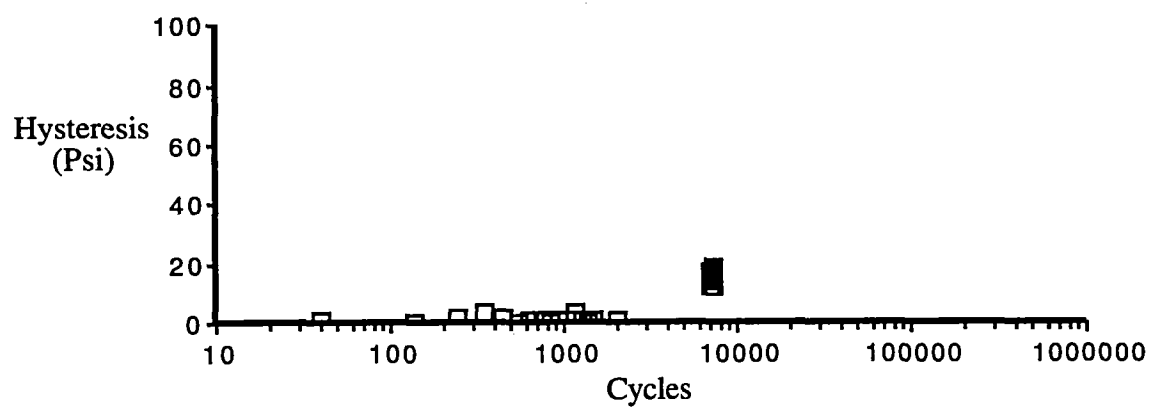
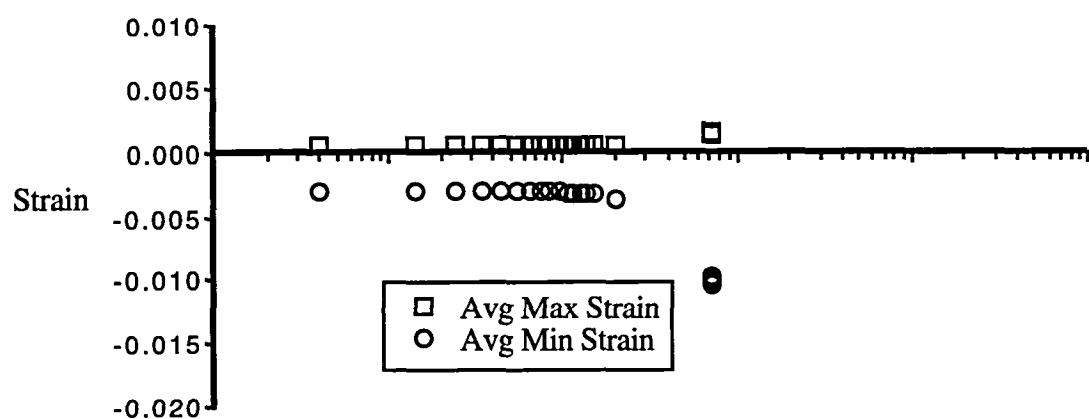
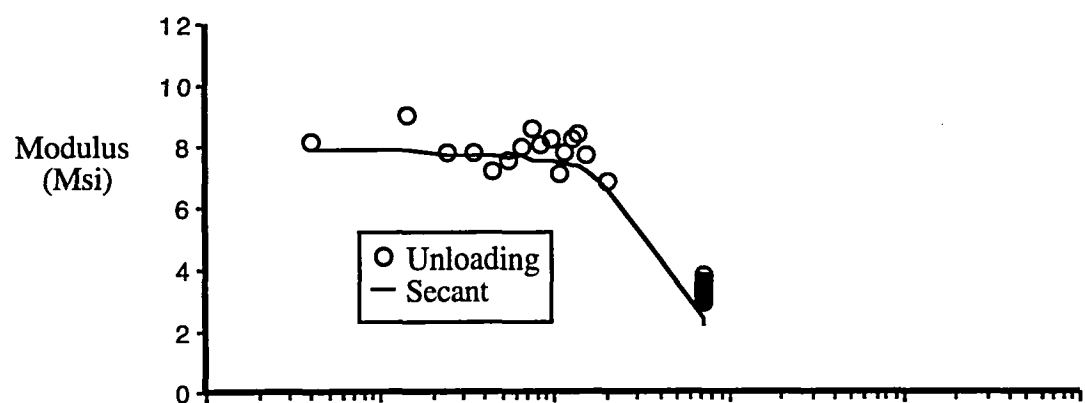
Sample B7-2
 $S_c = 20,977$ psi (63.4 % of static), $N_f = 431,774$ cycles



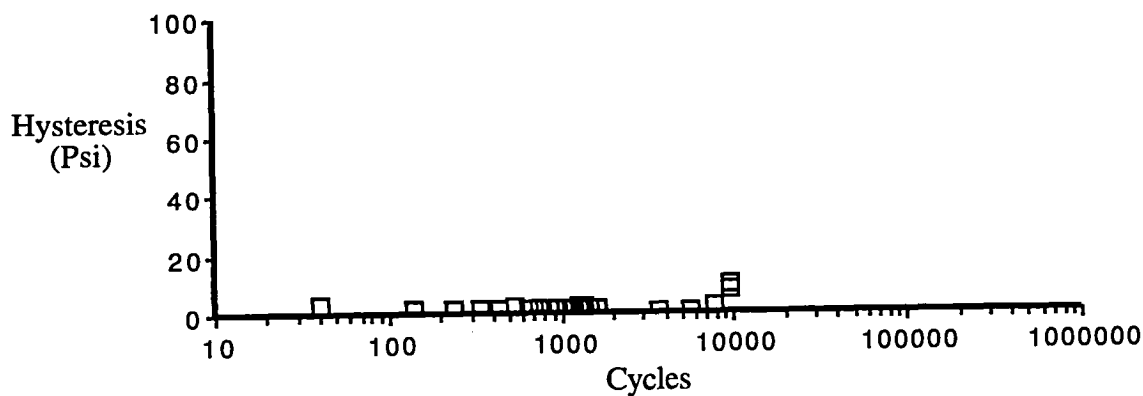
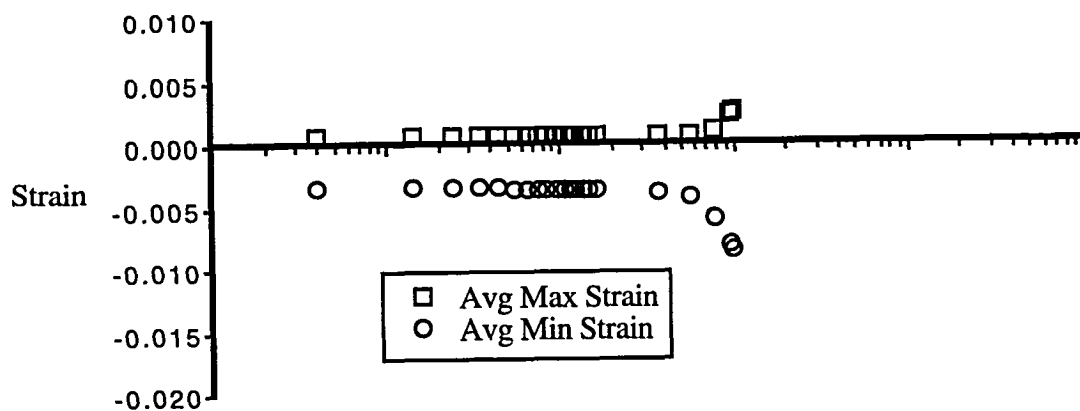
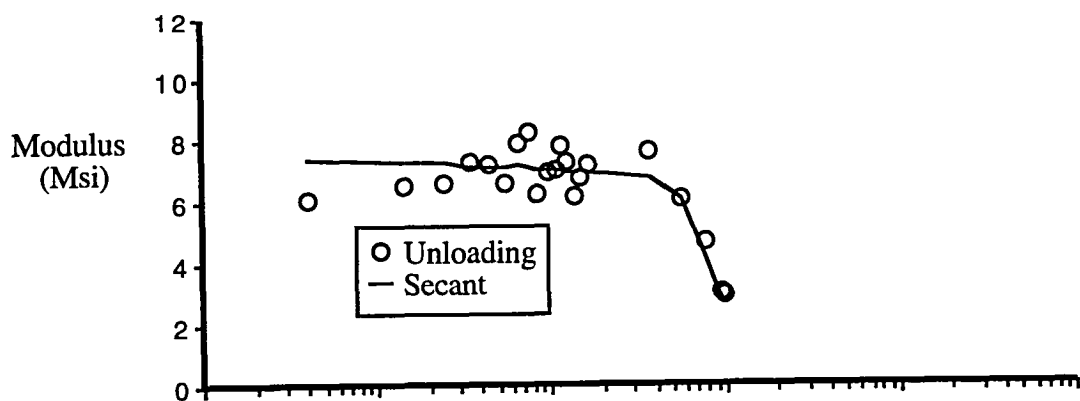
Sample B1-1
 $S_c = 19,190$ psi (58.0 % of static), $N_f = 1,000,000$ cycles (infinite)



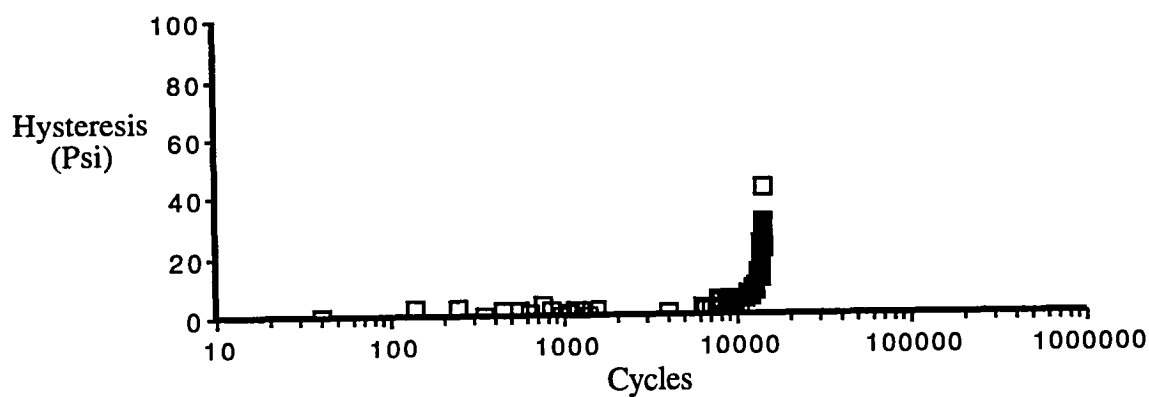
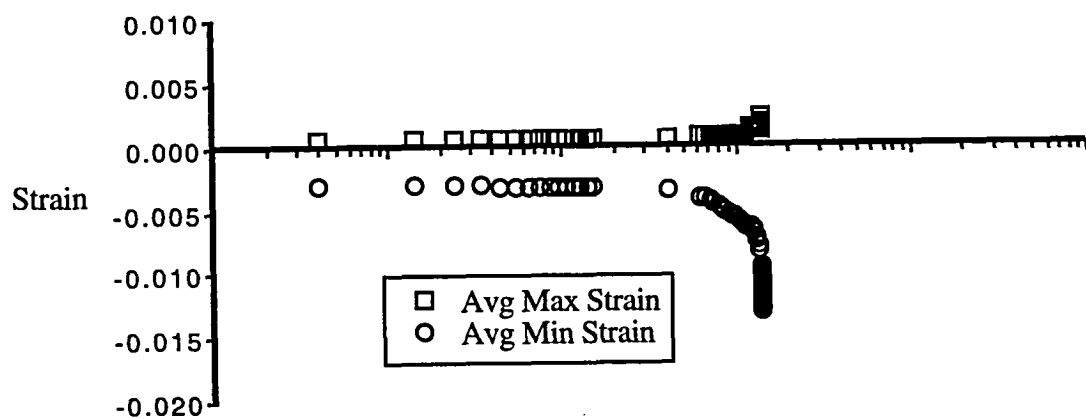
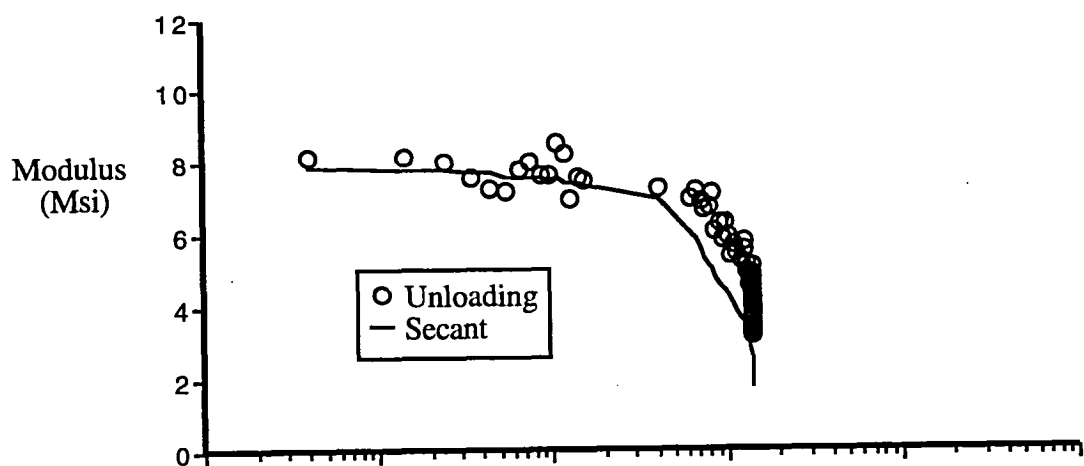
Sample C5-1
 $S_C = 25,915$ psi (72.2 % of static), $N_f = 46,550$ cycles



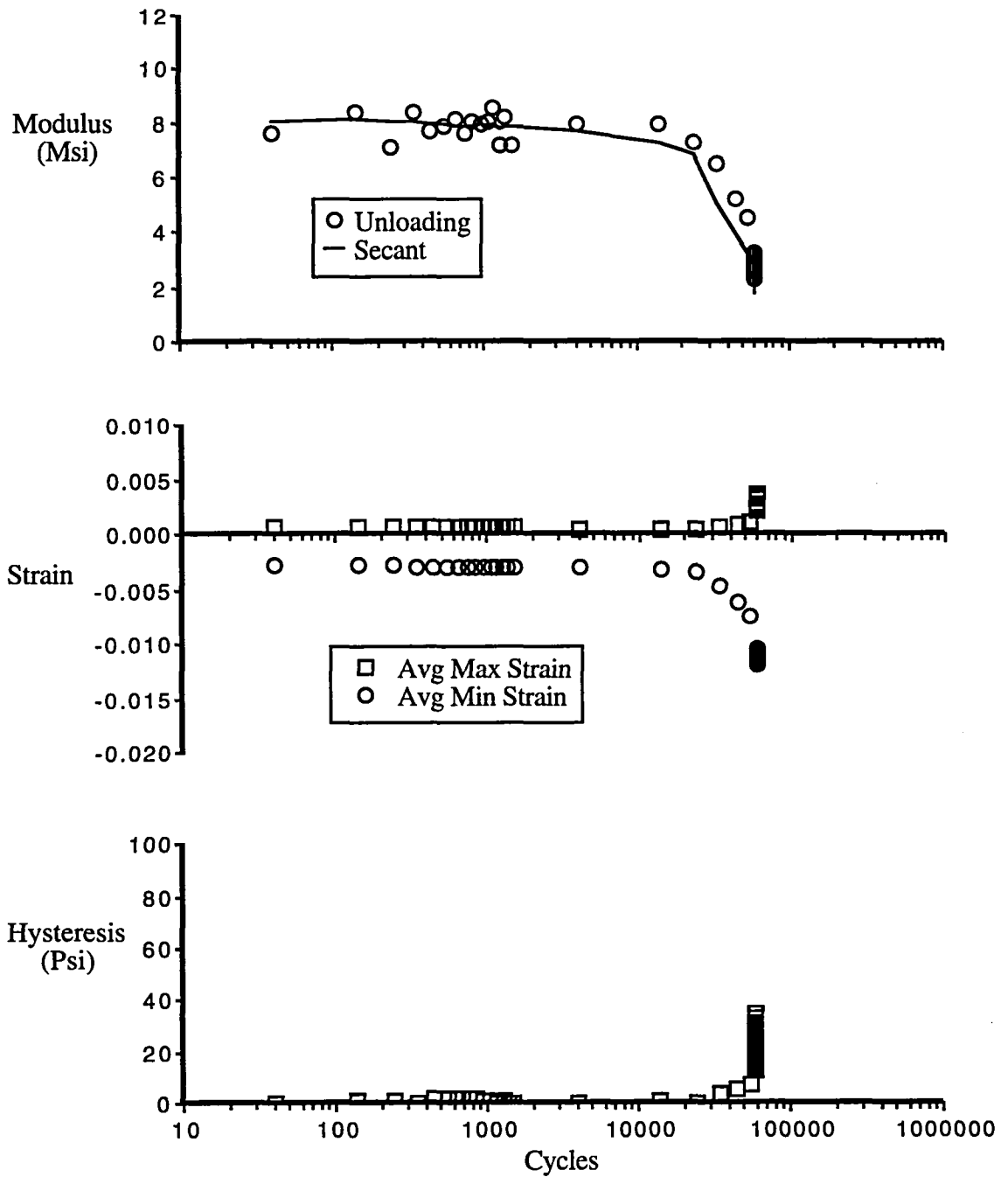
Sample C2-1
 $S_c = 22,573$ psi (62.9 % of static), $N_f = 7,181$ cycles



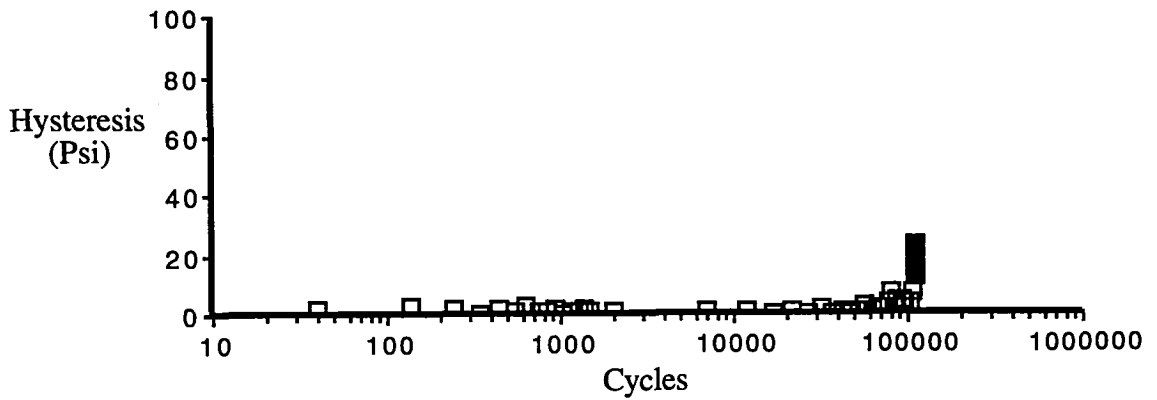
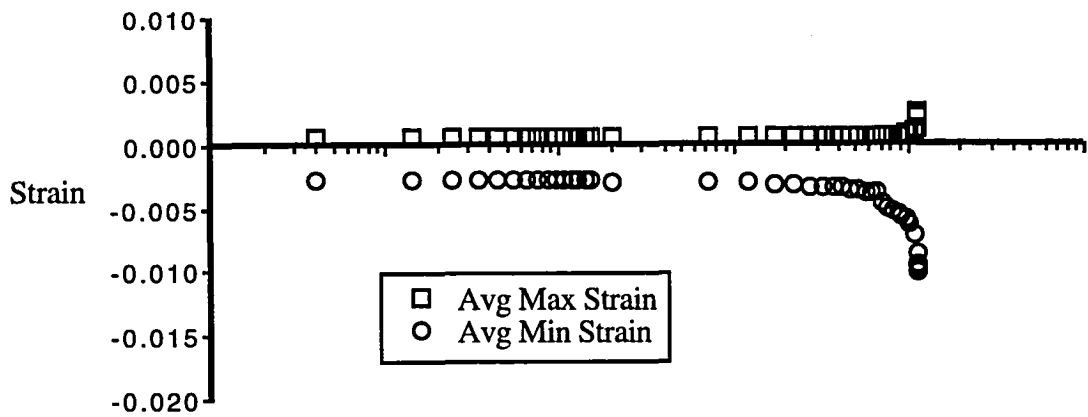
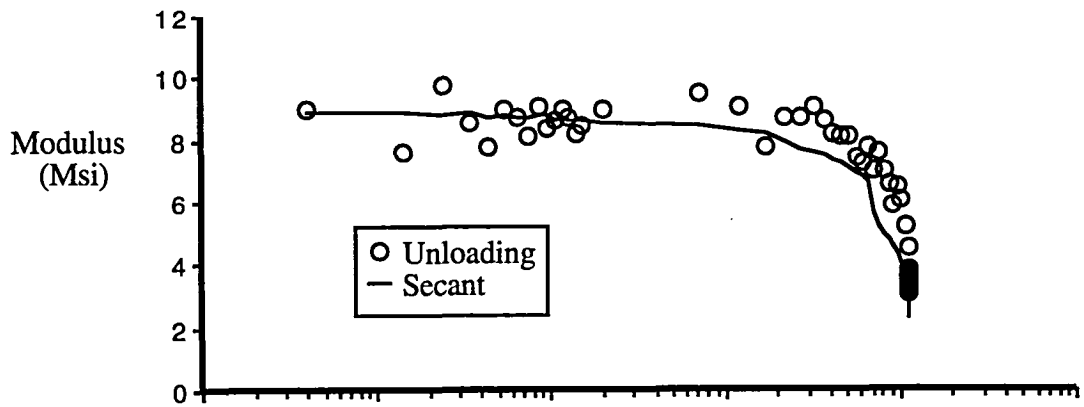
Sample C2-3
 $S_c = 24,408$ psi (68.0 % of static), $N_f = 9,704$ cycles



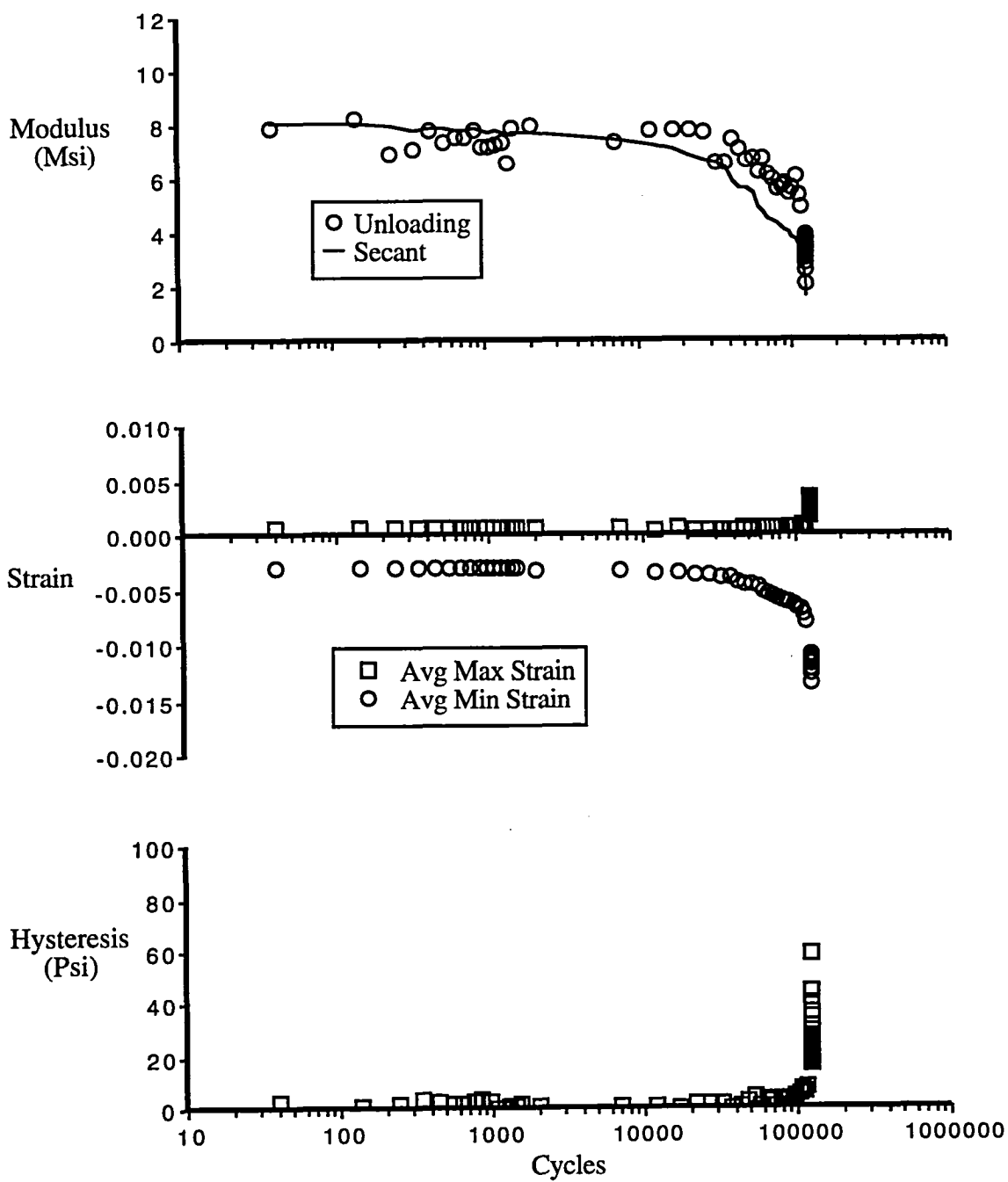
Sample C5-3
 $S_C = 23,152$ psi (64.5 % of static), $N_f = 14,053$ cycles



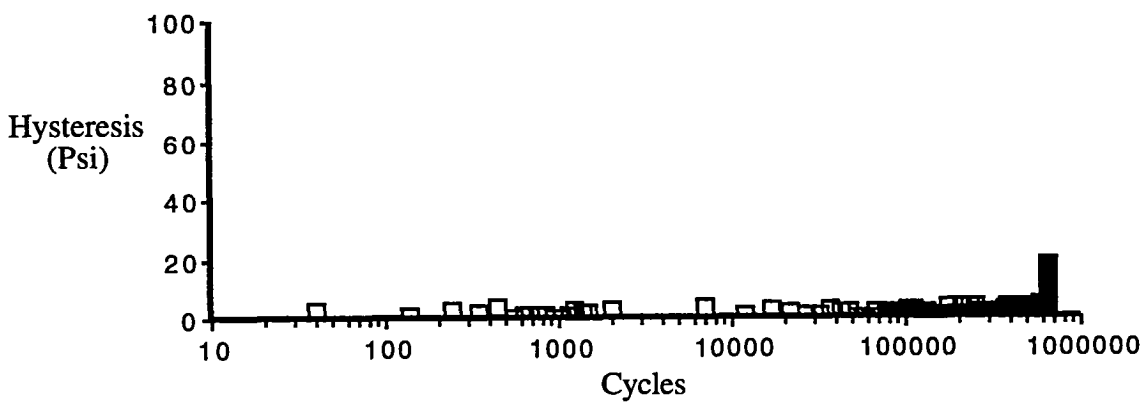
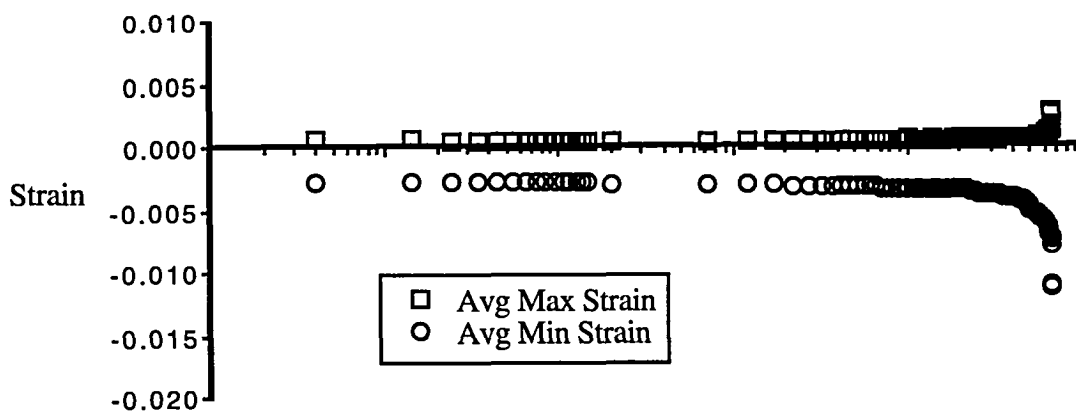
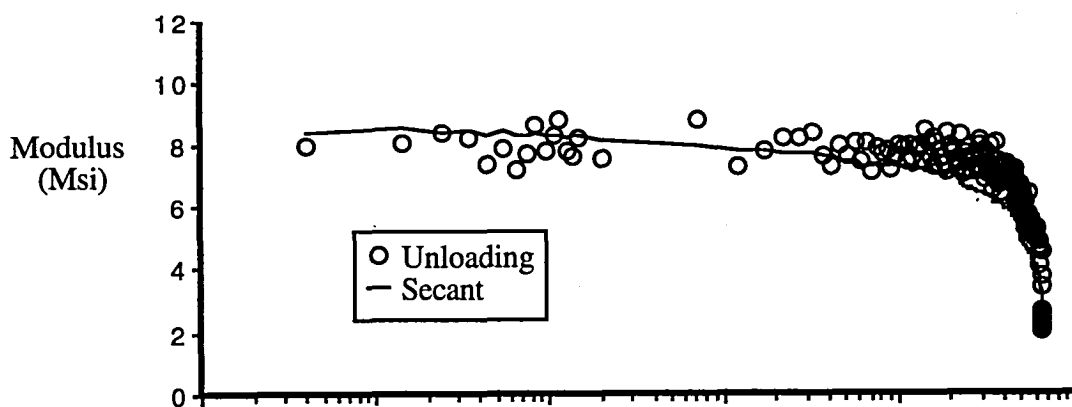
Sample C2-2
 $S_c = 22,613$ psi (63.0 % of static), $N_f = 58,940$ cycles



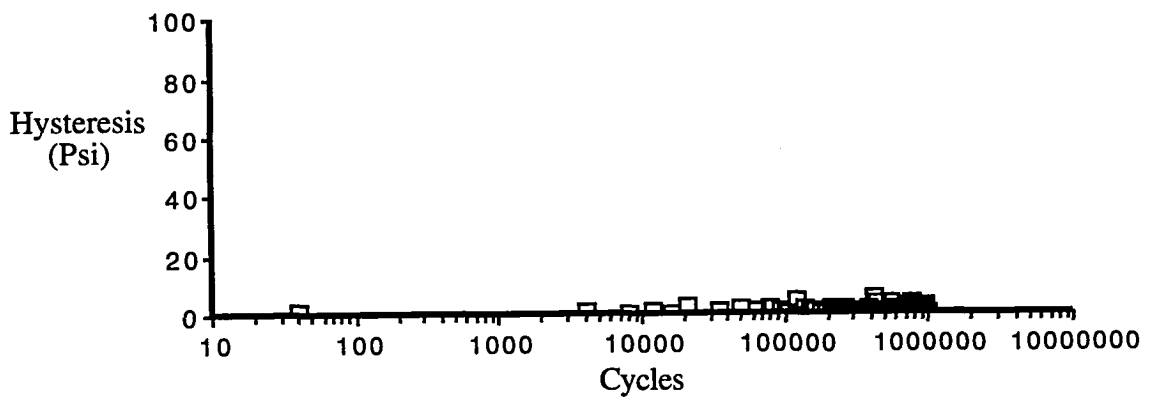
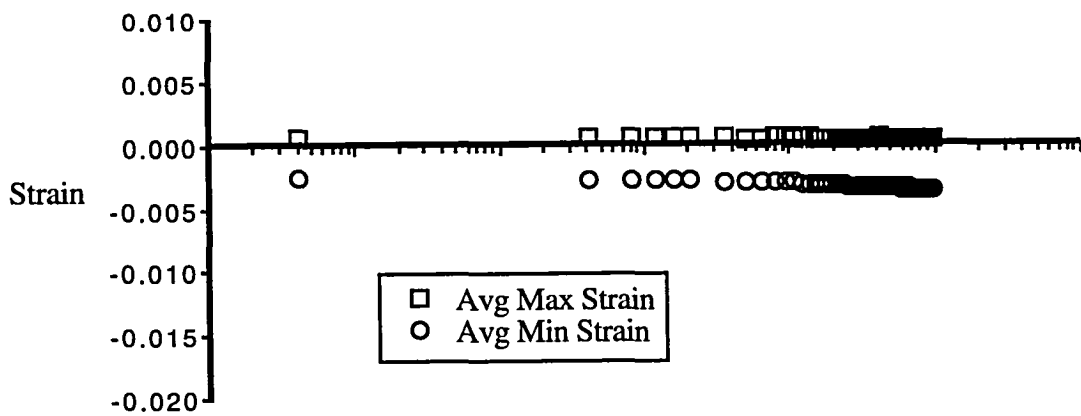
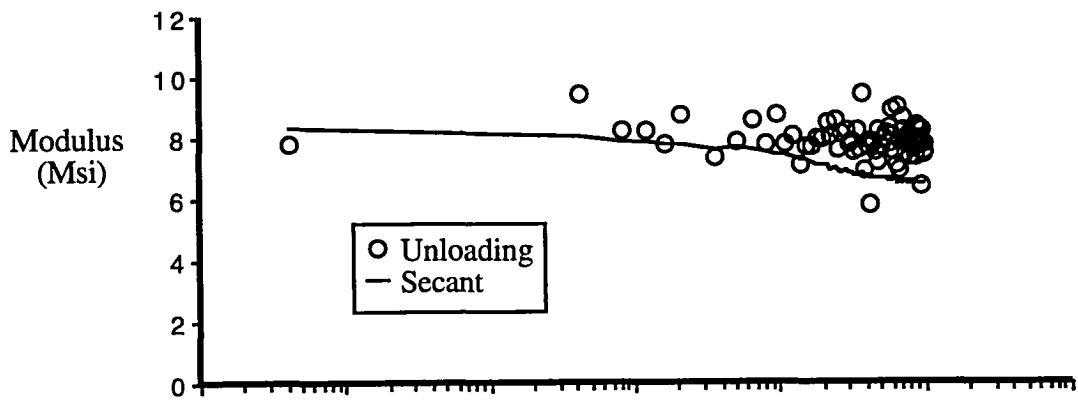
Sample C4-2
 $S_C = 24,474$ psi (68.2 % of static), $N_f = 113,100$ cycles



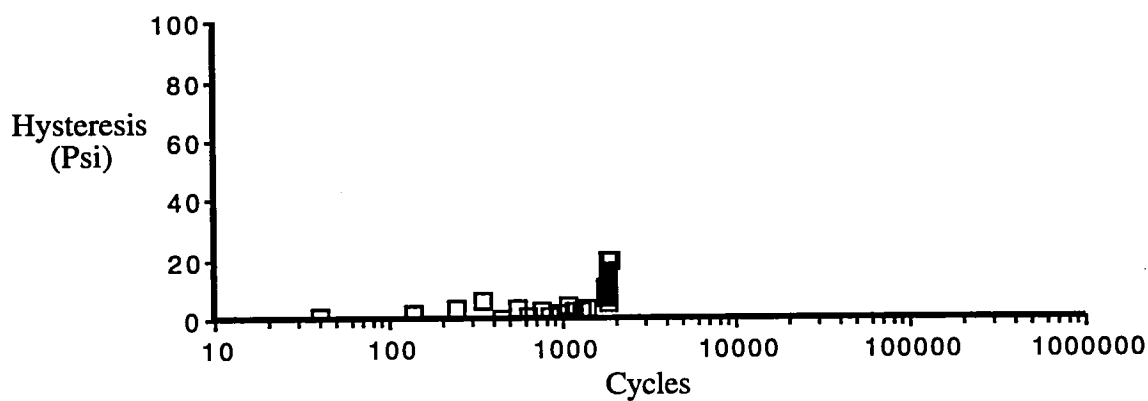
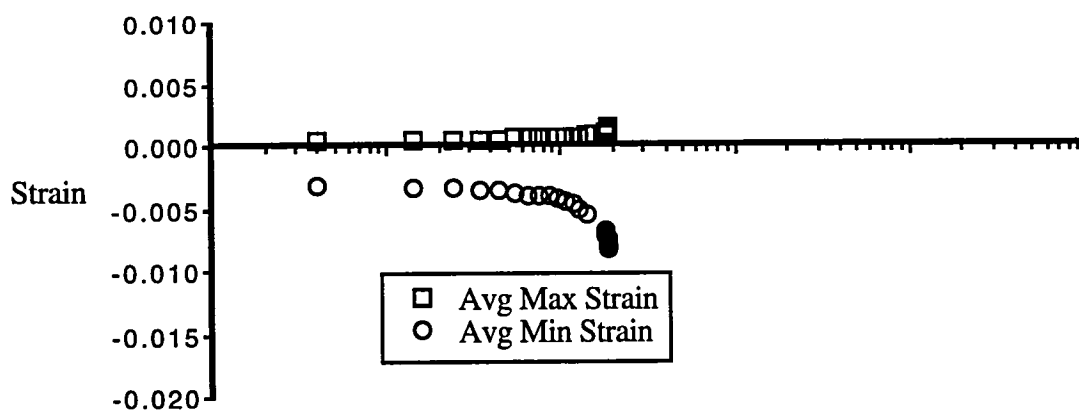
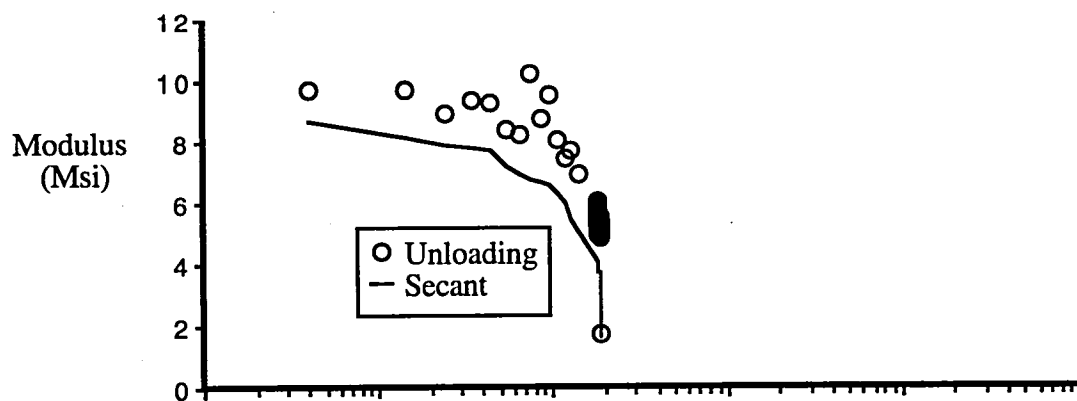
Sample C1-1
 $S_C = 23,331$ psi (65.0 % of static), $N_f = 123,507$ cycles



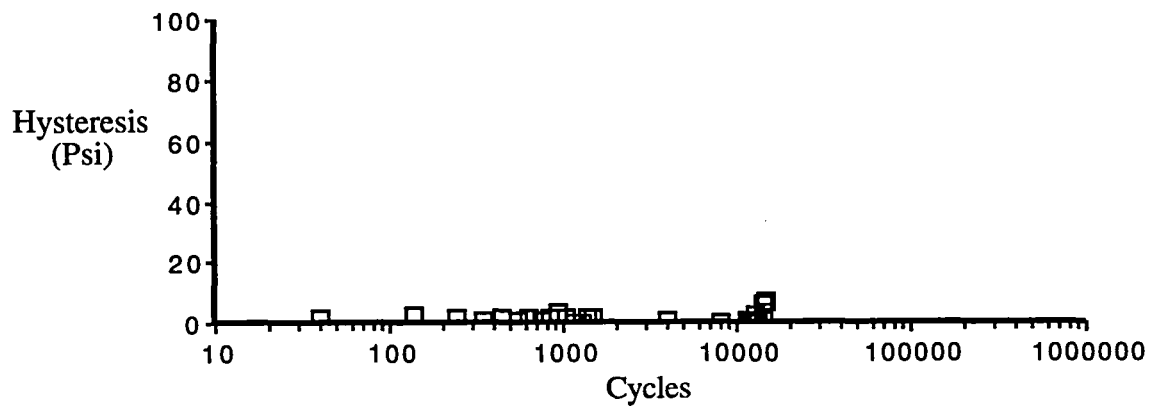
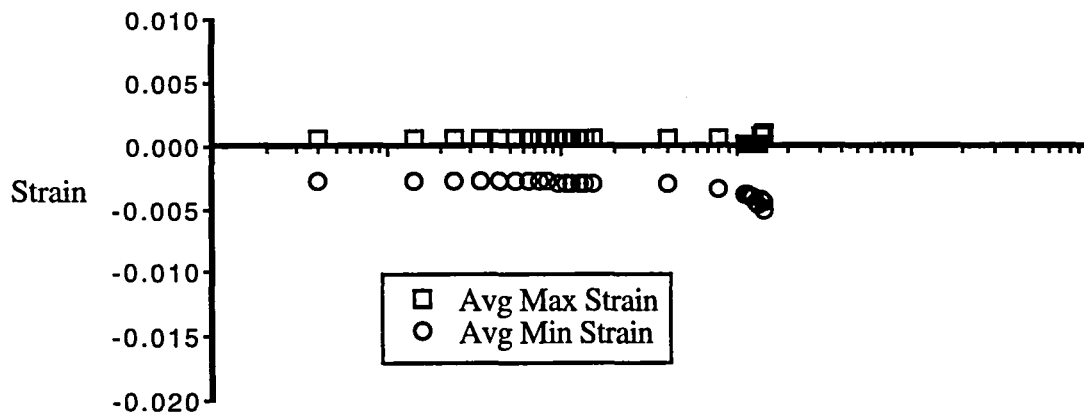
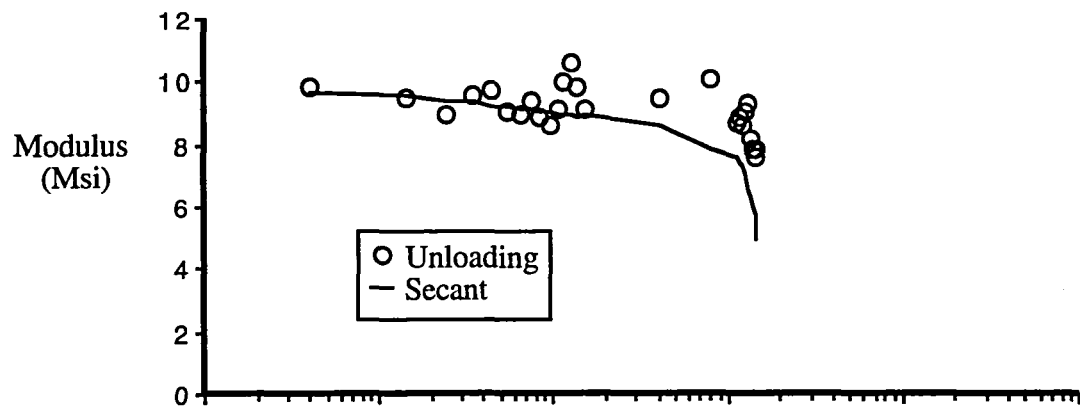
Sample C4-1
 $S_C = 22,830$ psi (63.6 % of static), $N_f = 664,218$ cycles



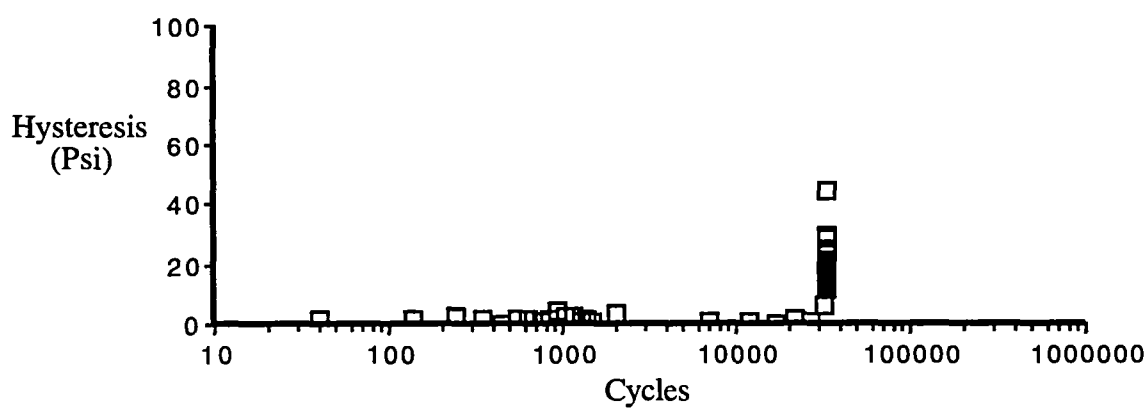
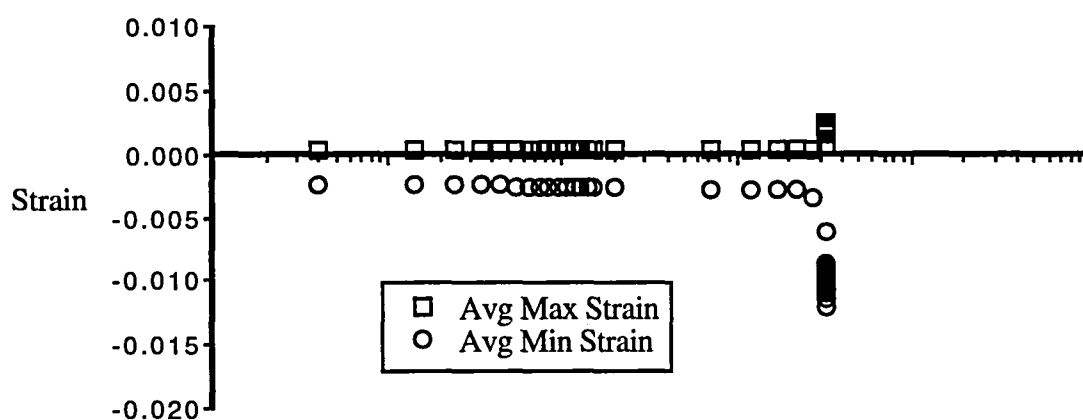
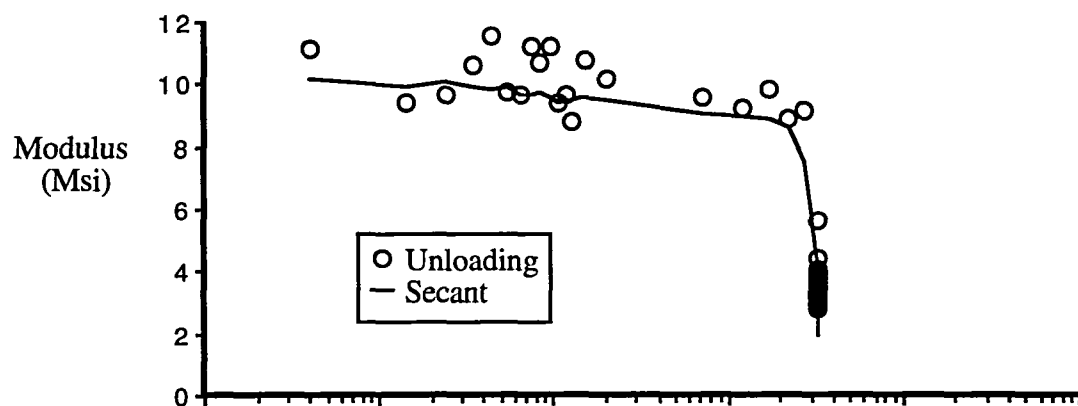
Sample C1-3
 $S_C = 21,536$ psi (60.0 % of static), $N_f = 1,000,000$ cycles (infinite)



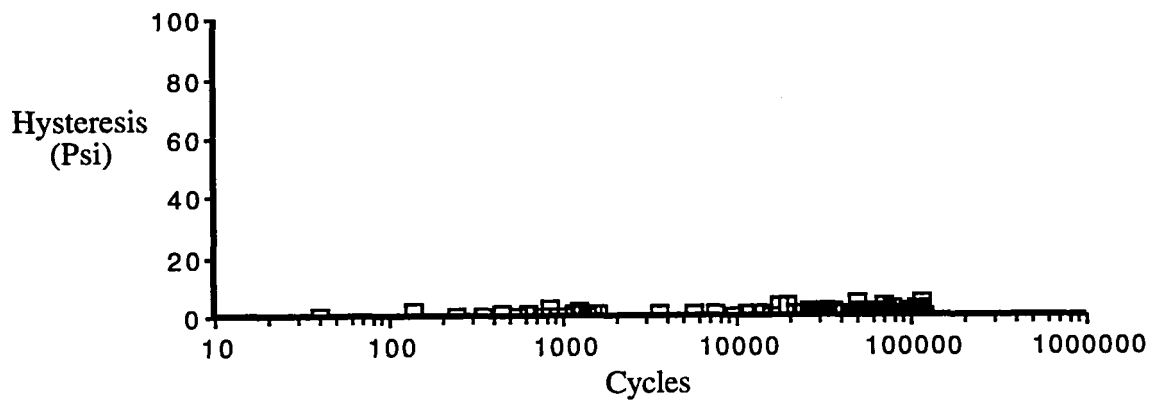
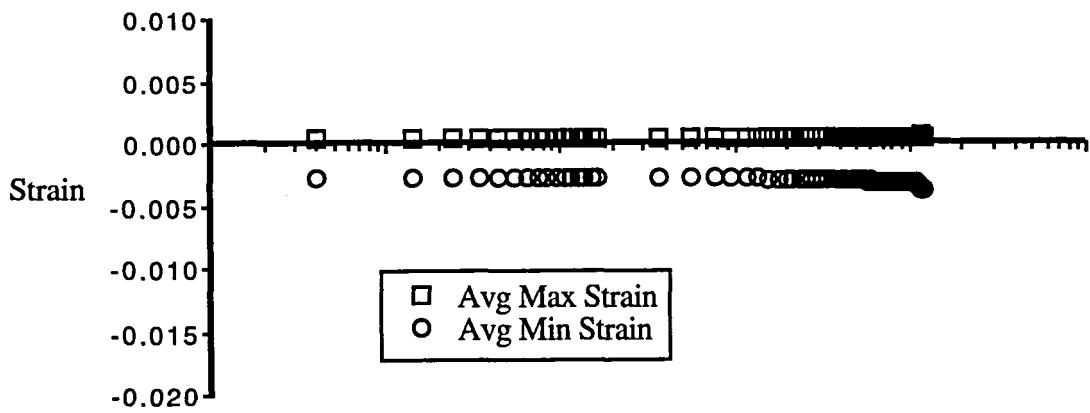
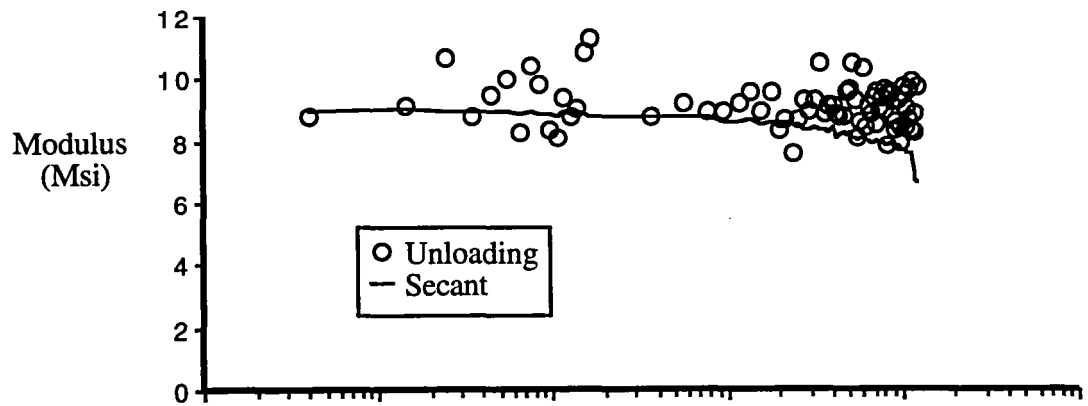
Sample D7-3
 $S_c = 26,119$ psi (79.0 % of static), $N_f = 1,705$ cycles



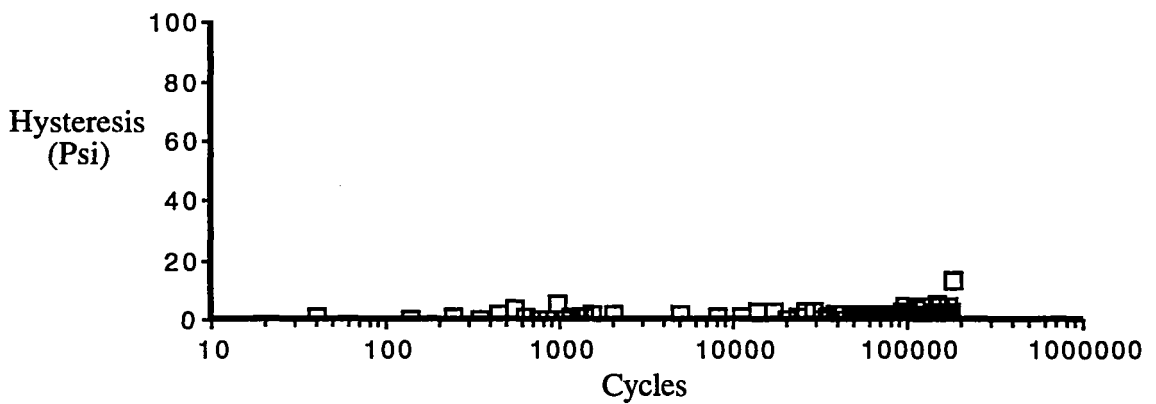
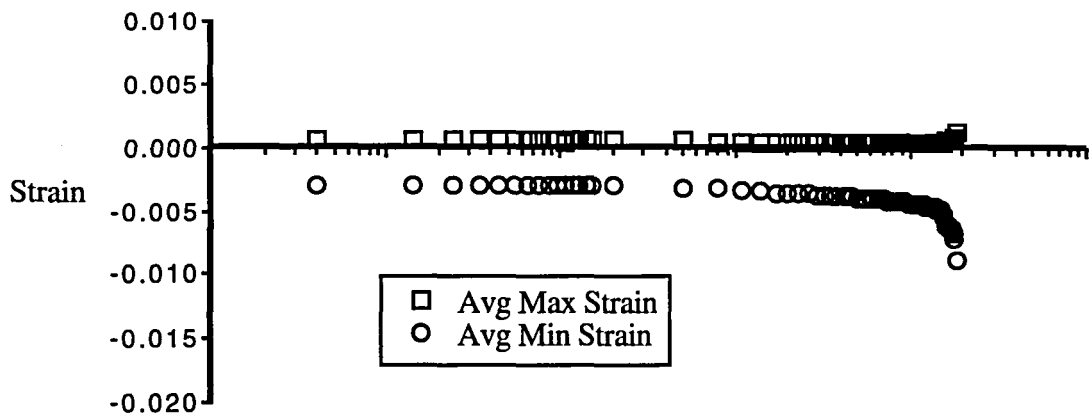
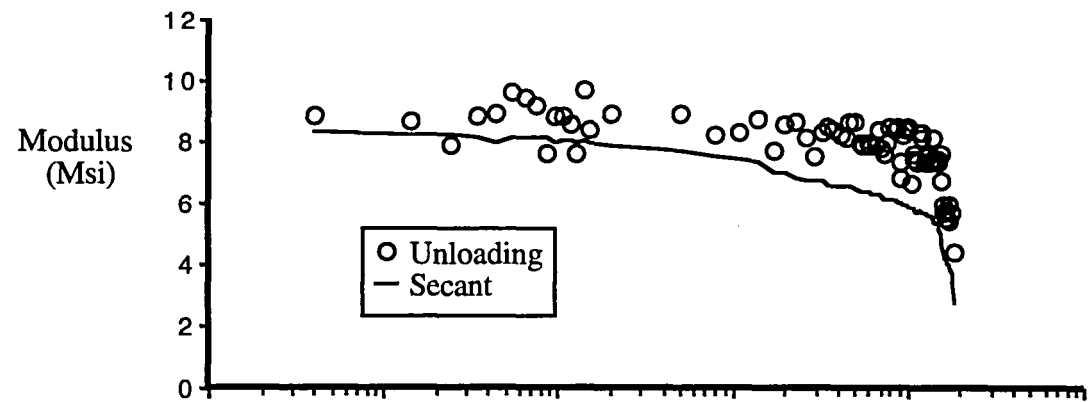
Sample D5-3
 $S_c = 25,458$ psi (77.0 % of static), $N_f = 14,751$ cycles



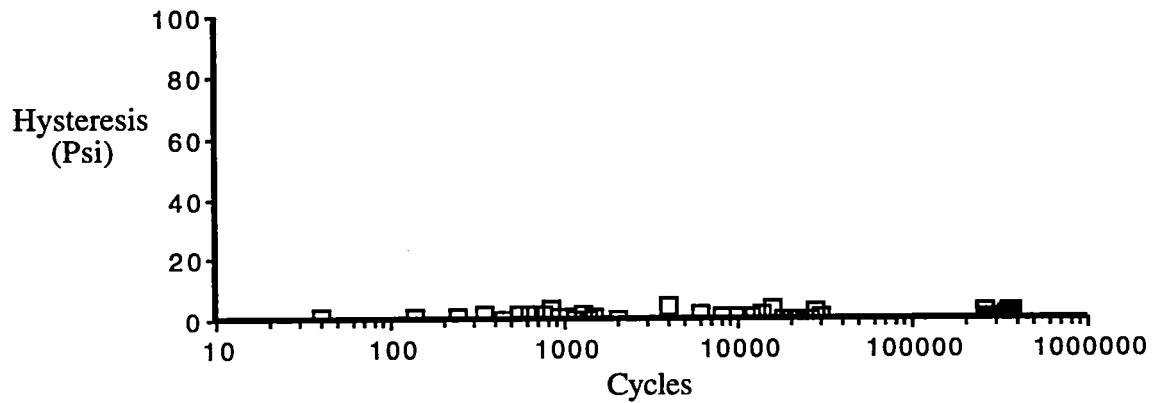
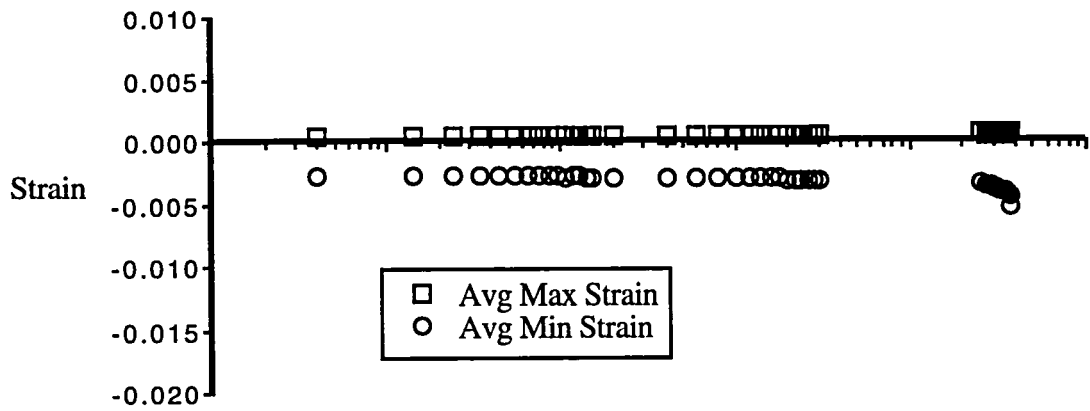
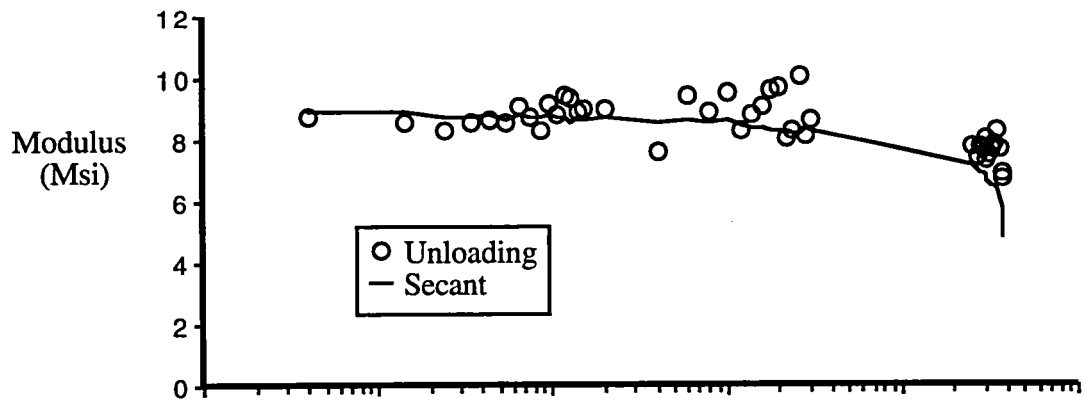
Sample D7-2
 $S_C = 23,520$ psi (71.1 % of static), $N_f = 33,062$ cycles



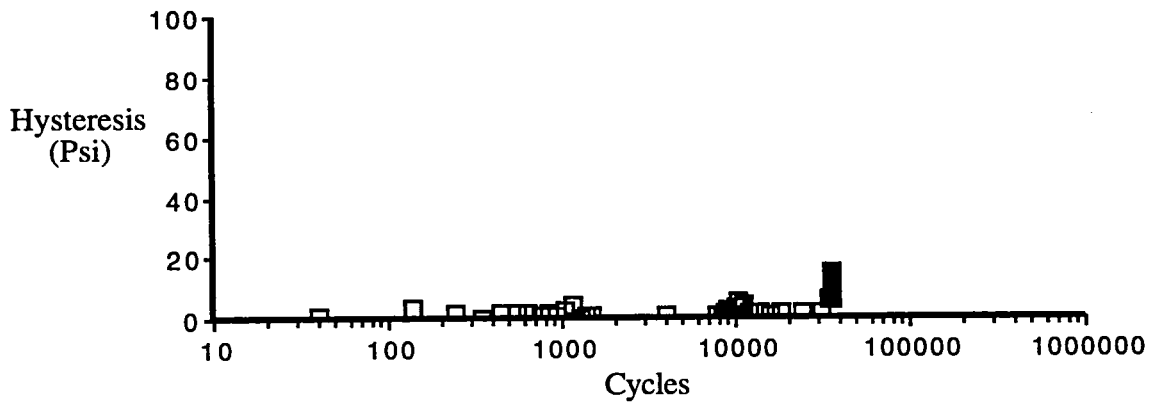
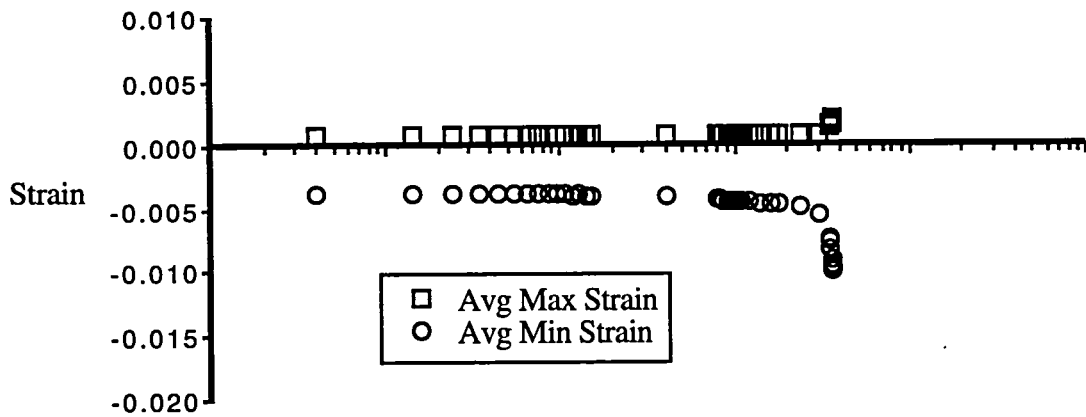
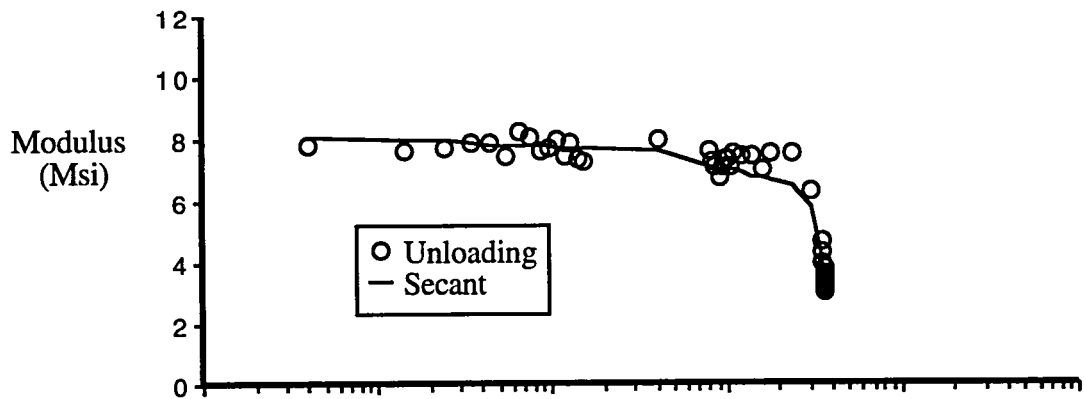
Sample D6-3
 $S_C = 23,682$ psi (71.6 % of static), $N_C = 131,266$ cycles



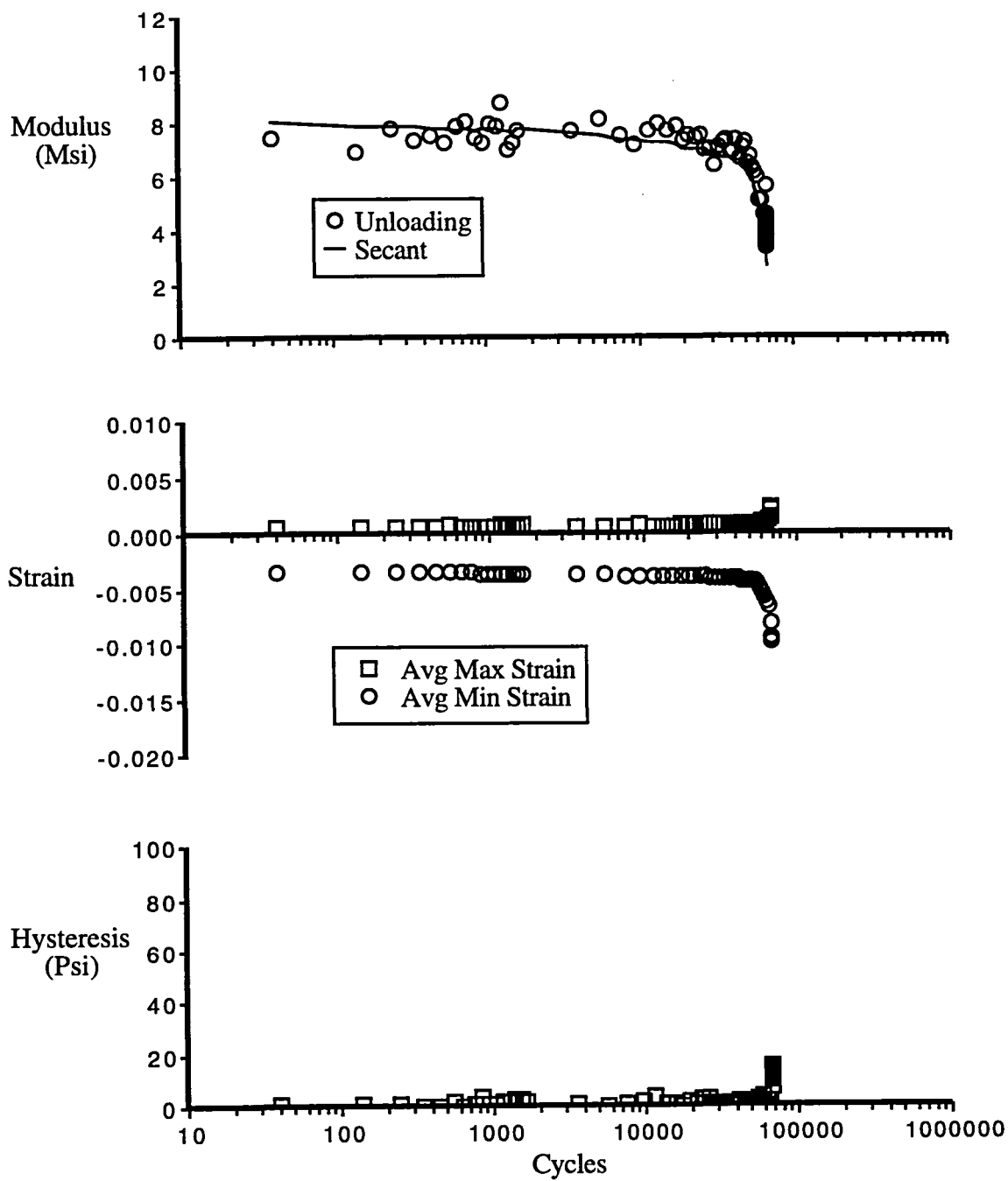
Sample D5-1
 $S_c = 23,143$ psi (70.0 % of static), $N_f = 185,858$ cycles



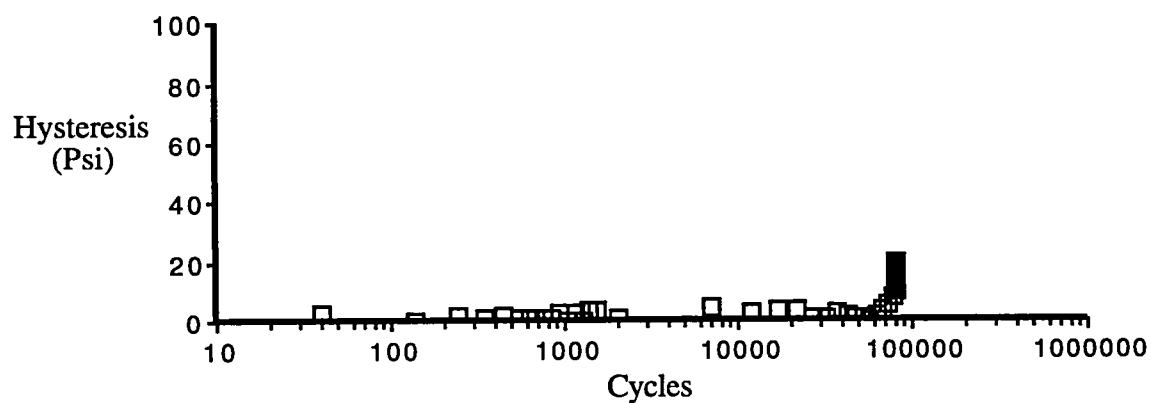
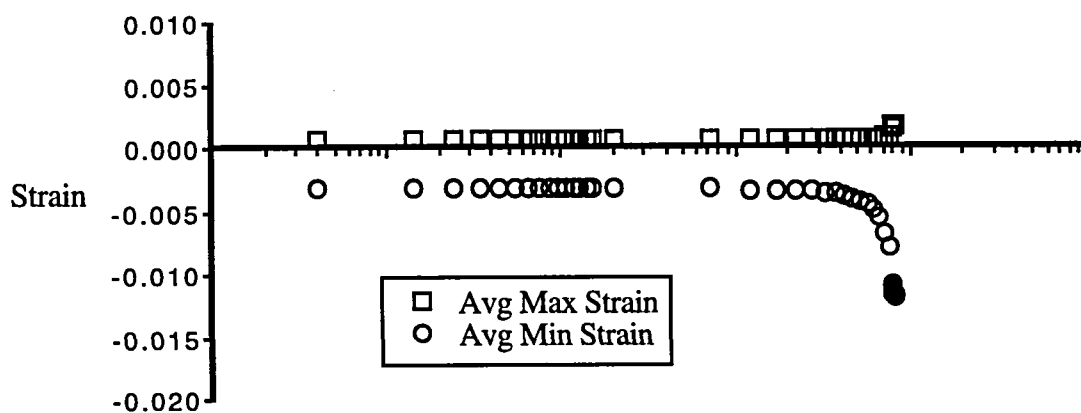
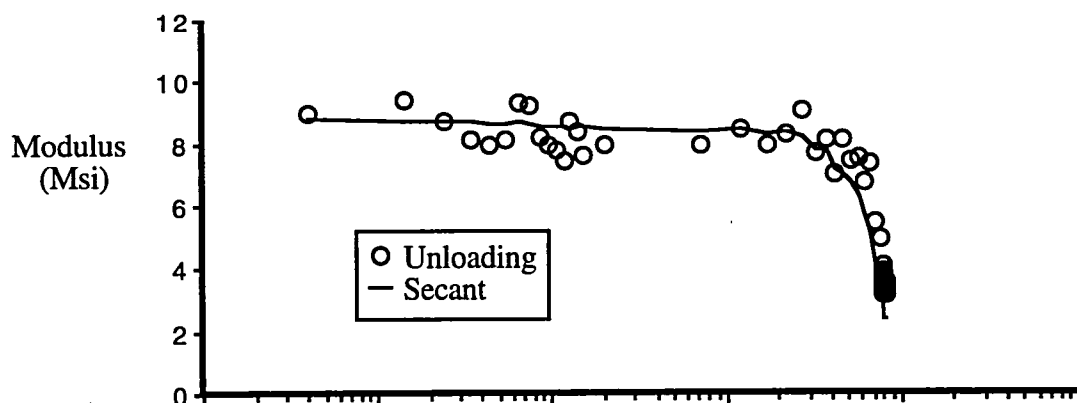
Sample D5-2
 $S_c = 24,108$ psi (72.9 % of static), $N_f = 385,190$ cycles



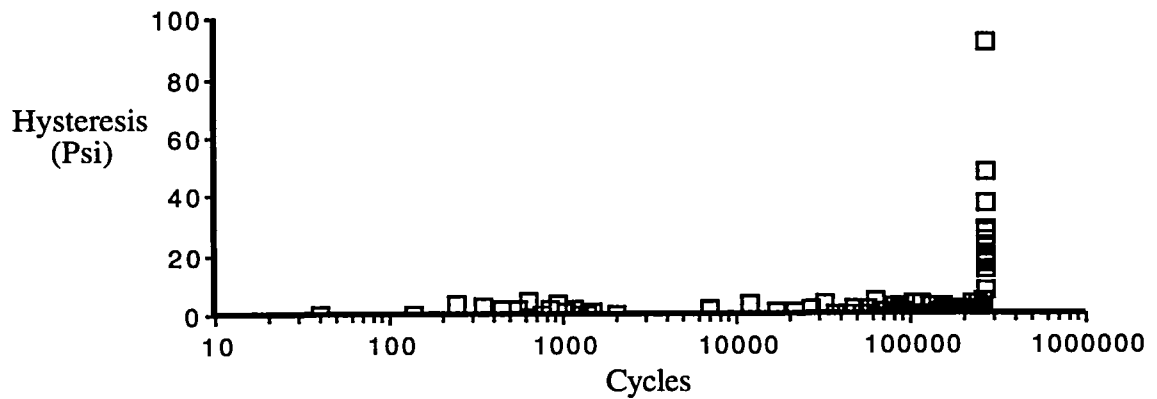
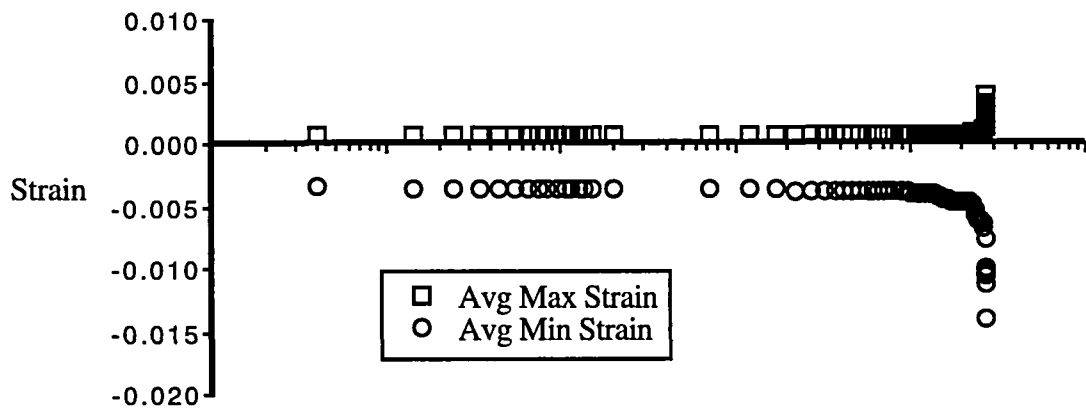
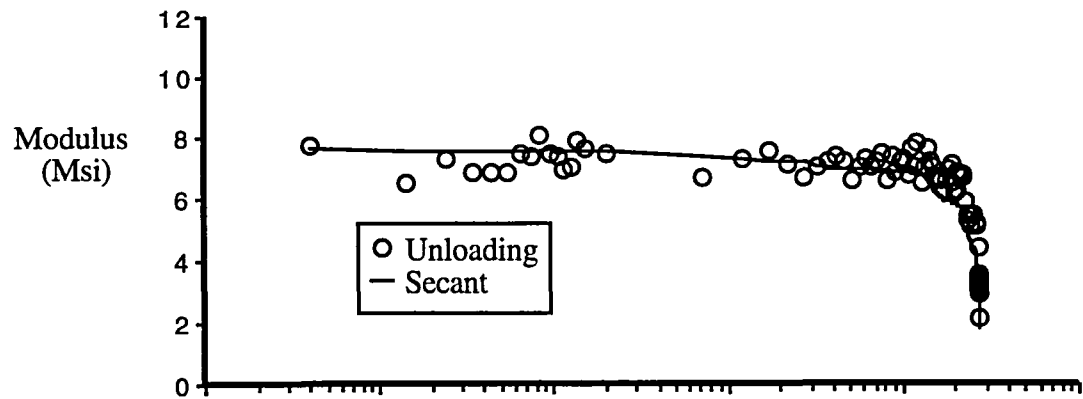
Sample F3-1
 $S_c = 29,688$ psi (74.0 % of static), $N_f = 36,002$ cycles



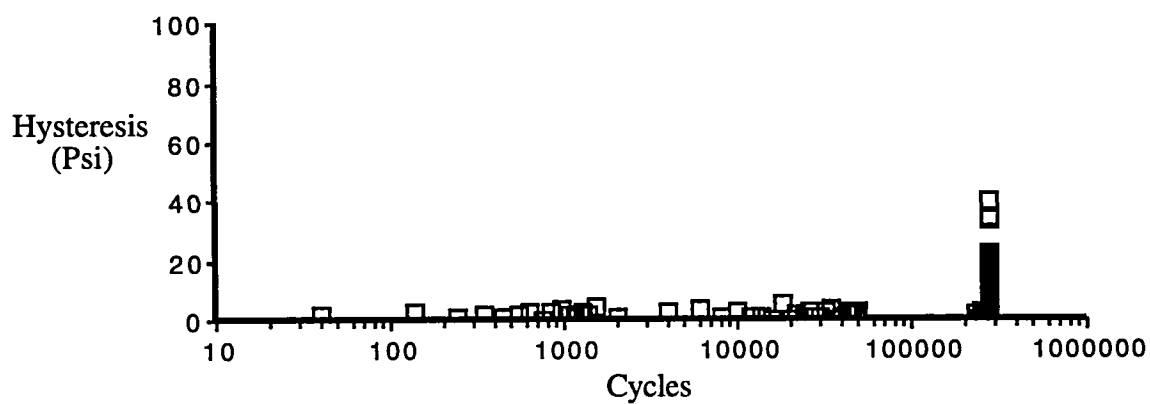
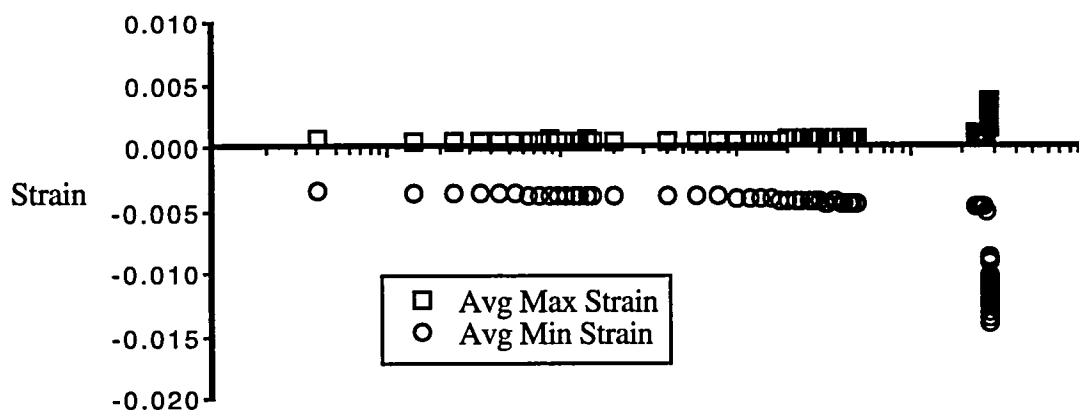
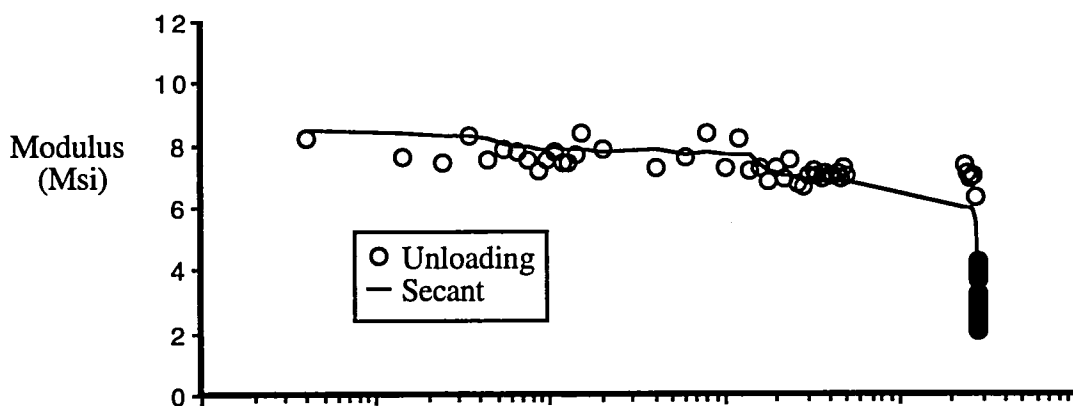
Sample F4-2
 $S_c = 26,878$ psi (67.0 % of static), $N_f = 68,857$ cycles



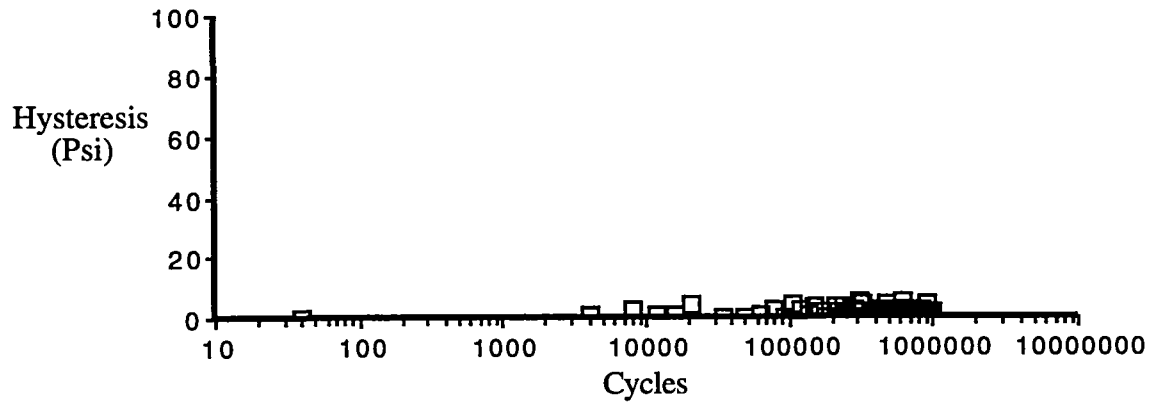
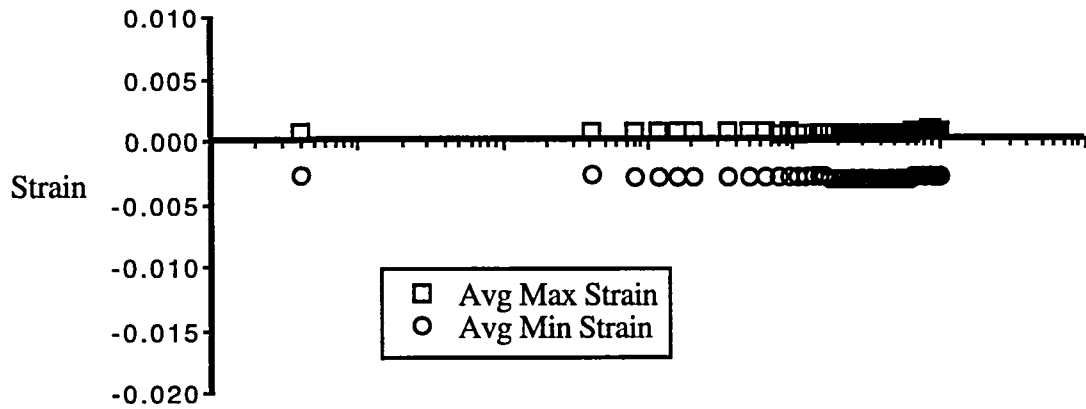
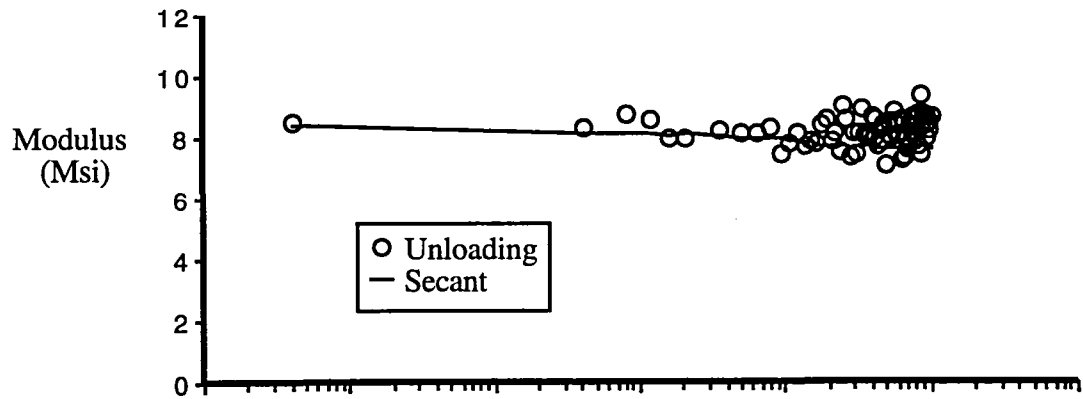
Sample F4-3
 $S_c = 26,917$ psi (67.1 % of static), $N_f = 80,134$ cycles



Sample F3-3
 $S_c = 26,077$ psi (65.0 % of static), $N_f = 269,009$ cycles



Sample F3-2
 $S_C = 28,083$ psi (70.0 % of static), $N_f = 277,875$ cycles



Sample F2-1
 $S_C = 23,000$ psi (57.3 % of static), $N_f = 1,000,000$ cycles (infinite)

LITERATURE CITED

1. Kam, C.Y., and Walker, J.V., "Toughened Composites Selection Criteria," Toughened Composites, ASTM STP 937, Norman J. Johnson, Ed., American Society for Testing and Materials, Philadelphia, 1987, pp. 9-22.
2. Bohon, H.L., "Opportunities for Composites in Commercial Transport Structures," Tough Composite Materials: Recent Developments, NASA Langley Research Center, Hampton Virginia (Noyes, Park Ridge, New Jersey, 1985), pp. 421-446.
3. Maddux, G.E. and Sendeckyj, G.P., "Holographic Techniques for Defect Detection Composite Materials," in Nondestructive Evaluation and Flaw Criticality for Composite Material, ASTM STP 696, R.B. Pipes, Ed., American Society for Testing and Materials, Philadelphia, 1979, pp. 26-44.
4. Avery, J.G., and Porter, T.R., "Comparisons of the Ballistic Impact Response of Metals and Composites for Military Aircraft Applications," Foreign Object Impact Damage to Composites, ASTM STP 568, American Society for Testing and Materials, Philadelphia, 1975, pp. 3-29.
5. Beaumont, P.W.R., Riewald, P.G., and Zweban, C., "Methods for Improving the Impact Resistance of Composite Materials," Foreign Object Impact Damage to Composites, ASTM STP 568, American Society for Testing and Materials, Philadelphia, 1975, pp. 134-158.
6. Baumann, K.J., Kennedy, W.H., and Herbert, D.L., "Computed Tomography X-Ray Scanning Nondestructive Evaluation of Graphite/Epoxy Coupons," Journal of Composite Materials, Vol 18, Nov 1984, pp. 536-544.
7. Chaturved, S.K. and Sierakowski, R.L., "Effects of Impactor Size on Impact Damage Growth and Residual Properties in and SMC-R50 Composite," Journal of Composite Materials, Vol 19, March 1985, pp. 100-113.
8. Walter, R.W., Johnson, R.W., June, R.R., and McCarty, J.E., "Designing for Integrity in Long-Life Composite Aircraft Structures," Fatigue of Filamentary Composite Materials, ASTM STP 636, K.L. Reifsnider and K.N. Lauraitis, Eds., American Society for Testing and Materials, Philadelphia, 1977, pp. 228-247.
9. Liu, D. and Lawrence, M.E., "Matrix Cracking in Impacted Glass/Epoxy Plates," Journal of Composite Materials, Vol 21, July 1987, pp. 594-609.
10. Liu, D., "Impact-Induced Delamination: A View of Bending Stiffness Mismatching," Journal of Composite Materials, Vol 22, July 1988, pp. 674-692.
11. Choi, H.Y., Wang, H.S., and Chang, F., "Effect of Laminate Configuration and Impactor's Mass on the Initial Impact Damage of Graphite/Epoxy Composite Plates due to Line-Loading Impact," Journal of Composite Materials, Vol 26, No. 6, 1992, pp. 804-827.

12. Avva, V.S., "Effect of Specimen Size on the Buckling Behavior of Laminated Composites Subjected to Low-Velocity Impact," Compression Testing of Homogeneous Metals and Composites, ASTM STP 808, Richard Chait and Ralph Papirno, Eds., American Society for Testing and Materials, Philadelphia, 1983, pp. 140-154.
13. Griffin, C.F., "Damage Tolerance of Toughened Resin Graphite Composites," Toughened Composites, ASTM STP 937, Norman J. Johnson, Ed., American Society for Testing and Materials, Philadelphia, 1987, pp. 23-33.
14. Williams, J.G., "Effect of Impact Damage and Open Holes on the Compression Strength of Tough Resin/High Strain Fiber Laminates," Tough Composite Materials: Recent Developments, NASA Langley Research Center, Hampton Virginia (Noyes, Park Ridge, New Jersey, 1985), pp. 54-71.
15. Finn, S.R. and Springer, G.S., Composite Plates Impact Damage: An Atlas, (Technomic, Lancaster, Pennsylvania, 1991.)
16. Moon, D.G. and Kennedy, J.M., "Experimental Evaluation of Damage Growth from Impacts in Stitched Composites," The Fifth Symposium on Composite Materials: Fatigue and Fracture, American Society for Testing and Materials, Atlanta, Georgia, May 4-6, 1993.
17. Liu, D., "Delamination Resistance in Stitched and Unstitched Composite Plates Subjected to Impact Loading," Journal of Reinforced Plastics and Composites, Vol. 9, Jan 1990, pp. 59-69.
18. Dexter, H.B. and Funk, J.G., "Impact Resistance and Interlaminar Fracture Toughness of Through-the-Thickness Reinforced Graphite/Epoxy," AIAA paper 86-1020-LP, May 1986.
19. Dow, M.B. and Smith, D.L., "Damage-Tolerant Composite Materials Produced by Stitching Carbon Fabrics," Proceedings of 21st International SAMPE Technical Conference, Atlantic City, New Jersey, Sept 1989.
20. Wolterman, R.L., Kennedy, J.M., and Farley, G.L., "Fatigue Damage in Thick, Cross-Ply Laminates with a Center Hole," Composite Materials: Fatigue and Fracture, Fourth Volume, ASTM STP 1156, W.W. Stinchcomb and N.E. Ashbaugh, Eds., American Society for Testing and Materials, Philadelphia, 1993, pp. 473-490.
21. Labor, J.D., "Impact Damage Effects on the Strength of Advanced Composites," Nondestructive Evaluation and Flaw Criticality for Composite Material, ASTM STP 696, R.B. Pipes, Ed., American Society for Testing and Materials, Philadelphia, 1979, pp. 172-184.
22. Ramkumar, R.L., "Compression Fatigue Behavior of Composites in the Presence of Delaminations," Damage in Composite Materials, ASTM STP 775, K.L. Reifsnider, Ed., American Society for Testing and Materials, Philadelphia, 1982, pp. 184-210.

23. Ratwani, M.M. and Kan, H.P., "Effect of Stacking Sequence on Damage Propagation and Failure Modes in Composite Laminates," Damage in Composite Materials, ASTM STP 775, K.L. Reifsnider, Ed., American Society for Testing and Materials, Philadelphia, 1982, pp. 211-228.
24. Badaliane, R. and Dill, H.D., "Damage Mechanism and Life Prediction of Graphite/Epoxy Composites," Damage in Composite Materials, ASTM STP 775, K.L. Reifsnider, Ed., American Society for Testing and Materials, Philadelphia, 1982, pp. 229-242.
25. Schütz, D., Gerharz, J.J., and Alschweig, E., "Fatigue Properties of Unnotched, Notched, and Jointed Specimens of a Graphite/Epoxy Composite," Fatigue of Fibrous Composite Materials, ASTM STP 723, American Society for Testing and Materials, Philadelphia, 1981, pp. 31-47.
26. Whitcomb, J.D., "Experimental and Analytical Study of Fatigue Damage in Notched Graphite/Epoxy Laminates," Fatigue of Fibrous Composite Materials, ASTM STP 723, American Society for Testing and Materials, Philadelphia, 1981, pp. 48-63.
27. Tsangarakis, N., Gruber, J.J., and Nunes, J., "Nondestructive Evaluation of Fatigue Damage in Alumina Fiber Reinforced Aluminum," Journal of Composite Materials, Vol 19, May 1985, pp. 250-268.
28. Porter, T.R., "Evaluation of Flawed Composite Structure Under Static and Cyclic Loading," Fatigue of Filamentary Composite Materials, ASTM STP 636, K.L. Reifsnider and K.N. Lauraitis, Eds., American Society for Testing and Materials, Philadelphia, 1977, pp. 152-170.
29. Tsai, G.C., Doyle, J.F., and Sun, C.T., "Frequency Effects on the Fatigue Life and Damage of Graphite/Epoxy Composites," Journal of Composite Materials, Vol 21, Jan 1987, pp. 2-13.
30. Soutis, C. and Fleck, N.A., "Static Compression Failure of Carbon Fiber T800/924C Composite Plate with a Single Hole," Journal of Composite Materials, Vol 24, May 1990, pp. 536-558.
31. Lessard, L.B. and Chang, F., "Damage Tolerance of Laminated Composites Containing an Open Hole and Subjected to Compressive Loadings: Part II - Experiment", Journal of Composite Materials, Vol 25, Jan 1991, pp. 44-64.
32. Soutis, C., Fleck, N.A., and Smith, P.A., "Failure Prediction Technique for Compression Loaded Carbon Fiber-Epoxy Laminate with Open Holes," Journal of Composite Materials, Vol 25, Nov 1991, pp. 1476-1498.
33. Guynn, E.G., Bradley, W.L., and Ochoa, O.O., "A Parametric Study of Variables That Affect Fiber Microbuckling Initiation in Composite Laminates: Part 2 - Experiments," Journal of Composite Materials, Vol 26, No. 11, 1992, pp. 1617-1643.

34. O'Brien, T.K., "Analysis of Local Delaminations and Their Influence on Composite Laminate Behavior," Delaminating and Debonding Materials, ASTM STP 876, W.S. Johnson, Ed., American Society for Testing and Materials, Philadelphia, 1985, pp. 282-297.
35. Reifsnider, K.L., "Fatigue Behavior of Composite Materials," International Journal of Fracture, Vol 16, No 6, Dec 1980, pp. 563-583.
36. Highsmith, A.L. and Reifsnider, K.L., "Stiffness-Reduction Mechanisms in Composite Laminates," Damage in Composite Materials, ASTM STP 775, K.L. Reifsnider, Ed., American Society for Testing and Materials, Philadelphia, 1982, pp. 103-117.
37. O'Brien, T.K. and Reifsnider, K.L., "Fatigue Damage Evaluation Through Stiffness Measurements in Boron-Epoxy Laminates," Journal of Composite Materials, Vol 15, Jan 1981, pp. 55-70.
38. Johnson, W.S., "Mechanisms of Fatigue Damage in Boron/Aluminum Composites," Damage in Composite Materials, ASTM STP 775, K.L. Reifsnider, Ed., American Society for Testing and Materials, Philadelphia, 1982, pp. 83-102.
39. Pipes, R.B., Nondestructive Evaluation and Flaw Criticality for Composite Materials, ASTM STP 696, American Society for Testing and Materials, Philadelphia, 1979, pp. 96-98.
40. Starnes, J.H., Jr., Rhodes, M.D., and Williams, J.G., "Effect of Impact Damage and Holes on the Compressive Strength of a Graphite/Epoxy Laminate," Nondestructive Evaluation and Flaw Criticality for Composite Materials, ASTM STP 696, American Society for Testing and Materials, Philadelphia, 1979, pp. 145-171.
41. Bakis, C.E., Simonds, R.A., and Stinchcomb, W.W., "A Test Method to Measure the Response of Composite Materials Under Reversed Cyclic Loads," Test Methods and Design Allowables for Fibrous Composites: 2nd Volume, ASTM STP 1003, C.C. Chamis, Ed., American Society for Testing and Materials, Philadelphia, 1989, pp. 180-193.
42. Farley, G.L., "A Mechanism Responsible for Reducing Compression Strength of Through-the-Thickness Reinforced Composite Material," Journal of Composite Materials, Vol 26, No. 12, 1992, pp. 1784-1795.
43. Chung, W.C., Jang, B.Z., Chang, T.C., Hwang, L.R., and Wilcox, R.C., "Fracture Behavior in Stitched Multidirectional Composites," Materials Science and Engineering, Structure Materials: Properties, Microstructures and Processing, Vol A112, No. 1-2, June 1989, pp. 157-173.
44. Annual Book of ASTM Standards: Part 41, American Society for Testing and Materials, Philadelphia, 1980, pp. 81-86.
45. Reifsnider, K.L., Stinchcomb, W.W., and O'Brien, T.K., "Frequency Effects on a Stiffness-Based Fatigue Failure Criterion in Flawed Composite Specimens," Fatigue of Filamentary Composite Materials, ASTM STP 636, K.L. Reifsnider and K.N. Lauraitis, Eds., American Society for Testing and Materials, Philadelphia, 1977, pp. 171-184.

46. Phillips, E.P., "Effects of Truncation of a Predominantly Compression Load Spectrum on the Life of a Notched Graphite/Epoxy Laminate," Fatigue of Fibrous Composite Materials, ASTM STP 723, American Society for Testing and Materials, 1981, pp. 197-212.
47. Written Communication with Buddy Poe, NASA Langley Research Center, Hampton Virginia, June 1992.
48. Written Communication with Suzanne Asselin, Nomex/Kevlar Sales, Wilmington Delaware, March 1994.
49. Personal Communication with Charlie Miller, Mitsui Plastics, Marietta Georgia, March 1994.
50. Personal Communication with Jeanne Hessling, Hercules Inc., Magna Utah, March 1994.
51. Personal Communication with Tim Collins, Owens Corning, Philadelphia, March 1994.

NASA Technical Library



3 1176 01422 0926